National Aerospace University "Kharkiv Aviation Institute"

Ministry of Education and Science of Ukraine

On the rights of the manuscript

TAN KUN

UDC 621.45.035.01: 621.794.4(043)

DISSERTATION

DEVELOPMENT OF SUPERSONIC NOZZLES FOR COLD SPRAYING

Specialty 134 – Aerospace engineering

Field of knowledge 13 – Mechanical engineering

Applied for the Doctor of Philosophy degree

The dissertation contains the results of my own research. The use of other authors' ideas, results and texts have references to the relevant source

_____K. TAN

Scientific adviser

Oleksandr SHORINOV, candidate of technical science, associate professor

Kharkiv‐2024

ABSTRACT

Tan Kun. Development of supersonic nozzles for cold spraying – Qualifying scientific work on the rights of the manuscript.

Dissertation for obtaining the scientific degree of Doctor of Philosophy in the field of knowledge 13 Mechanical engineering on specialty 134 – Aerospace engineering – National Aerospace University "Kharkiv Aviation Institute", Kharkiv, 2024.

The dissertation is devoted to the creation of an approach to the design of supersonic nozzles of various configurations for cold gas-dynamic spraying and the optimization of spraying parameters in the development of technological recommendations based on numerical modeling of the processes of the acceleration of powder particles in the gas flow and their high-speed deposition with the substrate surface. The object of research is the process of acceleration of powder particles by a supersonic flow in the nozzle channel for cold gas-dynamic spraying and high-speed interaction when the particles impact on the substrate. The subject of the study is the influence of the nozzle geometry and the parameters of the cold gas-dynamic spraying process on the temperature and speed of the powder particles in the flow.

The relevance and necessity of research is due to the development of cold gas-dynamic spraying technology in the field of surface engineering, as well as the use of technology to create volumetric additive materials. Increasing the productivity of the process and ensuring high performance indicators of coating quality can be achieved by improving equipment elements and optimizing spraying modes for forming coatings from given powder materials. In addition, the expansion of technological capabilities of equipment for spraying coatings on internal and hard-to-reach surfaces of parts will open new directions of practical application of technology in the field of spraying protective and restorative coatings.

The first chapter provides an overview of the current state of the researched problem and publications, the main focus of which is aimed at solving the problems

of the dissertation work, in particular, the use of numerical modeling methods to study the gas dynamics of two-phase flow in supersonic nozzles for cold gas dynamic spraying, and the study of the processes of interaction of powder particles with the substrate at high-speed depositions and formation of coatings. From the analysis of the publications, it was concluded that there is no comprehensive approach to the design of nozzles, as well as the optimization of the parameters of the cold gas-dynamic spraying process according to the criterion of particle speed at the moment of collision with the substrate.

The second chapter gives the main equations for describing the gas-dynamic features of the flow in supersonic nozzles for cold gas-dynamic spraying, which are used in the design of narrowing-expanding nozzles for spraying. A description of the phenomena that occur during the interaction of a powder particle with a surface during spraying is also presented. The models describing the interaction of a powder particle with a substrate, which are used for numerical simulation of high-speed deposition of a particle with a surface for homo- and heterogeneous materials are analyzed.

The third section presents the results of the development of a narrowing-expanding nozzle of optimal geometry. The effect of the length of the extended part of the supersonic nozzle (150 mm, 180 mm, 210 mm, and 240 mm) for low-pressure cold spraying (gas pressure up to 1.2 MPa) on the acceleration process of metal powder particles with a diameter of 25 mm was studied. The obtained results are compared with the results for the standard nozzle of the DYMET-405 installation with a length of the extended part of 120 mm. It was established that with an increase in the length of the expanding part, it is possible to obtain higher values of the velocity of the particle at the exit from the nozzle with the same initial parameters of the inlet gas. The effect of gas pressure at the nozzle inlet on the speed of powder particles for nozzles with different lengths of the extended part was studied. It was established that with an increase in pressure from 0.8 MPa to 1.2 MPa at a constant gas temperature of 900 K, the particle speed at the moment of deposition increases. The results of the development of rotary single-channel and multi-channel nozzles

for high-pressure cold gas-dynamic spraying for coating the internal surfaces of parts are presented. The process of acceleration of powder particles in the channels of these nozzles, depending on the sputtering modes and characteristics of the powders, as well as the schemes of feeding the powder into the nozzle was studied. On the basis of a multi-criteria analysis using the experiment planning methodology, response surfaces (dependence) of the speed of the powder particle on the spraying parameters in a wide range of values were constructed. Scientifically based recommendations have been developed for the selection of spraying modes of the investigated powders for the proposed nozzles based on the criterion of the maximum speed of the particle at the exit of the nozzle.

The fourth chapter presents the results of numerical modeling of the high-speed interaction of powder particles with the substrate at the moment of deposition for homo- and heterogeneous materials during cold gas-dynamic spraying. A comparative analysis of the existing approaches for describing the contact interaction of a powder particle with a substrate was carried out; conditions have been established for the use of one or the other for conducting research on the deposition of one and several particles. The effect of the temperature-velocity characteristics of the powder particle at the moment of contact with the substrate, as well as the temperature of the latter, on the degree of particle deformation according to the entered particle deformation coefficient K was studied. The optimization of spraying modes was carried out according to the criterion of minimum porosity on the example of a coating made of aluminum powder Al6061 due to the use of the developed and of the implemented software code into the calculation model for modeling the deposition of the number of powder particles. The given recommendations ensure that the porosity of the coating for the material under study is no more than 2%, and the deviation of the results using the model and numerical simulation does not exceed 3.5%.

The scientific novelty of the obtained results is as follows:

1) for the first time, a method of profiling supersonic single- and multi-channel right-angle nozzles for cold gas-dynamic spraying of coatings on internal and out-

off-view surfaces was proposed, which provides the necessary values of the speed of powder particles at the exit of the nozzle for their adhesion to the substrate when the flow is turned by 90°.

2) For the first time, based on the results of numerical modeling, the dependence of the temperature-velocity characteristics of the powder particles at the exit from the right-angle nozzle on the material of the particles, their size, temperature and gas pressure at the entrance to the nozzle was obtained.

3) For the first time, an approach to assigning cold gas-dynamic spraying modes is proposed, based on the planning of a multi-factor experiment, response surface methodology and GA+BPNN, which allows assigning the technological parameters of coating sputtering, which ensure that the powder particles achieve the speed necessary for their adhesion to the substrate.

4) For the first time, on the basis of numerical modeling and the planning methodology of a multifactorial experiment, the dependences of porosity on particle speed, its temperature, and the temperature of the substrate in the studied ranges of values were obtained.

The practical significance of the obtained results lies in the fact that the results obtained in the dissertation research can be used in solving a wide class of practical problems when developing technologies and technological recommendations for spraying protective and restorative coatings, in particular:

- the proposed method of profiling a right-angle supersonic nozzle for cold gas-dynamic spraying allows to determine the geometric parameters of the nozzle according to the specified characteristics of the used powder material, pressure and temperature of the gas at the nozzle entrance;

- the revealed features of the effect of the material of the powder particles, their size, initial values of temperature and gas pressure on the temperature and speed of particles at the exit from the nozzle, expand the understanding of the regularities of gas dynamics processes of two-phase flow in supersonic nozzles for cold gas dynamic spraying;

- the results of the study of the processes of acceleration of powder particles in

supersonic nozzles and high-speed deposition of particles on the substrate create a theoretical basis for improving the models of these processes, designing and creating equipment for cold gas-dynamic spraying;

- the approaches proposed in the dissertation regarding the designation of spraying modes can be used to optimize the parameters of cold gas-dynamic spraying in order to control and ensure the given characteristics of the coatings.

The results of the dissertation work on the development of supersonic nozzles for spraying and science-based recommendations for the selection of spraying modes can be implemented in research institutions, production and repair enterprises, which are engaged in researching the processes of cold gas-dynamic spraying and the practical application of technology for the formation of protective and restorative coatings.

Keywords: cold gas dynamic spraying, coating, numerical simulation, supersonic nozzle, optimization, porosity, high-speed deposition, powder.

АНОТАЦІЯ

Тань Кунь. Розроблення надзвукових сопел для холодного газодинамічного напилювання – Кваліфікаційна наукова робота на правах рукопису.

Дисертація на здобуття наукового ступеня доктора філософії з галузі знань 13 Механічна інженерія за спеціальністю 134 Авіаційна та ракетно-космічна техніка. – Національний аерокосмічний університет ім. М. Є. Жуковського «Харківський авіаційний інститут», Харків, 2024.

Дисертаційна робота присвячена створенню підходу до проєктування надзвукових сопел різної конфігурації для холодного газодинамічного напилювання та оптимізації параметрів напилювання при розробленні технологічних рекомендацій на основі чисельного моделювання процесів прискорення частинок порошку в газовому потоці та їх високошвидкісного зіткнення з поверхнею підкладки. Об'єктом дослідження є процес прискорення частинок порошку надзвуковим потоком в каналі сопла для холодного газодинамічного напилювання та високошвидкісної взаємодії при зіткненні частинок з підкладкою. Предметом дослідження є закономірності впливу геометрії сопла та параметрів процесу холодного газодинамічного напилювання на температуру та швидкість частинок порошку в потоці.

Актуальність та необхідність проведення досліджень обумовлена розвитком технології холодного газодинамічного напилювання в області інженерії поверхні, а також використання технології для створення об'ємних адитивних матеріалів. Підвищення продуктивності процесу та забезпечення високих експлуатаційних показників якості покриттів може бути досягнуто шляхом вдосконалення елементів обладнання та оптимізації режимів напилювання для формування покриттів із заданих порошкових матеріалів. Окрім того, розширення технологічних можливостей обладнання для напилювання покриттів на внутрішні та важкодоступні поверхні деталей,

відкриє нові напрямки практичного застосування технології в області напилювання захисних і відновлювальних покриттів.

В першому розділі наведено огляд сучасного стану досліджуваної проблеми та публікацій, основний фокус яких спрямовано на вирішення задач дисертаційної роботи, зокрема використання чисельних методів моделювання для дослідження газодинаміки двофазного потоку в надзвукових соплах для холодного газодинамічного напилювання, та дослідження процесів взаємодії частинок порошку з підкладкою при високошвидкісному зіткненні та формуванні покриттів. З аналізу публікацій зроблено висновок про відсутність комплексного підходу до проєктування сопел, а також оптимізації параметрів процесу холодного газодинамічного напилювання за критерієм швидкості частинки в момент зіткнення з підкладкою.

В другому розділі наведено основні рівняння для опису газодинамічних особливостей потоку в надзвукових соплах для холодного газодинамічного напилювання, що використовуються при проєктувані сопел для напилювання. Також представлено опис явищ, які протікають при взаємодії частинки порошку з поверхнею при напилюванні. Проаналізовано моделі опису взаємодії частинки порошку з підкладкою, яка використовуються для чисельне моделювання високошвидкісного зіткнення частинки з поверхнею для гомо- та гетерогенних матеріалів.

В третьому розділі представлено результати з розроблення сопла оптимальної геометрії. Досліджено вплив довжини розширної частини надзвукового сопла (150 мм, 180 мм, 210 мм, 240 мм) для холодного напилювання низького тиску (тиск газу до 1,2 МПа) на процес прискорення частинок порошку. Отримані результати порівняно з результатами для стандартного сопла установки ДИМЕТ-405 з довжиною розширної частини 120 мм. Встановлено, що зі збільшенням довжини розширної частини можна отримати більші значення швидкості частинки на виході з сопла за однакових початкових параметрах газу вході. Досліджено вплив тиску газу на вході в сопло на швидкість частинок порошку для сопел з різною довжиною

розширної частини. Встановлено, що зі збільшенням тиску з 0,8 МПа до 1,2 МПа при постійній температурі газу 900 К збільшується швидкість частинки в момент зіткнення. Представлено результати з розроблення поворотних одно- та багатоканальних сопел для холодного газодинамічного напилювання високого тиску для нанесення покриттів на внутрішні поверхні деталей. Досліджено процес прискорення частинок порошку в каналах цих сопел в залежності від режимів напилювання та характеристик порошків, а також схем підводу порошку в сопло. На основі багатокритеріального аналізу побудовано поверхні відгуку (залежності) швидкості частинки порошку від параметрів напилювання в широкому діапазоні значень. Розроблено науково-обґрунтовані рекомендації щодо вибору режимів напилювання досліджуваних порошків для запропонованих сопел за критерієм максимальної швидкості частинки на виході з сопла.

В четвертому розділі наведено результати чисельного моделювання високошвидкісної взаємодії частинок порошку з підкладкою в момент зіткнення для гомо- та гетерогенних матеріалів при холодному газодинамічному напилюванні. Проведено порівняльний аналіз існуючих підходів для опису контактної взаємодії частинки порошку з підкладкою; встановлено умови використання того чи іншого для проведення досліджень із зіткнення однієї та численності частинок. Досліджено вплив характеристик частинки порошку в момент зіткнення з підкладкою, а також температури останньої, на ступінь деформації частинки за введеним коефіцієнтом деформації частинки К. Проведена оптимізація режимів напилювання за критерієм мінімальної пористості на прикладі покриття з алюмінієвого порошку Al6061 за рахунок застосування розробленого та імплементованого програмного коду в розрахункову модель для моделювання осадження численності частинок порошку. Наведені рекомендації забезпечують отримання пористості покриття для досліджуваного матеріалу не більше 2%, а відхилення отриманих результатів з використанням моделі та чисельного моделювання не перевищує 3,5%.

Наукова новизна отриманих результатів полягає в такому:

1) уперше запропоновано метод профілювання надзвукових одно- та багатоканальних поворотних сопел для холодного газодинамічного напилювання покриттів на внутрішні та важкодоступні поверхні, яке забезпечує необхідні значення швидкості частинок порошку на виході з сопла для їх зчеплення з підкладкою при повороті потоку на 90°.

2) Уперше за результатами чисельного моделювання одержано залежності температурно-швидкісних характеристик частинок порошку на виході з поворотного сопла від матеріалу частинок, їх розміру, температури та тиску газу на вході в сопло.

3) Уперше запропоновано підхід до призначення режимів холодного газодинамічного напилювання, заснований на плануванні багатофакторного експерименту, методології поверхні відгуку і GA+BPNN, який дозволяє призначати технологічні параметри напилювання покриттів, що забезпечують досягнення частинками порошку швидкості, необхідної для їх зчеплення з підкладкою.

4) Уперше на основі чисельного моделювання та методології планування багатофакторного експерименту отримано залежності пористості від швидкості частинки, її температури, та температури підкладки в досліджуваних діапазонах значень.

Практична значущість отриманих результатів полягає в тому, що результати, отримані у дисертаційному дослідженні, можуть бути використані при розв'язуванні широкого класу практичних задач при розроблені технологій та технологічних рекомендацій з напилювання захисних і відновлювальних покриттів, зокрема:

- запропонований метод профілювання поворотного надзвукового сопла для холодного газодинамічного напилювання дозволяє визначити геометричні параметри сопла за заданими характеристиками використаного порошкового матеріалу, тиску та температури газу на вході в сопло;

- виявлені особливості впливу матеріалу частинок порошку, їх розміру,

початкових значень температури та тиску газу на температуру та швидкість частинок на виході з сопла, розширюють уявлення про закономірності процесів газодинаміки двофазного потоку в надзвукових соплах для холодного газодинамічного напилювання;

- результати дослідження процесів прискорення частинок порошку в надзвукових соплах та високошвидкісного зіткнення частинок з підкладкою створюють теоретичну базу для вдосконалення моделей цих процесів, проєктування та створення обладнання для холодного газодинамічного напилювання;

- запропоновані в дисертаційній роботі підходи щодо призначення режимів напилювання можуть бути використані для оптимізації параметрів холодного газодинамічного напилювання з метою керування та забезпечення заданих характеристик покриттів.

Результати дисертаційної роботи з розроблення надзвукових сопел для напилювання та науково-обґрунтовані рекомендації з вибору режимів напилювання можуть бути впроваджені в науково-дослідні установи, виробничі та ремонтні підприємства, які займаються дослідженнями процесів холодного газодинамічного напилювання та практичним застосуванням технології для формування захисних і відновлювальних покриттів.

Ключові слова: холодне газодинамічне напилювання, покриття, чисельне моделювання, надзвукове сопло, оптимізація, пористість, високошвидкісне зіткнення, порошок.

LIST OF APPLICANT'S PUBLICATIONS

Scientific works in which the main scientific results of the dissertation are published

Articles in scientific periodical publications included in category «A» of the List of scientific specialized publications of Ukraine, or in foreign publications indexed in the Web of Science Core Collection and/or Scopus databases:

1. Kun, T., Jie, H. W., Markovych, S., & Wang, Y. Dimet Laval nozzle expansion section analysis and optimization. Journal of Engineering Sciences, 2021, 8(2): F6-F10. DOI: https://doi.org/10.21272/jes.2021.8(2).f2. **(Scopus)**

2. Kun, T., Jie, H. W., Markovych, S., & Wang, Y. Optimization of cold spray nozzles based on the response surface methodology. Journal of Engineering Sciences, 2024, 11(1): F1-F11. DOI: https://doi.org/10.21272/jes.2024.11(1).f1. **(Scopus)**

3. Hu, W. J., Tan, K., Markovych, S., & Liu, X. L. Study of a cold spray nozzle throat on acceleration characteristics via CFD. Journal of Engineering Sciences, 2021, 8: 19-24. DOI: https://doi.org/10.21272/jes.2021.8(1).f3. **(Scopus)**

4. Hu, W., Tan, K., Markovych, S., & Cao, T. Research on structure and technological parameters of multi-channel cold spraying nozzle. Eastern-European Journal of Enterprise Technologies, 2021, 5(1(113)):6-14. DOI: https://doi.org/10.15587/1729-4061.2021.242707. **(Scopus, SJR=0.402, Q3)**

5. W. J. Hu, K. Tan, S. Markovych, T. T. Cao, and X. L. Liu. Research on the Adhesive Mechanism of Al + Ti Mixed Powders Deposited on Ti6Al4V Substrate by CS Using Abaqus/Explicit. Metallofiz. Noveishie Tekhnol, 2022, 44(5):613-621. DOI: https://doi.org/10.15407/mfint.44.05.0613. **(Scopus, SJR=0.402, Q3)**

Articles in scientific periodical publications included in the List of scientific specialized publications of Ukraine (category «Б»):

6. Tan, K., Markovych, S., Hu, W., Shorinov, O., & Wang, Y. R. Review of manufacturing and repair of aircraft and engine parts based on cold spraying technology and additive manufacturing technology. Aerospace Technic and Technology, 2020 (3): 53-70. DOI: https://doi.org/10.32620/aktt.2020.3.06.

7. Tan, K., Markovych, S., Hu, W., Shorinov, O., & Wang, YR. Review of application and research based on cold spray coating materials. Aerospace Technic and Technology, 2021 (1): 47-59. DOI: https://doi.org/10.32620/aktt.2021.1.05.

8. Tan, K., Hu, W., Shorinov, O., & Wang, YR. Simulating multi-particle deposition based on CEL method: studying the effects of particle and substrate temperature on deposition. Aerospace Technic and Technology, 2024, 1(193): 64-75. DOI: https://doi.org/10.32620/aktt.2024.1.06.

9. Tan, K. Analysis of spray particles entrance of Right-angle cold spray nozzle based on CFD. Mechanics and Advanced Technologies, 2023, 7(3(99)): F1-F11. DOI: https://doi.org/10.20535/2521-1943.2023.7.3.292244.

10. Tan, K. Numerical Study on Simulating the Deposition Process of Cold Spray Multi-Particle Al-6061 based on CEL Method. Mechanics and Advanced Technologies, 2024, 8(1(100)). DOI: https://doi.org/10.20535/2521-1943.2024.8.1 (100).295144.

11. Tan, K., Hu, W., Shorinov, O., & Wang, YR. Multi-parameter coupled optimization of Al6061 coating porosity based on the response surface method. Aerospace Technic and Technology, 2024, 3(195): 59-67. DOI: https://doi.org/10.32620/aktt.2024.3.05.

12. Hu, W., Markovych, S., Tan, K., Shorinov, O., & Cao, T. Research on wear resistance coating of aircraft titanium alloy parts by cold spraying technology. Aerospace Technic and Technology, 2020, (6): 61-71. DOI: https://doi.org/10.32620/aktt.2020.6.07.

13. Hu, W., Markovych, S., Tan, K., Shorinov, O., & Cao, T. Surface repair of aircraft titanium alloy parts by cold spraying technology. Aerospace Technic and Technology, 2020, (3): 30-42. DOI: https://doi.org/10.32620/aktt.2020.3.04.

Scientific works are certified for the approbation of dissertation materials

14. Tan Kun. Analysis of Particle Parameters of Multi-Channel Mixed Cross-Section Right-Angle Cold Spray Nozzle Structure. Integrated Computer Technologies in Mechanical Engineering (ICTM). ICTM 2023. Lecture Notes in Networks and Systems, LNNS. 1008, pp. 52–65, 2024, Kharkiv, Ukraine. DOI:

https://doi.org/10.1007/978-3-031-61415-6_5. **(Scopus)**

15. Tan, K., Markovych, S., Hu, W., Wang, Y., Shorinov, O., & Wang, Y. On the characteristics of cold spray technology and its application in aerospace industries. International Conference on Mechanical Engineering and Materials (ICMEM2020). Ser: Earth and Environmental Science. 2021. vol. 719(3), p.032023. DOI: https://doi.org/10.1088/1755-1315/719/3/032023. **(Scopus)**

16. Hu, W., Tan, K., Markovych, S., Cao, T. Structural Optimization of the Special Cold Spraying Nozzle via Response Surface Method. Integrated Computer Technologies in Mechanical Engineering (ICTM). ICTM 2021. Lecture Notes in Networks and Systems, vol. 367, pp. 110 – 122, 2022, Kharkiv, Ukraine. DOI: https://doi.org/10.1007/978-3-030-94259-5_11. **(Scopus)**

17. Hu, W., Tan, K., Markovych, S., Cao, T. A simple method for determining the critical velocity value of cold spraying via SPH. International Conference on Artificial Intelligence and Advanced Manufacturing (AIAM 2021). Manchester, England. pp. 215-221. 2021. DOI: https://doi.org/10.1109/AIAM54119.2021.00052. **(Scopus)**

18. Hu, W., Tan, K., Oleksandr, S., & Cao, T. Study on multi-parameter of cold spraying technology via RSM and BP+ GA methods. 5th International Conference on Artificial Intelligence and Advanced Manufacturing (AIAM 2023). pp. 272-278. 2021. DOI: https://doi.org/10.1049/icp.2023.2950. **(Scopus)**

19. Hu, W., Markovych, S., Shorinov, O., Tan, K. Deposition of protective and restorative cold spraying coating on aircraft parts made of titanium alloys. Відкрита науково-практична студентська конференція факультету авіаційних двигунів (ФАД) «Сучасні проблеми двигунобудування, енергетики та інтелектуальної механіки»: Збірник тез доповідей конференції. – Харків: Національний аерокосмічний університет ім. М.Є. Жуковського «Харківський авіаційний інститут», 2020. – С. 40. https://drive.google.com/file/d/1trS11rljWf1ylXnAkefWSohV8rkH5p28/view

20. Tan, K., Markovych, S., Shorinov, O., Hu, W. Deposition of protective and restorative coatings onto aircraft and engines parts printed with 3D technologies.

Відкрита науково-практична студентська конференція факультету авіаційних двигунів (ФАД) «Сучасні проблеми двигунобудування, енергетики та інтелектуальної механіки»: Збірник тез доповідей конференції. – Харків: Національний аерокосмічний університет ім. М.Є. Жуковського «Харківський авіаційний інститут», 2020. – С. 41. https://drive.google.com/file/d/1trS11rljWf1ylXnAkefWSohV8rkH5p28/view

CONTENT

LIST OF ABBREVIATIONS

CS	Cold Spray
CFD	Computational Fluid Dynamics
FDM	Finite Difference Method
FEM	Finite Element Method
FVM	Finite Volume Method
SPH	Smoothed Particle Hydrodynamics
ALE	Arbitrary Lagrangian Eulerian
CEL	Coupled Eulerian Lagrangian
JHC	MAT_JOHNSON_ HOLMQUIST_CERAMICS
J-C	Johnson-Cook
BBD	Box-Behnken Design
RSM	Response Surface Analysis Method
GA	Genetic Algorithm
BPNN	Back Propagation Neural Networks
LHS	Latin Hypercube Sampling
H	The Recovery Coefficient
K	The Deformation Coefficient
Y	The Degree Of Particle Deformation
ALIPIT	The Advanced Laser Induced Projectile Impact
EVF	The Euler volume Fraction
SEM	Scanning Electron Microscope
ALLKE	Kinetic Energy
ALLIE	Total Strain Energy

INTRODUCTION

Reasons for choosing the research topic.

Cold gas-dynamic spraying is an emerging coating preparation process technology developed in recent years. The cold gas-dynamic spraying system is mainly divided into two important parts: the powder particles are accelerated by the high-speed gas flow in the nozzle and the powder particles are deposited on the substrate to form a coating. Studying the acceleration characteristics of the powder particles in the nozzle and studying the structure of the nozzle will help determine the critical velocity of the powder particles. The time for the powder particles to deposit the substrate is extremely short. Simulating the particle deposition through numerical simulation will help observe and understand the coating formation, which can improve the productivity of the process and ensure high performance indicators of the coating quality. At present, the powder particles acceleration characteristics and the powder particles deposition are still in the exploratory stage, and there are still some problems that need to be solved:

1. At present, the methods of supersonic nozzle design and spray parameter optimization are not mature and perfect, and conventional single-channel nozzles have not been better developed. Therefore, combining the acceleration process of powder particles in the gas flow and their high-speed deposition process on the substrate surface according to the powder particle velocity standard during deposition, a new multi-channel mixed cross-section right-angle nozzle is developed through numerical simulation, especially to meet the spraying on the inner surface of parts. Spraying parameters are an important factor in determining whether powder particles can reach the critical deposition velocity. The single- and multi-factor coupling effect optimizes the cold spray technical parameters and structural parameters, which can more accurately simulate the real cold gas-dynamic spraying process.

2. The time for powder particles to deposit on the substrate surface is extremely

short. During the deposition process, the deformation process of powder particles cannot be accurately observed, and it is difficult to understand the principle and process of coating formation. Through numerical simulation, the deformation of powder particles during the deposition process is observed. Based on the finite element method, a new method is proposed to evaluate the influence of powder particle temperature-velocity parameters on substrate deposition using a particle deformation coefficient K.

3. At present, the main methods for simulating particle deposition are the ALE, the SPH, and the CEL methods. At present, the relevant research on the comprehensive analysis of the above three methods is still insufficient. Select a spraying material, simulate particle deposition through the above three methods, propose a comparative analysis method of numerical algorithms, and determine the model used to simulate particle deposition according to the required conditions and goals for powder particle deposition.

4. At present, the modeling method of multi-particle model is relatively simple. In actual cold gas-dynamic spraying, powder particles randomly impact the substrate to form a coating. Therefore, it is an important research part to establish a multi-particle model with disordered arrangement in space. By using Python software code to simulate the disordered arrangement of multi-particles in space, the development software is used to simulate the multi-particle deposition. The finite element calculation method is further used to optimize the coating, thereby developing the feasibility of optimizing the cold gas dynamic spraying parameters.

In summary, this dissertation is dedicated to the creation of a design method for supersonic nozzles of various configurations for cold gas dynamic spraying, as well as the optimization of spraying parameters in the formulation of technical recommendations based on numerical simulation of the powder particle acceleration process in the gas flow and its high-speed deposition with the substrate surface. It mainly involves four aspects. First, the optimization of the spraying parameters and structural parameters of the supersonic nozzle, and the development of a new type

of multi-channel mixed cross-section right-angle nozzle. Second, a new method of particle deformation coefficient K is proposed to evaluate the influence of powder particle temperature-velocity parameters on substrate deposition. Third, the CEL method is determined to simulate multi-particle deposition, which is used to observe the deformation inside and outside the coating and to predict the coating porosity. Fourth, the developed and implemented Python software code is used in the computational model to simulate the deposition of the number of powder particles.

The aim and tasks of the research. The aim of the research is the development of a supersonic nozzle for cold gas-dynamic spraying of coatings on internal and out-off-view surfaces and the detection of patterns of acceleration of powder particles in the nozzle and in the contact zone of the particle with the substrate during high-speed deposition.

In accordance with the aim of the research, the following main tasks are formed and solved:

1. To develop a supersonic nozzle, which will ensure that the powder particles reach the speed necessary for their adhesion to the substrate, when the flow is turned by 90°.

2. To study the process of acceleration of powder particles in the gas flow in the proposed right-angle supersonic single- and multi-channel nozzles, depending on the parameters of the flow at the entrance, the material of the particles and their size.

3. To propose an approach for determining the modes of cold gas-dynamic spraying of coatings when developing nozzles based on the criterion of the speed of a powder particle at the moment of contact with the substrate, which is necessary for its adhesion and formation of the coating.

4. Choose a model for describing the interaction of a powder particle with a substrate, which will allow numerical simulation of high-speed deposition of a particle in a wide range of velocities and temperatures for homo- and heterogeneous materials, and to investigate the deposition process of a single particle on the

substrate.

5. Investigate the process of simultaneous deposition of many powder particles with the surface of the substrate and parameters of spraying on the formation of porosity of the aluminum coating and develop recommendations for achieving its minimum values.

The **object** of research is the process of acceleration of powder particles by a supersonic flow in the nozzle channel for cold gas-dynamic spraying and high-speed interaction when the particles deposit on the substrate.

The **subject** of the research is the influence of the nozzle geometry and the parameters of the cold gas-dynamic spraying process on the temperature and speed of the powder particles in the flow.

The Research Methods. To solve the tasks in the dissertation, the methods of mathematical and numerical modeling were used for designing supersonic nozzles, researching the processes of particle acceleration in the flow and high-speed deposition, planning a multi-factorial experiment, regression analysis, and mathematical statistics for optimizing spraying parameters and predicting coating characteristics. Optimization methods are based on univariate and multivariate analysis, in particular on the GA+BPNN method.

The scientific novelty of the obtained results is as follows:

1) for the first time, a method of profiling supersonic single- and multi-channel right-angle nozzles for cold gas-dynamic spraying of coatings on internal and out-off-view surfaces was proposed, which provides the necessary values of the speed of powder particles at the exit of the nozzle for their adhesion to the substrate when the flow is turned by 90°.

2) For the first time, based on the results of numerical modeling, the dependence of the temperature-velocity characteristics of the powder particles at the exit from the right-angle nozzle on the material of the particles, their size, temperature and gas pressure at the entrance to the nozzle was obtained.

3) For the first time, an approach to assigning cold gas-dynamic spraying modes

is proposed, based on the planning of a multi-factor experiment, response surface methodology and GA+BPNN, which allows assigning the technological parameters of coating sputtering, which ensure that the powder particles achieve the speed necessary for their adhesion to the substrate.

4) For the first time, on the basis of numerical modeling and the planning methodology of a multifactorial experiment, the dependences of porosity on particle speed, its temperature, and the temperature of the substrate in the studied ranges of values were obtained.

Personal contribution of the applicant.

The results of the dissertation work were published in 20 articles. Among them 5 articles in scientific periodical publications included in category «А» of the List of scientific specialized publications of Ukraine, or in foreign publications indexed in the Web of Science Core Collection and/or Scopus database; 8 articles in scientific periodical publications included in the List of scientific specialized publications of Ukraine (category «Б»); and 7 conference proceedings (5 of them indexed in the Scopus database).

All the main results that constitute the essence of the dissertation are obtained by the author personally. Statement of tasks, analysis and interpretation of the main results, and formulation of scientific conclusions is performed together with the supervisor.

In work [172], the author performed an analysis of the literature and a study of the influence of the length of the extended part of the nozzle of the DYMET type gas-dynamic spraying installation on the acceleration characteristics of various particles; drafting the article and reviewing the final version. In work [133], the author performed the planning of a numerical study and the analysis of the obtained results using the response surface methodology. In work [66], the author constructed a model of the collision of one particle with the substrate, and set the initial and boundary conditions. In work [34], the author carried out research planning and built a model of a multi-channel nozzle. In work [188], the author performed a simulation

of the process of high-speed interaction of numerous particles with the substrate using the SPH algorithm. In work [8], the author analyzed the possibilities of using the technology of cold gas-dynamic sputtering as an additive production method and performed an analysis of the possibilities of using gas-dynamic sputtering in the aerospace industry. In work [71], the author performed an analysis of powder materials for cold gas-dynamic spraying and their scope of application. In work [113], the author performed a simulation of the collision process of numerous particles of Al6061 powder using the CEL algorithm; the effect of the temperature of the particles and the substrate on the sputtering process, as well as the formation of the porosity of the coating, was investigated. In work [167], the author performed an analysis of the geometry of the nozzle channel for the acceleration of powder particles; optimization of spraying modes was performed; the construction of a multi-channel nozzle for cold gas-dynamic spraying was developed. In work [112], the author performed a simulation of the process of dusting numerous powder particles using the CEL algorithm; the effect of parameters of cold gas-dynamic spraying on the process of coating formation was studied. In [190], the author performed a multi factorial analysis in order to optimize the porosity of the Al6061 coating by the method of numerical modeling. In work [38], the author performed an analysis of the possibilities of using the technology of cold gas dynamic spraying for the formation of titanium coatings. In work [57], the author performed an analysis of works devoted to the use of cold gas-dynamic spraying technology for the repair of aircraft parts. In work [35], the author performed a multi-channel rectangular nozzle was developed for spraying various powders. In work [126], t the author performed the influence of technological parameters of sputtering on the acceleration of powder particles in the nozzle was analyzed - gas pressure, gas and substrate temperatures, particle speed and size. In work [162], the author performed a study of the characteristics of the acceleration of various particles in a multi-channel rectangular nozzle and optimized the geometry of the channel. In work [97], the author performed a numerical simulation of the interaction of one particle using

the SPH algorithm. In work [189], the author developed a multi-parameter model for optimizing spraying modes and investigated the acceleration of the powder particle in the nozzle. In work [7], the author's personal contribution is performed an analysis of protective coatings that can be sprayed by cold gas-dynamic spraying. In work [2], the author's personal contribution is analyzed the possibility of using the technology of cold gas-dynamic spraying for applying coatings to parts obtained with the help of additive technologies.

Approbation of dissertation materials. The dissertation results were reported and discussed at international and national scientific conferences:

- Integrated computer technologies in mechanical engineering (ICTM). ICTM 2021 and ICTM 2023;

- International Conference on Mechanical Engineering and Materials (ICMEM2020);

- International Conference on Artificial Intelligence and Advanced Manufacturing (AIAM2021 and AIAM2023);

- Open scientific and practical student conference of the Faculty of Aviation Engines «Modern problems of engine construction, power engineering and intelligent mechanics», 2020. (Відкрита науково-практична студентська конференція факультету авіаційних двигунів (ФАД) «Сучасні проблеми двигунобудування, енергетики та інтелектуальної механіки»).

The structure and scope of the dissertation. The dissertation consists of an abstract, 4 chapters, conclusions and an appendix. The total volume of the dissertation is 273 pages, of which 226 pages are the main text. The dissertation contains 83 figures, 38 tables, 190 references and an appendix.

Connection of work with scientific programs, plans, topics. The results of the dissertation obtained by the author were carried out at the Department of Aircraft Engine Production Technology of the National Aerospace University named after M. E. Zhukovsky "Kharkiv Aviation Institute" in the implementation of the state budget research project of the Ministry of Education and Science of Ukraine: "Development

of aggregate technology of restoration and repair of aviation (helicopters) parts by cold spraying with post process machining of deposited coatings" (№ ДР 0122U001341) during 2020-2022. This research was funded by the China Scholarship Council (No. 201908360307).

The practical significance of the obtained results is that the results obtained in the dissertation research can be used in solving a wide class of practical problems in the development of technologies and technological recommendations for spraying protective and restorative coatings, in particular:

- the proposed method of profiling a rotary supersonic nozzle for cold gas-dynamic spraying allows to determine the geometric parameters of the nozzle according to the specified characteristics of the used powder material, pressure and temperature of the gas at the nozzle entrance;

- the revealed features of the effect of the material of the powder particles, their size, initial values of temperature and gas pressure on the temperature and speed of particles at the exit from the nozzle, expand the understanding of the regularities of gas dynamics processes of two-phase flow in supersonic nozzles for cold gas dynamic spraying;

- the results of the study of the processes of acceleration of powder particles in supersonic nozzles and high-speed deposition of particles on the substrate create a theoretical basis for improving the models of these processes, designing and creating equipment for cold gas-dynamic spraying;

- the approaches proposed in the dissertation regarding the designation of spraying modes can be used to optimize the parameters of cold gas-dynamic spraying in order to control and ensure the given characteristics of the coatings.

The results of the dissertation work on the development of supersonic nozzles for spraying and science-based recommendations for the selection of spraying modes can be implemented in research institutions, production and repair enterprises, which are engaged in researching the processes of cold spraying and the practical application of technology for the formation of protective and restorative coatings.

CHAPTER 1

OVERVIEW OF COLD SPRAY TECHNOLOGY

1.1 Metal Additive Manufacturing Technology

1.1.1 The development and research status of additive manufacturing technology

Additive manufacturing technology is also named 3D printing technology. This is based on the idea of "discrete/accumulation molding" and adopts a layered accumulation molding method, which is different from the traditional subtractive manufacturing technology of cutting processing. Rapid prototyping technology that adheres and stacks two-dimensional materials layer by layer based on the three-dimensional model completed by the modeling software and finally makes the actual object [1]. Since additive manufacturing uses raw materials to melt and accumulate layer by layer for parts processing, it can realize the manufacturing of complex structural parts that cannot be completed by traditional manufacturing technology. At the same time, this technology has diversified space design, consume less raw materials, and has low production costs, high manufacturing efficiency, short R&D and production cycle, and other advantages; especially suitable for the production of small batch customized products. At present, all major manufacturing powers in the world have established complete additive manufacturing industry systems.

Among additive manufacturing technologies, metal additive manufacturing technology is one of the most cutting-edge and potential technologies in additive manufacturing technology. It has broad application prospects in aerospace, bio-medicine, the automotive industry, art design, and national defense [2]. The number of companies selling additive manufacturing equipment has been increasing in the past decade, and most involve metal additive manufacturing. It is mainly used for

research, prototyping, or advanced applications in the aerospace industry, such as the F-15 tower manufactured by Boeing [3]. It is also used in the biomedical, defense, and automotive industries. Metal additive manufacturing can provide a great degree of freedom for parts with complex geometries or special connections [4]; For the development of multifunctional components, the protection and insulation treatment of materials have good application prospects. It can also meet the requirements for high-resolution printing of complex structures [5]. Metal additive manufacturing mainly melts powder or metal wire through the energy of a laser or electron beam, and prints it layer by layer according to a predetermined geometric model [6].

The main forming processes for metal additive manufacturing include the Selective Laser Sintering (SLS), the Fused Deposition Modeling (FDM), the Selective Laser Melting (SLM), the Laser Metal Powder Deposition (LMD), the Laser Solid Forming (LSF), the Direct Metal Laser Sintering (DMLS), the Electron Beam Melting (EBM), the Electron Beam Free Form Fabrication (EBF3), the Wire Arc Additive Manufacturing (WAAM) and the Laser Engineered Net Shaping (LENS) [7].

New additive manufacturing technologies in the past decade, such as adhesive spray forming technology, cold gas-dynamic spraying (cold spray or CS) technology, and friction stir welding technology. The methods and principles of traditional metal additive manufacturing technology are similar, but the advantages and disadvantages of these technologies are completely different; here are several representative metal additive manufacturing technologies:

1) The Selective laser melting (SLM).

The SLM technology is currently the mainstream and most mature laser additive manufacturing technology. Its basic principle is shown in Figure 1.1 [8]. Although DMLS is named direct metal sintering, but principle is the same, so it is introduced together. The laser scans a layer of metal powder pre-spread by the powder spreader according to the path set by the computer. The metal powder melts and forms a metallurgical bond with the previous layer. In this way, layer by layer is

accumulated to form the required entity; in addition, in order to prevent oxidation during the forming process phenomenon, it is necessary to use inert gases such as helium and argon as protective gases during the process, which can reduce the surface tension of the deposited layer, improve the wettability between layers, at the same time, it is helpful to improve the forming quality [9, 10].
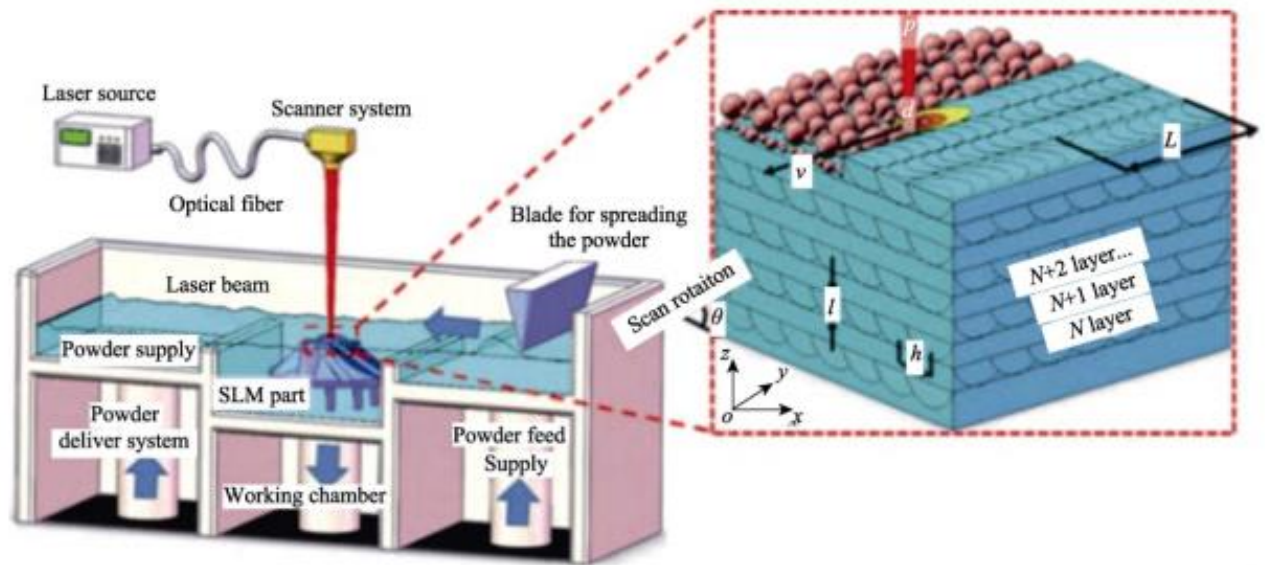
Fig. 1.1. The SLM technology principle [8]

The SLM is a process method that can directly form metal parts. The Selective Laser Melting technology (SLM) has typical advantages, such as increased design freedom: bionic geometric structure optimization, easy to modify; high functionality: conformal cooling runner, lattice structure; reduce the number of parts: inherit multiple parts as a whole, reduce assembly; reduce tooling and assembly costs: near net forming; lightweight: improve fuel efficiency through the use of organic component design; optimize material utilization: use only the amount of material required for forming to reduce material waste and high production strength alloy reduces the loss of tools; short production cycle, wide range of materials, high precision and other advantages. Common metal materials that can be printed using the SLM technology, are shown in Table 1.1.

Table 1.1 − Printable metal materials

Materials	Common metal materials
Ti-Alloys	Ti6Al4V Gd.23*, Ti6Al4V Gd.23*
Co-Alloys	CoCr28Mo6
Ni-Alloys	IN625, IN718, IN939
Al-Alloys	AlSi10Mg, AlSi12, AlSi7Mg0.6, AlSi9Cu3
Cu-Alloys	CuSn10
Tool and stainless steel	1.4404/316L, Invar 36

The SLM technology originated in Germany, and is developed based on the SLS technology; The material of SLS is generally a mixture of metal materials and low-melting point non-metals. The low-melting-point materials will be filled and bonded in the metal materials, and the surface of the formed parts is rough and porous, with low density, and usually requires post-processing. The SLM technology uses high-power laser equipment to melt metal materials without the need for other materials to assist bonding. Any complex structural parts can be directly formed from the three-dimensional model. The post-processing method is usually a nozzle or polishing process. The heating equipment of the SLM technology usually uses high-energy-density lasers as the heat source. The laser power is 50-400W and the spot size is 20-100 um. It can almost directly obtain metallurgical bonded functional parts of any shape and almost complete density. Its mechanical properties are almost close to the level of forgings [11]. Molded parts have fine grains, uniform structures, and surface roughness of up to 20-50 um. They are suitable for processing workpieces of various complex shapes. It is a rapid prototyping technology with great development prospects [2]. Although the SLM has high accuracy, spheroidization, and thermal stress will occur during the molding process of the parts, which affects the accuracy.

GE applies the SLM technology to the fuel nozzle of the aero engine. As shown in Figure 1.2, the original nozzle physical map (a) and the nozzle physical printed by the SLM technology (b) [12], mainly because SLM can achieve freedom

manufacturing technology advantages. This technology turns the original multiple nozzle parts into one, reducing the total weight by 13.5%, increasing the service life and durability by 4 times, and reducing the emissions by 15% [13]. Liu [14] studied the preparation of Ti-6Al-4V titanium alloy materials by SLM technology. Wang [15] and Chen [16] showed the turbine disk and engine combustion chamber manufactured by the SLM technology. Zou [17] studied the preparation of AlSi7Mg alloy using the SLM technology. Ti-6Al-4V titanium alloy and AlSi7Mg alloy materials are widely used in aviation.

a   *b*
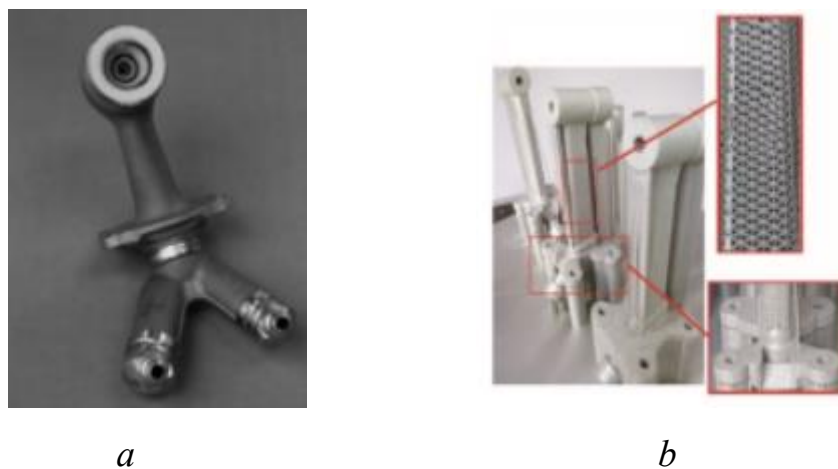
a − The original nozzle physical map; *b* − The nozzle physical printed by the SLM

Fig. 1.2. Parts obtained using SLM technology [12]

2) The Metal electron beam melting process EBF3.

Electron beam fused wire deposition technology mainly uses wire as the processing material [18]; EBF3 technology combines the advantages of EBM technology, and EBF3 technology is particularly suitable for molding in the microgravity environment of space, which is of great significance for spacecraft maintenance and deep space exploration [19]. In the 1990s, NASA conducted research on additive manufacturing technology for space metal materials, and successfully developed two types of deposition equipment, floor-standing and portable, based on EBF3 technology. Figure 1.3 shows a portable electron beam fuse forming system. At the same time, China's Beijing Aerospace Manufacturing

Engineering Research Institute has also developed EBF3 additive manufacturing equipment for related research work [20].
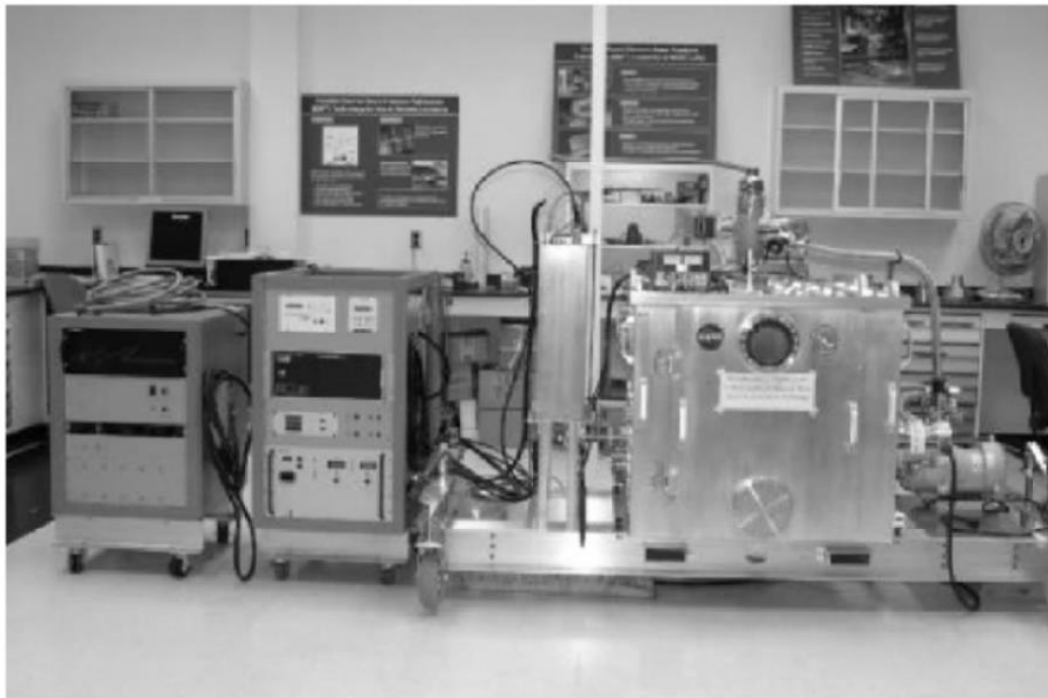
Fig. 1.3. NASA portable electron beam fuse forming system [20]

3) The Laser Engineered Net Shaping LENS.

The Laser Near Net Shaping (LENS) is a technology that originated in the 1990s and was commercialized by optomec company [21]. The principle of the LENS technology is laser cladding. The high-power laser will pass through the coaxial (lateral) powder sent into the molten pool by the powder feeding nozzle is completely melted and deposited layer by layer [22]. Usually, a high-power laser is used to completely melt the powder sent into the molten pool through a coaxial (lateral) powder-feeding nozzle to deposit and form layer by layer. The molded parts can achieve the required high density and usually do not require post-processing. The advantage of the LENS technology is that it can realize the forming of multi-metal and heterogeneous materials by adjusting process parameters, especially in large parts and multi-metal material combined parts [23]. The disadvantage is that the precision of the formed parts is not high, so only simple parts with certain

34

specific structures can be manufactured, and it is difficult to form parts with cantilever structures. The main application fields of the LENS technology are aerospace, bio-medicine, automobiles, and national defense, and has broad application prospects. For example, high-performance metal parts such as aircraft landing gear and engine blades are produced through the LENS technology; and engine blades made of high-temperature alloys and titanium alloys are repaired through the LENS technology. The performance of the repaired parts exceeds the performance of the original materials [24]. For the application of the LENS technology in the field of porous titanium and titanium alloys, the United States has successfully prepared a porous titanium hip bone stem [25]. As shown in Figure 1.4, porous titanium has more advantages than pure titanium in promoting faster differentiation of human osteoblasts. Some universities in China have used the LENS technology to optimize parameters through the process and studied the LENS forming of titanium alloys and Nickel alloys.
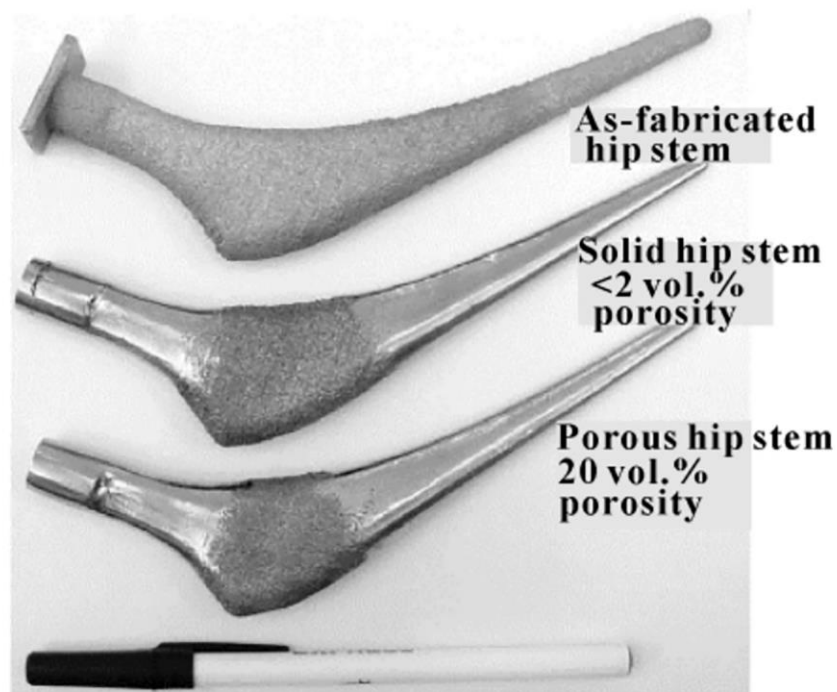
Fig. 1.4. Porous titanium hip bone stem [25]

4) The Wire Arc Additive Manufacturing (WAAM) technology.

The principle of the WAAM is based on layered additive manufacturing [2]. Commonly used heat sources include the Metal Inert Gas (MIG), the Tungsten Inert Gas (TIG), and the Plasma Arc (PA). The arc is generated through the welding process, and the forming material is usually welding wire; the forming of three-dimensional parts is completed by layer-by-layer cladding deposition; the forming principle is shown in Figure 1.5. The advantage of the WAAM technology is its high forming efficiency. Since the WAAM technology is based on automated production and integrates digital, intelligent, and parallel manufacturing, the time from model design to part processing is very short, and the formed parts can be put into use directly with only a small amount of machining. The equipment cost is low; the WAAM uses general welding equipment, has a high material utilization rate, and is suitable for forming precious metal materials and composite materials. The manufacturing form is flexible; the size and shape of the WAAM-formed parts are almost unlimited, and rapid prototyping of small batches and large parts can be achieved.

The formed parts have good performance; compared with traditional castings and forgings, the WAAM materials are metallurgically bonded, and have a dense organizational structure, excellent mechanical properties, high strength, and good toughness [26]. the WAAM technology manufacturing is a process of multi-parameter coupling, and during the welding process, the shape of the weld and the transition mode of the droplets are not easy to control, so they will be affected by other factors during the forming process. This leads to the accumulation of defects.

For example, companies in Germany and Switzerland were the first to use the SAW technology to manufacture large cylindrical pressure vessels with a quality of 500 tons in the 1960s. However, the surface of the parts was rough and was usually only suitable for large parts [27-29]. Later, someone invented the 3D Welding technology by combining welding process technology with additive manufacturing technology. This technology can be used for prototypes or direct manufacturing of parts.
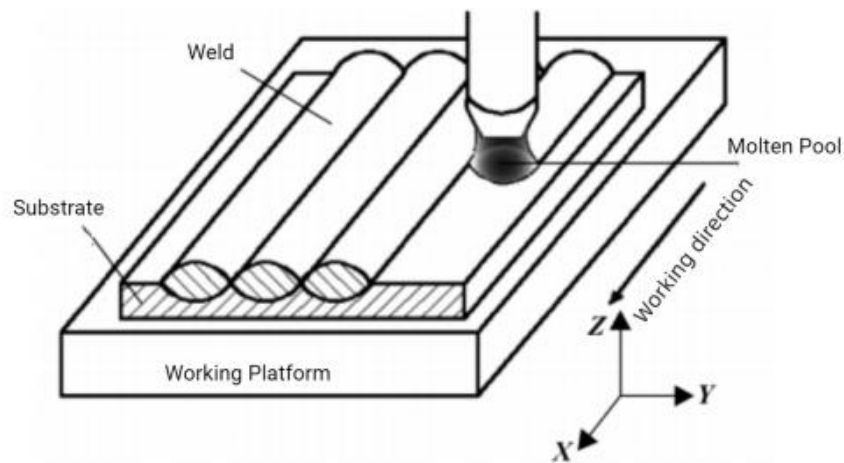
Fig. 1.5. The principle of the WAAM technology

1.2 The cold spray additive manufacturing technology

1.2.1 The development history of cold spray technology

Cold gas-dynamic spraying (cold spray or CS) technology is an emerging additive manufacturing technology, especially in the field of material processing, which has broad application prospects. Cold spray technology is a particle deposition method that combines particles with each other through the self-consolidation ability of powder particles. The condition is that high-speed impact is required to complete the self-consolidation of powder particles to form a coating. Cold spray technology was originally invented in the last century. After that, some scholars used blowers and accelerated gas to accelerate powder materials to ultra-high speeds. The high-speed powder materials deposit the substrate to form a coating. Some scholars innovated on the basis of the original technology. The high-speed gas from the Laval nozzle drove the spray material, thereby more effectively accelerating the spray material, and finally impacting the substrate to form a new coating. In the 1980s, Scholars discovered that when the speed of spraying materials exceeds a critical value, the effect of particles on the substrate changes from erosion

to adhesion. They conducted in-depth research on this, and their research results contributed to the advancement of modern cold spray equipment and cold spray manufacturing technology. Cold spray technology has developed rapidly in recent decades, and the number of articles and patents on cold spray technology has grown rapidly, covering the research and application of cold spray in various fields [7]. Nowadays, cold spray as a new spray technology, has become one of the most promising metal coating technologies. Cold spray technology has received very widespread attention in Germany's Bundeswehr University, ASB Company, Pennsylvania State University, and Sandia National Laboratory in the United States and other countries. Their main research contents include the development of various spray materials and special processes, research on cold spray deposition mechanisms, and high-speed gas dynamics.

Cold spray technology is a solid-state deposition technology with many advantages, which makes it have huge application potential; this technology has been increasingly used in aerospace, automobile, and shipbuilding, the electronics industry, bio-medicine, defense industry, and other fields of attention. The coating prepared by cold spray technology can be used as a protective coating to provide anti-corrosion, wear resistance, and high-temperature resistance; It can also be used as a functional coating, such as conductive coating, thermal conductive coating, biomedical coating layer, etc. At the same time, with the development of cold spray technology, cold spray is gradually being used in parts repair and additive manufacturing. Cold spraying has little thermal impact on parts and does not change the original properties of the sprayed powder particle. Therefore, cold spray has great advantages in repairing damaged parts. Cold spray technology has great potential in manufacturing rotating structural parts and can produce mesh structures or more complex geometric structures based on well-designed molds.

Cold spray technology has the following advantages:

1) The working temperature is low, and the sprayed powder particles will basically not undergo oxidation, burning, phase change, grain growth, or other

phenomena during the entire process. There will be no excessive heat transfer to the surface of the substrate, and the thermal impact on the substrate will be small. The grain growth rate is extremely slow (it is possible to maintain the nanostructure structure), close to the forged structure (harder than traditional coatings), has a stable phase structure and chemical composition, basically does not require masking, has small spraying losses, and the spray beam width is adjustable to less than 3mm; this enables a wider choice of materials for powder particles and substrates.

2) The spraying rate is high, and the spraying particles can reach 3 kg/h; the deposition rate of spraying particles is high, which can reach 80%.

3) The chemical composition and microstructure of the coating can be consistent with the raw materials. There is basically no oxidation, burning loss of alloy components or grain growth. It can spray heat-sensitive materials, active metals, and polymer materials, and is suitable for the preparation of amorphous and nanocrystalline coatings.

4) Powder particles uniformly mixed with different materials can be sprayed. Therefore, composite material coatings can be prepared by mechanical mixing of powders with different physical and chemical properties.

5) The appearance of the coating is consistent with the surface topography of the substrate, reaching a high level of surface roughness, and the spraying distance is extremely short. The coating is produced under compressive stress, and the residual stress of the coating is lower, which reduces the limit on coating thickness, which is beneficial to the preparation of thick coatings. Moreover, the bonding strength of the coating is high, and a coating with high hardness can be obtained. At the same time, the coating has good thermal conductivity, electrical conductivity, and corrosion resistance. The coating is dense, has few pores, and the density can reach 98%. It can prepare coatings with high thermal conductivity and high electrical conductivity.

6) The coating structure is dense and has low porosity. This is related to the impact of subsequent particles on the deposited coating. At the same time, since the

particles do not exist in a molten state, there is no volume shrinkage process after the particles are cooled.

7) No high heat source is required, which greatly reduces equipment costs and is lower than other spraying methods.

8) Compressed gas can be used as the working gas, and undeposited powders can be recycled. There is no combustion in the whole process, which is more economical.

9) Cold spray has basically no pollution to the environment. It is easy and safe to operate and has no heat radiation.

Cold spray technology has the following disadvantages:

1) Under special circumstances, helium is needed as the accelerating gas to prepare high-quality coatings; for example, helium must be used for Al -based, steel-based, nickel-based, and high-temperature alloys to meet the speed requirements for spraying materials. This allows the sprayed particles to achieve a higher speed, which satisfies the deposition of the sprayed powder particles on the substrate. This results in increased spraying costs.

2) Effective deposition of particles and the preparation of stable high-quality coatings largely depend on the characteristics of the particles and substrate materials.

1.2.2 The principles of cold spray and coating deposition process

The principles of cold spray technology as shown in Figure 1.6 [30, 31]. cold spray technology is a new type of spray deposition technology developed on the basis of aerodynamic science. Spray deposition is a process in which particles are accelerated in the Laval nozzle by the action of an acceleration medium (usually nitrogen, air, or helium). The final ultra-high speed (300 m/s-1200 m/s) powder particles deposit the substrate to achieve deposition, and eventually form a uniform and dense coating on the substrate [32-34].
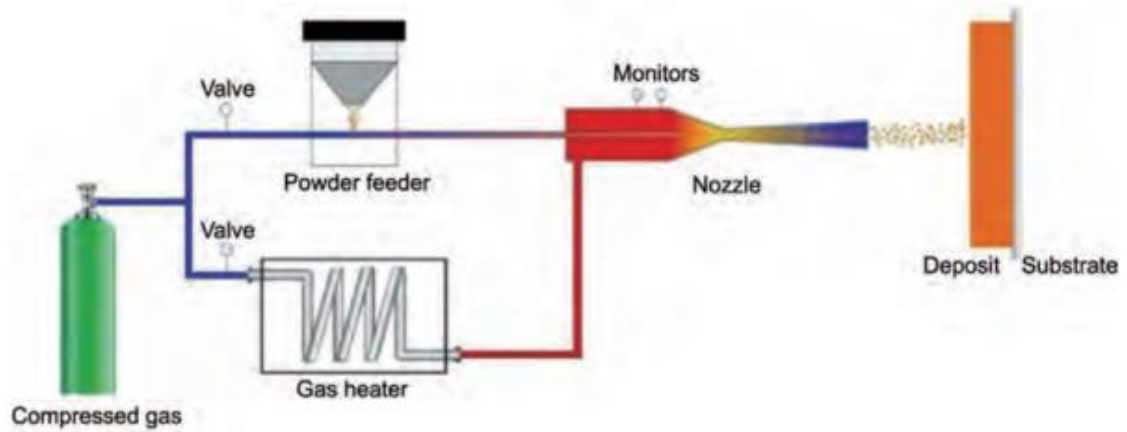
Fig. 1.6. The principles of cold spray technology

The cold spray system basically consists of six major parts: the high-pressure gas source, the spray gun system, the gas temperature control system, the powder feeding system, the gas regulating system, and the powder recovery system. After the particles are accelerated through the Laval nozzle, they will reach a supersonic state. Then, when the speed of the particles reaches or exceeds the critical speed, the deposition goal can be achieved only after the particles deposit the substrate. Therefore, making the particles reach or exceed the critical velocity is an important technical goal in cold spray technology. Among them, the core of cold spray technology is the analysis and design of the nozzle. Many scholars have studied the impact of the technical parameters of the throat, expansion section, and convergence section of the nozzle on factor acceleration; Tan [35] also studied different it is a multi-channel mixed cross-section right-angle cold spray nozzle based on the traditional Laval nozzle; the expansion ratio of the nozzle (the size ratio of the outlet and the throat) is the key factor that determines the Mach number at the outlet.

The deposition of particles on the substrate can be divided into two stages. The first is the combination of particles/substrate. The particles continuously impact the substrate, causing the substrate to deform, during the deposition process, the particles deform and bond to the substrate. The second is the bonding between particles/particles. The connection between particles is achieved through the plastic deformation of the particles, the particle interface undergoes high-rate strain during

the deposition process. The interface bonding method is mainly caused by atomic bonding or phase change [36-38]. The above two stages are completely different. When the deposited particles are non-plastic, such as ceramic particles, the particles break and self-compact, and the formation of the final coating is the result of the accumulation and interlocking of the fragments. A variety of oxide coatings can now be successfully prepared using this combination method [39].

1.2.2.1 Comparison between high-pressure cold spraying and low-pressure cold spraying

According to the spraying pressure, it is mainly divided into two types: high-pressure cold spray (HPCS) and low-pressure cold spray (LPCS) [31, 40]. Since the emergence of cold spray technology, the high-pressure cold spray technology, and the low-pressure cold spray technology have been developed almost simultaneously. The powder in the high-pressure cold spray equipment is introduced from the contraction section near the front section of the nozzle throat. The powder-feeding gas has a high pressure. The powder is sent to the open section through the nozzle throat for acceleration and sprayed to the surface of the workpiece. The advantage of this design is that the gas-solid two-phase flow can be easily concentrated, the powder particle is evenly distributed and deposited densely, and the coating quality is excellent and stable; the disadvantage is that the system structure is complex and bulky, making it unsuitable for transportation and on-site construction. In order to solve this problem, people started to develop the low-pressure cold spray system. In the low-pressure cold spray system, the powder is directly sent into the expansion section downstream of the nozzle throat. The gas flow drives the powder to accelerate and spray onto the surface of the workpiece, which can greatly reduce the amount of spray. The system is small in size and has a simple structure, making it easy to transport and conducive to on-site construction. However, the fluidity and uniformity of the powder are not ideal, which will affect the spraying quality to a

certain extent. Due to the low pressure and temperature, its spraying application range is greatly limited. Companies currently producing commercial cold spray equipment include German GGT Company, American ABS Innovation Company, and Japanese Plasma Technology Research Corporation. Among them, the working gas temperature of the cold spray equipment PCS-1000 system produced by the Japanese Plasma Giken Company can reach 1300K, the pressure can reach 6 MPa. The maximum working gas pressure and temperature of the DWCS cold spray system produced by Shaanxi Dewei Automation Co. Ltd. In China can reach 5 MPa and 1250 K respectively, reaching the international leading level.

The high-pressure cold spraying requires a pressure higher than 1.5 MPa, but it's noisy, with the noise exceeding 100dB. At the same time, the high-pressure cold spray equipment is huge and cannot be moved. It needs to operate under helium, nitrogen, or inert gas, resulting in high production costs. The carrier gas is heated by a heater and passes through the contraction-expansion nozzle to accelerate the sprayed material to supersonic speeds. The spray powder is injected axially in the upstream direction of the expansion part of the nozzle, and then sprayed onto the substrate, as shown in Figure 1.7(a). The pressure of the powder-feeding gas is higher than the pressure of the accelerating gas to ensure the stability of powder-feeding.

a

b
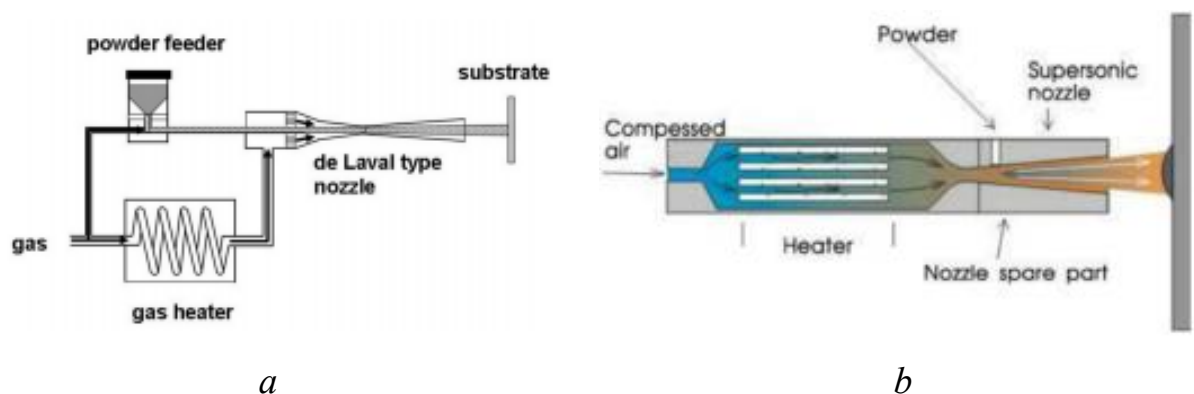
a – The high-pressure cold spray system; *b* – The low-pressure cold spray system

Fig. 1.7. The cold spray system.

The working pressure of the low-pressure cold spray equipment is from 0.5 to 1.2 MPa, the temperature is 350 K to 950 K, and the powder gas flow is accelerated to 350 to 700 m/s. The spray powder is injected radially downstream of the nozzle expansion part, and then deposit onto the substrate, as shown in Figure 1.7(b); its advantages are no flame, no dangerous gas, no radiation, and no chemical waste, and can be operated with bare hands. High safety and good directionality. The Dymet equipment produced by OCPS powder coating center has very low driving gas requirements and low enough power requirements. The working gas pressure is 0.5~1.2 MPa and can use compressed air, nitrogen, argon, and helium. The gas can be used to spray metal, ceramic, and glass surfaces.

The principles of the low-pressure cold spraying and the high-pressure cold spraying are basically the same; The difference between the two mainly lies in the pressure of the gas carrier and the way the powder is deposited. The powder flow in the former is relatively dispersed, and the powder scatters away from the nozzle; The latter is highly agglomerated and the powder leaves the nozzle straight away.

1.2.3 Bonding mechanism of cold spray coating

Cold spray powder particle deposition and coating formation mechanism have always been the focus of cold spray research.

Cold spray technology usually impacting the substrate surface below the melting point of the particles, so the mechanism of coating formation is very different from traditional thermal spraying. Whether ultra-high-speed spray particles impact the substrate to form a coating or to produce shot peening (erosion) on the substrate depends on the critical velocity before the particle impacts. Each type of spray particle has a critical velocity. When the speed of the particles is greater than the critical velocity, the particles will undergo plastic deformation after impacting the surface of the substrate and deposit on the surface of the substrate to form a coating. When the speed of the particles is less than the critical velocity, erosion

occurs between the particles and the substrate, or between the particles. It is generally believed that at the moment when the particles deposit the surface of the substrate, both the particles and the substrate undergo strong plastic deformation, and the location of the deposit surface is most significant. In this process, due to the extremely high strain and strain rate, most of the heat has no time to diffuse in a very short time, and the deformation process is regarded as an adiabatic process. The deposition area heats up rapidly and undergoes thermal softening. When the thermal softening effect is stronger than the work hardening effect, plastic flow occurs in the metal, forming metal spraying and moving toward the outside of the interface. With the generation and development of spraying, ultra-high-speed particles destroy the oxide film on the surface of the substrate, exposing a large amount of fresh metal surface to the substrate. The high-pressure ultra-high-speed particles directly contact and combine with the fresh metal on the surface of the substrate to form a similar physical bond. Combined and metal bonding [41], this is the shear instability mechanism known in spraying theory circles.

In order to better understand the coating formation process, it can be roughly divided into four steps: the first step is initial coating formation (deformation of particles and substrate, oxide film rupture, and combination); the second step is particle deformation and re- arrangement and combination; third step is metal bonds are formed between particles and porosity decreases; fourth step is the coating is further densified and hardened.

The shear instability mechanism can effectively explain the deformation behavior during particle deposition and bonding and provides a standard for judging particle bonding. However, due to limited scientific means, this theory is a conclusion drawn from numerical simulations and cannot fully explain the material. Effect of properties on coating quality. During the coating formation process, in addition to the shear instability mechanism, some scholars also believe that the cold spray coating has the following bonding methods: mechanical bonding mechanism, physical bonding, micro forging mechanism, metallurgical bonding, and chemical

bonding [42].

Mechanical combination.

The interface between the particles and the substrate forms a fit with each other due to the concave and convex surfaces, forming a mechanical bond, or a strong bite resulting from the vortex-like organizational morphology formed at the interface between the particles and the substrate. Therefore, it can also be explained as the material undergoes adiabatic shear instability and produces plastic flow or metal splash flow under pressure, causing the materials to mechanically combine with each other to form a mechanical interlocking structure. In most cases, the strength generated by mechanical bonding accounts for the majority of the total bonding strength [43].

Physical combination.

Adiabatic shear instability and its locally generated jets can take away the oxide film on the surface of the particles and substrate, produce a clean surface, and form a physical bond under higher pressure, that is, the effect of van der waals force, and when the particles and substrate can it is more conducive to physical bonding when generating jets [44].

Micro forging mechanism.

The particles deposited first are deposited by the particles deposited later, refining the grains and making the coating denser, thereby making the bonding between the coating and the substrate stronger.

Metallurgical bonding.

For spraying some materials with high deposition speed, high initial temperature, poor thermal conductivity, and low melting point, if the local maximum temperature rise at the contact surface between the particles and the substrate exceeds the melting point of the material, the local position of the contact surface may produce a diffusion bonding mechanism of atoms, thereby facilitating the production of metallurgical bonding. It can also be explained as a large amount of heat energy is generated during adiabatic shear instability, and the temperature can

reach the melting point of the material, thereby forming a metallurgical bond at the interface. This occurs between particles and at the coating-metal interface and requires an oxide-free interface. To ensure metal-to-metal contact. Metallurgical bonding generally provides higher bond strength. Evidence of metallurgical bonding has been observed during experiments [45, 46]. Currently, the generally accepted theory is that the metal jet flow extrudes the oxide from the interface in order to allow new metal interfaces to contact each other to achieve metallurgical bonding [47]. No metallurgical bonding occurs with single-particle deposition.

Chemical bonding.

During the plastic deformation process of particles, adiabatic temperature rise may induce chemical bonding.

Under different deposition materials/substrates and process conditions, one or more of the above combination methods may exist in the coating, but one of them may play a dominant role.

1.2.4 The cold spray equipment and research status

With the development of cold spray technology, in addition to the high-pressure and the low-pressure cold spray systems, there are also the vacuum cold spray systems, the laser-assisted cold spray systems, the electrostatic-assisted cold spray systems, the pulse gas cold spray systems, and the shock wave wind tunnel cold spray systems. This helps achieve the requirements for the preparation of high-quality coatings and special coatings, and can also promote the development and application of cold spray technology.

The vacuum cold spray system; the acceleration characteristics of the vacuum cold spray particles are similar to those of traditional cold spray. the vacuum spray chamber is introduced into traditional cold spray equipment, and the environmental pressure is reduced from traditional normal pressure to vacuum. In the process of traditional cold spraying of micro-nano particles, it was found that due to the small

size of the particles, when a gas-solid two-phase high-speed flow is formed outside the nozzle and shoots towards the base material, it will be significantly slowed down due to the obstruction of the atmosphere medium [48, 49].

The Laser-assisted cold spray system; the introduced laser energy improves the mechanical properties of particles and substrates, and at the same time has a softening effect on particles, thereby improving coating thickness, deposition efficiency, compactness, and bonding strength, and reducing porosity. At the same time, the material selection of particles and substrates is broadened, and the preparation of coatings of difficult-to-deposit materials is achieved. Due to the special properties of the laser, the heating temperature can be precisely controlled. Even under some working conditions, laser-assisted technology can be used instead of gas-heating devices [50, 51].

The Electrostatic-assisted cold spray system; the electric field-assisted vacuum cold spray technology is a new spray technology based on the vacuum cold spray technology and the electric field-assisted cold spray technology. It aims to solve the problem of nanometer-scale bow shock waves generated in the front section of the substrate during the traditional spraying process. Technical difficulties in which particles cannot be effectively deposited [52, 53].

The Pulse gas cold spray system; due to the structural characteristics of the Laval nozzle, when the gas passes through the open section of the Laval nozzle, the volume expands rapidly, and the pressure and temperature decrease rapidly as the flow rate increases. The actual temperature of the gas sprayed onto the workpiece surface has been greatly reduced, so heating the particles with preheated gas is not a very ideal method in cold spray systems with Laval nozzles. The method of designing the nozzle as a straight tube and using pulse gas as the working gas provides a new idea for solving the problem [54].

The Shock wave wind tunnel cold spray system; uses wind tunnel shock wave technology to accelerate particles to achieve the purpose of depositing and preparing coatings. The advantage is that this technology can accelerate particles to extremely

high speeds (1500 m/s) to achieve particle deposition [55]. Due to the large size, complex structure, and high price of the equipment, this technology is still in the laboratory research stage.

1.3 Current research status of cold spray process parameters

Cold spray process parameters can be roughly divided into technical parameters and structural parameters; technical parameters can be mainly divided into the pressure and temperature of the accelerating gas, the particle size, temperature, velocity and shape of the particles, the substrate temperature, the distance, and angle of spraying; the structural parameters are mainly the size and structure of the Laval nozzle [56-58]. The above technical parameters will all produce the coating quality and deposition efficiency influences.

Particle size and shape.

Different particle sizes and shapes will also affect the quality of the deposit. Zhao [59] studied by studying the maximum contact area of powder particles with diameters of 10, 20, and 30 um after depositing the substrate. When the speed is within a certain range, by changing the powder particles in an irregular base at the speed of spraying on the material, the contact area of the powder particles and the substrate will change. When the speed is too large, this effect will reach saturation, and the contact area will not increase with the increase in speed. Fukanuma [60] found that because the traction coefficient of gas flow to non-spherical particles is larger than that of spherical particles, the cross-sectional area and drag coefficient of powder particles will seriously affect the drag of particles the drag force is greater than that of spherical particles and irregular particles. Therefore, the speed of non-spherical particles is significantly higher than that of spherical particles due to acceleration under equal working conditions. Jodoin [61] also found that non-spherical particles have a larger drag coefficient than spherical particles. Therefore, the drag force of non-spherical particles is greater, and the particles can obtain higher

speeds, so it is of great significance to reduce the critical speed and improve the deposition efficiency. Zhao [59] studied the comparison of plastic deformation and temperature distribution of Al and Mg alloy powder particles of different sizes and shapes, as shown in Table 1.2.

Table 1.2 − Comparison of plastic deformation and temperature distribution effects of Al alloy and Mg alloy particles of different sizes and shapes after deposition at 500m/s

Shape	Size / um	Plastic deformation (along the long axis)	Temperature distribution (along the long axis)	Plastic deformation (along the short axis)	Temperature distribution (along the short axis)
Ball a / b / c	10 /20/30	Symmetrical distribution	Symmetrical distribution	Symmetrical distribution	Symmetrical distribution
Ellipsoid a	9*9*12.35	Symmetrical distribution	Symmetrical distribution	Asymmetric distribution	Asymmetric distribution
Ellipsoid b	8.17*8.17*15	Symmetrical distribution	Symmetrical distribution	Asymmetric distribution	Asymmetric distribution

Particle velocity.

When the speed reaches a certain value, the powder particles are attached to the substrate to form a coating. This speed is named the critical velocity. The critical velocity can be obtained through experimental testing and numerical simulation, Khai has been committed to using simulation software to study the critical velocity. Generally, the critical velocity is regarded as the lower limit of the velocity that can be deposited, so in the deposition process, the particle speed must be greater than the critical velocity to achieve the deposition of powder particles on the substrate. When the speed of the powder particles is lower than the critical velocity, the powder particles cannot be deposited on the substrate but rebound, leaving an impact on the substrate crater. The deposition and combination of powder particles and substrate during cold spraying mainly depend on the kinetic energy of the particles. At the same speed, the kinetic energy of particles with smaller particle sizes is also smaller,

and the plastic energy consumption of the substrate and particles during deposition is less. In the spray deposition process, the powder particles can be driven by the acceleration medium to obtain supersonic speed in the Laval nozzle. The speed of the powder particles affects the deposition efficiency. Figure 1.8 shows the relationship between the particle speed of Cu, Ni, and Al powder and the deposition efficiency (DE) [62, 63], it can be seen from Figure 1.8 that the deposition efficiency changes with the increase of speed at different gas temperatures. Increasing the particle speed and temperature can appropriately increase the deposition efficiency.
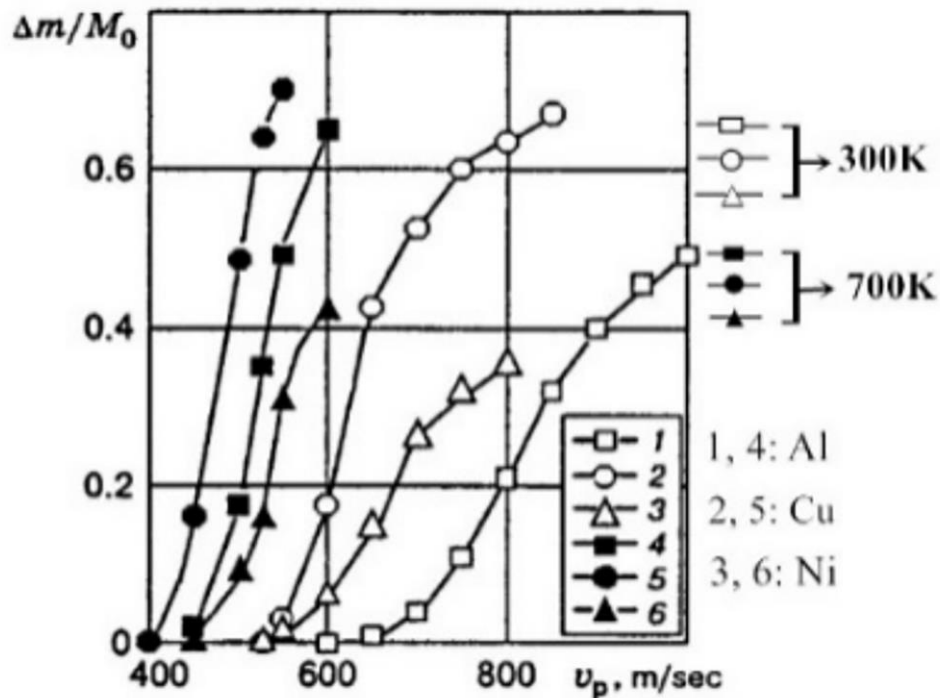
Fig. 1.8. The relationship between the particle speed of Cu, Ni, and Al powder and the deposition efficiency (DE)

Spray angle.

When the particles are deposited perpendicular to the surface of the substrate, the depth of the deposition has the best effect. As the incident angle increases, the depth will gradually decrease, resulting in a weakening of the coating effect. Wang [65] found that the spray angle will affect the supersonic flow field structure and

particle acceleration behavior inside and outside the nozzle, as shown in Table 1.3.

Table 1.3 – The depth and depth change rate of particles deposited on the substrate under different incident angles at an initial velocity of 500m/s

Spray angle	Depth /um	Depth change rate
0°	7.995	0%
10°	7.897	-1.25%
20°	7.406	-7.37%
30°	6.744	-15.65%
40°	5.735	-28.27%

Particle and substrate temperature;

Increasing the preheating temperature of Cu particles will reduce the microhardness of the coating after deposition. Therefore, preheating can soften the Cu particles, which is conducive to more severe plastic deformation of the Cu particles, which is beneficial to the particles in deposition on the substrate. Hu and Tan [66] found that when the particle impact velocity is 375m / s, preheating the powder particles and the substrate will help reduce the porosity and enhance the combination of the coating.

Yin [67] studied the impact of Cu powder particles at 300K, 500K, 700K, and 900K on the Cu substrate, as shown in Figure 1.9 (a); Fe powder particles temperature 400K, 600K, and 800K and 1000K, Fe particles deposit on the Fe substrate, as shown in Figure 1.9 (b); Ni particles temperature of 400K, 600K, 800K, and 1000K deposit on the Ni substrate, as shown in Figure 1.9 (c) As shown. It can be seen from the Figure 1.9 that as the temperature of the particles increases, the degree of deformation of the particles gradually increases, the metal sputtering generated around the particles becomes more and more obvious, and the temperature of the particles after deposition also shows an upward trend.
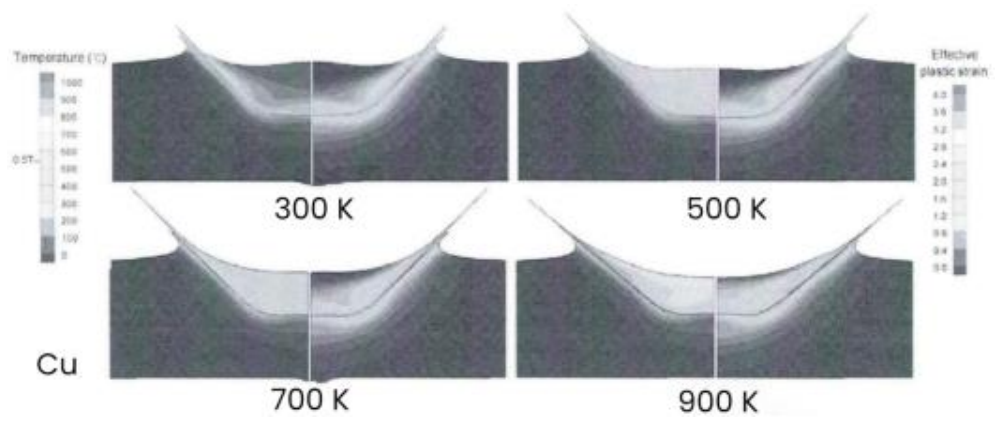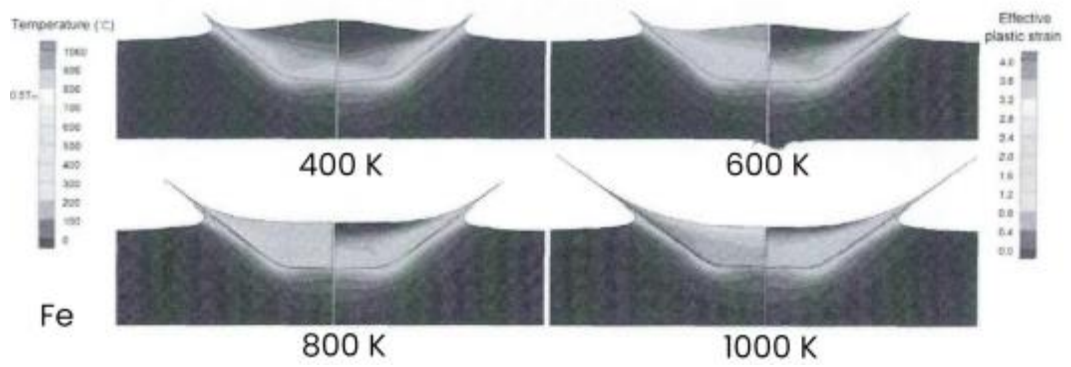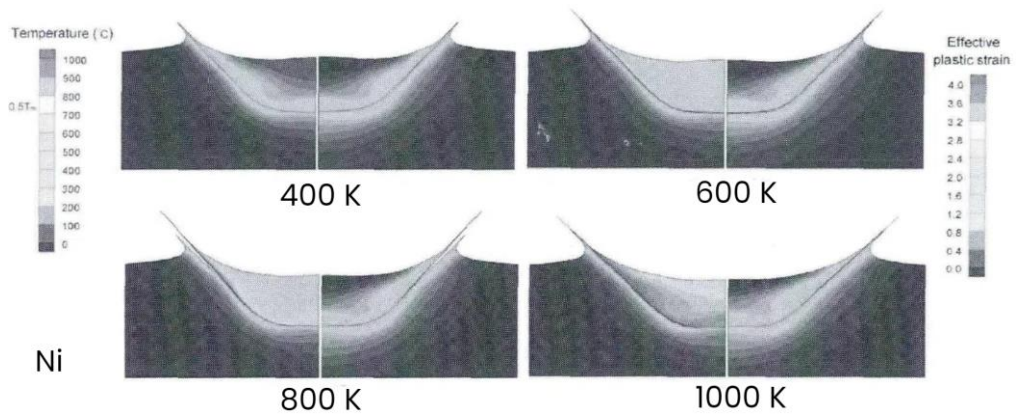
a − Cu powder particles at different temperatures depositing on the Cu substrate; *b* − Fe powder particles depositing on Fe substrate; *c* − Ni powder particles depositing on Ni substrate

Fig. 1.9. The temperature changes and plastic strain distributions [67]

1.4 Application and research based on cold spray coating materials

Cold spray technology prepares other functional coatings such as corrosion-resistant coatings, high-temperature-resistant coatings, wear-resistant coatings, conductive coatings, and oxidation-resistant coatings by depositing coatings. Which can repair parts that have the above problems in order to improve the physical and mechanical properties of parts and extend service life. it has a very good economy, such as turbine blades, pistons, bearings, cylinders, valves, seals, casings and other parts. Now cold spray technology has broad application prospects in the fields of aviation, aerospace, ships, automobiles, chemicals, electronics, paper making, and machinery.

The materials of the cold spraying technology are initially developed around conventional metal materials. Through continuous research and development, they have been extended to other materials. They have been successfully used in cold spraying technology and have achieved good results. The materials currently available for cold spray technology can be classified into six categories: metals, metal matrix composites, ceramics, polymers, nanostructured materials, and non-metallic base materials. For example, repairing space shuttle solid fuel rocket thrusters with Al coating, repairing components in aircraft structures, and repairing gas turbine sealed enclosures [68, 69]; cold spray technology MCrAlY and TBCS materials have very good high-temperature resistance, so they are often used as a material for preparing high-temperature resistant coatings and thermal barrier coatings; cold spray technology Cu-Cr-Al material has very good oxidation resistance, so it is often used to prepare anti-oxidation layers; In cold spray technology, cermet, metal-based Composite materials, and wear-resistant alloys have very good wear resistance, so they are often used to prepare wear-resistant coatings; Mg, Al, Cu, Ti, Mg, and Al are light metals and are often used in aircraft, missiles, torpedoes, radar, and satellites; with high specific strength characteristics alloys are mainly used in aircraft and engine structural parts [70]. Table 1.4 shows

the spraying materials commonly used in current cold spraying technology [71].

Table 1.4 − The materials that can be used for cold spraying technology

Materials	Specific materials
Metal	Al, Zn, Cu, Ni, Ca, Ti, Ag
Polymer	UHMWPE, HDPE, PA-12, PFA
High melting point metal	Mo, Ta
Alloy	Ni-Al, Al-Fe, Al-Cu, Cu-W, Al 7075, Al A357, Ti-6Al-4V
Ceramic	Al_2O_3, Cr_2O_3, SiC, WC, TiO_2, Cr_3C_2-NiCr, WC-Co, TiN

At present, the reliability of rare metal coatings is still some problems worthy of study, how to improve the reliability of rare metal coatings and thus improve the mechanical properties of the coatings. The mechanical properties of the joint between the coating of the non-metallic material and the substrate are poor and the bonding mechanism is unclear, especially in the case of low bonding force. The use of ceramic powder as a cold spray material for deposition on metal substrates, especially for the preparation of high-temperature coatings, has very little application research, which will be the focus of future research.

1.5 Research and progress of cold spray nozzles

In the cold spray device, the nozzle system is the core device and has been widely used and studied in engineering applications. The particles and accelerated gas are mixed in the nozzle system, accelerated to a certain speed, and deposit on the substrate to form a coating. Compared with other thermal spray processes, in the cold spray process, whether the spray particles can be deposited on the surface of the substrate to form a coating mainly depends on the speed of the particles before they deposit on the substrate. Therefore, the cold spray process mainly depends on the particles. kinetic energy rather than its thermal energy.

The nozzle system usually uses a Laval nozzle with a scaled flow section, so that the accelerated gas obtains supersonic gas flow in the nozzle flow, and the

supersonic working gas flow is used to accelerate the particles. The cross-sectional shape of the nozzle can be divided into circular and rectangular [72]. At present, the widely recognized nozzle cross-section is circular. Its advantages are mature technology and simple structure. rectangular nozzle is not common, this type of nozzle is mainly used for spraying rotating specimens. Among them, the rectangular nozzle the disadvantage of the nozzle is that the gas flow field in the nozzle is unevenly distributed, and turbulence easily occurs at the edges and corners, which will hinder the acceleration of particles and cause particles to accumulate inside the nozzle. Laval nozzles usually come in two forms conical and bell-shaped [73]. The difference between these two nozzles lies in the design of the expansion section. At present, most cold spray nozzle structures are conical nozzles. Single-channel axially symmetric cold spray nozzles are more common, but there are relatively few research works on multi-channel cold spray nozzles. Hu [34], Tan [35], and Dolmatov [74] studied multi-channel cold spray nozzles with rectangular cross-sections. The cold spray nozzle is mainly used to accelerate the particles, in which the study of the velocity and temperature of the particles before they reach the substrate is the most important.

During the cold spraying process, there are many methods for injecting spray particles into the nozzle system, which can be roughly divided into axial injection, vertical injection, and oblique injection. Currently commonly used are axial injection and vertical injection, as shown in Figure 1.10. Axial injection particles are injected axially into the convergence section of the nozzle inlet. The gas pressure of the particles accelerated gas needs to be slightly higher than the pressure of the working gas so that the particles can be injected into the high-pressure gas flow. In order to reduce the pressure of the particles feeding carrier gas and prevent particle clogging, the particle feeding pipe is extended to the throat or expansion section of the nozzle. During the cold spraying process, the working gas flow pressure decreases due to gas expansion in the expansion section of the nozzle. Compared with injecting particles from the contraction section of the nozzle inlet, the pressure

of the particles feeding gas flow can be significantly reduced.
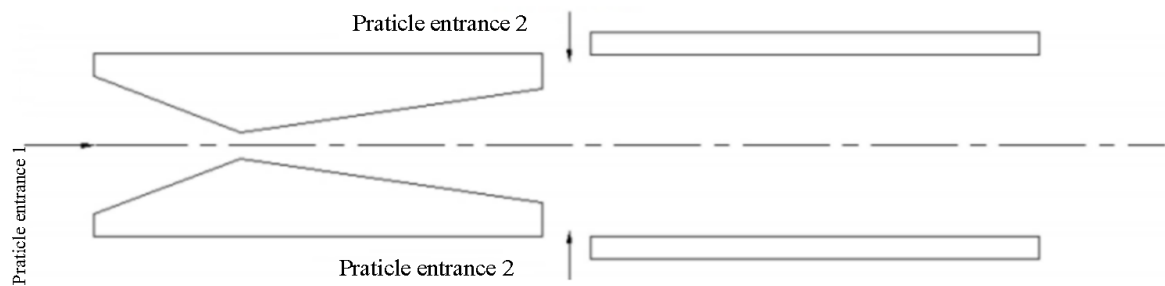
Fig. 1.10. Axial injection and vertical injection of spray particles

Li [75, 76] studied the effects of different nozzle structures on the carrier gas flow and spray particle acceleration performance by establishing tapering, gradually expanding, and tapering equal-section nozzles.

1.6 Research and progress on methods for simulating cold spray deposition

1.6.1 Research on micron-level cold spraying

Studying the deposition deformation behavior of cold spray particles and the substrate is an important means to explore the deposition and coating formation mechanisms of cold spray particles. However, due to the instantaneous characteristics of high-speed deposition of particles, it is difficult to conduct direct experimental observations of the deformation process of particles, and finite element numerical the analysis rules provide an effective way to study the deformation behavior of particles and matrix. By simulating the whole deposition process, it can intuitively observe the entire process of deposition and deformation of particles and matrix. The resulting deformation of particles and matrix the appearance is also in good agreement with the experimental observation results. Therefore, the numerical simulation method is becoming the main means to study the deposition deformation behavior of cold spray particles and the matrix.

Zhou [77] used the finite element numerical calculation method to study the

deposition of various particles of Cu, Al, Ni alloy, and Ti alloy on the Cu substrate, and studied the influence of the material properties of the particles on the deformation and bonding behavior during the deposition process. Ding [78] used numerical methods to study the impact of the deposition velocity of single particles on coating properties, and discussed that sudden changes in the stress and strain process are caused by the combination of particles and substrates. Li [79] used the finite element numerical calculation method to study the deposition behavior of both particles and substrates, and studied the effects of particle velocity and temperature on the deformation behavior after deposition with the matrix, the interface temperature change and the contact area of the matrix. Su [80] used the nonlinear finite element analysis software ANSYS/LS-DYNA to simulate the deposition process of single particles on the substrate and analyze its deformation behavior. Wang [81] used the finite element numerical calculation method to simulate the deposition behavior of Cu particles and Cu substrates, By changing the particle incident angle, the expected bonding strength, penetration depth and occurrence conditions of adiabatic shear instability of the particles. Huang [82] used numerical simulation calculation methods to study the deformation and bonding of Zn particles on Q235 steel substrate. Dykhuizen [83] used numerical simulation methods to simulate the deposition of Cu particles depositing on the surface of the stainless-steel substrate, and studied the melting phenomenon between the particles and the substrate during the deformation process. Assadi [32] used the finite element method to simulate the deposition of Cu particles through ABAQUS to study the adiabatic shear instability phenomenon that occurs during the deposition process; this is the well-known shear instability mechanism in spraying theory circles.

1.6.2 Molecular dynamics simulation cold spray research

Some scholars have expanded the research content of the cold spray deposition process to molecular dynamics simulation. By studying the film growth process of

particles during the deposition process, it can understand the microscopic mechanism of film growth, the relationship between the quality of the grown film and the coating environment. According to the different kinetic energy of the clusters, the cluster deposition process can be divided into three categories: soft-landing (kinetic energy < 0.1 eV/atom), low-energy cluster beam deposition, LECBD) (kinetic energy < 0.1 eV/atom), energy-carrying cluster impact (EIC) (kinetic energy > 10 eV/atom) [84].

Gao [85] summarized some research on molecular dynamics simulations. Kari-Heinz [86] used the two-dimensional molecular dynamics method to simulate related issues in the film formation process in ICBD. The Lennard-Jones potential function was used, the number of cluster atoms was 700, and the cluster incident velocity was 0.1 ε /atom. 0.5 ε /atom, 1 ε /atom, 2 ε /atom, 4 ε /atom. Horngming Hsieh [87] studied the deposition dynamics of Cu_{92}, Cu_{13}, Cu_4, Al_{92}, Ni_{92} and metal surfaces. The initial kinetic energy of the cluster ranged from 92-1000eV, and the EAM potential function was used to calculate the interatomic interaction force. Hellmut [88] used the F-S many-body potential to study the process of Mo1043 with kinetic energy of 0.1eV/atom, 1eV/atom, and 10eV/atom hitting the surface of Mo (001) matrix. Hou [85] used molecular dynamics methods to study the deposition process of clusters on the substrate. Li [89] used molecular dynamics simulation to study the deposition process of Cu13 atomic clusters with an energy of 5-20eV/atom and a regular icosahedral structure on the Cu (001) surface. Xie [90] used molecular dynamics simulation methods and Tersoff many-body potential functions to simulate the deposition process of low-energy incident C60 molecules on the surface of reconstructed diamond (100). Zhang [91] used molecular dynamics methods to simulate the growth process of a thin film of energy-carrying Au atoms deposited on the (100) surface of an Au matrix. Zhang [92] used the Monte Carlo method to study the initial growth process of Au/Au (100) thin films deposited with energy-carrying particles, and explored the impact of energy-carrying particle deposition on film growth and its changes with substrate temperature. Zhang [93] used molecular

dynamics simulation methods to study in detail the generation and distribution of surface adsorbed atoms, sputtered atoms, and surface vacancies caused by the interaction between low-energy Pt atoms and the Pt (111) surface, and gave The relationship between the surface adatom yield, the sputtered atom yield and the surface vacancy yield as a function of the incident Pt atom energy was studied. Kazumasa [94] used molecular dynamics simulation methods to study the mechanism of thin films formed by ion cluster deposition on the surface. The simulation used a combination of embedded atom potential (EAM) and average modified Lenz-Jensen potential function (AMLJ). function. Ralf [95] studied the process in which Cu13 and Cu43 hit the substrate with initial kinetic energies of 5000eV and 20000eV and formed pits on the substrate. Lee [96] studied the deposition process of 1000K Au clusters containing 300-1500 atoms on an 800K Au matrix. The EAM potential function was used in the simulation. Molecular dynamics methods to study the deposition process of Al clusters on the Al(100) surface. The simulation uses a tight binding potential.

1.6.3 Research on methods to simulate cold spray deposition

The above summarizes some research on deposition methods of cold spray technology. Through analysis, it can be seen that micron-level deposition analysis and molecular dynamics simulation are completely different research fields and methods. In this dissertation work, the deposition of micron-sized cold spray particles is mainly studied. Currently commonly used simulation software included Abaqus-Explicit and LS-DYNA; currently the main research methods include the Smoothed Particle Hydrodynamics method (SPH), The Arbitrary Lagrangian Eulerian (ALE) and The Coupled Lagrangian-Eulerian method (CEL).

1.6.3.1 Research on the SPH method

The SPH (Smoothed Particle Hydrodynamics) is a smooth particle hydrodynamics method. As a Lagrangian particle method, this method can effectively simulate complex problems such as large material deformation, moving material interfaces, and phase changes. Hu and Tan [97] used the SPH method to simulate the cold spray deposition process of various particulate materials. The ratio coefficient K between the depth of the foundation pit and the particle size after deformation of the powder is proposed to determine the critical velocity of the particles. Hu [98] used the SPH method to simulate the deposition of Al, TC4, Cu, W alloy, and Ti particles on the TC4 substrate to study the effects of hardness, particle velocity and substrate pit depth. Malachowska [99] used the SPH method to simulate the deposition process of Al, Cu, and Ti particulate materials on polymer substrates, the effects of particle shape and temperature on coatings were studied. Fernandez [100] used the SPH method to simulate the deposition of various mixtures of Al and alumina. Deposition efficiency was studied by adding oxides to the particles. Simultaneous interaction between ceramic particles during shot peening affecting Al particles was found to be a possible mechanism to improve the deposition efficiency of Al particles. Manap [101] used the SPH method to simulate the cold spray process and estimated the critical, maximum and optimal velocities of individual cold spray particles by evaluating the recovered impact shape coefficient, rebound and deposition energy ratio. Abreeza [102] used the SPH method to simulate the deposition of spherical Al-Si particles on a mild steel substrate, and established that the adhesive interaction between contact surfaces was described as the inter-surface force using the adhesion zone model. Xie [103] used the SPH method to simulate the Al/Al cold spraying process and observed the plastic deformation of the periphery of the Al substrate contact center. Profizi [104] used the SPH method to simulate the Al/Al cold spraying process. By establishing an adhesion model, it studied the relationship between particle size and surface force.

It also studied the impact of the selection of the type of interaction rules in the adhesion zone, and the impact of fast dynamics on some conclusions are made about the modeling relevance of adhesion under scientific impact.

1.6.3.2 Research on the ALE method

The ALE method has been widely used to study deformation problems in solid mechanics, such as deposition, contact and elastic fracture mechanics. The principle is that large deformation occurs after the particle deposition with the substrate, so the ALE method is widely used in the simulation of cold spray technology. However, excessive deformation of particles during the spraying process is difficult to calculate, so this method is not recommended [105]. Wang [106] used the ALE method to simulate the distribution of residual stress after NiCrAl particles were deposited on the TA-15 Ti alloy substrate, and verified it experimentally; The results show that the residual stress of the coating is compressive stress and increases with the increase in thickness; at the same time, the distribution of residual stress is related to the shape and size of the specimen and there is significant stress concentration near the edge. Li [107] compared the deformation behavior of particles simulated by the SPH method with the deformation behavior of particles simulated by the ALE method. Yin [108] used the ALE method to simulate the deposition of single particle Cu and study the effective plastic strain profile of the impact of single particles with different grid sizes on the substrate. Mesh size has a significant effect on particle deformation. In fact, the essence is that refining the mesh can effectively improve accuracy. It should be noted that ALE method mainly uses hexahedral elements for meshing, with the mesh being refined in particles and closer to the substrate impact region to obtain similar deformation behavior and mesh convergence [109]. Wang [110] used the ALE method to simulate the deposition on Cu particles/Fe substrate and the deposition on stainless steel particles/Q235 steel substrate, and studied the temperature, plastic deformation and bonding morphology of the particles; Wang

[111] used the ALE method to simulate the distribution of residual stress after deposition of NiCrAl/TA-15 Ti alloy substrate. The main disadvantage of the ALE method is that the particles and substrate may be seriously distorted during the simulated deposition process, which will lead to the termination of the simulation calculation process.

1.6.3.3 Research on the CEL method

The full name of the CEL method is the Coupled Euler-Lagrangian method. It essentially adds a Euler domain to the ALE method, and the particles can flow in the Euler domain. The CEL method has been proven to be more suitable for analyzing large deformation situation problems that occur during cold spraying. The method has higher accuracy and robustness than other finite element techniques in the range of large deformation, large displacement and large strain. Its advantage is that the particles are wrapped in Eulerian domains, which avoids the need for remeshing and highly distorted elements [112].

The CEL method cannot numerically study the deformation of particles. Instead, it tracks the material as it flows through the grid by calculating the EVF in each cell. If the material completely fills the cell, its volume fraction is 1, which is not present in the element. This material, then its EVF is 0, and the sum of the EVF of all materials in the unit is less than 1, then the rest of the unit will automatically fill the void material, and the void material has no mass and strength [113]. The single-particle deposition model simulated by the CEL method cannot represent the interaction between coating accumulation, particle size, velocity and temperature [114]. Therefore, it is necessary to simulate the process of multi-particle formation of coatings. The multi-particle deposition model is between the microscopic method of single particle simulation and the macroscopic method of homogeneous material deposition [115]; multi-particle deposition models can be used to simulate complex interactions between multiple particles, which are beyond the reach of single-particle

deposition models. Therefore, the CEL method is a very good method to detect the porosity of coatings after deposition. Xie [116] analysis concluded that the CEL method is the most effectively way to study substrate deformation and predict porosity levels. Many scholars have studied the large deformation of particles during cold spraying through the CEL method [37, 117-120]; MacDonald [121] used the CEL method to study the thermal softening effect of single particle temperature. As the particle temperature increases, the particle flatness rate increases; thus, further studying porosity. Zahiri [122] studied the impact of single Cu particles on Al substrates, and increasing the particle temperature and speed can increase the density of sprayed samples; The above are dedicated to predicting the porosity level of fabricated samples.

Matteo [123] used the CEL method to simulate the spraying of multi-particle Ti-Al and Ti-Cu particles. The weight of the particles and the mass of the raw material particles were calculated through the particles to calculate the corresponding volume percentage, thereby predicting the porosity of the coating. This is not a direct study of the porosity of the coating after deposition. Weiller [124] used the CEL method to simulate the deposition of multi-particle Al/Al2017 to study the formation mechanism of porosity. They concluded that interface porosity and stacking porosity have a great influence on the porosity of the coating. The interface porosity is determined by the particles. Caused by the arrangement between them, stacking porosity is caused by changes in particle density in gas flow; randomly generated particles will cause irrationality in the distribution of particles in the Euler domain, thus affecting the final porosity result. Song [125] used the CEL method to simulate the deposition process of Ti6Al4V particles on the Ti6Al4V substrate to study the effects of temperature and speed on the coating.

1.7 The research purpose and research content

1.7.1 Theoretical basis required for supersonic flow field, particle acceleration and particle deposition analysis

Based on the existing cold spray nozzle, the theoretical basis of the supersonic flow field in the cold spray process is described in detail, including control equations, turbulence models and discrete term models; these are all based on the numerical simulation of the nozzle later, required theoretical basis. The second is the theoretical basis required for particle deposition in the cold spray process and the mathematical methods required for simulation.

1.7.2 Based on analysis and optimization of existing cold spray nozzles and methods

Based on the existing cold spray nozzle, a comparative analysis is conducted on the impact of structural parameters and technical parameters on particle acceleration during the cold spray process; first, a single factor are used to study the effect on the velocity of particles at the exit of the nozzle and when they reach the surface of the substrate; the main function of the nozzle is to accelerate the spray particles, so it is very necessary to study. Then the RSM was used to influence the acceleration of particles in the nozzle through the interaction of multi-factor coupling, thereby further approaching the real cold spraying process. At the same time, it is also proposed to use the BPNN based on the GA to optimize the spraying parameters of the existing cold spray nozzle. This is also a study of the role of multi-factor coupling, in this way, a better optimization method is selected, and the optimal spraying parameters of the particles are finally obtained.

Based on the analysis and optimization of the existing cold spray nozzle, a new type of right-angle cold spray nozzle is further studied; the analysis of right-angle

cold spray nozzles can be divided into analysis of the gas flow field inside the single-channel circular right-angle nozzle and research and analysis of multi-channel mixed cross-section right-angle cold spray nozzles. Simulate the internal flow field of the right-angle cold spray nozzle under different pressure and temperature conditions, as well as the acceleration of various sprayed particle materials in the nozzle. Preparation for further cold spray deposition work.

1.7.3 Research on calculation methods of high-speed deposition process between multi-particles and matrix

Based on the ALE, the CEL, and the SPH methods, multiple sets of finite element analysis models were established to solve the local velocity deposition process between cold spray particles and the substrate. By comparing different calculation models, the performance of various models was analyzed. Advantages and disadvantages, and then select the research focus and needs to select an appropriate calculation model to provide a reference for subsequent research on the deformation behavior and deposition mechanism of cold spray particles.

1.7.4 Research, analysis and optimization of porosity

The research part of this dissertation on particle deposition is mainly to study the porosity of the coating and optimize it. The multi-particle model was established using Python codes and then embedded into the CEL deposition simulation to simulate the cold spray process. Then a multi-particle deposition model was established to simulate the deposition of Al6061 particles/substrate, and the porosity of the coating was studied by changing the particle temperature. The CEL method has the characteristics of high accuracy and robustness and was selected as the method for multi-particle deposition model simulation. Take several groups of cuboid samples from the coating, and calculate the value of the void area of each

group of samples. Finally, find the average value as the value of the void area of the coating under a certain working condition, and identify this value as the porosity of the coating.

This dissertation uses the RSM to analyze the coupling effects of multi-factors on the coating after Al6061 particle deposition and optimizes it; by adding three influencing factors: particle temperature, substrate temperature and particle velocity; the three factors interact with each other in pairs. Obtain the best spraying parameters and thus the best coating void ratio.

1.8 Conclusion for the Chapter 1

This chapter mainly describes the development history of cold spray technology. Cold spray technology is a type of additive manufacturing technology, but it is different from other additive manufacturing technologies; the characteristics of cold spray technology and other types of additive manufacturing technologies and their applications in scientific and technological production are listed. The principle and acceleration characteristics of particle acceleration in cold spray technology are described in detail; the combination mechanism of the coating formation process. The characteristics of high-pressure and low-pressure cold spray equipment are listed and compared. The research on cold spray process parameters, the application of cold spray materials, the development of cold spray nozzles, and the process of numerical simulation of particle deposition are described. Among them, the characteristics of the ALE, the SPH, and the CEL methods for numerical simulation of cold spray particle deposition are described in detail. Finally, the research content of this dissertation is summarized.

CHAPTER 2

SUPERSONIC GAS FLOW FIELD AND NUMERICAL ANALYSIS OF PARTICLE ACCELERATION AND THEORETICAL BASIS OF PARTICLE DEPOSITION

2.1 The theory of numerical analysis of supersonic flow field and particle acceleration and the design basis of Laval nozzle

Cold spray technology is a new material surface modification technology invented based on aerodynamic principles. Cold spray technology is different from traditional thermal spray technology; the performance of cold spray technology to modify the surface of materials is mainly based on whether the spray particles can combine with the substrate to form a coating. It mainly depends on the speed of the particles when they impact the substrate. Therefore, the study of particles the acceleration inside the Laval nozzle and the acceleration after the Laval nozzle exit are a very important part. Tan [8, 34, 58, 126] proposed that the single- and multi factors affecting the velocity of particles can be divided into technical parameters and structural parameters; technical parameters can be mainly divided into the pressure and temperature of the accelerating gas; the particle size, temperature, velocity and shape of the particles; the substrate temperature; the distance and angle of spraying; the structural parameters are mainly the size and structure of the Laval nozzle; Ultimately it depends on the structure and flow characteristics of the carrier gas jet flow field outside the Laval nozzle. The equipment of cold spray technology is relatively expensive, and the experimental environment requirements are high. Therefore, the current mainstream method for cold spray jet flow field is to use CFD method to numerically simulate the gas and particle flow field inside the Laval nozzle to obtain some target results; and the feasibility and accuracy of this set of numerical simulation calculation methods have been guaranteed. Therefore, through

numerical calculation of the supersonic flow field inside and outside the cold spray Laval nozzle, Observe the internal flow field and the acceleration process of particles in the Laval nozzle, Parameters can also be changed according to target requirements. The effects of other parameters on the flow characteristics and particle acceleration behavior of the flow field are further studied.

2.1.1 Theoretical basis

2.1.1.1 The governing equations

Fluid flow is governed by physical conservation laws, and any flow problem must satisfy the mass conservation law. This law is: the increase in mass in the fluid micro-element body per unit time is equal to the net mass flowing into the micro-element body within the unit time interval. According to this, the differential expression of conservation of mass conservation equation can be obtained,

$$\frac{\partial \rho}{\partial t} + \frac{\partial(\rho u_i)}{\partial x_i} = S_m,$$

(2.1)

where S_m – the mass added to the continuous phase, other custom source terms can also be used;

u_i – the velocity vector.

This equation, also known as the continuity equation, is the general form of the mass conservation equation, which applies to both compressible and incompressible flows.

The continuity equation of the two-dimensional axisymmetric problem is:

$$\frac{\partial \rho}{\partial t} + \frac{\partial(\rho u)}{\partial x} + \frac{\partial(\rho v)}{\partial x}\frac{\rho v}{\gamma} = S_m,$$

(2.2)

The law of conservation of momentum is the sum of the change rate of the momentum of the fluid in the micro-element body with respect to time and the various external forces acting on the micro-element body. According to this law, the momentum conservation equations in the three directions of x, y, and z can be derived.

$$\frac{\partial(\rho u)}{\partial t} + div(\rho uU) = \frac{\partial P}{\partial x} + \frac{\partial \tau_{xx}}{\partial x} + \frac{\partial \tau_{yx}}{\partial y} + \frac{\partial \tau_{zx}}{\partial z} + F_x; \tag{2.3}$$

$$\frac{\partial(\rho v)}{\partial t} + div(\rho vU) = \frac{\partial P}{\partial y} + \frac{\partial \tau_{xy}}{\partial x} + \frac{\partial \tau_{yy}}{\partial y} + \frac{\partial \tau_{zy}}{\partial z} + F_y; \tag{2.4}$$

$$\frac{\partial(\rho w)}{\partial t} + div(\rho wU) = \frac{\partial P}{\partial z} + \frac{\partial \tau_{xz}}{\partial x} + \frac{\partial \tau_{yz}}{\partial y} + \frac{\partial \tau_{zz}}{\partial z} + F_z, \tag{2.5}$$

where p – the pressure on the fluid micro-element;

τ_{xx}, τ_{yx}, and τ_{zx} – the components of the viscous stress τ acting on the surface of the micro-element due to the viscosity of molecules;

F_x, F_y, and F_z – the physical force on the micro-element.

If the physical force is only gravity, and the z-axis is vertically upward, then F_x=0, F_y=0, and $F_z = -\rho g$.

The above equation is a momentum conservation equation that is valid for any type of fluid (including non-Newtonian fluids). For Newtonian fluids:

$$\frac{\partial(\rho u)}{\partial t} + div(\rho uU) = div(\mu gradu) - \frac{\partial P}{\partial x} + S_u; \tag{2.6}$$

$$\frac{\partial(\rho v)}{\partial t} + div(\rho vU) = div(\mu gradv) - \frac{\partial P}{\partial y} + S_v; \tag{2.7}$$

$$\frac{\partial(\rho w)}{\partial t} + div(\rho wU) = div(\mu gradw) - \frac{\partial P}{\partial z} + S_w, \tag{2.8}$$

where S_u, S_v and S_w – the generalized source terms of the momentum conservation equation.

S_u=F_x+s_x, S_v=F_y+s_y, and S_w=F_z+s_z, Among them, the expression of s_x,

s_y, and s_z are as follows:

$$s_x = \frac{\partial}{\partial x}\left(\mu\frac{\partial u}{\partial x}\right) + \frac{\partial}{\partial y}\left(\mu\frac{\partial v}{\partial x}\right) + \frac{\partial}{\partial z}\left(\mu\frac{\partial w}{\partial x}\right) + \frac{\partial}{\partial x}(\lambda divU); \qquad (2.9)$$

$$s_y = \frac{\partial}{\partial x}\left(\mu\frac{\partial u}{\partial y}\right) + \frac{\partial}{\partial y}\left(\mu\frac{\partial v}{\partial y}\right) + \frac{\partial}{\partial z}\left(\mu\frac{\partial w}{\partial y}\right) + \frac{\partial}{\partial y}(\lambda divU); \qquad (2.10)$$

$$s_z = \frac{\partial}{\partial x}\left(\mu\frac{\partial u}{\partial z}\right) + \frac{\partial}{\partial y}\left(\mu\frac{\partial v}{\partial z}\right) + \frac{\partial}{\partial z}\left(\mu\frac{\partial w}{\partial z}\right) + \frac{\partial}{\partial z}(\lambda divU), \qquad (2.11)$$

where s_x, s_y, and s_z – a small quantity.

For an incompressible fluid with constant viscosity, the formula on $s_x = s_y = s_z = 0$ is the momentum conservation equation, also known as the equation of motion.

The law of conservation of energy is the basic law that all flow systems involving heat exchange must satisfy. This law is expressed as: the rate of increase of energy in a micro-element body is equal to the net heat flow entering the micro-element body plus the work done by physical and surface forces on the micro-element body. Energy conservation equation with temperature T as a variable:

$$\frac{\partial(\rho T)}{\partial t} + div(\rho UT) = div\left(\frac{k}{C_p}gradT\right) + S_T, \qquad (2.12)$$

where C_p - the specific heat capacity;

T – the temperature;

k – the heat transfer coefficient of the fluid;

S_T – the internal heat source of the fluid and the part of the fluid's mechanical energy converted into thermal energy due to viscosity;

S_T – the viscous dissipation coefficient.

For incompressible fluids, if the heat exchange amount is so small that it can be ignored, the energy conservation equation does not need to be considered. Ideal

gas equation of state:

$$\rho = \frac{P_0 + P}{\left(\frac{R_u}{M_w}\right) \cdot T},$$ (2.13)

where ρ, u, P, T, e, τ, q, R_u, and M_w – gas density, velocity, pressure, temperature, body energy, viscous shear stress, heat flux, gas constant, and molecular weight respectively;

P – the static pressure;

P_0 – the total pressure (stagnation pressure).

2.1.1.2 The turbulence model

Turbulent flow is a common flow phenomenon in nature. In most engineering problems, the flow of fluid is often turbulent. Turbulent flow occupies an important position in engineering. Fluid experiments show that when the Reynolds number is greater than a certain critical value, a series of complex changes will occur, eventually leading to essential changes in the flow characteristics and the flow into a disorderly chaotic state. At this time, even if the boundary conditions remain unchanged, the flow is unstable and the flow characteristics such as velocity change randomly. This state is called turbulent flow.

Considering the incompressible flow, using the Cartesian coordinate system, the velocity vector U is at the bottom, and the components in the x, y, and z directions are u, v, and w, the instantaneous control equation of turbulence is obtained as follows:

$$\text{div}u = 0;$$ (2.14)

$$\frac{\partial u}{\partial t} + \text{div}(uU) = \frac{1}{\rho}\frac{\partial p}{\partial x} + v\text{div}(\text{grad}u);$$ (2.15)

$$\frac{\partial v}{\partial t} + \text{div}(vU) = \frac{1}{\rho}\frac{\partial p}{\partial y} + v\text{div}(\text{grad}v); \qquad (2.16)$$

$$\frac{\partial w}{\partial t} + \text{div}(wU) = \frac{1}{\rho}\frac{\partial p}{\partial z} + v\text{div}(\text{grad}w), \qquad (2.17)$$

where div – divergence.

Ignoring the influence of density pulsation, but considering the change of average density, the governing equation of the average flow of compressible turbulent flow is obtained as follows:

$$\frac{\partial \rho}{\partial t} + \frac{\partial}{\partial x_i}(\rho u_i) = 0; \qquad (2.18)$$

$$\frac{\partial}{\partial t}(\rho u_i) + \frac{\partial}{\partial x_j}(\rho u_i u_j) = -\frac{\partial \rho}{\partial x_j} + \frac{\partial}{\partial x_j}\left(\mu\frac{\partial u_i}{\partial u_j} - \rho\overline{(u_i' u_j')}\right) + S_j; \qquad (2.19)$$

$$\frac{\partial(\rho \emptyset)}{\partial t} + \frac{\partial}{\partial x_j}(\rho u_j \emptyset) = \frac{\partial}{\partial x_j}\left(\Gamma\frac{\partial \emptyset}{\partial x_j} - \rho\overline{(u_i' \emptyset')}\right) + S. \qquad (2.20)$$

Basic turbulence models include zero-equation model, one-equation model, and two-equation model. Because it is difficult to determine the mixing length for the zero-equation model, and difficult to scale the length for the one-equation model, they are less commonly used. The most widely used is the standard two-equation model. In the calculation of turbulent flow, the control equation uses Reynolds time-averaged control equation. The quadratic term will generate additional terms containing pulsation values after time-averaged processing. The generation of additional terms causes the originally closed control force range to become a non-closed equation. In order to close the system of governing equations describing turbulence, it is necessary to find the relationship that determines this additional term. The turbulence model refers to a residual specific relationship that links the additional term of the pulsation value of turbulence with the time mean value [127]. Two turbulence models are standard $k - \varepsilon$ and RNG $k - \varepsilon$ models.

On the basis of the turbulent kinetic energy k, and then introducing an equation

about the turbulent dissipation rate ε, a two-equation model is formed, which is called the standard $k - \varepsilon$ model [73]. In the model, the ε of the turbulent dissipation rate is defined as:

$$\varepsilon = \frac{\mu}{\rho} \overline{\left(\frac{\partial u_i'}{\partial x_k}\right)\left(\frac{\partial u_j'}{\partial x_k}\right)}. \tag{2.21}$$

Turbulent viscosity μ_t can be expressed as a function of k and ε:

$$\mu_t = \rho C_\mu \frac{k^2}{\varepsilon}, \tag{2.22}$$

where C_μ – the empirical constant 0.09.

In the standard $k - \varepsilon$ model, k and ε are two basic unknown quantities, and the corresponding transport equation:

$$\frac{\partial}{\partial t}(\rho k) + \frac{\partial}{\partial x_i}(\rho k u_i) = \frac{\partial}{\partial x_j}\left(\mu + \frac{\mu_t}{\sigma_k}\right) \cdot \frac{\partial k}{\partial x_j} + G_k + G_b - \rho \varepsilon -$$

$$- Y_M + S_k; \tag{2.23}$$

$$\frac{\partial(\rho \varepsilon)}{\partial} + \frac{\partial(\rho \varepsilon u_i)}{x_i} = \frac{\partial}{\partial x_j}\left[\left(\mu + \frac{\mu_t}{\sigma_\varepsilon}\right) \cdot \frac{\partial \varepsilon}{\partial x_j}\right] + C_{1\varepsilon}\frac{\varepsilon}{k}(C_k + C_{3\varepsilon}G_b) - C_{2\varepsilon}\rho\frac{\varepsilon^2}{k} +$$

$$+ S_\varepsilon - R_\varepsilon, \tag{2.24}$$

where G_k – the generation term of turbulent kinetic energy.

k due to the average velocity gradient, which is calculated by the following formula.

$$G_k = \mu_t \left(\frac{\partial u_i}{\partial x_j} + \frac{\partial u_j}{\partial x_i}\right)\frac{\partial u_i}{\partial x_j}, \tag{2.25}$$

where G_b – the term generated by the turbulent kinetic energy k.

For an incompressible fluid, $G_b = 0$; if it is a compressible fluid, it is as follows:

$$G_b = \beta g_i \frac{\mu_t}{Pr_t} \frac{\partial T}{\partial x_i}, \qquad (2.26)$$

where $Pr_t = 0.85$ – the turbulence Prandtl coefficient;

g_i – the component of gravity acceleration in the i-th direction;

β – the thermal deposition coefficient.

As follows:

$$\beta = -\frac{1}{\rho} \frac{\partial \rho}{\partial T}, \qquad (2.27)$$

where Y_M – represents the contribution of pulsating expansion in compressible turbulent flow.

And for incompressible fluids, $Y_M = 0$. For compressible fluids, this is as follows:

$$Y_M = 2\rho\varepsilon M_t^2, \qquad (2.28)$$

where M_t – the turbulent Mach number, $M_t = \sqrt{\frac{k}{\alpha^2}}$;

α – the velocity of sound, $\alpha = \sqrt{\gamma RT}$;

$C_{1\varepsilon}$, $C_{2\varepsilon}$, and $C_{3\varepsilon}$ – empirical constants.

$C_{1\varepsilon} = 1.44$, $C_{2\varepsilon} = 1.92$, and $C_{3\varepsilon} = 1$ (the main flow direction is parallel to the direction of gravity), $C_{3\varepsilon} = 0$ (the main flow direction is perpendicular to the direction of gravity).

where σ_k and σ_ε – the Prandtl coefficients corresponding to the turbulent kinetic energy k and the dissipation rate ε respectively; $\sigma_k = 1.0$, $\sigma_\varepsilon = 1.3$;

S_k and S_ε – user-defined source items.

If the user-defined source items are not considered, $S_k = 0$, $S_\varepsilon = 0$. This model is currently the most widely used turbulence model.

The RNG $k - \varepsilon$ model is deduced from the transient N-S equation through the mathematical method of renormalization group. Its analytical properties are directly derived from the standard $k - \varepsilon$ model. The form of the equation is very similar to the standard $k - \varepsilon$ model, but with larger changes improve. An extra term is added to the $k - \varepsilon$ equation of the RNG $k - \varepsilon$ model. The model also considers the impact of turbulence on turbulence. The calculation of the turbulent Prandtl number uses a new set of analytical formulas instead of the user input constants in the standard $k - \varepsilon$ model. The model $k - \varepsilon$ set of analytical formulas considering low Reynolds number effective viscosity are also provided, which can accurately handle the flow situation in the near-wall region. These characteristics make the RNG $k - \varepsilon$ model more reliable and accurate than the standard $k - \varepsilon$ model in a wider range of flows. The turbulence RNG $k - \varepsilon$ model equation is as follows equation 2.23 and 2.24 [128, 129]:

Among them, R_ε is an extra term added in the turbulence model of RNG $k - \varepsilon$, which is obtained by the following equation:

$$R_\varepsilon = \frac{C_\mu \rho \eta^3 \left(1 - \frac{\eta}{\eta_0}\right)}{1 + \beta \eta^3} \cdot \frac{\varepsilon^2}{k}. \tag{2.29}$$

In equation (2.29), $\eta = \frac{Sk}{\varepsilon}$, $\eta_0 = 4.38$, and $\beta = 0.012$, the other parameters have the same meaning as in the standard $k - \varepsilon$ model.

Substituting equation (2.29) into equation (2.24), equation ε can be written as:

$$\frac{\partial(\rho\varepsilon)}{\partial} + \frac{\partial(\rho\varepsilon u_i)}{x_i} = \frac{\partial}{\partial x_j}\left[\left(\mu + \frac{\mu_t}{\sigma_\varepsilon}\right)\cdot\frac{\partial\varepsilon}{\partial x_j}\right] + C_{1\varepsilon}\frac{\varepsilon}{k}(C_k + C_{3\varepsilon}G_b) - C_{2\varepsilon}^*\rho\frac{\varepsilon^2}{k}. \qquad (2.30)$$

Among them, $C_{2\varepsilon}^*$ has the following equation:

$$C_{2\varepsilon}^* = C_{2\varepsilon} + \frac{C_\mu\rho\eta^3\left(1-\frac{\eta}{\eta_0}\right)}{1+\beta\eta^3}. \qquad (2.31)$$

2.1.1.3 Discrete item model

After writing the basic system of equations, some systems of equations often cannot be closed. Different models should be selected according to the actual situation before calculation. Before performing CFD calculations on a specified problem, the calculation area must first be discretized, that is the continuous calculation area must be divided into many sub-areas, and the nodes in each area must be determined to generate a grid. Then the governing equations are discretized on the grid, that is the governing equations in partial differential format are transformed into a system of algebraic equations on each node [128].

Common discrete methods in the numerical simulation process include the following: the finite difference method (FDM), the finite element method (FEM), and the finite volume method (FVM) [130]. This is also a more commonly used discretization method at present.

The FDM is the oldest and most classic method among numerical solutions. It divides the solution domain into differential grids, uses a finite number of grids, and nodes to replace the finite solution domain, and then replaces the derivatives of the governing equations of the partial differential equations with difference quotients to derive a system of differential equations containing a finite number of unknowns at discrete points. Finding the solution to the system of differential equations and algebraic equations is the numerical approximate solution to the definite solution of the differential equation. This is an approximate numerical solution method that

directly turns the differential problem into an algebraic problem.

The FDM is the oldest method for obtaining numerical solutions to partial differential equations. It replaces the solution area with a set of points composed of intersections (nodes) of grid lines. At each node, each derivative term in the partial differential equation describing the flow and heat transfer problem under study is expressed by a corresponding differential expression, thereby forming an algebraic equation at each node, which contains this node and the unknown values of the requested quantity on some nearby nodes. Solving these systems of algebraic equations yields the required numerical solutions. There are a large number of monographs and literature on the application of the finite difference method in the numerical solution of three types (parabolic, hyperbolic and elliptical) partial differential equations and the corresponding mathematical problems. On structured grids in regular areas, the finite difference method is very simple and effective, and it is easy to introduce high-order schemes for convection terms. Its disadvantage is that the conservation properties of discrete equations are difficult to guarantee, and its adaptability to irregular areas is not as good as finite volume method and finite element method.

The FEM arbitrarily divides a continuous solution domain into many tiny units with appropriate characteristics, and constructs interpolation functions in each small unit. Then, according to the extreme value principle, the governing equations of the problem are converted into finite element equations on all units. The overall extreme value is taken as the sum of the extreme values of each unit, that is, the local units are synthesized as a whole to form a system of algebraic equations embedded with specified boundary conditions. Solving this system of equations will obtain the function values to be found at each node.

The FVM starts from the conservation equation describing flow and heat transfer problems, and integrates it on the control volume. During the integration process, it is necessary to calculate the function itself (convection flux) and its first derivative on the control volume interface. Assumptions are made about the way the

(diffusive flux) structure is structured, which results in different formats. Since the diffusion terms mostly use linear interpolation equivalent to second-order precision, the difference in format is mainly reflected in the convection terms. The discrete format derived by the FVM can guarantee conservation (as long as the interpolation method on the interface is the same for the control volumes on both sides of the interface), and its adaptability to the regional shape is better than the FDM. It is currently the Apply one of the most common numerical methods. Currently, commercial CFD software with wide versatility such as FLUENT, CFX, PHOENICS, STAR-CD all use the FDM.

The FVM is also known as the control volume method. The basic idea is to divide the calculation area into grids, and have a non-repeating control volume around each grid point; integrate the differential equation control equation to be solved for each control volume to obtain a set of discrete equations. The unknowns are the dependent variables at the grid points. In order to find the integral of the control volume, it is necessary to assume a regular variation of values between grid points. From the perspective of the selection method of the integration region, the finite volume method belongs to the subdomain method in the weighted residual method. From the perspective of the approximation method of the unknown solution, the finite volume method belongs to the discrete method using local approximation. Subdomain method plus discretization is the basic method of finite volume method.

In FVM the calculation area is divided into a set of discrete volumes or elements (in two-dimensional cases, the shape of the element is usually a triangle or a quadrilateral), and then the discrete equation is obtained by integrating the governing equations. The main difference between it and the FVM is A shape function (the simplest is a linear function) must be selected for each element, and the shape function is represented by the value of the variable being sought at the node in the element, and substitute the assumed shape function into the control equation before integration; The control equation should be multiplied by a selected weight function before integration, and the weighted mean of the remainder of the control equation

over the entire region is required to be zero, so that derive a set of algebraic equations about the variables being evaluated at the node. The biggest advantage of the FEM is that it has good adaptability to irregular collection areas. The FEM is not as mature as the FVM in the discretization of convection terms and the original variable method for solving the incompressible N-S equation. However, with the finite volume with the application of unstructured meshes in the method, the difference between the FVM and the FEM is narrowing. Among the currently widely used CFD software, only FIDAP uses the finite element method.

After the governing equations have been discretized, it can be solved. There are two solution methods for the FVM: coupling algorithm: solve the discrete algebraic equations of all variables in one time layer simultaneously, or solve only some of the variables (velocity component, energy) simultaneously for the entire field. Separation algorithm: solve the discrete equations of each variable sequentially. Generally, coupling algorithms are used for compressible flows and separation algorithms are used for incompressible flows. In computational fluid dynamics, methods that use non-primitive variables (such as vorticity-stream function method, vorticity-velocity method, vorticity-velocity potential method.) have become increasingly rare, whether they are self-developed programs or commercial software, more and more people are using the original variable method (using original variables density, pressure, speed as solution variables). The original variable flow field can be divided into two categories: density as the basic variable and pressure as the basic variable. The former type of method is mostly used to solve the compressible flow field, and the latter type of method is mostly used to solve the flow field of incompressible fluid. The density-based solution method is designed for compressible flows. When solving unsteady flows, there are also two options: explicit and implicit in time difference. Display is generally used for supersonic flow, and the discrete format at this time should use the second-order upwind format.

The fluid in this dissertation belongs to supersonic flow, so the solution method of the discrete control method is a density-based coupling algorithm based on the

second-order upwind style.

The discrete phase model in Fluent assumes that the dispersed phase is very thin, so the interaction between particles and the effect of particle volume fraction on the continuous phase are not considered. This assumption means that the volume fraction of the dispersed phase must be very low, generally less than 10-12% [129]. The orbits of discrete phase particles are solved by integrating the particle force differential equation in the Lagrange coordinate system. The form of the force balance equation of particles (particle inertia = various forces acting on the particles) in the Cartesian coordinate system (x direction) is:

$$\frac{du_p}{dt} = F_D(u - u_p) + \frac{g_x(\rho_p - \rho)}{\rho_p} + F_x, \tag{2.32}$$

where $F_D(u - u_p)$ – the drag force per unit mass of the particle.

$$F_D = \frac{18\mu}{\rho_p d_p^2} \cdot \frac{C_D Re}{24}, \tag{2.33}$$

where F_D – the drag force;

   u – the fluid velocity;

   u_p – the particle velocity;

   ρ – the fluid density;

   ρ_p – the particle density;

   d_p – the particle diameter;

   C_D – the drag coefficient;

   Re – the relative Reynolds number (particle Reynolds number).

Which is defined as:

$$\text{Re} = \frac{\rho d_p |u_p - \mu|}{\mu}. \tag{2.34}$$

The drag force coefficient C_D is expressed as:

$$C_D = a_1 + \frac{a_2}{\text{Re}} + \frac{a_3}{\text{Re}^2}. \tag{2.35}$$

For spherical particles, within a certain Reynolds number range a_1, a_2, and a_3 in the above equation are constants.

Regarding the heating behavior of the particles, ignoring the heat conduction process within the particles, the temperature change rate of the particles is given by the following equation:

$$\frac{T_p}{dt} = \frac{6h}{C_{pp}\rho_\rho d_p}(T - T_p), \tag{2.36}$$

where T_p – the particle temperature;

T – the gas temperature;

C_{pp} – the specific heat capacity of the particles;

h – the heat transfer coefficient.

The relationship between h, the heat transfer rate of the gas, and the Nusselt number is given by the following equation:

$$h = \frac{\lambda_g \text{Nu}}{d_p}, \tag{2.37}$$

where λ_g – the gas thermal conductivity;

Nu – the Nusselt number.

Defined as:

$$Nu = 2 + 0.6Pr^{1/3}Re^{1/2}, \tag{2.38}$$

where Pr – Prandtl number.

Defined as:

$$Pr = \frac{\mu_g C_{pg}}{\lambda_g}, \tag{2.39}$$

where C_{pg} – the specific heat capacity of the gas.

2.1.2 Gas dynamics theory in the nozzle

The gas in the nozzle during the cold spraying process is very complicated. In order to simplify the problem, the friction between the nozzle wall and the gas is usually not considered. The gas is considered as a complete gas with a constant specific heat. The flow in the nozzle can be regarded as a one-dimensional steady state flow.

According to the basic equation of one-dimensional steady flow, combined with the continuity equation (2.1), the relationship between the nozzle cross section and the gas parameters can be derived:

$$Pr = \frac{\mu_g C_{pg}}{\lambda_g}. \tag{2.40}$$

The variable-section tube flow is an isentropic adiabatic flow, and the Bernoulli equation can be derived:

$$d\frac{c^2}{2} + \frac{d\rho}{\rho} = 0; \tag{2.41}$$

$$Ma^2 = \left(\frac{c}{a}\right)^2 = \frac{\rho c^2}{\gamma p}, \tag{2.42}$$

$$p = \frac{\rho c^2}{\gamma Ma^2}. \tag{2.43}$$

Combining equations (2.41), (2.42), and (2.43):

$$\frac{dT}{T} + \frac{cdc}{c_p T} = 0. \tag{2.44}$$

Substituting $Ma = \frac{c^2}{\gamma RT}$; $c_p = \frac{\gamma}{\gamma-1} R$ into equation (2.42), and then taking the logarithm of the state equation $P = \rho RT$ and then differentiating it:

$$\frac{dp}{p} - \frac{d\rho}{\rho} - \frac{dT}{T} = 0. \tag{2.45}$$

Further take the logarithm of 2.42 and differentiate it to get:

$$\frac{dMa}{Ma} - \frac{dc}{c} + \frac{dT}{T} = 0. \tag{2.46}$$

Combining the above equations, the relationship between the sum of other variables and the other variables is solved as follows:

$$\frac{dc}{c} = -\frac{1}{1-Ma^2}\frac{dA}{A}; \tag{2.47}$$

$$\frac{dp}{p} = \frac{\gamma Ma^2}{1-Ma^2}\frac{dA}{A}; \tag{2.48}$$

$$\frac{d\rho}{\rho} = \frac{Ma^2}{1-Ma^2}\frac{dA}{A}; \tag{2.49}$$

$$\frac{dT}{T} = \frac{(\gamma-1)Ma^2}{1-Ma^2}\frac{dA}{A}; \tag{2.50}$$

$$\frac{dMa}{Ma} = -\frac{1+\frac{\gamma-1}{2}Ma^2}{1-Ma^2}\frac{dA}{A}. \tag{2.51}$$

According to equations2.47-2.51, it can be seen that for one-dimensional steady adiabatic isoentropy flow, whether it is subsonic or supersonic airflow, the acceleration will be accompanied by a decrease in gas pressure, density and temperature, that is the gas undergoes an expansion process. On the contrary, the gas decelerates. It is inevitably accompanied by an increase in gas pressure, density, and temperature, the gas undergoes a compression process [130, 131]. It can also be seen that the relative changes in gas parameters are related to the Mach number. This is because during the flow process with changing pressure, the density of the gas is also constantly changing, and the Mach number is closely related to the rate of change of density to pressure. These are the basic laws that one-dimensional steady absolute isentropic flow must obey.

According to the relationship of Equations 2.47-2.51, the relationship between the influence of the nozzle cross section on the gas parameters is as follows [131, 132]:

Table 2.1 − The displacements and errors of five reference points

Parameters	$dA < 0,$ $Ma <1$	$dA < 0,$ $Ma >1$	$dA > 0,$ $Ma <1$	$dA > 0,$ $Ma >1$	$dA < 0,$ $Ma <1$
c	Increase	Decrease	Decrease	Increase	Increase
p	Decrease	Increase	Increase	Decrease	Decrease
ρ	Decrease	Increase	Increase	Decrease	Decrease
T	Decrease	Increase	Increase	Decrease	Decrease

According to Table 2.1, it can be seen that for subsonic gas flow, the gas velocity in the nozzle increases as the cross-sectional area of the nozzle decreases. Therefore, in the subsonic section, the gas velocity is inversely proportional to the cross-sectional area of the nozzle. For supersonic gas flow, the gas velocity in the nozzle increases as the cross-sectional area of the nozzle increases. Therefore, in the supersonic section, the gas velocity is proportional to the cross-sectional area of the nozzle.

In gas flow, in order to describe the state of a certain point in the flow field, parameters such as pressure, density, and temperature of the gas flow at that point are often given. These parameters are called static parameters in gas dynamics. If the gas velocity is stagnated to zero according to a certain process, the parameters at this time are called stagnation parameters or total parameters, which are the actual stagnation parameters in the flow field. For the convenience of analysis and calculation, it is often assumed that the gas velocity is isentropically stagnated to zero, and the stagnation parameters corresponding to the static parameters of each point are obtained, and this is used as the reference state. Obviously, such a stagnation state has nothing to do with the actual flow process of gas. The stagnation parameter or total parameter is represented by the subscript "T".

Important parameters about gas flow are stagnation parameters of gas flow, limit speed, and critical parameters.

Stagnation parameter: In gas dynamics, the stagnation parameter is also named the total parameter. The state where the gas flow can absolutely isentropically stagnate from a certain state to the speed of zero is named the stagnation state. The gas flow parameters in the stagnation state are named is the stagnation parameter, and the stagnation state is an imaginary reference state; the stagnation parameters mainly include: stagnation temperature: mainly reflects the total energy of the airflow; Stagnation pressure: the pressure at which the gas velocity absolutely and isentropically stagnates to zero; stagnation density [133]. Its expression can be as follows:

stagnation temperature:

$$T^* = T + \frac{C^2}{2C_p},\tag{2.52}$$

stagnation pressure:

$$P^* = \left(\frac{T^*}{T}\right)^{\frac{\gamma}{\gamma-1}},\tag{2.53}$$

stagnation density:

$$\rho^* = \frac{P^*}{RT^*},\tag{2.54}$$

The Limit velocity (V_{max}): The maximum velocity that the gas can reach through the absolute energy process is called the limit velocity; its expression (2.55). When the gas velocity increases isentropically to V_{max}, it will inevitably reach the velocity of sound state, which is named the critical state. The temperature, density, and pressure at this time can be defined as: critical temperature, critical density, and critical pressure [131]; the relationship between stagnation parameters and critical parameters is expressed as follows:

limit velocity:

$$V_{max} = \sqrt{\frac{2}{\gamma-1} kRT^*},$$

(2.55)

critical temperature:

$$\frac{T_{cr}}{T^*} = \frac{2}{\gamma+1},$$

(2.56)

critical pressure:

$$\frac{P_{cr}}{P^*} = \left(\frac{2}{\gamma+1}\right)^{\frac{\gamma}{\gamma-1}},$$

(2.57)

critical density:

$$\frac{\rho_{cr}}{\rho^*} = \left(\frac{2}{\gamma+1}\right)^{\frac{1}{\gamma-1}},$$

(2.58)

exit velocity:

$$V_2 = \sqrt{\frac{2\gamma}{\gamma-1} RT^* \left[1 - \left(\frac{p_2}{P^*}\right)^{\frac{\gamma-1}{\gamma}}\right]},$$

(2.59)

exit temperature:

$$T_2 = T^* \left(\frac{p_2}{P^*}\right)^{\frac{\gamma-1}{\gamma}},$$

(2.60)

specific heat capacity at constant pressure:

$$c_p = \frac{\gamma R}{\gamma-1},$$

(2.61)

where p_2 – outlet pressure.

The above is the calculation formula for some gas thermal parameters in the Laval nozzle.

2.1.3 Flow state of classic Laval nozzle

The classic Laval nozzle can accelerate subsonic gas flow to supersonic gas flow through the convergence-divergence nozzle. It can be seen from this that the expansion section of the Laval nozzle in the cold spray nozzle is a supersonic gas flow. According to aerodynamics, shock waves may appear in the nozzle; therefore, the gas flow in the nozzle is a non-isentropic flow through the shock wave; but in the flow region before and after the shock wave can be treated according to adiabatic isentropic flow [134]. The isentropic area ratio equation in the Laval nozzle can be expressed as:

$$\frac{A_e}{A_t} = \frac{1}{Ma}\left[\frac{2}{\gamma+1} + \frac{\gamma-1}{\gamma+1}Ma^2\right]^{\frac{\gamma+1}{2(\gamma-1)}}, \qquad (2.62)$$

where A_e – nozzle throat area;

A_t – represents any cross-sectional area in the nozzle.

It can be seen from equation (2.62) that if want to achieve supersonic gas flow in the nozzle, both the nozzle section ratio and the pressure ratio need to achieve certain conditions. The gas flow in the nozzle can be divided into three states: critical state, subcritical state, and supercritical state.

Critical state. When the gas pressure ratio inside the nozzle is within a suitable value range, the velocity of the gas inside the nozzle increases in the contraction section, the velocity of the gas decreases in the expansion section and the Mach number at the nozzle outlet is less than 1, and in the nozzle the Mach number at the throat of the tube is 1; this state is named the critical state of the gas in the nozzle.

Subcritical state. The gas inside the nozzle is subsonic flow. This state is named the subcritical state of the gas in the nozzle. The characteristic of the subcritical state is that the Mach number is less than 1.

Supercritical state. This situation can be divided into several situations:

a) the gas velocity continues to increase in the nozzle expansion section, the gas flow fully expands at the nozzle outlet, the exit Mach number is greater than 1, and no shock wave is generated in the entire nozzle expansion section;

b) the gas velocity continues to increase in the expansion section of the nozzle, the exit Mach number is greater than 1, the gas flow does not fully expand at the nozzle outlet, and there is an expansion wave at the nozzle outlet;

c) the gas velocity continues to increase in the expansion section of the nozzle, the exit Mach number is greater than 1, and there is an oblique shock wave at the nozzle exit;

d) shock waves are generated in the expansion section of the nozzle.

The flow characteristics of the Laval nozzle is summarized in Table 2.2 [133]:

Table 2.2 − Flow characteristics of Laval nozzle

Characteristic Parameters	Nozzle
	$p_1/p^*, p_2/p^*, p_3/p^*$
Gas flow state inside the nozzle	$p_b/p^* < p_1/p^*$, Expansion wave at the exit
	$p_1/p^* < p_b/p^* < p_2/p^*$, Shock wave outside the nozzle exit
	$p_2/p^* < p_b/p^* < p_3/p^*$, Shock wave in the nozzle
	$p_b/p^* = p_3/p^*$, Critical state
	$p_3/p^* < p_b/p^*$, subcritical state

where p_b/p^* – gas pressure ratio in the nozzle;

p_1/p^* –   pressure ratio in the expansion section of the nozzle;

p_2/p^* – pressure ratio in the convergence section of the nozzle;

p_3/p^* – pressure ratio at the nozzle outlet.

Combining equations (2.52) to (2.58) and Table 2.2, it can be seen that the change process of the velocity, pressure, density, and temperature of the fluid in the nozzle is related to the cross-sectional area in the nozzle. Cold spray Laval nozzles are usually composed of convergent section, throat, and expansion section; the shape is like a thin-waisted cylindrical drum, with large ends and a small middle. The convergence section gradually decreases, and the expansion section gradually increases, with the middle throat as the boundary. When the fluid in the nozzle enters the nozzle throat through the convergence section of the nozzle: when the Mach number is less than 1, the cross-sectional area decreases, the pressure decreases, the density decreases, the temperature decreases, the velocity of the gas increases, and the Mach number gradually increases. When the gas reaches the throat, $M = 1$; after the gas enters the expansion section, the cross-sectional area increases, the pressure decreases, the density decreases, the temperature decreases, the gas velocity further increases, and the Mach number of the gas at the nozzle exit greater than 1. The changes of the pressure, density, temperature, and the gas velocity in the nozzle to the cross-sectional area are shown in Table 2.3.

Table 2.3 − Changes in gas parameters in the nozzle

Parameters	Convergence section	Expansion section
Pressure	Decrease	Decrease
Density	Decrease	Decrease
Temperature	Decrease	Decrease
Speed	Increase	Increase

2.1.4 Design theory of classic cold spray nozzle

The flow of gas in the cold spray nozzle is a compressible flow. However, in the actual process, compressible flow is a complex and comprehensive phenomenon, and the gas flow inside the nozzle is non-isentropic; in order to further purposefully study the Laval nozzle, it is necessary to simplify the model, usually the nozzle is the flow in the tube is regarded as a one-dimensional steady isentropic flow. For

specific expressions, refer to Chapter 2.1.3 The flow state of the classic Laval nozzle.

The design process of the Laval nozzle mainly includes: the gas dynamics theory of the nozzle, the gas thermodynamics theory, and the parameter calculation theory of the Laval nozzle. For the gas dynamics theory and gas thermodynamics theory of the nozzle, refer to Chapter 2.1.2 and Chapter 2.1.3; some other theories will be supplemented.

The gas flow in the nozzle undergoes an expansion process accelerated by pressure reduction. The relative change trend of the nozzle cross-sectional area is not only related to the relative change trend of the velocity, but also related to the Mach number. The cross-sectional area of the subsonic section of the supersonic nozzle should gradually decrease, and the cross-sectional area of the supersonic section should gradually increase, while the cross-sectional area at the critical section remains unchanged. It can be seen that in order to obtain supersonic gas flow using a nozzle, in addition to ensuring that there is a pressure difference sufficient to generate supersonic gas flow from the inlet to the outlet of the nozzle, there must also be a nozzle cross-section change suitable for the continuous depressurization and expansion acceleration of the gas flow. That is, the nozzle must first gradually shrink, causing the subsonic flow to gradually accelerate to reach the velocity of sound at the throat, and then the nozzle will gradually expand, allowing the gas flow to continue to accelerate into a supersonic flow. For this purpose, a scaling nozzle composed of a tapering nozzle and a diverging nozzle should be used. This is the Laval nozzle. Thereby further realizing the supersonic flow of gas.

According to equation (2.51):

$$\text{Ma} = \sqrt{\frac{2}{\gamma-1}\left(\left(\frac{T^*}{p_2}\right)^{\frac{\gamma-1}{\gamma}} - 1\right)}. \qquad (2.63)$$

The size of the throat determines the mass flow of the gas. If the mass flow of the gas is too large, more high-pressure gas will be consumed, which makes it

difficult to maintain a stable and uniform air flow during the spraying process. If the mass flow of the gas is too small, the quality will be reduced to a certain extent spraying efficiency. The throat mass flow is expressed as follows:

$$q_{mcr} = A_{cr} \left(\frac{2}{\gamma+1}\right)^{\frac{\gamma+1}{2(\gamma-1)}} (\gamma P^* \rho^*)^{\frac{1}{2}};$$
(2.64)

$$\rho^* = \frac{P^*}{RT^*}.$$
(2.65)

Nozzle inlet area:

$$A_i = \frac{q_{mcr}}{\rho_1 v_1}.$$
(2.66)

The calculation of the convergence section and expansion section of the nozzle is based on recommended experience. The inlet convergence angle α of the convergence section has a selection range of 30°-60°; the outlet diffusion angle β of the expansion section has a selection range of 10°-12°. The length of the convergence section and the length of the expansion section are expressed as follows:

$$L_1 = \left(\frac{d_i - d_t}{2}\right) ctg\left(\frac{\alpha}{2}\right);$$
(2.67)

$$L_3 = \left(\frac{d_e - d_t}{2}\right) ctg\left(\frac{\beta}{2}\right),$$
(2.68)

where ρ_1 – nozzle gas inlet density;

v_1 – nozzle gas inlet velocity;

γ – gas adiabatic index;

L_1 – Length of nozzle convergence section;

L_3 – Length of nozzle expansion section.

2.2 Theoretical basis of particle deposition

In the cold spray process, particles are accelerated by supersonic carrier gas to an ultra-high velocity of 300-1200m/s, and combine with the matrix at a temperature well below the melting point of the material, thereby forming a cold spray coating [135, 136]. During this process, the narrow area where the particles and the matrix are in contact with each other undergoes strong plastic deformation. The strong strain breaks the oxide film on the contact surface between the particles and the matrix. The jet-like metal sputtering formed around the contact area extrudes the broken oxide film. The contact surface makes direct contact between the particles and the matrix material, and finally the particles and the matrix are combined under high pressure conditions. Although this hypothesis can reasonably explain certain phenomena during the deposition between cold spray particles and the substrate, the essential mechanism of cold spray coating formation is still not completely understood.

Studying the deposition deformation behavior of cold spray particles and the substrate is an important means to explore the deposition and coating formation mechanisms of cold spray particles. However, due to the instantaneous characteristics of high-velocity deposition of particles, it is difficult to conduct direct experimental observations of the deformation process of particles, and finite element numerical the analysis rules provide an effective way to study the deformation behavior of particles and matrix. By simulating the entire deposition process, it can intuitively observe the entire process of deposition and deformation of particles and matrix. The resulting deformation of particles and matrix the appearance is also in good agreement with the experimental observation results. Therefore, the numerical simulation method is becoming the main means to study the deposition deformation behavior of cold spray particles and the matrix. Currently, commonly used calculation software includes Abaqus-Explicit and LS-DYNA, and the numerical calculation methods used mainly include: The SPH, the ALE, and CEL methods [137,

138].

Conservation equation of deposition process: the conservation equations that should be followed during the deposition between particles and substrates in simulated cold spraying are: mass conservation equation, momentum conservation equation and energy conservation equation [74].

$$\rho = J\rho_0; \tag{2.69}$$

$$\sigma_{ij} + \rho f_i = \rho \ddot{x}_i; \tag{2.70}$$

$$\dot{E} = VS_{ij}\dot{\delta}_{lj} - (p + q)\dot{V}, \tag{2.71}$$

where ρ – current mass density;

J – relative volume coefficient;

ρ_0 – initial mass density;

σ_{ij} – Cauchy stress;

f_i – volume force per unit mass;

$\ddot{x}_i$ – acceleration;

$\dot{E}$ – energy change rate;

V – current configuration volume;

δ_{ij} – deviatoric stress tensor;

$\dot{\delta}_{lj}$ – strain Rate tensor;

p – pressure;

q – volume viscous resistance;

$\dot{V}$ – volume change rate.

Among them, the expressions of the deviatoric stress tensor and stress are as follows:

$$S_{ij} = \sigma_{ij} + (p + q)\sigma_{ij}; \tag{2.72}$$

$$p = -\frac{1}{3}\sigma_{kk} - q. \tag{2.73}$$

Material constitutive model: there are more than 160 metallic and non-metallic material models to choose from in the currently known LS-DYNA program. The cold spray deposition process has the characteristics of short deposition time, large strain rate, and increased temperature caused by plastic deformation. The current material models for applying the cold spray particle deposition process mainly include the C-S model, the J-C model, the JHC model, and the bilinear isotropic hardening material model [139].

The C-S model is a hybrid model of isotropic and kinematic hardening. The material parameters involved in cold spraying are small, considering material failure, and are relatively easy to obtain. Choose isotropic or kinematic hardening by adjusting the hardening parameters between 0 and 1 dynamic hardening. The C-S model only considers the effect of strain rate on yield strength and does not consider the effect of temperature on the deposition process. Therefore, the C-S model is incomplete when used directly to characterize the deposition process of cold spray particles, because in the deposition process of cold spray particles, temperature is an important parameter that affects deposition. The strain rate is considered using the C-S model, and the yield force is represented by factors related to the strain rate, expressed as follows:

$$\sigma_y = \left[1 + \left(\frac{\dot{\varepsilon}}{C}\right)^{\frac{1}{p}}\right]\left(\sigma_0 + \beta E_P \varepsilon_p^{eff}\right); \tag{2.74}$$

$$E_P = \frac{E_{tan} E}{E - E_{tan}}, \tag{2.75}$$

where $\dot{\varepsilon}$ – strain rate;

   C and P – strain rate parameters;

   σ_0 – initial yield stress;

ε_p^{eff} – effective plastic strain;

E_P – plastic hardening modulus;

E – elastic modulus;

E_{tan} – tangential modulus.

The J-C model takes into account the temperature of the particles and the substrate during the cold spray particle deposition process, and also adds the effects of work hardening and strain rate to the model at the same time; the characteristics of the J-C model are simple form and easy to use. The J-C model involves many materials constitutive parameters, and some parameters must be obtained through a large number of experiments, so this also limits the applicable scope of the J-C model.

The J-C model is suitable for large strain rate changes and material softening problems caused by adiabatic heating. Aiming at the high speed and high strain characteristics of Al particles depositing with steel substrates [140, 141]. The flow stress and equation of state are expressed as follows:

Flow stress of the J-C model:

$$\sigma_y = \left(A + B\overline{\varepsilon p}^n\right)(1 + C \ln \varepsilon^*)(1 - T^{*m}). \tag{2.76}$$

Among them, the parameters A, B, C, n, and m are determined by the material properties.

where ε^p – effective plastic strain;

$\varepsilon^* = \frac{\dot{\varepsilon}_p}{\dot{\varepsilon}_0}$, the effective plastic strain rate when $\dot{\varepsilon}_0 = 1s^{-1}$.

The state equation used in the J-C model is the Mie-Cruneisen state equation:

$$P = C_0 + C_1\mu + C_2\mu + C_3\mu^2 + (C_4 + C_5\mu + C_6\mu^2)E. \tag{2.77}$$

The J-C model assumes that the material is an isotropic material, that is an isotropic hardening material model, which includes strain, strain rate hardening, and

temperature softening effects. Therefore, it is often used to calculate the dynamic flow stress of materials under high strains. No other cyclic effects or possible anisotropy are considered in the model.

During the cold spray deposition process, much of the plastic deformation energy is converted into heat, causing an increase in material temperature [141]. Experiments show that for most metals, the percentage of plastic energy converted into heat is about 90%, and about 10% of the plastic energy is consumed by others. Assume that the inelastic heat fraction is 0.9, which is stated in Chapter 4 of the dissertation. The thermal response of a material depends on its specific heat capacity, heat conduction and thermal expansion. The elastoplastic and thermal properties of the material are input into Abaqus-Explicit to calculate the heat.

The J-C model has powerful advantages in solving nonlinear problems. Therefore, compared with the ideal elastic-plastic model, it can better calculate the deposition process in cold spraying.

The JHC model can effectively characterize the plastic deformation failure of brittle materials (such as glass and ceramics, as shown in Table 2.4), including parameters such as pressure-related strength, strain rate, failure expansion and thermal expansion effects. Its failure criterion and state equation are expressed as follows [140]:

- undamaged ceramic strength:

$$\sigma_i = A(P + T)^N (1 + C \ln \varepsilon); \qquad (2.78)$$

- fractured Ceramic Strength:

$$\sigma_f = B(P)^M (1 + C \ln \varepsilon); \qquad (2.79)$$

- current stress:

$$\sigma = \sigma_i - D(\sigma_i - \sigma_f). \tag{2.80}$$

State equation of the JHC model:

$$P = k_1 u + k_2^2 u + k_3^3, \tag{2.81}$$

where σ_i – Unbroken ceramic strength;

σ_f – Broken ceramic strength;

σ – Current strength;

P – Static pressure;

E – Elastic fracture strain.

Table 2.4 − JHC constitutive model parameters of Al_2O_3 materials [140]

Parameters	Al_2O_3
Shear Modulus, E (N/m2)	0.90e12
Density, ρ (kg/m3)	3680
A	0.93
B	0.31
C	0.0
m	0.6
n	0.6
Reference strain rate,0 (1/s)	1.0
Tensile Strength (Pa)	0.2
HEL (Pa)	2.79e9
HEL Pressure (Pa)	1.46e9
HEL Vol. Strain	0.01117
HEL Strength (Pa)	2.0e9
D1	0.005
D2	1.0
K1(GPa) (Bulk Modulus)	130.95
K2 (GPa)	0
K3 (GPa)	0
Beta	1.0
FS	0.5

The bilinear isotropic hardening material model used to simulate the material

parameters in the cold spray deposition process is relatively small and easy to obtain. The bilinear isotropic hardening material model is also commonly used in the cold spray deposition process. Its disadvantage is that it does not consider the influence of the material's strain rate.

2.2.1 The SPH method

The SPH (Smoothed Particle Hydrodynamics) is the abbreviation of smoothed particle hydrodynamics method. It is a meshless method that has been gradually developed in the past 20 years. The basic idea of this method is to describe a continuous fluid (or solid) by a group of interacting particle points. Each material point carries various physical quantities, including mass, and velocity, by solving the dynamic equation of the particle group and tracking each the motion trajectory of the particle is determined to obtain the mechanical behavior of the entire system [142]. The SPH method as a Lagrangian particle method, can effectively simulate complex problems such as large material deformation, moving material interfaces, and phase changes [143-149]. Therefore, the SPH method is widely used in the field of deposition manufacturing.

The SPH method is based on the interpolation theory. In the SPH method, macroscopic variables can be conveniently expressed as integral interpolation calculations by expressing values on a set of disordered points, and the interaction of particle points is described by the interpolation function [136]. The interpolation function is used to give the core estimate of the quantity field at a point, and the conservation law of continuum dynamics is converted from the differential equation form to the integral form, and then converted to summation [150]. In the SPH method, the mass point approximation function can be defined as [151, 152]:

$$f(r) = \int_{\Omega} W(x - x', h)dx'; \qquad (2.82)$$

where Ω – the volume of the integration that contains x and x′;

h – the smoothing length defining the influence domain of the "kernel estimate";

$W(x - x', h)$ – the kernel.

Smoothing function, which must satisfy the following three properties:

The first one is the normalization condition,

$$\int_\Omega^{\square} W(x - x', h)dx' = 1. \tag{2.83}$$

The second condition is that when the smoothing length approaches zero, the Dicra function can be obtained:

$$\lim_{h \to \infty} W(x - x', h) = \delta(x - x'). \tag{2.84}$$

The third condition is the compact condition:

$$W(x - x', h) = 0 \quad \text{when} \quad |x - x'| > kh. \tag{2.85}$$

There are many possible choices for kernel functions that satisfy equations 2.84, 2.85, and 2.86. However, the most popular one is the cubic spline interpolation function. R is defined as the relative distance between point x and point x′, R $=|x - x'|/h$, then the cubic spline function has the form:

$$W(R, h) = \frac{1}{h} * \begin{cases} \frac{3}{2} - R^2 + \frac{1}{2}R^3 & 0 \le R < 1 \\ (2 - R)^3 & 1 \le R < 2 \\ 0 & R \ge 2 \end{cases} \tag{2.86}$$

The SPH method is used to simulate the deposition process between particles

and matrix. The deposition process can be regarded as an adiabatic process. The J-C model is usually used, which is characterized by considering the effects of work hardening and thermal softening in the material [153].

The equivalent plastic stress of materials can generally be expressed as [153] using the J-C model:

$$\sigma_Y = \left[A + B\varepsilon_p^n\right]\left[1 + C\ln\dot{\varepsilon}^*\right]\left[1 - (T^*)^m\right];\tag{2.87}$$

$$T = \begin{cases} 0 & T < T_0 \\ \dfrac{T-T_0}{T_m-T_0} & T_0 \le T \le T_m \\ 1 & T_m < 2 \end{cases}.\tag{2.88}$$

Among them, A, B, n, C, and m are all material-related parameters.

where ε_p – effective plastic strain;

T^* – dimensional parameters;

T_m – material melting point;

T_0 – ambient temperature.

The ratio of $\dot{\varepsilon}^*$ strain rate ε to reference strain rate ε_0.

In the simulation calculation process, it is also necessary to add the linear EOS GRUNEISEN equation of state of the J-C model. The equation for compressible materials is [154, 155]:

$$\rho = \frac{\rho C^2 \mu\left[1 + \left(1 + \frac{\gamma_0}{2}\right)\mu - 0.5*a*\mu^2\right]}{\left(1 - (S_1 - 1)\mu - S_2\frac{\mu^2}{\mu+1} - S_3\frac{\mu^3}{(\mu+1)^3}\right)^2} + (\gamma_0 + a*\mu)E,\tag{2.89}$$

where E – Internal energy per unit initial volume;

C – Intercept of $V_s - V_p$ curve;

S_1, S_2, S_3, $V_s - V_p$ – Curve slope;

γ_0 – Gruneisen;

101

a - First volume correction $\mu = \frac{\rho}{\rho_0} - 1$ of γ_0.

2.2.2 The ALE Method

The ALE method is one of the early commonly used methods to study the deformation behavior of single particles, and the Lagrangian method has been widely used to simulate high-speed impact problems. This method establishes a model in which the mesh changes as the material changes. The finer the mesh, the more accurate the calculation results will be. When solving particle deformation problems, the Lagrangian method helps track the interface between the particle and the substrate during the calculation process, can simulate the changes in temperature and residual stress at the interface between the particle and the substrate, and has high calculation speed and accuracy. The disadvantage is that when the particle speed is too high, the high-speed impact of the particles will cause serious deformation of the grid, eventually forcing the calculation to terminate [156], and because the elastic energy stored in the substrate is greater than the elastic energy stored in the particles, the particles are prone to rebound.

In order to solve the problem of grid distortion, it can be controlled from three aspects: first, reducing the grid size, which needs to be adjusted for different materials. The disadvantage is that it will lead to inaccurate calculation results. Second, in the Abaqus grid module, to control the distortion of the matrix and particles to a reasonable value. Third, use the ALE adaptive mesh for the simulated part, the ALE method for the simulated part. The purpose of adaptation can be achieved by re-gridding the grid distortion area, but this will lead to an unrealistic jet state at the edge of the base, so some scholars do not recommend the use of this method.

The ALE method there are two classic motion description methods in continuum mechanics, and these two methods are also used when describing the finite element motion interface. The basic idea is that the calculation grid is no longer

102

fixed, nor attached to the fluid particles, but can move arbitrarily relative to the coordinate system. Since this description contains both the Lagrange point of view and the Euler point of view, it overcomes the unsatisfactory disadvantages of grid distortion common in pure Lagrange methods. The Lagrangian method is essentially designed to handle motion with a constant velocity. the Euler method essentially handles steady-state problems without time. The ALE method can not only handle the above two types of problems, but also handle large deformation problems.

The ALE method will be compared by simulating the deposition of particles and substrates [155]. Figure 2.1 shows a comparison of the jets after single particle deposition under the two methods. In the results of the Lagrangian method simulation, due to the distortion of the grid, the jet at the interface between the particles and the substrate is flat and has a tendency to expand outward. The jet shape obtained by the ALE method is more regular, which is inconsistent with the reality.

a   *b*
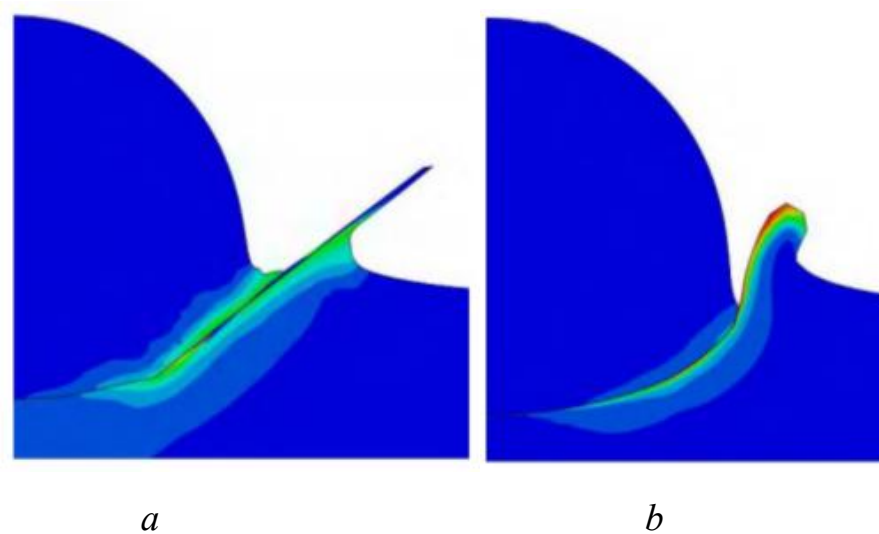
a − the Lagrangian method; *b* − the ALE method

Fig. 2.1. Jet diagram after single particle deposition simulated by different method [155]

2.2.3 The CEL Method

The full name of the CEL method is the Coupled Euler-Lagrangian method,

which essentially adds a Euler domain to the ALE method, and particles flow in the Euler domain, as shown in Figure 2.2.
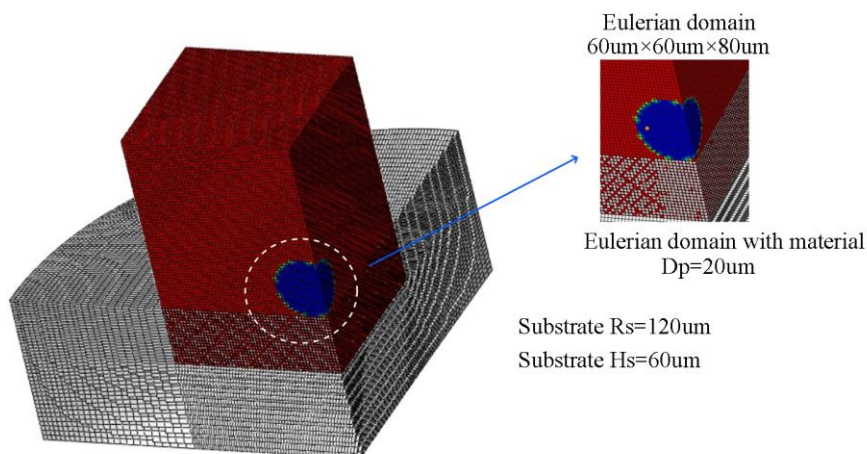

Fig. 2.2. The 3D CEL deposition model

Lagrangian is a function used to describe continuously moving objects at specified material coordinates and time [157-160]. Often used in particle motion in solid mechanics, Lagrangian nodes move with the material in the simulation, so the interface between the two parts can be well tracked and defined. Euler is the function of displacement and time of the motion of a continuum; it is often used in fluid mechanics. In Euler analysis, when simulating the deposition of cold spray particles, the Euler grid is always fixed. The essence is that the particles is in Euler the particles flow within the grid, so the particles is also equivalent to the Lahrangian unit at each time step. While the particles are deformed at each time step, its various physical quantities should also be mapped to the Euler grid. The advantage of Euler's quation is that elemental distortion does not occur; the disadvantage is that it can simulate the spraying simulation of multiple particles, but it can only be used for pure particles and cannot simulate the particles deposition process of different materials. Or two or more materials will undergo numerical diffusion. The CEL method can well solve the grid contact distortion problem that occurs in the ALE method. The CEL model can solve single-particle and multi-particle deposition processes. The CEL model does not need to define contact types. Different materials flow between grids. In addition to particles and matrix, the surrounding area must also be meshed

to provide particles. and the space required for movement and deformation of the base material.

Xie [157] used the CEL method to simulate the deposition of Al particles on an Al substrate to study equivalent plastic strain and temperature changes, as shown in Figure 2.3. Research shows that the CEL method can eliminate the problems of excessive mesh deformation and large deformation. After the particles are deposited, although there is jet flow in the deformed particles at the bottom layer, it will not have any impact on the calculation. It shows that in the Euler model, any node-based displacement can be ignored, indicating that the Euler part is rigid. By calculating the equivalent plastic strain as a weighted average, the average is definitely much lower than the Lagrangian analysis. The equivalent plastic strain; at the same time, this explanation also applies to the temperature distribution of the particles.
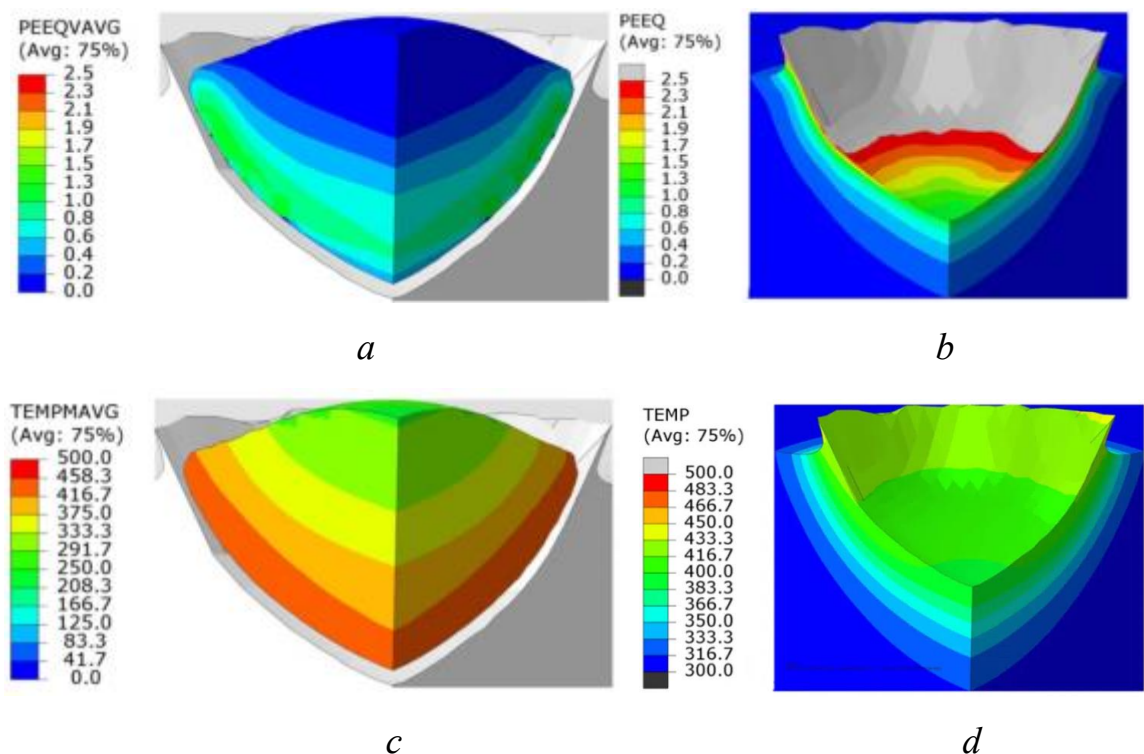
a – Powder PEEQVAVG; *b* − Substrate PEEQ; *c* – Powder TEMPMAVG; *d* − Substrate TEMP

Fig. 2.3. Analysis of equivalent plastic strain and temperature after impact of Al powder on Al substrate using the CEL method [157].

It shows that the CEL method is used to simulate the deposition process in cold spray technology, and can be used to solve the problems of large strain and high strain rate that occur in certain materials during deposition, and the grid will not be affected by super large deformation.

The CEL model can solve single-particle and multi-particle deposition processes. Many scholars have used the CEL method to simulate the deposition of single particles and observe temperature changes and equivalent plastic strain. Few scholars have used CEL method to study the deposition of multi-particles. This is because the multi-particle deposition model are completely different models. And based on what was mentioned in Chapter 1.6.3.3, it can be known that the unique advantage of the multi-particle deposition model can better observe the porosity of the coating after deposition. In this process, the failure model in the J-C model also needs to be added, and the linear EOS_GRUNEISEN state equation model must also be added.

The failure model in the J-C model is represented as follows:

$$\varepsilon_f = \left[d_1 + d_2 exp\left(d_3 \frac{p}{q}\right)\right]\left[1 + d_4 \ln\left(\frac{\dot{\varepsilon}_p}{\dot{\varepsilon}_0}\right)\right](1 + d_5 T^*), \qquad (2.91)$$

where ε_f – fracture strain;

$d_1 - d_5$ – material fracture constants;

p – static pressure;

q – mises yield stress.

The linear EOS_GRUNEISEN state equation model is characterized as follows:

$$U_s = C_0 + sU_p. \qquad (2.92)$$

The C_0 and s define the linear relationship between the linear shock velocity U_s and the particle velocity U_p.

2.3 Conclusion for the Chapter 2

This chapter mainly lists the theoretical basic knowledge required for the cold spraying process and design theory on conventional cold spray nozzles. The overall cold spray process can be divided into two stages. One is the acceleration stage of particles in the Laval nozzle; the next is the deposition process after the particle deposition with the substrate. The acceleration of particles in the Laval nozzle is the knowledge of two-phase flow of gas and solid. Therefore, the basic theories about flow fields mainly include: gas governing equations, turbulence models, and discrete term models. In the flow state of the classic Laval nozzle, it is necessary to clearly explain the changes in the velocity, temperature, and pressure of the gas in the nozzle, analyze and summarize the relationship between the three parameters. The design theory of the classic cold spray nozzle can be used to complete the design of the traditional Laval nozzle in Chapter 3, as well as the research on the right-angle cold spray nozzle and the multi-channel nozzle as a reference. The theoretical basis of particle deposition and the model methods required to simulate the particle deposition process, such as the ALE, the SPH, and the CEL methods. By elaborating the principles and characteristics of the three methods, it provides reference and basis for the analysis and research in Chapter 4.

CHAPTER 3

BASED ON THE ANALYSIS AND OPTIMIZATION OF EXISTING COLD SPRAY NOZZLES AND RESEARCH OF RIGHT-ANGLE NOZZLES

The main purpose of cold spray technology is to obtain high-speed spray particles. Its core device is the supersonic nozzle. This chapter conducts structured simulation on the structural parameters of the existing cold spray nozzle to find the optimal nozzle structural parameters and spraying technical parameters, and finally obtain the speed required for target particle deposition.

The current research points on the cold spray nozzle optimization method are mainly divided into the optimization of technical parameters and structural parameters; technical parameters mainly include: temperature and pressure of the carrier gas; temperature, velocity, particle size and shape; substrate temperature; spraying distance and angle. The structural parameters mainly include: the size of the nozzle throat, the length of the expansion section, and the structural type of the nozzle. Optimization methods can be mainly divided into single- and multi-factor optimization methods.

3.1 Single factor analysis of existing cold spray nozzles and optimization methods

3.1.1 Single factor optimization of existing cold spray nozzle

First analyze the Laval nozzle that has been developed. Figure 3.1 shows the cold spray Dymet Laval nozzle [161]. The characteristic of the Dymet Laval nozzle is that the accelerating gas inlet and the particle inlet are perpendicular to each other, and the particle inlet is located at the throat of the Dymet Laval nozzle.

Fig. 3.1. Dymet nozzle design parameters

The length of the expansion section of the Dymet Laval nozzle is an important factor affecting the acceleration of particles in the Dymet Laval nozzle. If the expansion section is too short, the particles cannot be fully accelerated in the Dimet Laval nozzle. If the expansion section is too long, the particles may be accelerated. Deceleration has already begun in the Dymet Laval nozzle; therefore, it is crucial to study the effect of the length of the expansion section on the particle velocity at the nozzle exit. In this section, the velocity distribution of Al particles at the exit of the Dymet Laval nozzle is studied at the pressures of 0.8 MPa, 1.0 MPa, and 1.2 MPa respectively for the lengths of the Dymet Laval nozzle expansion section of 120 mm, 150 mm, 180 mm, 210 mm, and 240 mm. The accelerating gas is air, the total inlet temperature is set to 900 K, and the spraying material is spherical Al particle with a diameter of 25 um.

The velocity distribution of Al particle in the Dymet Laval nozzle is simulated by SolidWorks. Firstly, research the velocity distribution of the Al particle in the expansion section of the Dymet Laval nozzle with different lengths under the same pressure inlet; secondly, research the velocity distribution of Al particle in the nozzle at different pressure inlets of the expansion section of the Dymet Laval nozzle of the same length.

3.1.1.1 Analysis of Al particle velocity under the same pressure

Analyze the expansion section of different lengths under same pressure inlet conditions, the acceleration of the Al particle in the Dymet Laval nozzle and the velocity at the nozzle outlet; respectively simulate the pressure inlets at 0.8 MPa, 1.0 MPa, and 1.2 MPa. As shown in Figure 3.2, the pressure inlet is 0.8 MPa, and the velocity distribution of Al particle in the expansion section of different lengths. It can be seen from the Figure 3.2 that when the pressure inlet is 0.8 MPa, the Al particle has been accelerated near the expansion section of the nozzle 220 mm, so the expansion section length is 120 mm, 150 mm, and 180 mm nozzles, the Al particle is still in a state of acceleration before the nozzle exit. Expansion section length of 210 mm and 240 mm nozzles, Al particle has been accelerated before the nozzle exit, and the Al particle decelerates in the nozzle. With five expansion section nozzles of different lengths, the Al particles have reached the critical velocity, it can be deposited on the substrate.
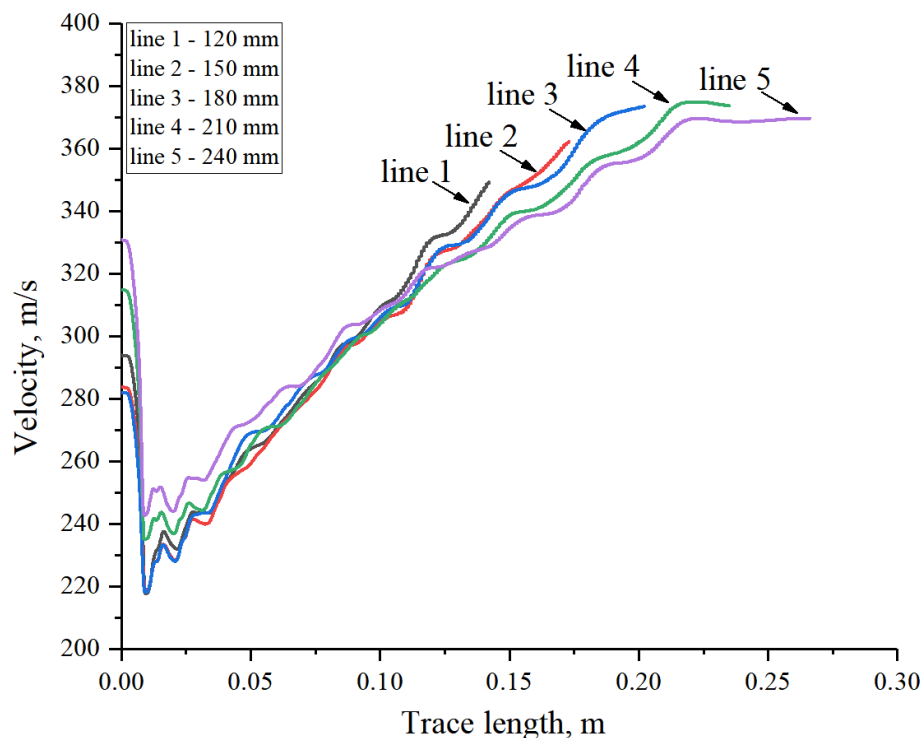

Fig. 3.2. The velocity distribution of Al particles in the expansion section of different nozzle lengths; the pressure inlet is 0.8 MPa

110

As shown in Figure 3.3, the pressure inlets are 1.0 MPa (a) and 1.2 MPa (b) respectively, and the velocity distribution of Al particle in the expansion section of different lengths.
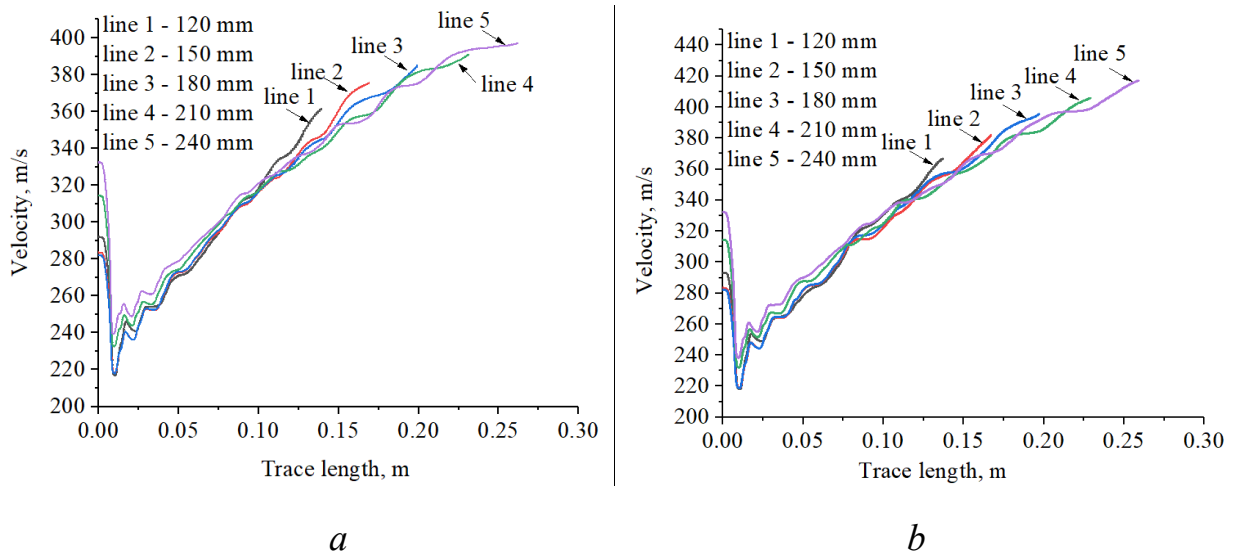
a − 1.0 MPa; *b* − 1.2 MPa,

Fig. 3.3. The velocity distribution of Al particles in the expansion section of different lengths.

Figure 3.3 (a) shows that when the pressure inlet is 1.0 MPa, for nozzles with expansion section length of 120 mm, 150 mm, 180 mm, and 210 mm, the Al particle is still accelerating in the nozzle; for nozzles with expansion section length of 240 mm, the velocity of Al particle in the nozzle slowly stabilizes. Figure 3.3 the curvature of the curve represents the acceleration of the Al particle. Combined with the curvature analysis of the five curves, it can be seen that as the length of the expansion section increases, the curvature of the curve gradually becomes smaller, indicating that the Al particles accelerate smaller and slower inside the nozzle. It can be seen from Figure 3.3(b) that when the pressure inlet is 1.2 MPa, the Al particle in the nozzles of the five different length expansion sections is still accelerating, because the pressure inlet is increased; combined with the five curves in Figure 3.3

it can be seen that as the length of the expansion section increases, the curvature of the curve gradually becomes smaller, indicating that the acceleration effect of the Al particle in the nozzle is gradually weakened.

3.1.1.2 Analysis of Al particles velocity in the same expansion section length

Under the condition of equal expansion section length, analyze the different pressures inlet, the Al particles accelerate in the Dymet Laval nozzle and the velocity at the nozzle outlet; through simulation, the expansion section length of the nozzle is 120 mm, 150 mm, 180 mm, 210 mm, and 240 mm the Al particle velocity distributions. As shown in Figure 3.4, the velocity distribution of the Al particle in the nozzles of the expansion section of different lengths when the pressure inlets are 0.8 MPa, 1.0 MPa, and 1.2 MPa; From Figure 3.4 (a), (b), and (c), it can be seen that the pressure inlets are an important factor that determines the velocity of Al particle acceleration in the nozzle. The higher the pressure inlet, the shorter the acceleration time of the Al particle; the expansion section the length of the Al particle is also an influencing factor that affects the acceleration velocity of the Al particle in the nozzle. The expansion nozzle within a certain length range, as the length of the expansion section increases, the faster the Al particle can obtain in the nozzle. It can be seen from Figure 3.4(d) and (e) that when the length of the expansion section of the nozzle reaches a certain value, the acceleration effect of Al particle is reduced; The expansion nozzle of the same length can improve the acceleration effect of the Al particle in the nozzle, and can appropriately increase the pressure inlet; When the pressure inlet is 0.8MPa, the velocity of Al particle in the nozzle increases first and then decreases; when the pressure inlet is 1.0 MPa, the acceleration effect of Al particles in the nozzle is obviously weakened.
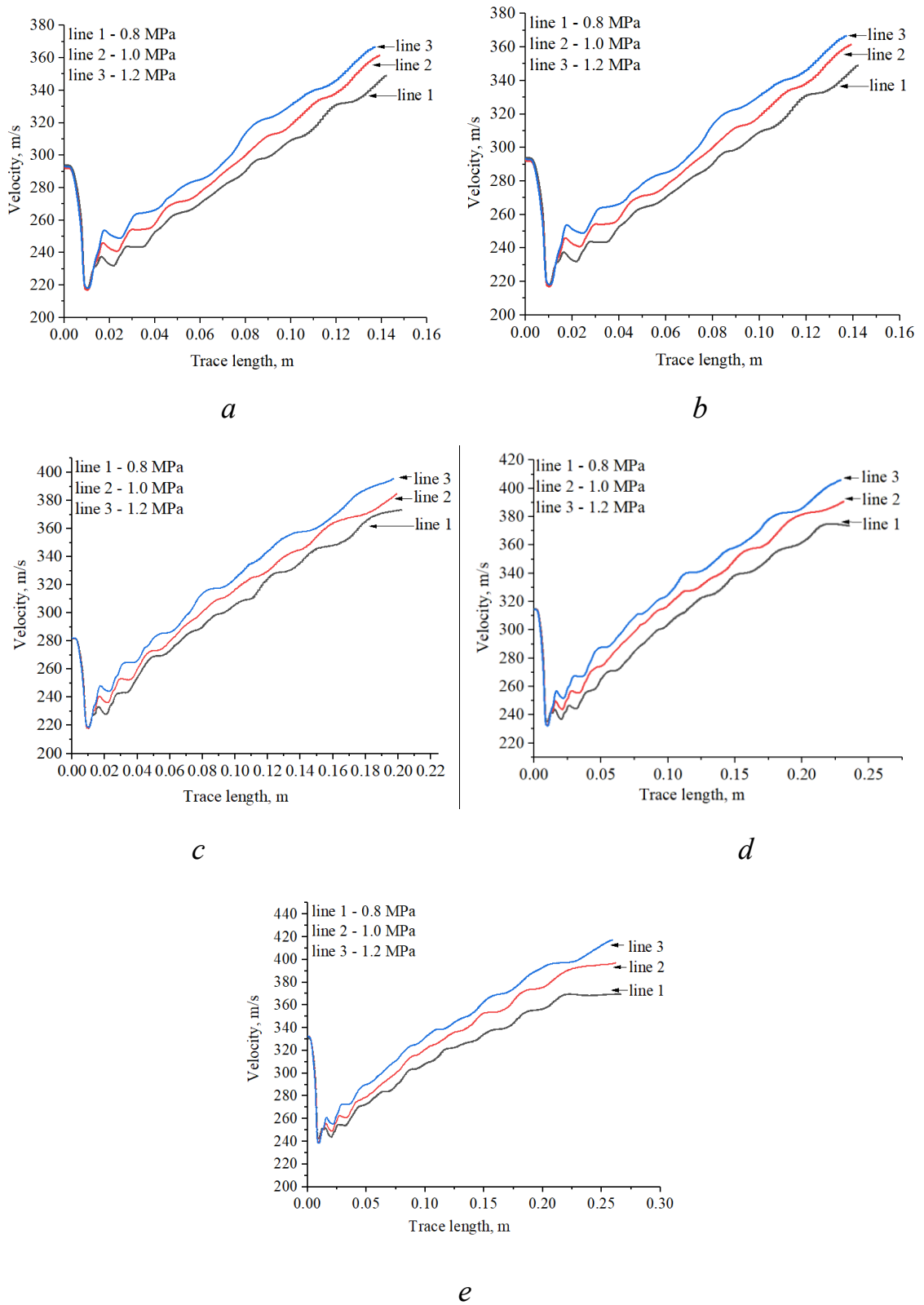
a – 120 mm; *b* – 150 mm; *c* – 180 mm; *d* – 210 mm; *e* – 240 mm

Fig. 3.4. The Al particle velocity distribution under different pressure inlets
conditions for the different expansion section of the nozzle

By comparing the slopes of all the velocity curves in Figure 3.4, as the length of the expansion section increases, the curvatures of the different pressure curves have been decreasing, indicating that the acceleration effect of Al particle is gradually weakening. Therefore, the pressure inlet is too small and the nozzle expansion section is too short, which is not conducive to the acceleration of the Al particle in the nozzle. It is very necessary to choose the proper length of the expansion nozzle in the proper pressure range; increasing the pressure inlet to increase the velocity of the Al particle, or increasing the expansion section length to obtain a larger outlet velocity, it will increase the spraying cost. Therefore, in the pressure inlet range of 1.0 MPa, the length of the expansion section of the nozzle is about 210 mm, which can ensure that the Al particle has a better acceleration effect in the nozzle, and has an ideal exit velocity at the nozzle outlet, so as to ensure smooth completion on the substrate deposition.

3.1.1.3 Summary

Based on the above analysis, it can be seen that the length of the expansion section of the Dymet Laval nozzle is one of the key factors affecting the exit velocity of Al particles; in the pressure range of 1.0 MPa, the length of the expansion section is approximately 210 mm, which can ensure better acceleration of Al particles in the nozzle, and has a good exit velocity at the nozzle outlet. The expansion section of the Dymet Laval nozzle is divided into four parts, each part is 30 mm; it is recommended that the connection between each part be rounded so that the accelerated gas will not produce excessive gas back flow at the connection, thereby ensuring the velocity of the accelerating gas remains uniform and stable throughout the entire nozzle, thereby ensuring better acceleration of the sprayed material.

3.2 The multi-factor optimization of developed cold spray nozzles

3.2.1 Optimization analysis of cold spray nozzle spraying parameters based on the RSM

In the spraying process, the factor that affects the particle velocity is not a single factor, but the result of the coupling of many factors; among them, gas temperature, particle size and gas pressure are the three most important factors that affect cold spraying, and are also the factors that many scholars currently influencing factors for joint research. Hu and Tan [162] studied the effects of nozzle length, spraying distance, and fillet radius on particle deposition velocity.

In this section, the RSM is used to analyze the acceleration of particles affected by multi-factor coupling; gas temperature (T_G), particle size (D_p), and gas pressure (P_s) are used as independent variables, and the three independent variables interact with each other in pairs. Through Design- Expert established a linear regression equation model for the velocity of Al and Cu particles at the Laval nozzle outlet (V_e) and the velocity before deposition on the substrate (V_p). The RSM method was used to predict the optimal spraying parameters and velocity of Al and Cu particles. comparing the predicted values with the simulation values, and verifying the impact of RSM on cold spraying technical parameters feasibility and accuracy of optimization. The RSM combines mathematical and statistical methods and is often used to find optimal parameters in multi-factor systems.

3.2.1.1 Nozzle parameters

The Laval nozzle is divided into a convergence section, throat section, and expansion section, as shown in Figure 3.5. The main parameters of the Laval nozzle length of convergent section L_1, length of throat L_2, length of expansion section L_3, inlet diameter D_i, throat diameter D_t, outlet diameter D_e, inlet convergence

angle α, and outlet diffusion angle β. The main design parameter of the convergence section is the entrance convergence angle, and its selection range is 30°-60°. The outlet diffusion angle of the expansion section is 10°-12° as refer to Chapter 2.1.4. In order to reduce energy loss, the radius of curvature R of the throat is equal to the radius of the throat.
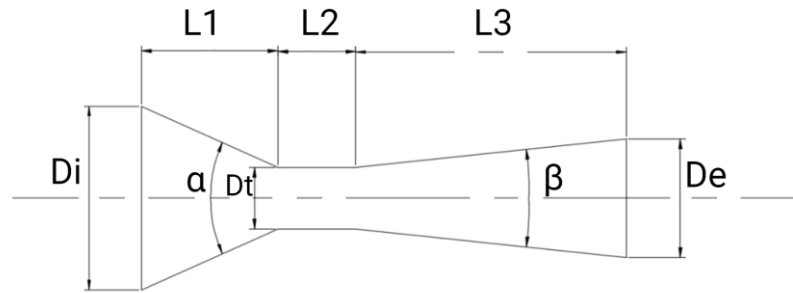

Fig. 3.5. Laval nozzle parameters

The inlet pressure P_i is 0.8 - 1.6 MPa, and the gas temperature is between 697-1074 K. According to the calculation, the contraction ratio is about 3.0 [66]. The accelerating gas is air, the adiabatic index of air γ is 1.4, and the air constant R is 287.1 J/(kg · K). The inlet velocity of particles material V_i is 25 m/s. The particle entrance is located above the throat, and the diameter of the entrance is D_p= 1 mm. Table 3.1 shows the technical parameters of the Laval nozzle.

Table 3.1 − The technical parameters of the Laval nozzle

Parameter	D_t	D_i	D_e	D_p	L_1	L_2	L_3
Value/mm	3.5	11.5	6.06	1	15	5	65

Two particles of Al and Cu are used as spraying materials. The spraying distance of Al particle is 30 mm and the spraying distance of Cu particle is 15 mm. The spray gun is perpendicular to the surface of the substrate. As can be seen from Table 3.2, the gas temperature will affect the deposition of particle deposition on the substrate [163]. H [164] only studied the effect of gas temperature on critical velocity.

Table 3.2 − The technical parameters of the Laval nozzle

Parameters	Material	
Air Temperature	Al	Cu
424°C	327-651 m/s	447-905 m/s
526°C	314-647 m/s	449-883 m/s
632°C	301-638 m/s	437-872 m/s

3.2.1.2 Experimental methods

Using the BBD method the temperature of the gas temperature (T_G), the particle size (D_p), and the gas pressure (P_s) are selected as the key test factors. The velocity of the particles at the Laval nozzle outlet and the velocity before deposition on the substrate is used as the target; and -1, 0, and +1 are used to represent the numerical simulation factor levels, as shown in Table 3.3, which are the design parameters for the spraying materials of Al and Cu particles. The density of Cu is greater than that of Al, so a higher gas pressure is required for Cu, and the particle size of Cu particle should not be too large.

Table 3.3 − Design parameters of Al and Cu particles

Level	Factors					
	T_G /°C		D_p / um		P_s / MPa	
	Al	Cu	Al	Cu	Al	Cu
-1	450	600	10	10	0.8	1.4
0	550	700	20	15	1.0	1.5
+1	650	800	30	20	1.2	1.6

3.2.1.3 The impact and analysis summary of the interaction of various influencing factors on indicators

Design-Expert DX10 data analysis software is used to process and analyze the numerical simulation results. Experimental results data for different materials of

particles are shown in Table 3.4, where X_1: the temperature of gas (T_G); X_2: the particle size (D_p); X_3: the gas pressure (P_s); Y_1: The velocity of the particles at the Laval nozzle outlet (V_e); Y_2: The velocity before deposition on the substrate (V_p).

Table 3.4 − Experimental results data for different materials of particles

No:	High- and Low-level code			The Output parameters, m/s			
				Al		Cu	
	X_1	X_2	X_3	Y_{Al1}	Y_{Al2}	Y_{Cu1}	Y_{Cu2}
1	-1	0	-1	465.43	454.72	459.42	460.81
2	+1	+1	0	418.15	404.91	479.41	480.52
3	0	0	0	503.66	495.37	478.45	478.83
4	+1	0	+1	563.84	550.99	507.97	508.57
5	+1	0	-1	563.84	550.99	494.63	495.63
6	0	+1	-1	441.82	428.34	441.07	443.02
7	0	-1	-1	612.44	550.03	545.49	543.81
8	-1	0	+1	498.51	482.75	462.80	460.61
9	0	0	0	503.66	495.37	478.45	478.83
10	-1	+1	0	455.98	465.71	425.66	428.83
11	0	0	0	503.66	495.37	478.45	478.83
12	0	0	0	503.66	495.37	478.45	478.83
13	0	-1	+1	652.01	588.16	551.84	552.43
14	0	+1	+1	442.08	428.41	446.79	446.11
15	0	0	0	503.66	495.37	478.45	478.83
16	-1	-1	0	588.30	551.84	525.53	525.25
17	+1	-1	0	622.70	583.58	568.24	568.32

The regression equation for outlet velocity Y_{Al1} of Al particles at the exit of the Laval nozzle is as follows:

$$Y_{Al1} = 503.66 + 20.04X_1 - 89.68X_2 + 9.11X_3 - 18.06X_1X_2 - 8.27X_1X_3 - 9.83X_2X_3 + 1.72X_1^2 + 15.9X_2^2 + 17.53X_3^2. \qquad (3.1)$$

Table 3.5 shows the variance analysis of the velocity of the Al particles at the Laval nozzle outlet. It can be seen from the Table 3.5 that the value of model P =

0.0008, the model regression equation is extremely significant, and the value of Lack of fit P = 2.19. (greater than 0.05) [165], not significant, and the correction value of the model = 0.9771 (greater than 0.8) [165]. These values indicate that the equation fits well with the simulation, the correlation between the three factors and the experimental indicators is significant, and the fit degree is acceptable. Overall, the model is suitable for predicting the velocity of the Al particles at the Laval nozzle outlet.

Table 3.5 − Variance analysis of the velocity of the Al particles at the Laval nozzle outlet

Source	Sum of Squares	df	Mean Square	F Value	P-Value Prob>F	Significance
model	72720.08	9	8080.01	15.13	0.0008	Significant
X_1	3212.41	1	3212.41	6.02	0.0439	-
X_2	64336.43	1	64336.43	120.50	<0.0001	-
X_3	664.48	1	664.48	1.24	0.3014	-
X_1X_2	1304.29	1	1304.29	2.44	0.1620	-
X_1X_3	273.57	1	273.57	0.51	0.4973	-
X_2X_3	385.32	1	386.32	0.72	0.4231	-
X_1^2	12.46	1	12.46	0.023	0.8829	-
X_2^2	1064.80	1	1064.80	1.99	0.2008	-
X_3^2	1293.16	1	1293.16	2.42	0.1636	-
Residual	3737.41	7	533.92	-	-	-
Lack of Fit	3737.41	3	1245.80	2.19	0.2337	Not Significant
Pure Error	0.000	4	0.000	-	-	-
Cor Total	76457.49	16		-	-	-

The regression equation for outlet velocity Y_{Cu1} of Cu particles at the outlet of the Laval nozzle is as follows:

$$Y_{Cu1} = 479.11 + 20.18X_1 - 48.13X_2 + 3.6X_3 + 6.6X_1X_2 + 2.49X_1X_3 - \\ - 0.16X_2X_3 - 0.14X_1^2 + 16.61X_2^2 + 1.4X_3^2. \qquad (3.2)$$

It can be seen from the Table 3.6 that the value of the model P < 0.0001, the

model regression equation is significant; the value of the Lack of fit F = 2.41, (greater than 0.05) [166], not significant. The correction value of the model = 0.9477 (greater than 0.8) [166], indicating that the equation fits well with the simulation.

Table 3.6 − Variance analysis of sprayed Cu powder at the outlet velocity of Laval nozzle

Source	Sum of Squares	df	Mean Square	F Value	Value Prob>F	Significance
model	25277.45	9	2808.61	122.87	<0.0001	Significant
X_1	3401.41	1	3401.41	144.81	<0.0001	-
X_2	17075.92	1	17075.92	747.04	<0.0001	-
X_3	103.61	1	103.61	4.53	0.0708	-
X_1X_2	190.41	1	190.41	8.33	0.0234	-
X_1X_3	24.80	1	24.80	1.08	0.3322	-
X_2X_3	0.099	1	0.099	4341	0.9493	-
X_1^2	0.15	1	0.15	6590	0.9376	-
X_2^2	1093.26	1	1093.26	47.83	0.0002	-
X_3^2	8.04	1	8.04	0.35	0.5718	-
Residual	160.01	7	22.86	-	-	-
Lack of Fit	160.01	3	53.34	2.41	0.1962	Not Significant
Pure Error	0.000	4	0.000	-	-	-
Cor Total	25437.45	16	-	-	-	-

The regression equation for outlet velocity Y_{Al2} of Al particles at the outlet of the Laval nozzle is as follows:

$$Y_{Al2} = 495.37 + 16.93X_1 - 68.28X_2 + 8.28X_3 - 23.13X_1X_2 - 7.01X_1X_3 -$$
$$- 9.51X_2X_3 + 8.63X_1^2 - 2.49X_2^2 + 5.86X_3^2, \quad (3.3)$$

As shown in Table 3.7, it is the variance analysis of the velocity (V_p) before the sprayed Al particle deposits on the substrate. From Table 3.7, it can be seen that the value of model P = 0.0084, the model regression equation is significant, and the value of Lack of fit F = 0.0027 (greater than 0.05) [166], not significant, which shows that the model has a good fitting degree and a small error. The model is very

suitable, indicating that the model can be used to predict the velocity (V_p) of the particle before deposition on the substrate.

Table 3.7 − Variance analysis of the velocity (V_p) before spraying Al particle deposition on the substrate

Source	Sum of Squares	df	Mean Square	F Value	P-Value Prob>F	Significance
model	43332.60	9	4814.73	7.12	0.0084	Significant
X_1	2293.34	1	2293.34	3.39	0.1080	-
X_2	37297.27	1	37297.27	55.18	0.0001	-
X_3	548.30	1	548.30	0.81	0.3977	-
X_1X_2	2140.91	1	2140.91	3.17	0.1183	-
X_1X_3	196.42	1	196.42	0.29	0.6065	-
X_2X_3	362.14	1	362.14	0.54	0.4880	-
X_1^2	313.86	1	313.86	0.46	0.5175	-
X_2^2	26.18	1	26.18	0.039	0.8496	-
X_3^2	144.53	1	144.53	0.21	0.6578	-
Residual	4731.21	7	675.89	-	-	-
Lack of Fit	4731.21	3	1577.07	2.37	0.0027	Not Significant
Pure Error	0.000	4	0.000	-	-	-
Cor Total	48063.81	16		-	-	-

The regression equation for outlet velocity Y_{Cu2} of Cu particles at the oulet of the Laval nozzle is as follows:

$$Y_{Cu2} = 479.64 + 20.16X_1 - 47.23X_2 + 3.06X_3 + 6.21X_1X_2 + 3.28X_1X_3 -$$
$$- 1.38X_2X_3 - 0.14X_1^2 + 16.83X_2^2 + 0.89X_3^2 \qquad (3.4)$$

Table 3.8 shows the variance analysis of the velocity (V_p) before the Cu particle deposition on the substrate. It can be seen that the value of model P = 0.0001, and the regression equation of the model is significant. The value of Lack of fit F = 4.83, (more than 0.05) [166], not significant, indicating that the equation fits well with the simulation.

Table 3.8 − Variance analysis of the velocity (V_p) before spraying Cu particle deposition on the substrate

Source	Sum of Squares	df	Mean Square	F Value	P-Value Prob>F	Significance
model	24637.94	9	2737.55	103.77	<0.0001	Significant
X_1	3394.64	1	3394.64	128.68	<0.0001	-
X_2	16442.83	1	16442.83	623.31	<0.0001	-
X_3	74.73	1	74.73	2.83	0.1362	-
X_1X_2	168.59	1	168.59	6.39	0.0393	-
X_1X_3	43.16	1	43.16	1.64	0.2416	-
X_2X_3	7.65	1	7.65	0.29	0.6070	-
X_1^2	0.15	1	0.15	5852	0.9412	-
X_2^2	1121.81	1	1121.81	42.53	0.0003	-
X_3^2	3.22	1	3.22	0.12	0.7370	-
Residual	184.66	7	26.38	-	-	-
Lack of Fit	184.66	3	61.55	4.83	0.0081	Not Significant
Pure Error	0.000	4	0.000	-	-	-
Cor Total	28422.60	16	-	-	-	-

According to the F Value, the contribution rate of the three influencing factors to the Cu particle velocity at the exit of the Laval nozzle (V_e) and the velocity before the Cu particle deposition on the substrate (V_p) can be judged, as shown in Table 3.9.

Table. 3.9 − Contribution rate of factors to experimental indicators

Test index	Contribution rate of experimental factors			Contribution ranking
	X_1	X_2	X_3	
Y_{Al1}	6.02	120.50	1.24	$X_2 > X_3 > X_1$
Y_{Al2}	3.39	55.18	0.81	$X_2 > X_1 > X_3$
Y_{Cu1}	148.81	747.04	4.53	$X_2 > X_1 > X_3$
Y_{Cu2}	103.77	128.68	623.31	$X_3 > X_2 > X_1$

The contribution rate of the Al particle velocity at the Laval outlet is as follows: $D_p > P_s > T_G$; the contribution rate of the Al particle velocity before deposition on the substrate is as follows: $D_p > T_G > P_s$. The contribution rate of the Cu particle

velocity at the Laval outlet is as follows: $D_p > T_G > P_s$; the contribution rate of the Cu particle velocity before deposition on the substrate is as follows: $P_s > D_p > T_G$.

Figure 3.6 shows the influence of three factors on the outlet velocity of the Laval nozzle for Al particle.
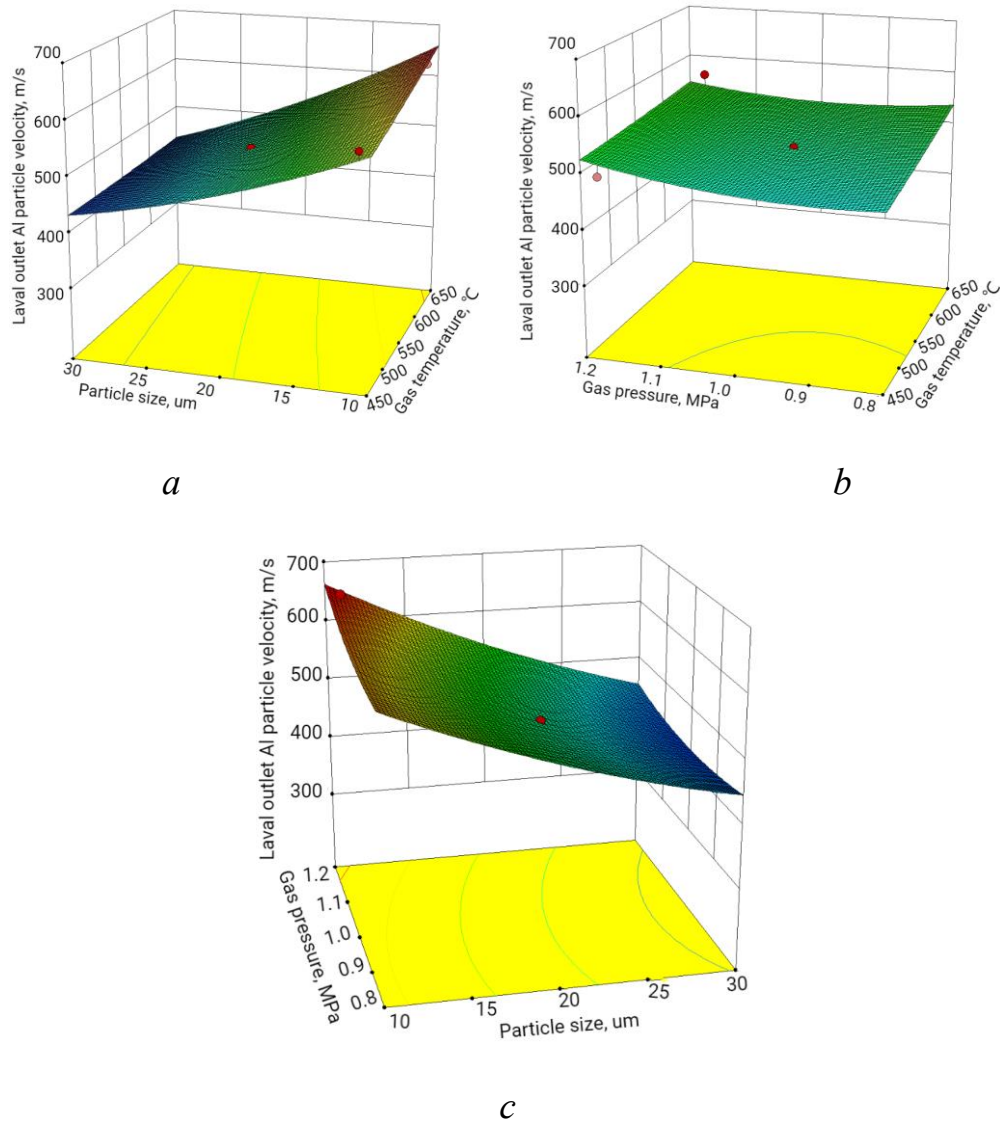
a

b

c

a − the influence of the interaction between particle size and gas temperature; *b −* the influence of interaction between gas pressure and gas temperature; *c −* the effect of the interaction between gas pressure and particle size

Fig. 3.6. The influence of three factors on the velocity of Al particle at the outlet of Laval nozzle

Combining the analysis of the contribution rate of the experimental factors to the experimental indicators in Table 3.9, the contribution rate of the Al particle size is more significant. The design point gas temperature is 550 °C, and the Al particle size is 20 um.

Figure 3.6(b) shows the contribution of gas pressure the design point is that the gas temperature is 550°C and the gas pressure is 1 MPa.

From Figure 3.6(c), the contribution rate of the Al particle size is more significant. The design point is that the Al particle size is 20 um, and the gas pressure is 1.0 MPa; Among them, the red point in the contour map is the design point, which is the optimal solution. At this time, the V_e of the corresponding Al particle can reach 503.66 m/s.

Figure 3.7 shows the influence of three factors on the velocity of the Cu particles at the Laval nozzle outlet, combined with the analysis of the contribution rate of the experimental factors in Table 3.9 to the experimental indicators.

Figure 3.7(a) shows that the contribution rate of the size for Cu particles is more significant. The gas temperature of the design point is 700°C, and the size of the Cu particle is 15um.

As shown in Figure 3.7(b), the contribution rate of the gas temperature is more significant. The design point is the gas temperature of 700°C, and the gas the pressure is 1.5 MPa.

It can also be seen from Figure 3.7(c) that the contribution rate of the Cu particle diameter is more significant, the design point is that the size of the Cu particle is 15 um, and the gas pressure is 1.5 MPa; in the case of the optimal solution, the Cu particle is sprayed the V_e can reach 479.12 m/s.
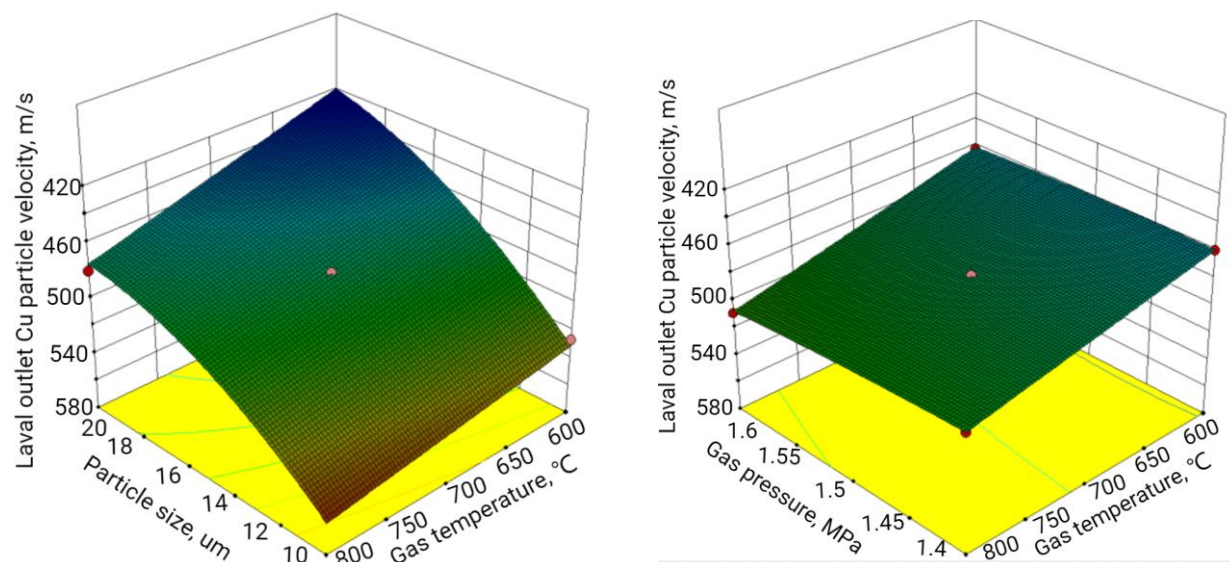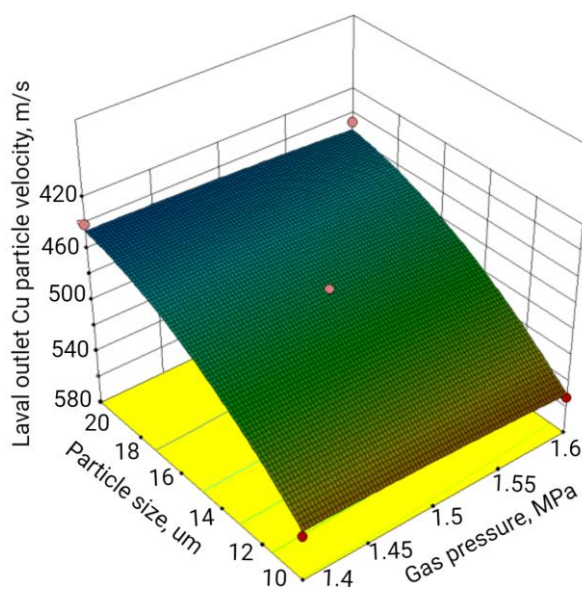
a − the influence of the interaction between particle size and gas temperature; *b* − the influence of interaction between gas pressure and gas temperature; *c* − the effect of the interaction between gas pressure and particle size

Fig. 3.7. The influence of three factors on the velocity of the Cu particle at the Laval nozzle outlet

Figure 3.8 shows the influence of three factors on the V_p before the Al particle deposition on the substrate.
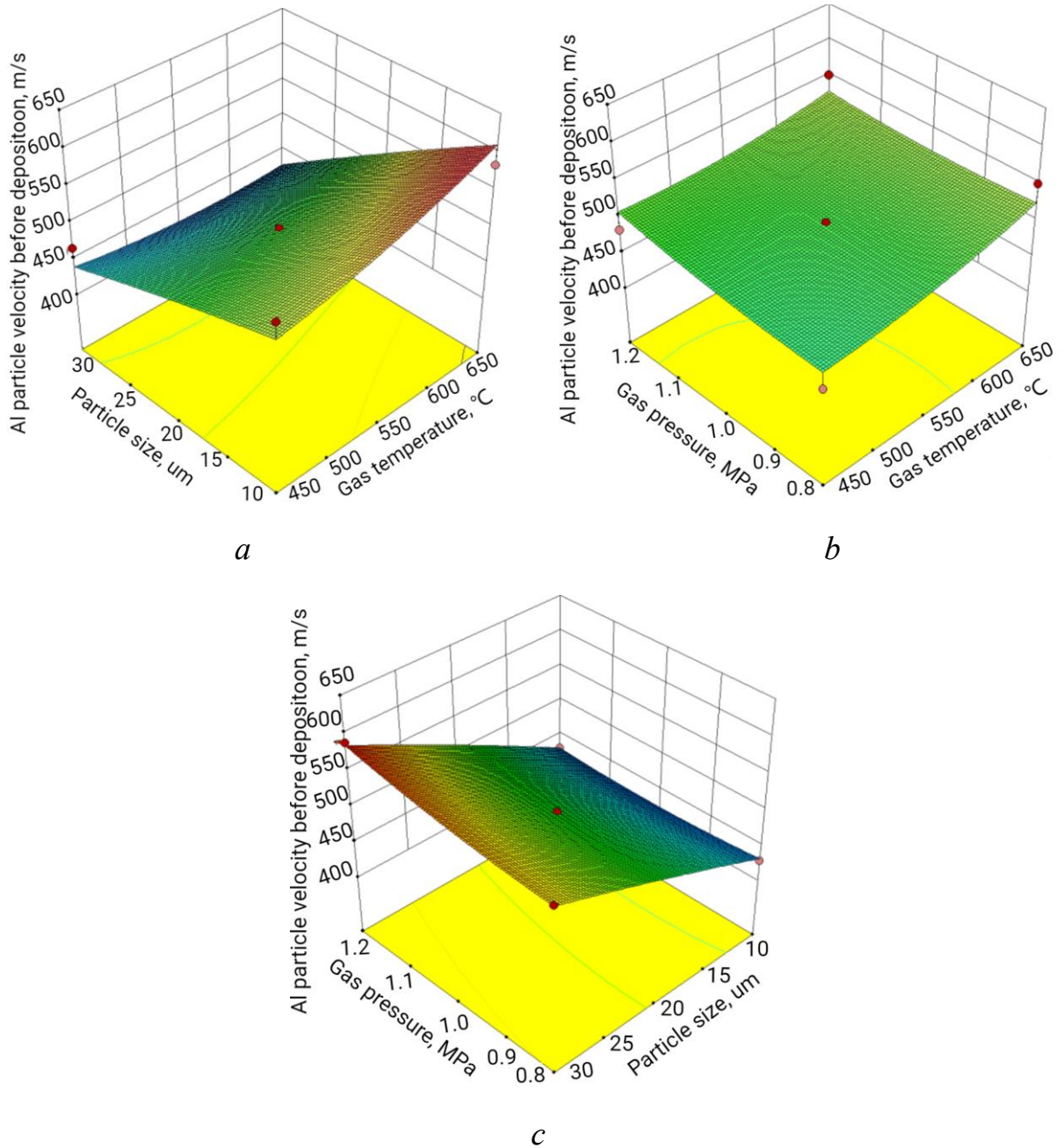
a − the influence of the interaction between particle size and gas temperature; *b* − the influence of interaction between gas pressure and gas temperature; *c* − the effect of the interaction between gas pressure and particle size

Fig. 3.8. The influence of three factors on the V_p before the Al particle deposition on the substrate

Combining Table 3.9, the analysis of the contribution rate of the experimental

factors to the experimental indicators.

It can be seen from Figure 3.8(a) that the contribution rate of the size of the Al particle is more significant, the design point gas temperature is 550 °C, and the size of the Al particle 20 um.

From Figure 3.8(b) it can be seen that the contribution rate of the gas temperature is even greater. Obviously, the design point is that the gas temperature is 550 °C and the gas pressure is 1.0 MPa.

Figure 3.8(c), it can be seen that the contribution rate of the Al particle size is more significant, and the design point is that the Al particle size is 20 um and the gas pressure is 1.0 MPa.

In the case of the optimal solution, the V_p before the Al particle deposited with the substrate can reach 495.37 m/s.

Comparative analysis of the optimal solution for the velocity of the Al particles at the Laval nozzle outlet is 503.66 m/s, indicating that the Al particle is in a stage of decreasing velocity from leaving the Laval nozzle exit to the substrate surface, so it can be used as a reference for studying the spraying distance. Spraying distance is also an important factor affecting spraying efficiency [71].

Figure 3.9 shows the influence of three factors on the V_p before the Cu particle deposition on the substrate. Combining Table 3.9, the analysis of the contribution rate of the experimental factors to the experimental indicators.

It can be seen from Figure 3.9(a) that the contribution rate of the size of the Cu particle is more significant; the design point gas temperature is 700 °C, and the size of the Cu particle is 15 um.

From Figure 3.9(b) it can be seen that the contribution rate of the gas temperature is more obviously, the design point is that the gas temperature is 700 °C and the gas pressure is 1.5 MPa.

From Figure 3.9(c) that the contribution rate of the diameter of the Cu particle is more significant. The Design point is that the size of the Al particle is 15 um and the gas pressure is 1.5 MPa; The V_p can reach 479.64 m/s.

Comparative analysis of the optimal solution for the velocity of the Cu particles at the Laval nozzle outlet is 479.12 m/s, indicating that the Cu particle is still in the accelerated stage from leaving the Laval nozzle exit to the substrate surface.

a

b

c
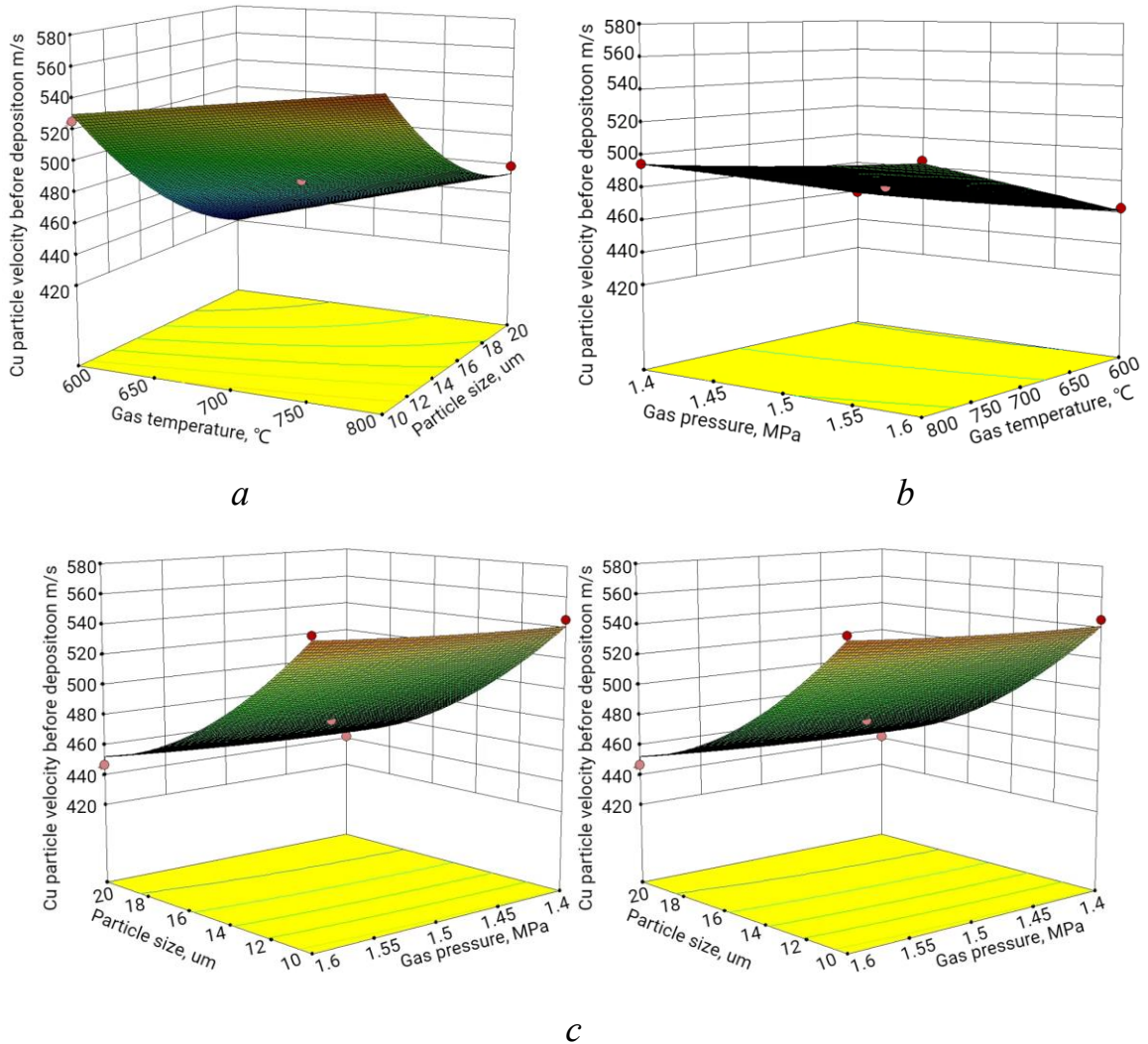
a − the influence of the interaction between particle size and gas temperature; *b* − is the influence of interaction between gas pressure and gas temperature; *c* − the effect of the interaction between gas pressure and particle size

Fig. 3.9. The influence of three factors on the velocity (V_p) before the Cu particle deposition on the substrate

Therefore, for Cu particle, it can increase the spraying distance, so as to obtain the V_p before the Cu particle deposition on the substrate. Combining the

contribution rate of the experimental factors to the simulation indicators in table 3.9, the velocity of Cu particle before deposition on the substrate V_p is analyzed. The influence of gas temperature is obviously greater than that of gas pressure, mainly because the density of Cu particle is large, so it increases within a certain range the gas temperature is the best solution.

3.2.1.4 Analysis of optimization results

Optimal spraying parameters obtained through Design-Expert optimization. The predicted value is compared with the simulated simulation value. Table 3.10 shows the optimized parameter predicted value, simulation value, and error. From the results.

Table. 3.10 − The optimized parameter velocity predicted value and simulation value and error

Material	Factor			Predicted value		Simulation value		Error	
	T_G / °C	D_p / um	P_s / MPa	V_{Te} / m/s	V_{Tp} m/s	V_{Re} / m/s	V_{Rp} m/s	δ_e/%	δ_p/%
Al	550	20	1	503.66	495.37	502.54	494.5	1.6	0.2
Cu	700	15	1.5	479.12	479.64	478.41	478.83	0.1	0.2

The error between the predicted value and the simulation value of the velocity of the Al particles at the Laval nozzle outlet is 1.6 %. The error between the predicted value and the simulation value of the Al velocity before deposition on the substrate is 0.2 %.

The error between the predicted value and the simulation value of the velocity of the Cu particles at the Laval nozzle outlet is only 0.1%. The error between the predicted value and the simulation value of the Cu velocity before deposition on the substrate is only 0.2%.

It shows that the velocity (V_e) regression equation of the velocity of the particles

at the Laval nozzle outlet and the V_p regression equation of the velocity before deposition on the substrate, which are established by using Design-Expert data analysis are reliable, and the simulation results can be effectively used by the regression equation prediction.

Figure 3.10 shows the velocity distribution of Al particle after spraying parameters are optimized. Figure 3.11 shows the velocity distribution of Cu particle after spraying parameters are optimized.

In Table 3.10 V_{Te} – the predicted value of the velocity of the particles at the Laval nozzle outlet; V_{Tp} – the predicted value of the velocity before deposition on the substrate; V_{Re} – the true value of the velocity of the particles at the Laval nozzle outlet; V_{Rp} – the true value of the velocity before deposition on the substrate.
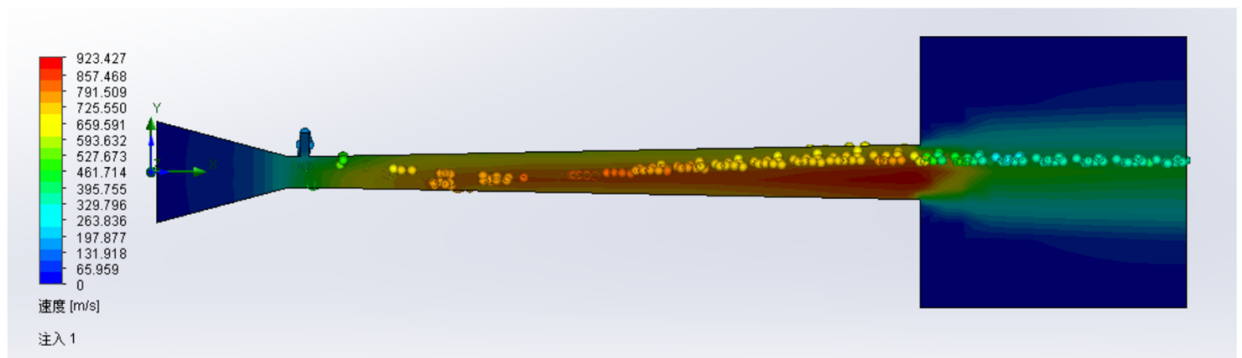
Fig. 3.10. Velocity distribution of Al particle after spraying parameters are optimized
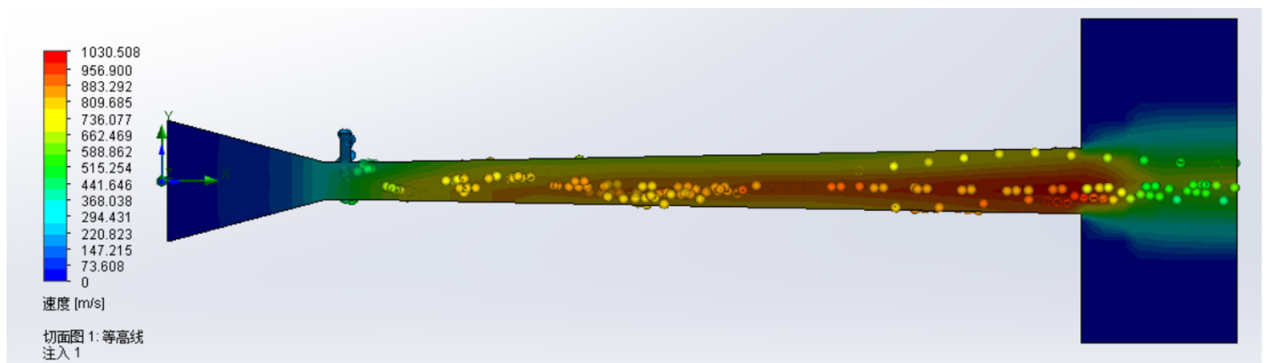
Fig. 3.11. Velocity distribution of Cu particle after spraying parameters are optimized

130

3.2.2 Optimization of special cold spray nozzle structure based on RSM

Most researchers generally use the single-factor method to find rules, but the actual operation process is often the interaction of multiple factors. Therefore, multi-factor interaction analysis is more scientific and realistic. Hu and Tan [162] used RSM to study the 90° nozzle. A multi-factor, multi-level the RSM was established with diffusion L, spraying D and fillet radius of throat R as independent variables; particle deposition velocity as dependent variable. A three-factor, three-level response surface quadratic regression equation was established.

$$y = \beta_0 + \sum_{i=1}^{m} \beta_i x_i + \sum_{i=1}^{m} \beta_{ij} x_j + \sum_{i=1}^{m} \beta_{ii} x_i^2 + \varepsilon, \qquad (3.5)$$

where y – the response value of the regression equation;

x_i and x_j – independent variables;

m – the number of independent variables;

β_0 – the regression intercept;

β_i – is the linear effect of x_i;

β_{ij} – the interaction effect of x_i and x_j;

β_{ii} – the secondary effect of x_i;

ε – The random error.

Parameter design: X_1: Diffusion L; X_2: Spraying D; X_3: Fillet radius of throat R; Y: Powder deposition speed; and high independent variable +1: X_1; medium independent variable 0: X_2; low independent variable -1: X_3. Get the optimal test plan. The test methods and test results are shown in Table 3.11 [162].

Table 3.11 − Simulation arrangement and results [162]

Run	High and Low level code			Actual value
	X_1	X_2	X_3	Y
1	0	0	0	666 m/s
2	-1	+1	0	578 m/s
3	0	0	0	666 m/s
4	+1	0	-1	677 m/s
5	+1	+1	0	664 m/s
6	0	+1	-1	599 m/s
7	0	0	0	666 m/s
8	+1	0	+1	684 m/s
9	+1	-1	0	700 m/s
10	0	+1	+1	630 m/s
11	0	0	0	666 m/s
12	-1	0	+1	645 m/s
13	0	-1	+1	675 m/s
14	-1	0	-1	637 m/s
15	0	-1	-1	643 m/s
16	-1	-1	0	604 m/s
17	0	0	0	666 m/s

According to the F value in Table 3.12, the model is significant; and a regression equation with the three independent variables diffusion L, spraying d and fillet radius of throat R and the powder deposition speed as the dependent variable is derived:

$$Y = 666 + 32.75X_1 - 19.25X_2 + 9.75X_3 - 1.75X_1X_2 - 0.25X_1X_3 -$$
$$- 0.25X_2X_3 - 2.88X_1^2 - 26.88X_2^2 - 2.37X_3^2. \qquad (3.6)$$

The coefficient of determination of the regression equation is R2 = 0.9006, and the correction coefficient is R2 = 0.754. These results show that the regression model can explain 90.06% of the variation in particle velocity response.

Table 3.12 − Variance analysis of the velocity

Source	Sum of Squares	df	Mean Square	F Value	P-Value Prob>F	Significance
model	15505.76	9	1722.86	7.04	0.0087	Significant

Table 3.12 continuation

X_1	8580.5	1	8580.5	35.08	0.006	-
X_2	2964.5	1	2964.5	12.12	0.0102	-
X_3	760.5	1	760.5	3.11	0.1212	-
X_1X_2	12.25	1	12.25	0.05	0.8293	-
X_1X_3	0.25	1	0.25	1.022e-3	0.9754	-
X_2X_3	0.25	1	0.25	1.022e-3	0.9754	-
X_1^2	34.8	1	34.8	0.14	0.7172	-
X_2^2	3041.12	1	3041.12	12.43	0.0096	-
X_3^2	23.75	1	23.75	0.097	0.7644	-
Residual	1712	7	244.57	-	-	-
Lack of Fit	1712	3	570.67	-	-	Not Significant
Pure Error	0	4	0	-	-	-
Cor Total	17217.76	16	-	-	-	-

Figure 3.12 shows the numerical simulation deposition velocity under optimal parameter conditions under N2 [162]. where the particle deposition velocity is the dependent variable as the target, and the model predicts that the best velocity is 707.2 m/s. The optimal spraying parameters obtained according to the corresponding surface analysis method are: diffusion L = 12 mm, spraying D = 13.02 mm; fillet radius of throat R = 26 mm.
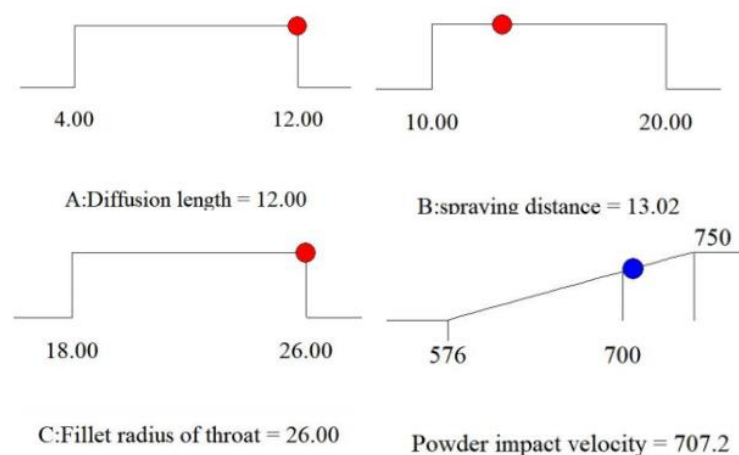
Fig. 3.12. Numerical simulation deposition velocity under optimal parameter conditions under N2. [162].

In order to further verify the optimized parameters, the optimal spraying parameters were input into the simulation model and the velocity of the particles was calculated to be 705 m/s [162], as shown in Figure 3.13. It shows that RSM has high accuracy.
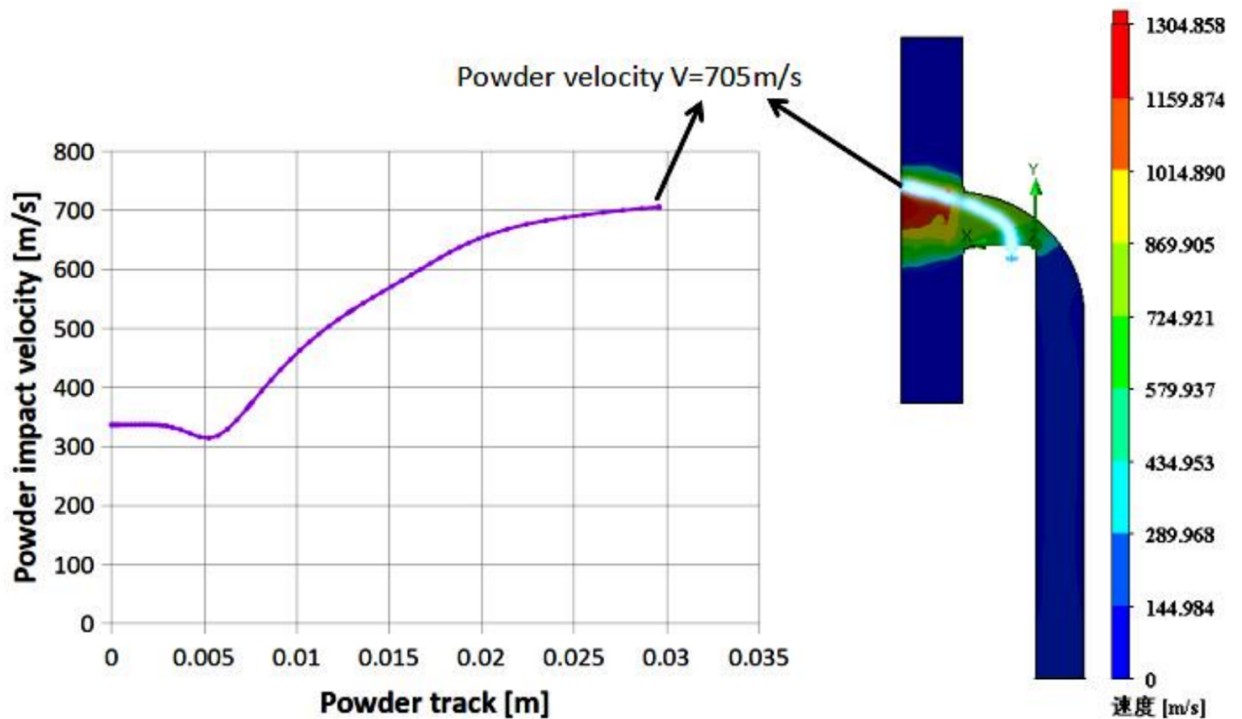
Fig. 3.13. Powder velocity trajectory and velocity nephogram after structure optimization [162].

3.3. Optimization analysis of right-angle nozzle spraying parameters based on GA optimization BPNN

This section optimizes cold spray parameters based on GA optimization BPNN, which is a multi-factor optimization analysis method. By establishing the technical parameters of gas temperature, gas pressure, and particle size as input parameters, the particle velocity at the nozzle outlet is the response model as the output parameter. Fifty groups of samples were taken from the three technical parameters of spraying

through the LHS method, of which 40 groups were used for BPNN training and the remaining 10 groups were used for result prediction. Construct a 3-8-1 layer topological structure cold spray technology parameter optimization NN model; use BPNN to predict the exit velocity of Al6061 particle and Cu particle in the cold spray nozzle, and then use a GA to predict the velocity of the particles in the right-angle nozzle the exit velocity is calculated iteratively to find the optimal velocity value. This enables the study of the effect of multi-technical parameter coupling on the velocity of particles at the exit of the right-angle nozzle.

3.3.1 Simulation model and method design

3.3.1.1 Parameters of Right-angle nozzle

The Laval right-angle nozzle is mainly composed of three parts: convergence section, throat and expansion section. The main parameters of the Laval nozzle are: convergence section length L_1, throat length L_2, expansion section length L_3, inlet diameter D_i, throat diameter D_t, outlet diameter D_e. The right-angle turning radius of the throat is R = 5 mm. The particle entrance is entrance. particle entrance diameter is 1mm. Figure 3.14 shows a right-angle cold spray nozzle parameters. Table 3.13 shows the main design parameters of the cold spray nozzle [167].
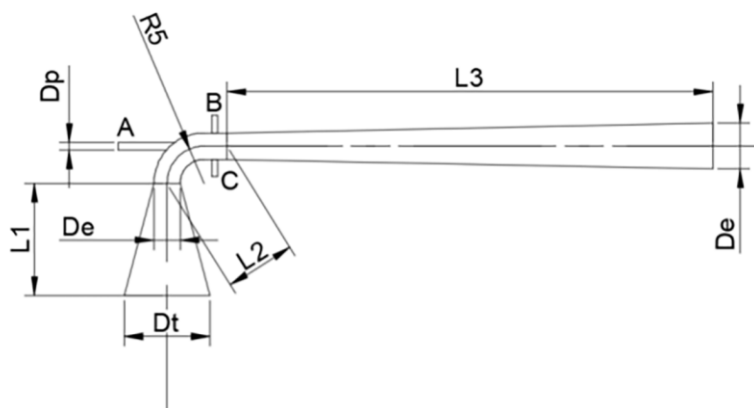
Fig. 3.14. The parameters of right-angle cold spray nozzle [167]

Table 3.13 − The design parameters of the right-angle cold spray nozzle are as follows [167]

Parameter	D_t	D_i	D_e	D_p	L_1	L_2	L_3
Value/mm	3.5	11.5	6.06	1	15	6.9	65

3.3.1.2 The Latin Hypercube Sampling (LHS)

The LHS is widely used in the field of parameter optimization. This method has the characteristics of uniform stratification, and it can obtain the sample value of the tail with less sampling. Based on the above two characteristics, The LHS is more efficient than ordinary sampling methods.

As shown in Table 3.14, the numerical ranges of the three parameters of gas pressure, gas particle temperature, and particle size are used; The LHS is used to extract 50 groups of samples for the three parameters of gas pressure, gas temperature, and particle size, and the numerical values of each group of sampling samples are the velocity of the particles at the exit of the Laval right-angle nozzle is calculated by simulation (V_e), as shown in Table 3.15. Among them, 40 groups are used for BPNN training, and the remaining 10 groups are used for prediction.

Table 3.14 − Cold spray spraying parameter range

Parameter	Range	
	Al6061	Cu
Gas pressure / MPa	0.8-1.2	1.4-1.6
Particle temperature / K	450-650	600-800
Particle size / um	5-45	5-45

Table 3.15 − Sample data and particle velocity at the nozzle exit

Sample No.	Gas pressure (Mpa)		Particle temperature (K)		Particle size (um)		$V_{Al6061\ e}$ (m/s)	$V_{Cu\ e}$ (m/s)
	Al6061	Cu	Al6061	Cu	Al6061	Cu		

Table 3.15 continuation

1	1.13	1.58	630	624	31	44	476.90	355.77
2	1.01	1.47	605	788	12	35	642.94	371.89
3	0.99	1.40	460	791	8	9	567.36	576.67
4	1.14	1.47	647	633	40	24	466.87	405.97
5	0.88	1.58	534	721	28	32	461.24	384.28
6	0.86	1.45	544	714	23	28	509.68	395.41
7	1.06	1.56	571	694	9	10	612.34	555.26
8	0.89	1.49	579	656	27	16	458.92	473.24
9	0.85	1.43	643	649	10	44	644.58	331.10
10	0.91	1.48	620	613	15	40	589.61	342.64
11	0.94	1.46	562	673	11	43	604.73	336.48
12	0.81	1.54	625	633	17	20	539.23	434.28
13	0.87	1.55	540	708	20	14	505.42	523.45
14	1.08	1.48	464	732	41	32	410.68	383.12
15	1.20	1.43	516	620	38	20	470.06	431.73
16	0.90	1.42	527	759	33	23	437.00	423.13
17	1.06	1.44	556	784	6	41	649.62	353.62
18	1.19	1.51	563	761	24	41	506.76	360.21
19	0.99	1.56	609	703	22	22	509.38	440.05
20	0.94	1.52	532	728	22	37	495.99	360.70
21	1.06	1.46	640	689	43	17	442.03	470.95
22	1.03	1.42	506	682	16	18	550.78	452.59
23	0.84	1.44	614	607	9	18	640.97	439.07
24	1.04	1.53	634	778	35	7	473.66	654.27
25	0.84	1.41	588	609	5	42	715.77	330.28
26	0.91	1.48	631	697	41	33	431.87	375.81
27	1.02	1.59	466	666	35	15	427.56	478.87
28	1.11	1.59	585	718	43	26	435.51	413.39
29	1.09	1.50	454	795	32	39	448.89	394.66
30	1.00	1.55	488	775	29	22	449.55	455.20
31	1.15	1.55	549	603	45	14	424.40	480.38
32	1.17	1.54	499	747	29	36	467.19	351.17
33	0.97	1.53	577	704	26	38	484.03	360.00
34	0.92	1.45	521	669	17	34	522.28	360.29
35	1.16	1.50	612	753	13	31	600.84	385.37
36	1.00	1.51	594	770	26	38	479.23	362.58
37	1.12	1.57	505	799	32	28	450.39	419.48
38	0.87	1.40	471	629	44	19	385.77	436.34
39	0.82	1.43	458	765	18	5	487.53	689.18
40	0.83	1.60	458	643	13	30	556.26	385.98
41	1.04	1.57	566	679	19	12	523.55	514.61
42	0.98	1.51	596	748	7	12	620.09	530.36

Table 3.15 continuation

43	0.94	1.53	481	660	30	11	450.56	544.39
44	1.10	1.57	483	687	20	27	490.26	408.78
45	0.97	1.45	522	616	37	6	421.70	621.37
46	1.09	1.52	475	730	25	25	474.55	417.27
47	1.16	1.41	552	739	39	8	451.06	584.01
48	1.12	1.49	512	639	15	24	549.02	406.92
49	0.82	1.49	601	655	34	11	436.12	514.13
50	1.18	1.59	496	742	37	29	446.19	406.92

3.3.1.3 The Back Propagation Neural Networks Model

The BPNN is a training algorithm that uses error back propagation; the entire structure mainly includes: input layer, hidden layer, and output layer; adjust the weights and thresholds of the network so that the mean square error of the network's output value and the expected output value is minimum.

This section uses a three-layer BPNN structure, with an input layer of 3 neurons, an output layer of 1 neuron, and the number of hidden neurons is 8; the BPNN structure is a 3-8-1 model, as shown in Figure 3.15.
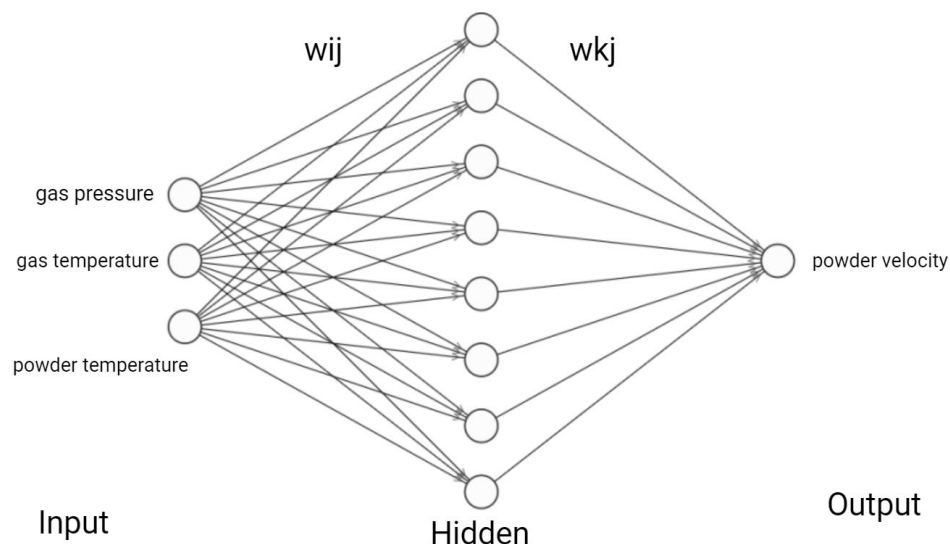
Fig. 3.15. 3-8-1 BPNN structure diagram

The hidden layer transfer function uses the tansing function, the output layer

138

transfer function uses the Logsig function, and the normalization method is used to process the input parameters. At the same time, the inverse operation of the normalization method is used to restore the output units to the original units.

In order to prevent the impact of strange test sample data on BPNN training, the data needs to be normalized and limited to the range of [-1.1].

$$y_i = 2 \times \frac{x_i - x_{min}}{x_{max} - x_{min}} - 1, \qquad (3.7)$$

where x_i (i =1, 2, ...40) – the training sample;

x_{max} and x_{min} – the maximum and minimum values in the training sample respectively;

y_i – the normalized training sample.

The BPNN structure model is 3-8-1, and the relationship expression between its input model and output model:

$$y = purelin \left\{ \sum_{i=1}^{XX} \left[W_{ki} \times tansig \left(\sum_{j=1}^{3} W_{ij} \times x_j + b_i^{(1)} \right) + b_k^{(2)} \right] \right\}, \quad (3.8)$$

where x_j – the jth spraying parameter of the input layer;

W_{ij} – the weight from the output layer to the hidden layer;

W_{ki} – the weight from the hidden layer to the output layer, k=1;

$b_i^{(1)}$ – the threshold of the hidden layer;

$b_k^{(2)}$ – the weight of the output layer threshold;

y – the network output.

3.3.1.4 GA optimizes BPNN

GA is essentially an evolutionary algorithm that can better solve nonlinear

function optimization problems. Therefore, the GA is used to optimize the initial weights and thresholds of the BPNN to improve the training and prediction accuracy of the BPNN. The BPNN with the 3-8-1 structure has many weights and thresholds. In order to avoid mapping errors, real number encoding is used. The chromosome is composed of the weights and thresholds of the BPNN, and the coding length is calculated by equation (3-4). The weights and threshold number of the BPNN with 3-8-1 structure are determined by equation (3.4)

$$L = 3 \times 8 + 8 + 8 \times 1 + 1 = 41. \tag{3.9}$$

After encoding the chromosomes, the fitness of each individual needs to be determined. If the optimization criteria are met, the best individual is output, which is the optimal BPNN weight and threshold. Otherwise, select individuals based on their fitness, perform crossover and mutation on individuals according to a certain probability, generate new individuals, determine individual fitness again, and determine whether it meets the optimization criteria. The fitness of an individual is defined as equation (3.5).

$$\text{fitness} = \frac{1}{M} \sum_{j=1}^{M} \sum_{i=1}^{q} (Y_i - T_i)^2, \tag{3.10}$$

where M – the number of samples;

     q – the number of neurons in the output layer;

     Y_i – the actual BPNN output;

     T_i – the expected output.

The roulette strategy is used to select individuals. The smaller the individual fitness value, the greater the probability of being selected. The crossover method is real-valued recombination, and the mutation method is real-valued mutation. The GA optimization BPNN process is shown in Figure 3.16.
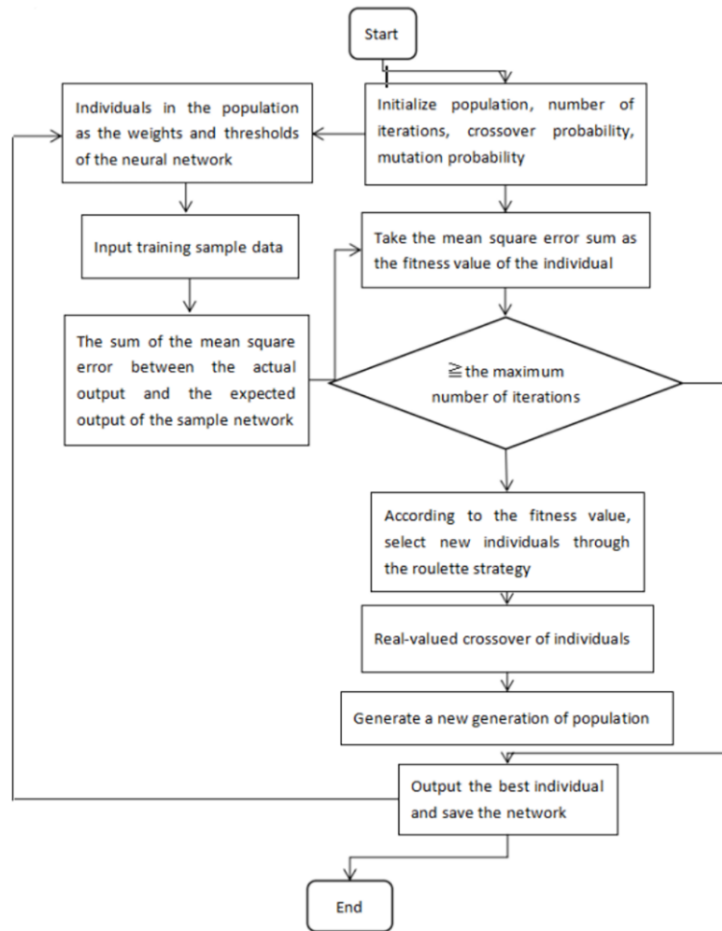
Fig. 3.16. The GA optimization BPNN flow chart

3.3.2 Result analysis and Discussion

By comparing the training and prediction accuracy of BPNN on sample data before and after GA optimization, the training accuracy and prediction accuracy of the optimized BPNN are higher than those before optimization; and the relative prediction error does not exceed 6.6 %.

Figure 3.17 shows the comparison of Cu particle sample data training output before optimization and after optimization.
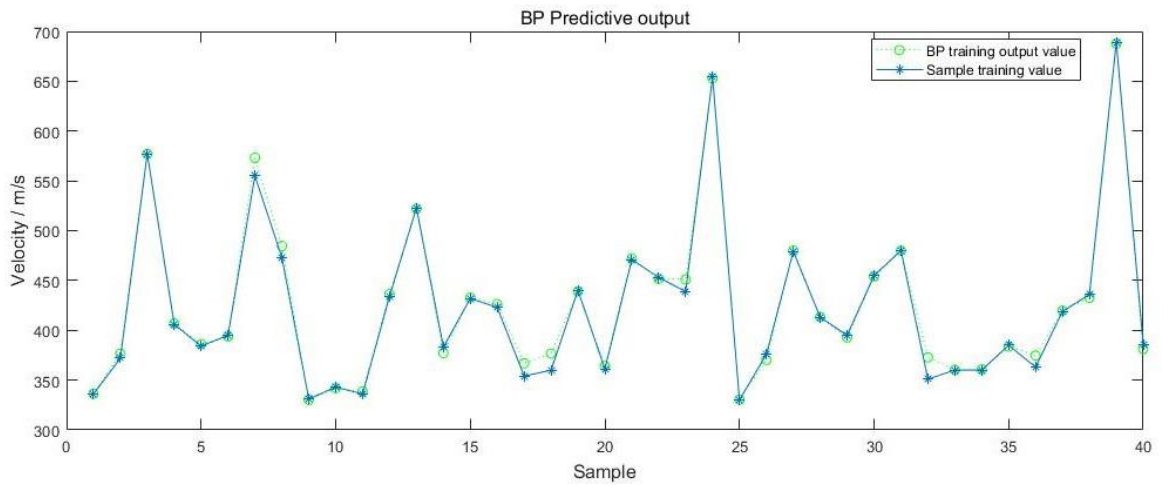
a
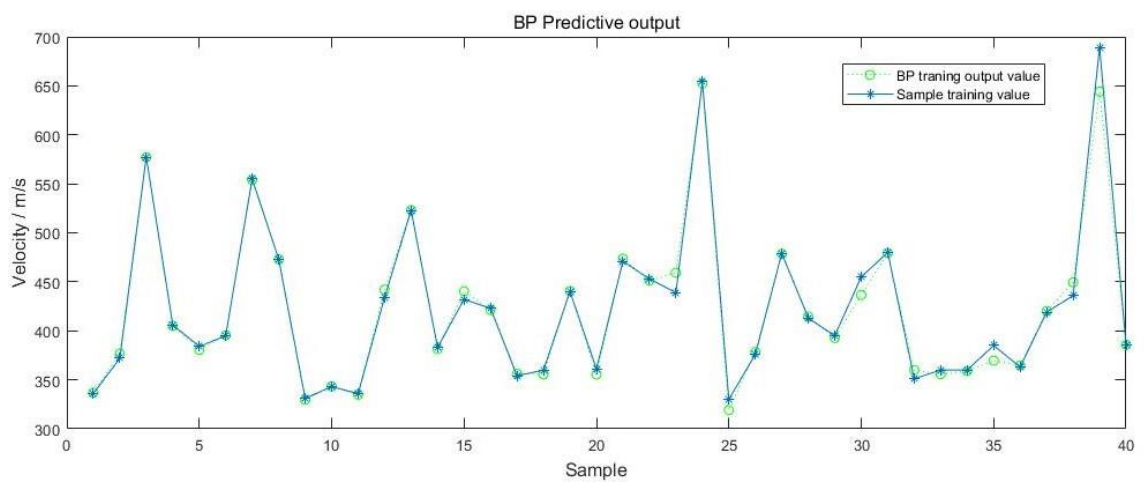
b

a − training output before; *b −* after optimization

Fig. 3.17. Comparison of Cu particle sample data

Figure 3.18 shows the comparison of Cu particle sample data prediction output before optimization and after optimization.

a

b
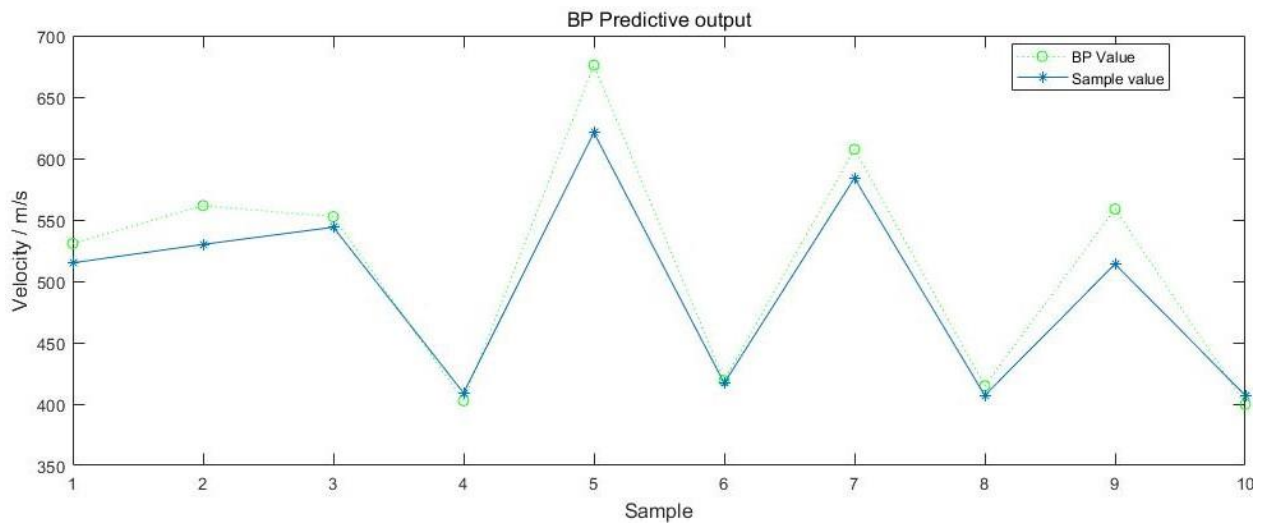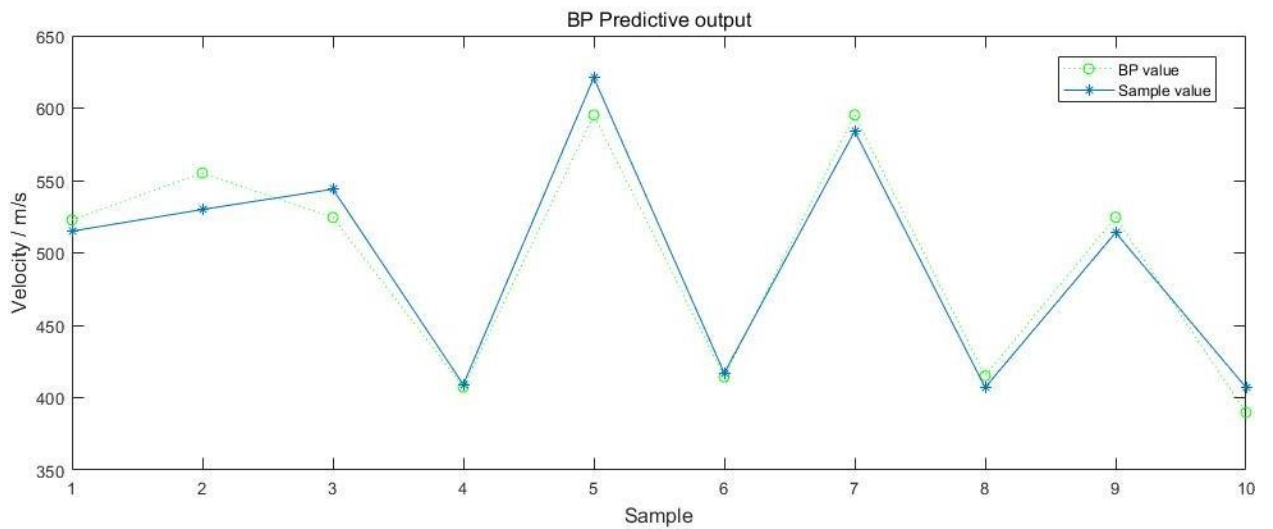
a − prediction output before; *b* − after optimization

Fig. 3.18. Comparison of Cu particle sample data

Figure 3.19 shows the comparison between Al6061 particle sample data training output before optimization and after optimization.
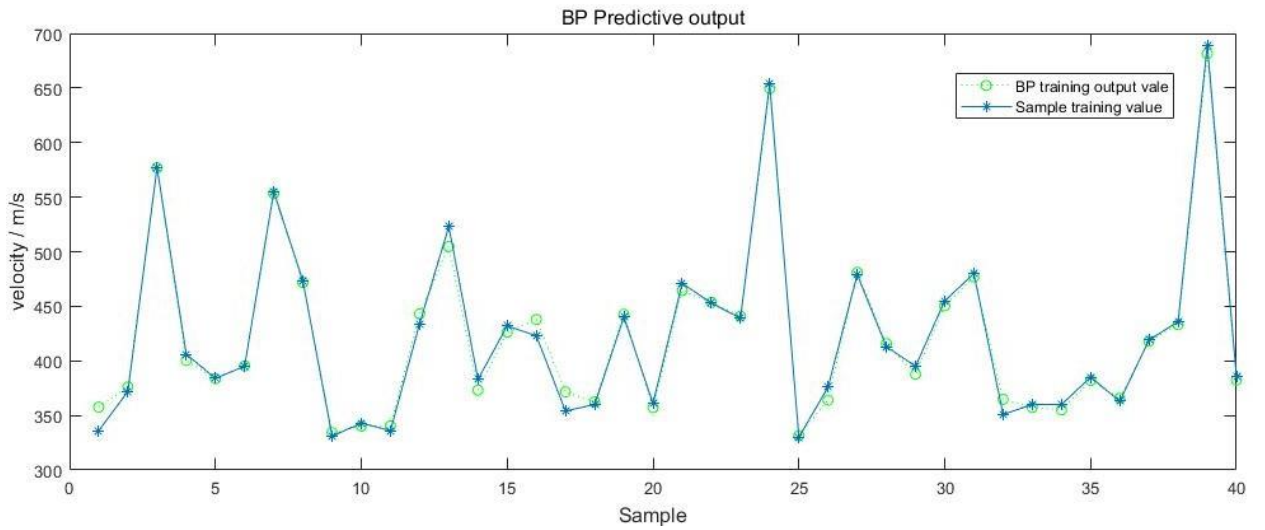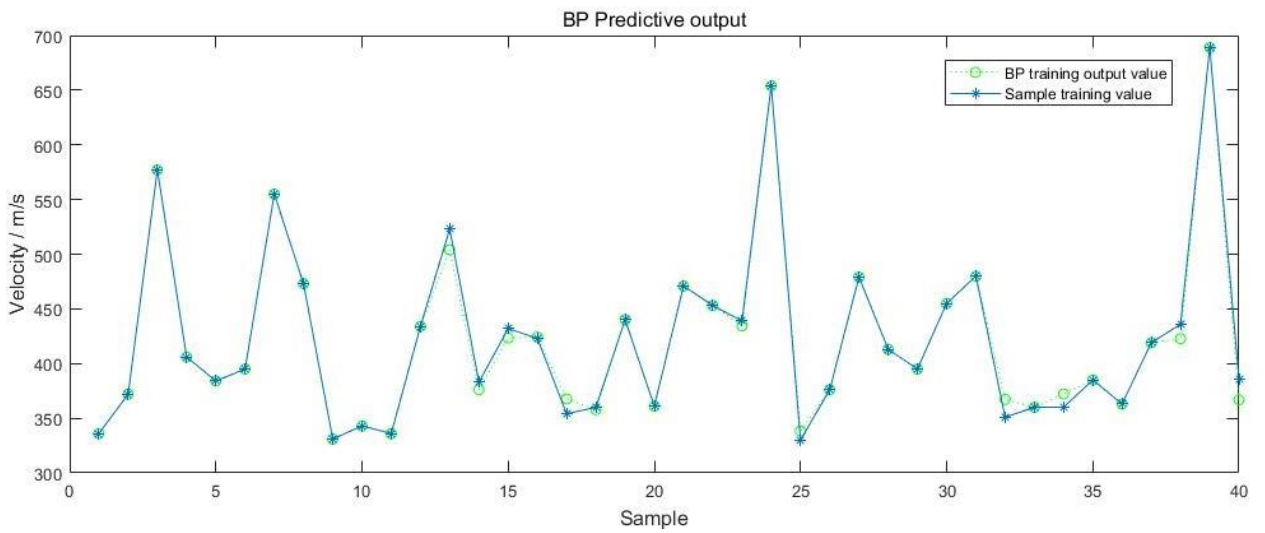
a − training output before; *b* − after optimization

Fig. 3.19. Comparison of Al6061 particle sample data

Figure 3.20 shows the comparison between Al6061 particle sample data prediction output before optimization and after optimization.

a

b
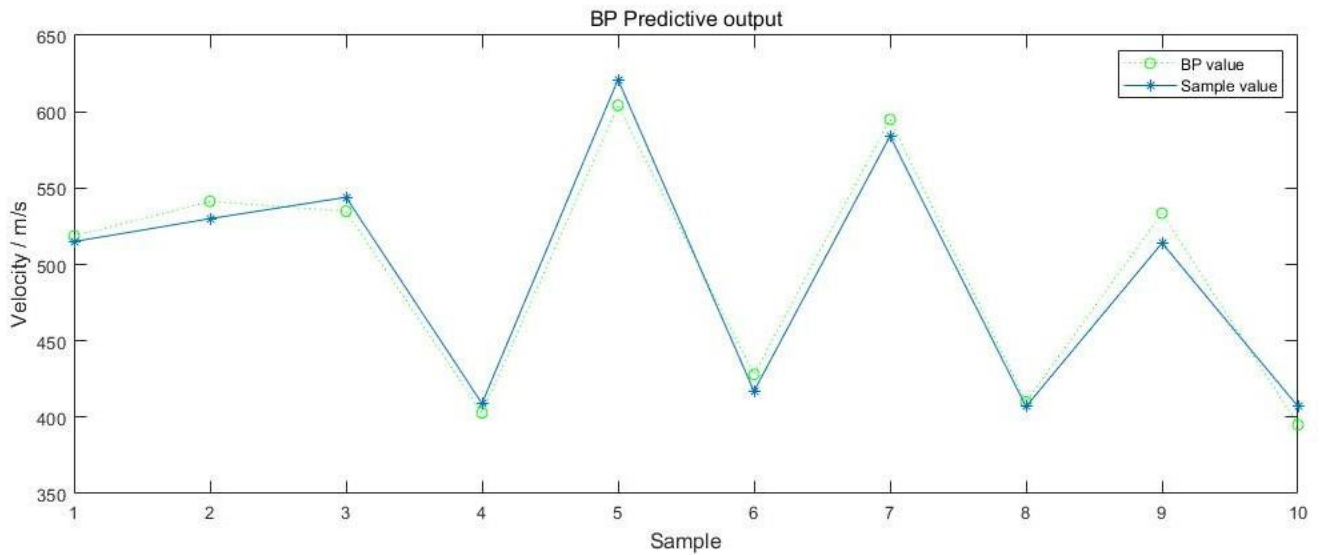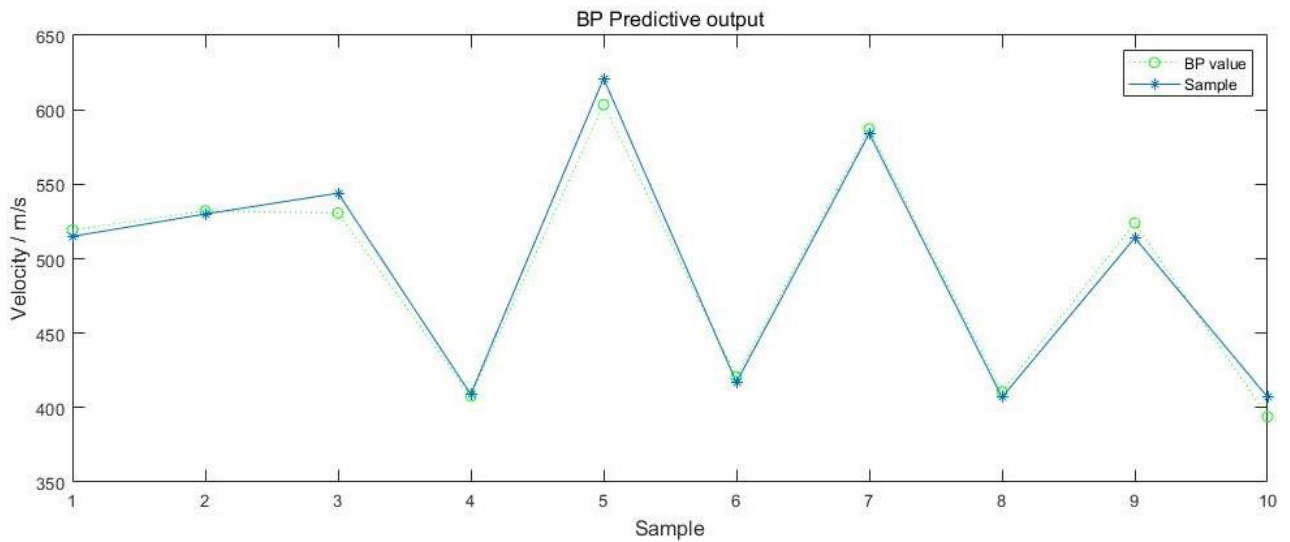
a − prediction output before; *a* − after optimization.

Fig. 3.20. Comparison of Al6061 particle sample data

Table 3.16 − Sample data and particle velocity at the nozzle exit

Model	Training mean square error		Forecast mean square error	
	Al6061	Cu	Al6061	Cu
BPNN	0.0092	0.05	0.066	0.035
GA+BPNN	0.0083	0.015	0.001	0.003

According to the analysis of BPNN training and prediction results of Cu

particles and Al6061 particles as shown Table 3.16, the BPNN optimized by the GA can more accurately establish the response relationship between multi-factor spraying parameters and the velocity of Cu particles and Al6061 particles at the right-angle nozzle outlet (V_e). Therefore, this model is used as the objective function of GA to optimize process parameters.

3.3.3 Optimizing particle velocity through GA

The optimized BPNN was used to establish the response model between the spraying parameters and the velocity of the particles at the right-angle nozzle outlet (V_e), and the model was used as a GA to find the optimal objective function for the process parameters

$$F = \min f(x_1, x_2, x_3), \tag{3.11}$$

where $0.8 \leq x_1 \leq 1.2, \ 450 \leq x_2 \leq 650, \ 5 \leq x_3 \leq 45$.

Through the global search capability of the GA, the objective function is iterated to find the optimal solution. The GA is defined to iteratively find the optimal fitness function for process parameters as follows:

$$Y = |y - x|, \tag{3.12}$$

where y － the actual output of the BPNN after normalization of the output data;

x － the normalized value of the velocity of the particles at the right-angle nozzle outlet;

Y － the normalized value corresponding to the actual output of the BPNN and the velocity of the particles at the right-angle nozzle outlet absolute value error.

Through the selection, crossover and mutation of the GA, the three sets of

process parameter combinations corresponding to the optimal velocity of the particles at the right-angle nozzle outlet are solved. Binary coding is used for the three process parameters, and iterative calculation is performed to obtain three sets of process parameters corresponding to the optimal velocity of the particles at the right-angle nozzle outlet through multiple iterations.

Table 3.17 shows the velocity and process parameter combination of Cu and Al6061 particles at the right-angle nozzle outlet. It can be seen from Table 3.17 that as the number of iterations increases, the velocity of particles predicted by the GA network at the right-angle nozzle outlet gradually decreases. After the number of iterations reaches a certain number, a set of process parameter combinations and the particles velocity at the right-angle nozzle exit can be obtained. A better velocity value can be exported, but this does not prove that the obtained process parameter combination is the best globally. The calculation results can only show that the GA can obtain a higher quality solution within a reasonable iteration period. Therefore, it is necessary to conduct simulation calculations on the results to remove solutions with large errors. By numerically simulating the process parameters in Table 3.17 and obtaining the velocity of the particles at the right-angle nozzle outlet, the simulation results and the solution results were analyzed for errors. The analysis is shown in Table 3.18.

Table 3.17 – The velocity and process parameter combination of Cu and Al6061 particles at the right-angle nozzle outlet

No.	Gas pressure (MPa)		Particle temperature (K)		Particle size (um)		V_e (m/s)	
	Al6061	Cu	Al6061	Cu	Al6061	Cu	Al6061	Cu
1	1.3078	1.5069	560.79	676.32	17	11	570.74	526.80
2	1.3158	1.4133	558,31	621.91	17	10	569.39	526.58
3	1.2953	1.4952	565.69	685.73	16	11	568.50	526.35
4	1.3152	1.4658	562.81	650.75	16	10	568.33	526.09

Through the error analysis of Table 3.18, the best combination parameters of

Al6061 particles and Cu particles are obtained. Al6061 particle No:1 is the best combination parameter, and Cu particle No:3 is the best combination parameter. The two particle combination parameters and the particle size the optimal velocity of the right-angle nozzle outlet is shown in Table 3.19.

Table 3.18 − Velocity and process parameter combination of Cu and Al6061 particles at the right-angle nozzle outlet

No.	Solution value		Simulation value		Error	
	Al6061	Cu	Al6061	Cu	Al6061	Cu
1	570.74	526.80	571.23	516.15	0.09%	2.02%
2	569.39	526.58	570.12	519.55	0.13%	1.34%
3	568.50	526.35	566.24	520.71	0.4%	1.07%
4	568.33	526.09	568.96	537.93	0.11%	2.2%

Table 3.19 − Cu and Al6061 particle combination parameters and optimal velocity at the right-angle nozzle outlet

Parameter	Gas pressure (MPa)	Particle temperature K	Particle size (um)	V_e (m/s)
Al6061	1.3078	560.79	17	571.23
Cu	1.4952	685.73	11	520.71

3.3.4 Conclusion for the section

This section establishes a mathematical model in which the technical parameters of gas temperature, gas pressure, and particle size are input parameters, and the particle velocity at the nozzle exit is the output parameter. Fifty groups of samples were extracted from the three technical parameters using the LHS method, 40 groups were used for BPNN training, and 10 groups were used for result prediction. BPNN is used to predict the velocity of particles at the outlet of the right-angled nozzle, and then GA is used to iteratively calculate the velocity of particles at the exit of the right-angled nozzle to find the best velocity value.

When the number of hidden neurons is 8, the mean square errors of training

148

and prediction are both smallest. Determine the BPNN structure to be the 3-8-1 model. The multi-technical parameter BPNN structure model established by BPNN accurately predicts the velocity of particles at the right-angle nozzle exit, and the prediction error of the response model is very small.

The GA can obtain reliable solutions within the iterative interval. Through comparative analysis of the solution and simulation results, the Cu and Al6061 particle combination parameters and the optimal velocity of the right-angle nozzle outlet are finally obtained. The optimal velocity of Cu particles is 520.71 m/s; the optimal velocity of Al6061 particles is: 571.23 m/s.

The GA optimized BPNN is applied to cold spray technology parameters through a specific coding program, highlighting the research trend of interdisciplinary integration of materials science + mathematical model + computer.

3.4 Research of single-channel right-angle nozzle and particle inlet

The conventional Laval nozzle structure currently being studied is of the tapered axial symmetry type, in order to further expand the application areas of the nozzle, especially structural parts with complex surfaces, and areas where conventional Laval nozzles cannot be applied. Therefore, based on the existing conical axial symmetry type, further research is conducted on right-angled nozzles with circular and square cross-sections.

3.4.1 Analysis of single-channel circular right-angle nozzle

As shown in Figure 3.21, cold spray nozzles can be divided into conical (a) and bell-shaped (b) [168]; cold spray nozzles are mainly composed of three parts it consists of: convergence section, throat and expansion section. As can be seen from Figure 3.21, the curvatures of the constriction section and the throat of the cone-shaped and bell-shaped nozzles are different. Research shows that when the

curvature radii of the convergence section and the throat are not the same. When it is large, the energy loss of accelerating the medium and particles in the nozzle is minimal. The converging section, expansion section, and throat of the conical cold spray nozzle are connected smoothly at three parts, while the connection curvature of the three parts of the bell-shaped cold spray nozzle changes greatly. From the perspective of structure and processing, the conical nozzle is selected. The management is more reasonable.
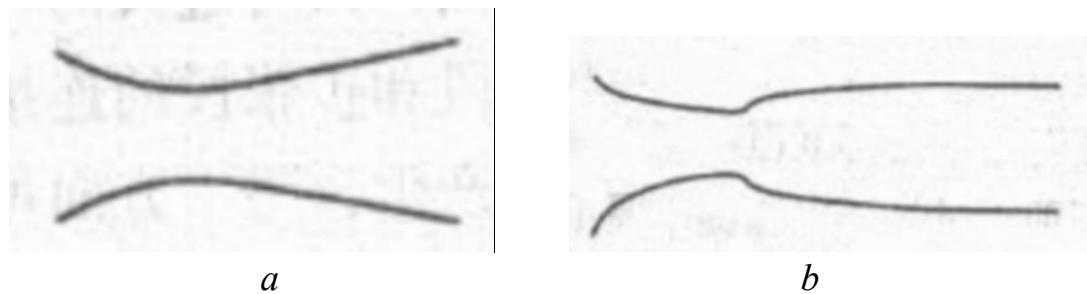
a − Cone-shaped nozzle; b − Bell-shaped nozzle

Fig. 3.21. The different shape of cold spray nozzle

As shown in Figure 3.22, the cross-sectional shape of the nozzle can be divided into circular (a) and rectangular (b) [169]. At present, the widely recognized nozzle cross-section is circular. Its advantages are mature technology and simple structure; rectangular nozzle is not common. This type of nozzle is mainly used for spraying rotating body specimens. Among them, rectangular nozzle the disadvantage of the nozzle is that the gas flow field in the nozzle is unevenly distributed, and turbulence easily occurs at the edges and corners, which will hinder the acceleration of particles and cause particles to accumulate inside the nozzle. Figure 3.23 shows the velocity cloud diagrams of the circular nozzle (a) and the rectangular nozzle (b) with exit cross sections; it can be seen from the Figure 3.23 that the velocity in the central area of the circular nozzle is greater than that of the rectangular nozzle. Moreover, the viscous boundary layer effect is better than that of a rectangular nozzle, and the effective flow area is large. Summarizing the above advantages, this dissertation

chooses a nozzle with a circular throat section.

<center>*a*   *b*</center>
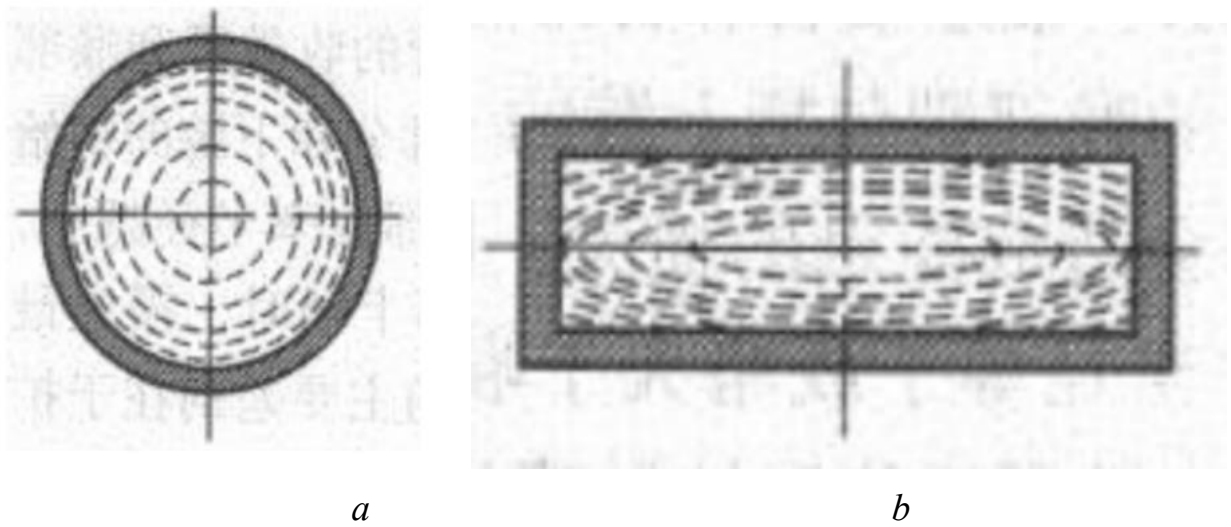
a − The circular cross-section; *b* − The rectangular cross-section

Fig. 3.22. The throat cross-section of cold spray nozzle

<center>*a*   *b*</center>
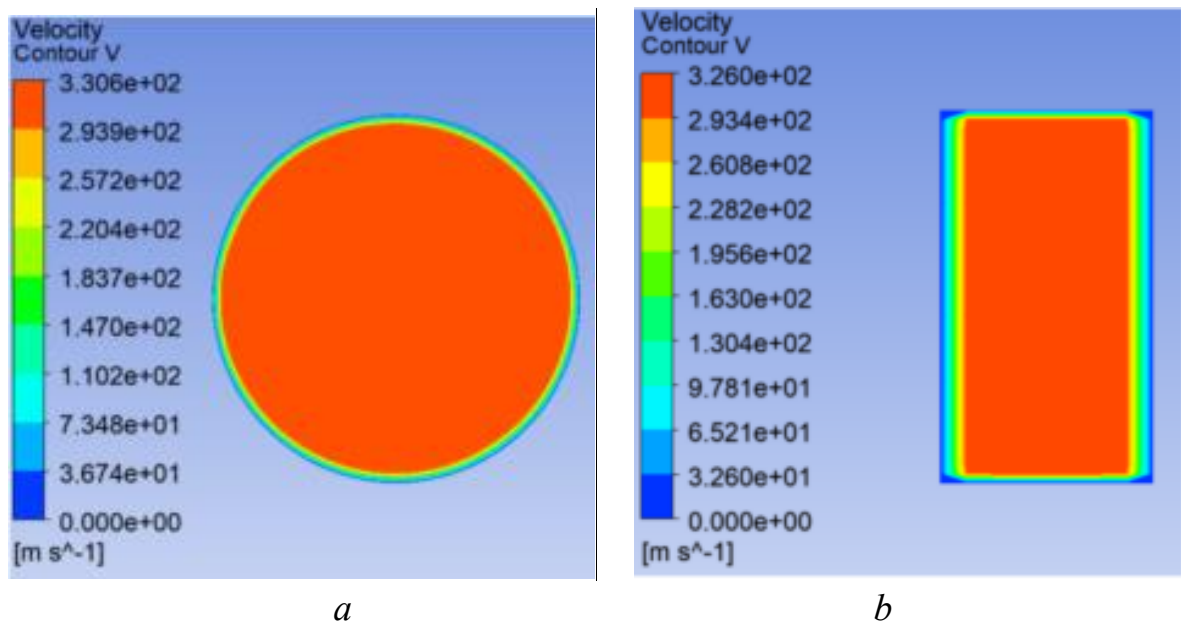
a – The circular nozzle; *b* – The rectangular nozzle

Fig. 3.23. The nozzle outlet gas velocity diagrams

3.4.2 Parameters and experimental methods of single-channel right-angle nozzle

Determine the nozzle model according to the following equations, and then study the impact of right-angle nozzles with different particle inlets on the acceleration characteristics of five types of particles: Al, Al6061, Cu, Ni, and Zn.

It can be obtained by calculation, D_i=11.5 mm. According to empirical values [170, 171], the selection range of the inlet convergence angle α of the convergence section is 30°-60°; the selection range of the exit diffusion angle β of the expansion section is 10°- 12°; According to equations (2.68) and (2.69), the converging section length L_1=15 mm and expansion section length L_{3_1}=65 mm of the right-angle nozzle. All parameters are shown in Table 3.20. The right-angle turning radius of the throat is R=5 mm, as shown in Figure 3.24.
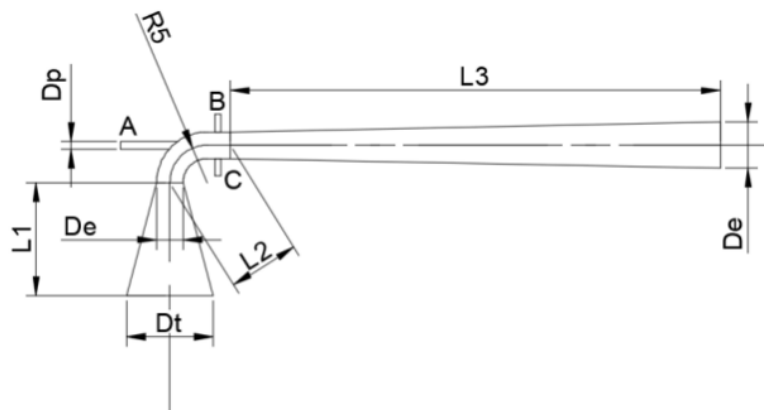
Fig. 3.24. Parameters of right-angle cold spray nozzle

Table 3.20 − The design parameters of the right-angle cold spray nozzle are as follows

Parameter	D_t	D_i	D_e	D_p	L_1	L_2	L_3
Value/mm	3.5	11.5	6.06	1	15	6.9	65

Five types of particles are accelerated in a right-angle cold spray nozzle at

different particle entrances. The A, B, and C entrances of particle injection is shown in Figure 3.24; the pressure inlet is 1.2 MPa, the gas temperature is 500 K, and the acceleration gas is nitrogen, the spray particles are: Al (25 um), Al6061 (20 um), Cu (20 um), Ni (20 um), and Zn (20 um).

3.4.3 Analysis of the gas flow the single-channel right-angle nozzle

Figure 3.25 shows the velocity flow field cloud diagrams of right-angle nozzles with three different particle entrances. It can be seen from the Figure 3.25 that the maximum velocity of the gas flow in the right-angled nozzle at particle entrance A is 663.4 m/s; the maximum velocity of the gas flow in the right-angled nozzle at particle entrance B is 643.6 m/s; the maximum velocity of the gas flow in the right-angled nozzle at particle entrance C is 652.8 m/s. among them, the velocity of the right-angle nozzle of particle entrance A is the largest; the maximum gas flow speed areas of the right-angle nozzle of the three particle entrances are all it is located at the center of the exit, indicating that the gas in the right-angle nozzle is always in an accelerated state and does not reach the maximum speed before the nozzle outlet. This is the same as the result in the study in reference [172].

It can be seen from Figure 3.25 that there is an obvious coupling phenomenon between the particle entrance gas flow of the right-angle nozzle at particle entrance B and the gas flow after 90° turning, so that the gas velocity in the expansion section of the nozzle is symmetrically distributed along the axial direction; particle entrance A and for the right-angle nozzle C, the coupling between the gas flow at the particle entrance and the gas flow after 90° turning is small, resulting in the high-velocity zone inside the nozzle located in the upper part of the nozzle expansion section, showing an asymmetric distribution, but as the right-angle nozzle expansion section as the length increases, the velocity distribution of the gas flow gradually becomes symmetrical, so at the end of the right-angle nozzle; due to the influence of the viscous boundary layer, the velocity near the inner wall of the nozzle is lower and

the velocity in the center area is larger.
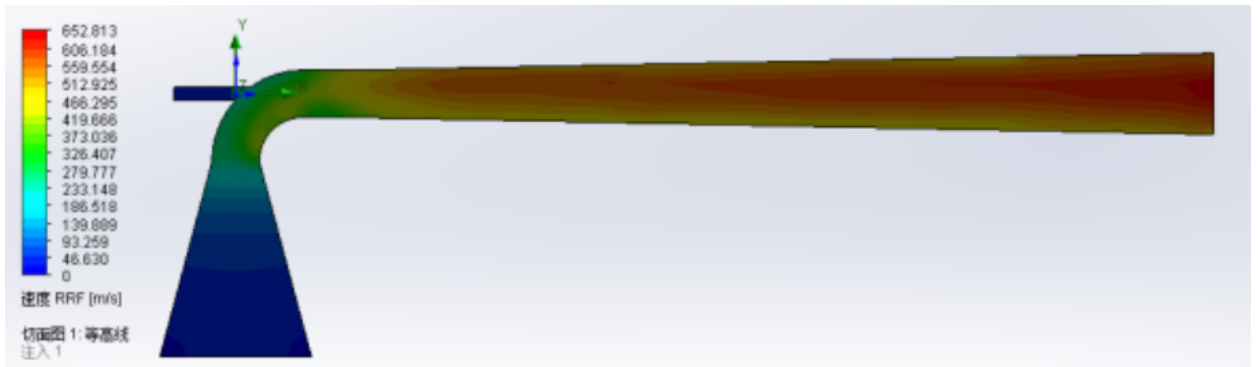
a
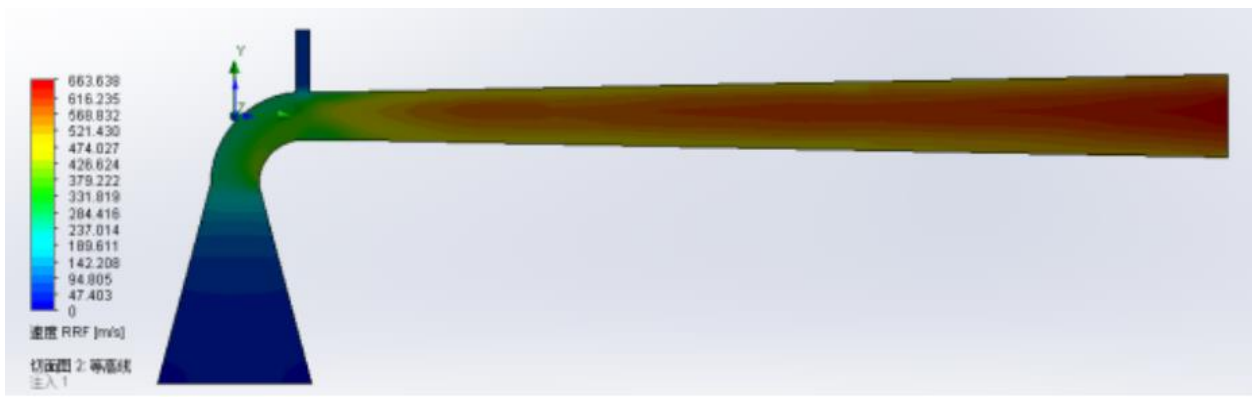
b
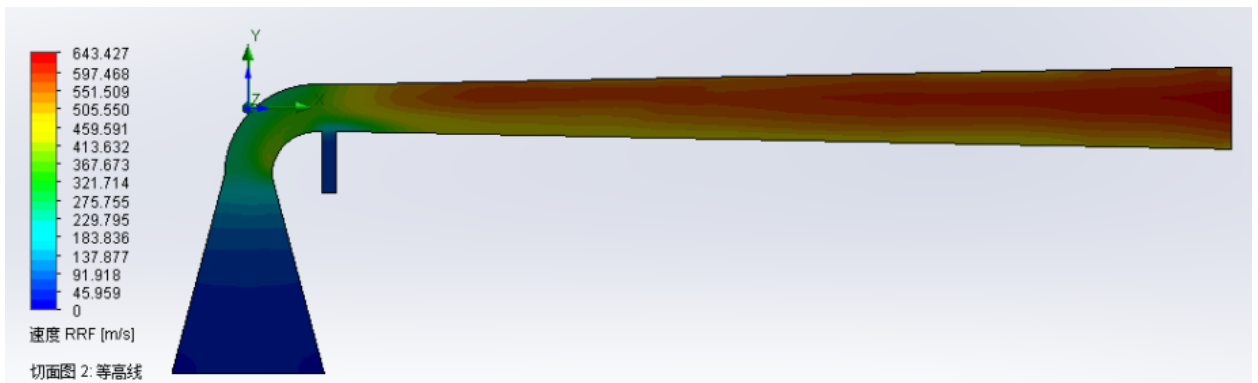
c

a − entrance A; *b* − entrance B; *c* − entrance C

Fig. 3.25. The velocity flow field cloud diagram inside the right-angle cold spray nozzle with different spray particle entrances

## 3.4.4 Analysis of particles velocity in single-channel circular right-angle nozzle

Figure 3.26 shows the velocity characteristic curves of five types of particles in right-angle nozzles with different entrances.
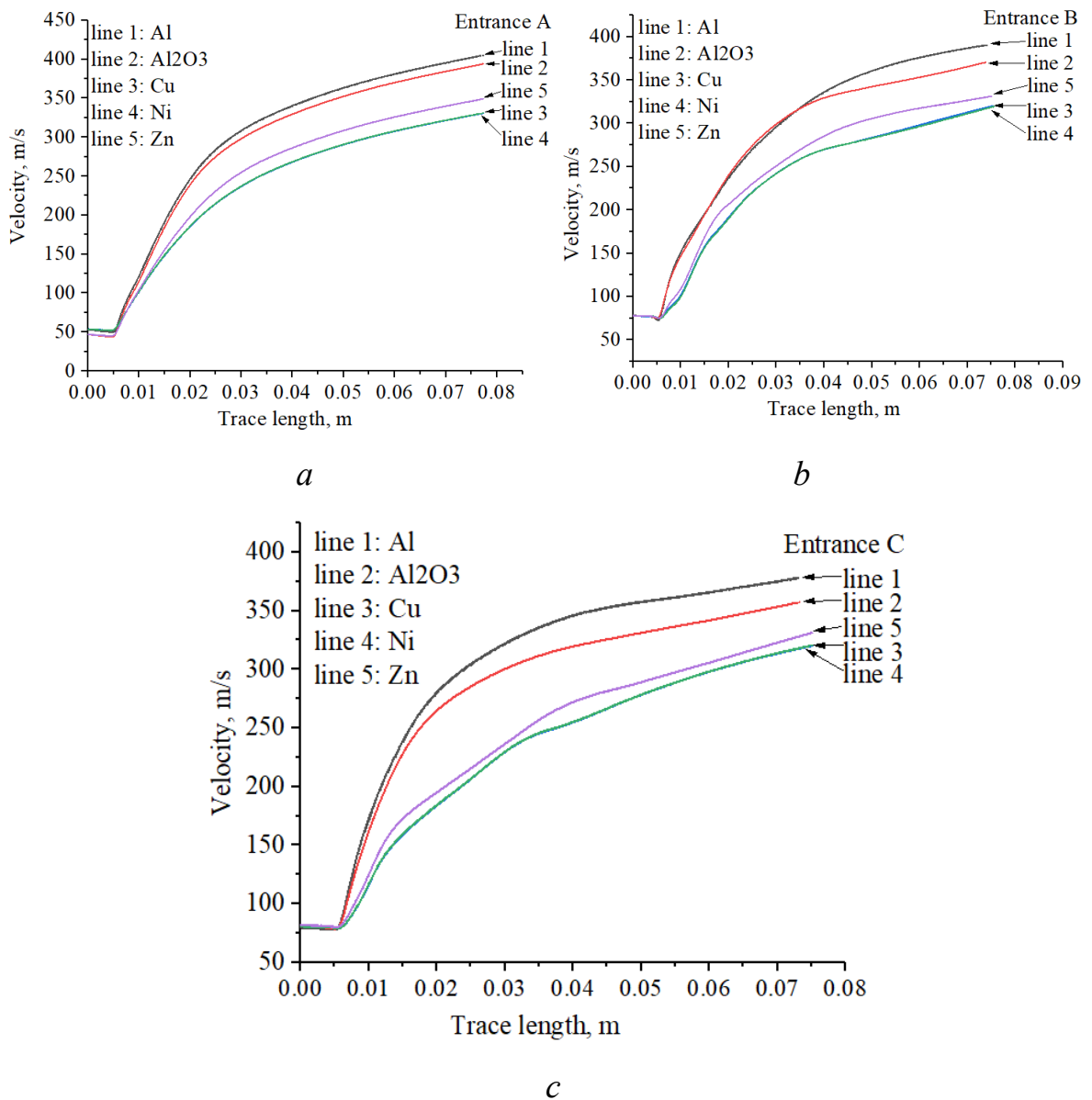
a – The entrance A; *b* – The entrance B; *c* – The entrance C

Fig. 3.26. The velocity characteristic curves of five types of particles in right-angle nozzles with different entrances

It can be seen from the Figure 3.26 that the five types of particles are accelerated in the right-angle nozzle until they flow out from the nozzle outlet. This is different from that in Figure 3.26 the results of the velocity flow field nephogram inside the right-angle nozzle are the same. The particles velocity is smaller than the gas velocity, because the acceleration of the particles in the right-angle nozzle is driven by the drag force of the high-velocity gas in the nozzle, This verifies the equation 2.35.

During the acceleration of the particles in the right-angle nozzle there is friction which satisfies Newton's second law. The velocity curves of the five types of particles in Figure 3.26 represent the acceleration of the particles. The particles move with decreasing acceleration in the right-angle nozzle. From the analysis of the smoothness of the curve, the right angle of the particle entrance A the velocity curve of the cold spray nozzle is relatively smooth, followed by the particle entrance B and C.

Under the same working conditions, the velocities of the five types of particles are different, which is determined by the physical properties of the particles themselves.

As shown in Figure 3.27, the velocity characteristic curves of five types of particles in right-angle nozzles with different particle entrances. It can be seen from Figure 3.27 that the particle entrance A right-angle nozzle has the best acceleration effect on the particle, and the particles velocity can reach the maximum value; because the particle entrance is located on the left side of the throat, which increases the acceleration time and distance of the particles, so that the particles are always accelerated when they reach the outlet of the right-angle nozzle. This is the expected result of the study; it shows that the expansion section of the right-angle nozzle has the length affects the time it takes for the particles to be accelerated, thus determining the maximum velocity of the particles in the right-angle nozzle.
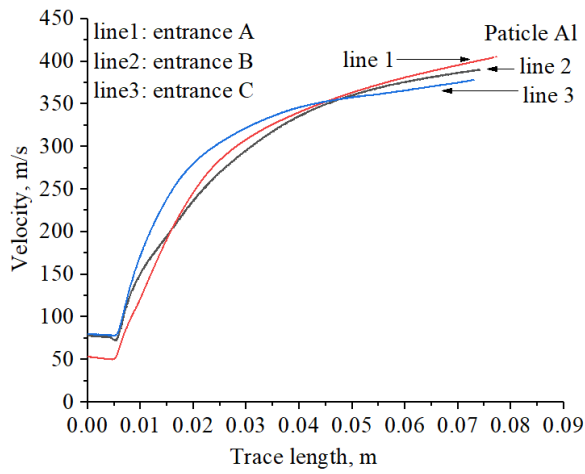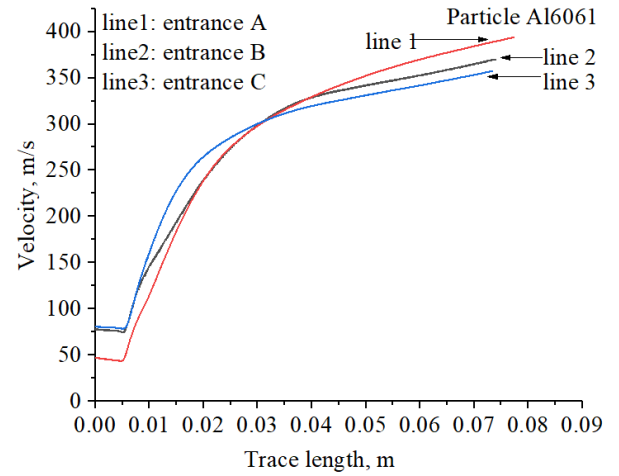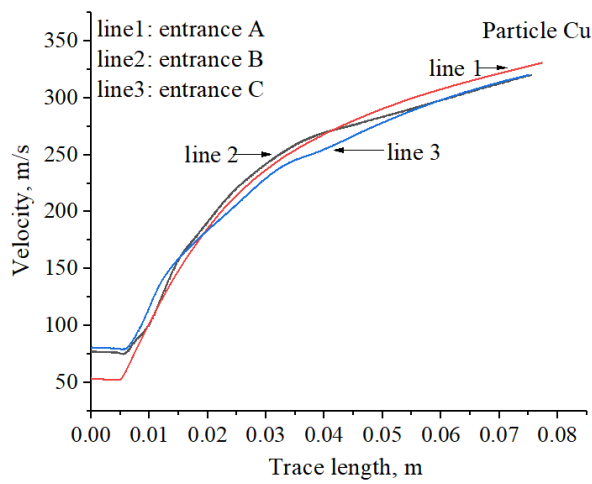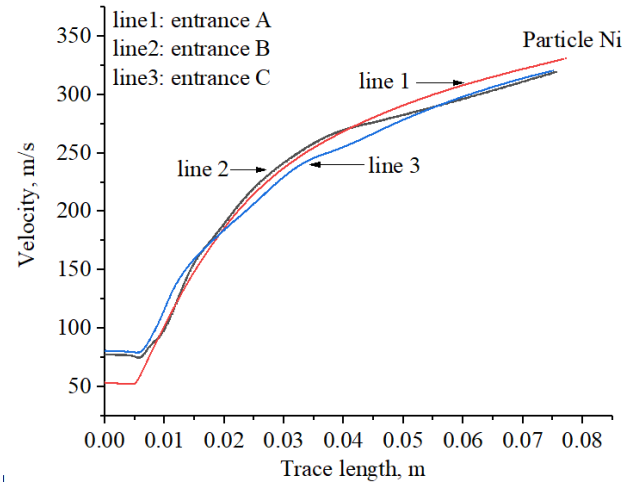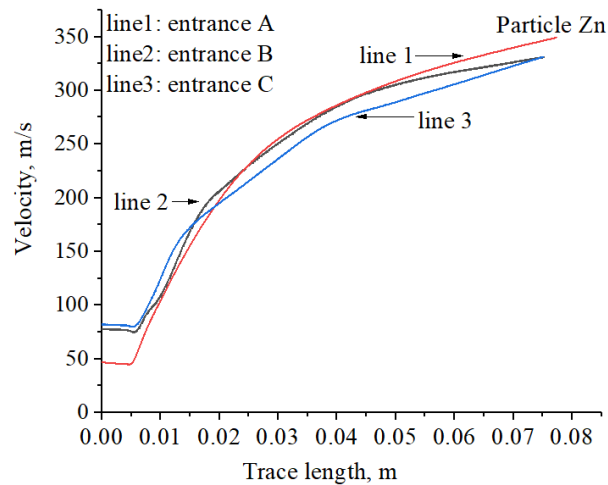
a − Al; b − Al6061; *c* − Cu; *d* − Ni; *e* − Zn

Fig. 3.27. The velocity characteristic curves of five types of particles in right-angle nozzles with different particle entrances

157

Figure 3.28 shows the accelerated flow trajectory of five types of particles in right-angle nozzles with different particle entrances.

a

b

c

d

e
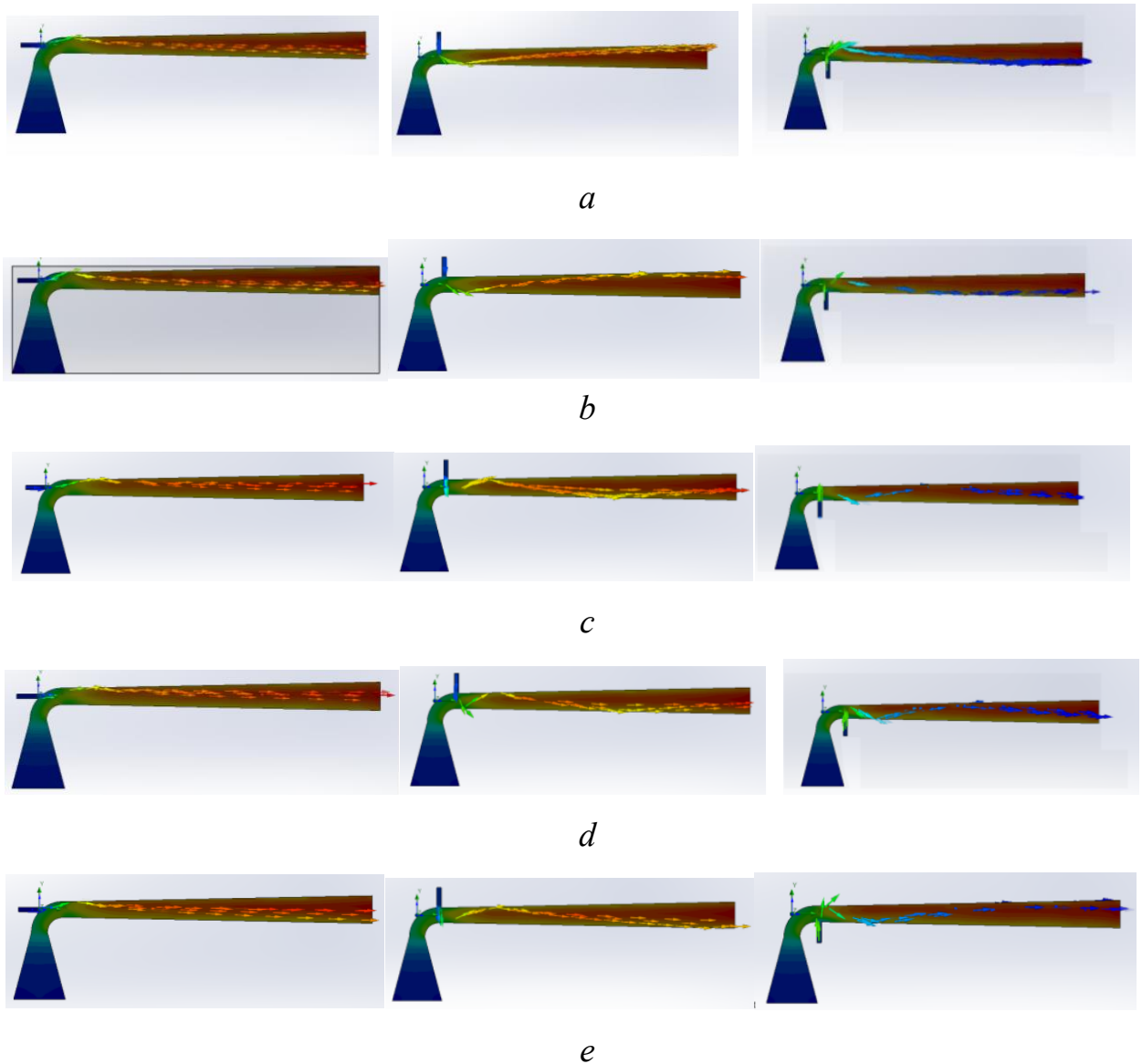
a − The Al particles flow trajectory; *b* − The Al6061 particles flow trajectory; *c* − The Cu particles flow trajectory; *d* − The Ni particles flow trajectory; *e* − The Zn particles flow trajectory

Fig. 3.28. Accelerated flow trajectory of five types of particles in right-angle nozzles with different particle entrances.

From Figure 3.28 it can be seen that the right-angle nozzle with particle entrance C has the worst acceleration effect on particles, and the location of the particles flowing out of the nozzle offset from the center of the nozzle outlet; the right-angle nozzle at particle entrance A and B has a better acceleration effect on particles. The outflow position of the particles is close to the center of the nozzle outlet.

However, according to the analysis of the flow of particles in the right-angle nozzle, the accelerated particles in the right-angle nozzle at the entrance B deposit multiple times on the inner wall of the right-angle nozzle, resulting in the loss of kinetic energy of the particles, which is detrimental to the acceleration of the particles; combined with the velocities of the five types of particles in the right-angle nozzle in Figure 3.28 analysis shows that it is better to choose the right-angle nozzle with particle entrance A.

3.4.5 Results and discussion

The exit center velocity of a circular nozzle with the same cross-section is greater than that of a rectangular nozzle; the viscous boundary layer effect is better and the effective flow area is larger, so the circular nozzle has a better effect than the rectangular nozzle. The maximum velocity of the gas flow near the exit of the right-angle nozzle at particle entrance A is 663.4 m/s. The five types of particles accelerate best in the right-angle nozzle at particle entrance A. The particle entrance A right-angle nozzle can effectively prevent particles from colliding inside the right-angle nozzle, thereby reducing the loss of kinetic energy during the acceleration of particles in the right-angle nozzle.

3.5 Research and analysis of multi-channel mixed cross-section right-angle cold spray nozzle

Single-channel axially symmetric cold spray nozzles are more common, but there are relatively few research works on multi-channel cold spray nozzles. Hu [34] and Dolmatov [161] studied multi-channel cold spray nozzles with rectangular cross-sections. The cold spray nozzle is mainly used to accelerate the particles, in which the study of the velocity and temperature of the particles before they deposition on the substrate is the most important.

This section studies the particle acceleration and heating characteristics of single-channel, dual-channel, and three-channel hybrid cross-section right-angle cold spray nozzles. The multi-channel mixed cross-section right-angle cold spray nozzle is a handheld cold spray device that solves the problem that some parts cannot be sprayed with long straight cold spray nozzles. Hu and Tan [34] verified the authenticity of this problem. The throat of the multi-channel hybrid cross-section right-angle cold spray nozzle is designed with a multi-channel right angle, so that the internal gas flow and particles can turn at the throat. The particles passing through the throat can achieve a $90°$ turn under the action of the carrier gas coupling force, and the particles continue to flow. Acceleration continues in the expansion section of the nozzle; a new multi-channel mixed cross-section right-angle cold spray nozzle is studied. By analyzing the particle injection position and combining the spray parameters (nitrogen pressure, temperature, and particle size), the acceleration after particle injection is and the influence of heating characteristics, ultimately achieving the spraying of a variety of materials.

For the convenience of description in this dissertation, the single-channel mixed cross-section right-angle cold spray nozzle is referred to as the single-channel nozzle; the double-channel mixed cross-section right-angle cold spray nozzle is referred to as the two-channel nozzle; the three-channel mixed cross-section right-angle cold spray nozzle is referred to as the three-channel nozzle.

3.5.1 Simulation method, material model and mixed cross-section right-angle cold nozzle model

3.5.1.1 Simulation and material models

SolidWorks simulation software was used to simulate and analyze the particle flow in single-channel and multi-channel mixed cross-section right-angle cold spray nozzles. Comparing the residual diagram, the $\kappa - \varepsilon$ turbulence model has a better convergence velocity; comparing the mass flow error, the $\kappa - \varepsilon$ turbulence model has the smallest mass flow error, so the turbulence model is used [17]; without considering wall slip and heat transfer, the $\kappa - \varepsilon$ turbulence intensity is 2% [17]; the carrier gas is nitrogen, the pressure inlet is 3 MPa-5 MPa, the pressure outlet is ambient atmospheric pressure, the initial temperature of nitrogen is 400 K-1200 K, the inlet of the convergence section is the pressure inlet, and the outlet of the expansion section is the pressure outlet.

The purpose of developing the multi-channel mixed cross-section right-angle cold spray nozzle is to achieve the spraying needs of a variety of particles; spraying particles Al, Al6061, Cu, Ni, Zn, Mg, and Al_2O_3; the materials are all spherical particles, and the particle size range is 10-40 um.

3.5.1.2 Hybrid cross-section right-angle cold spray nozzle

This section focuses on single-channel, dual-channel and three-channel mixed cross-section right-angle cold spray nozzles; for the research method of multi-channel right-angle cold spray nozzles refer to Hu [34], who also use computational fluid dynamics based on single-channel mixed cross-section right-angle cold spray nozzle further study on multi-channel mixed cross-section right-angle cold spray nozzle. Figure 3.29 shows a single-channel right-angle cold spray nozzle. The internal channel of the single-channel right-angle cold spray nozzle is composed of

four parts a cylindrical section, a contraction section, a throat, and an expansion section; the cross-sections of the cylindrical section and the expansion section are circles. The cross-section of the constriction section and throat is rectangular; the hybrid cross-section right-angle cold spray nozzle is a combination of rectangular cross-section and circular cross-section nozzle. The diameter of the cylindrical section is 11.5 mm, the curvature of the lower part of the contraction section is 97 mm, the thickness of the contraction section and the throat is 3.5 mm, the turning radius of the throat is 6mm, and the exit diameter of the expansion section is 6.06 mm.

B: Contraction section cross-sectional: rectangular

C: Throat cross-sectional: rectangular

A: Cylindrical section cross-sectional: circle

D: Expansion section cross-sectional:circle
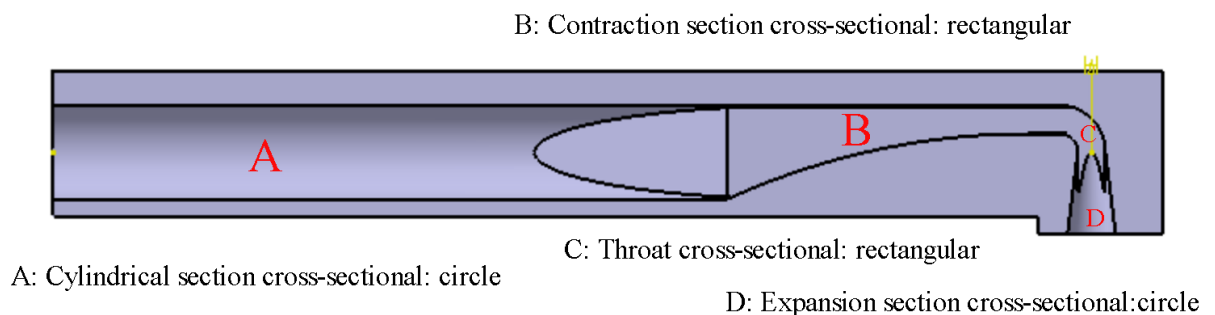
Fig. 3.29. Single-channel mixed cross-section right-angle cold spray nozzle

3.5.2 Single-channel mixed cross-section right-angle cold spray nozzle

The analysis shows that it is more reasonable for the particle inlet of the single-channel mixed cross-section right-angle cold spray nozzle to be located outside the turning part of the throat; as shown in Figure 3.30(a), it is a spherical Al_2O_3 with an inlet pressure of 3 MPa, an initial temperature of 700 K, and a particle size of 40 um. Flow conditions inside the nozzle. It can be seen from the Figure 3.30(a) that the Al_2O_3 particles do not deposit with the inner wall of the nozzle, which is related to the position and angle of injection of Al_2O_3 particles; the velocity V1 of particle Al_2O_3 injection and the nitrogen flow velocity V2 are acute angles, so the velocity of particle Al_2O_3 in the expansion section of the nozzle is the resultant speed is V3,

162

as shown in Figure 3.30(b). The position of the Al_2O_3 particle inlet is located outside the turning part of the throat and very close to the expansion section of the nozzle. The particles are accelerated by nitrogen, and the high-temperature nitrogen can heat the particles. The temperature of the particles has a greater impact on the deposition process and coating performance [173], by studying the location of the particle inlet, thereby increasing the heating time of the nitrogen gas to the particles. Therefore, the single-channel mixed cross-section right-angle cold spray nozzle cannot fully heat the particles, and the position of the Al_2O_3 particle inlet is not conducive to later actual operations.
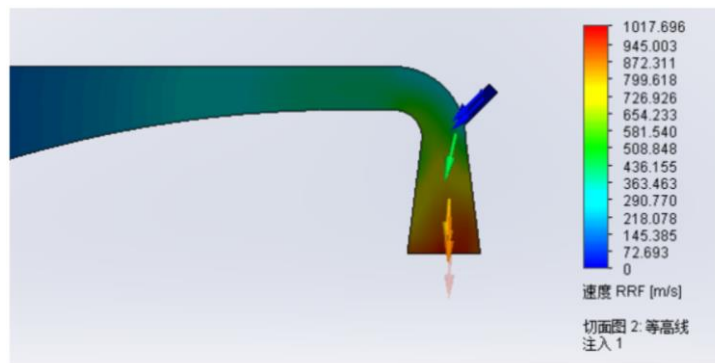
a
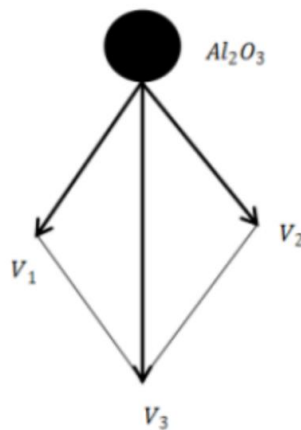
b

a − the flow of in the nozzle; *b* − the velocity analysis of Al_2O_3 particles in the nozzle

Fig. 3.30. Simulation of single-channel mixed cross-section right-angle cold spray nozzle

3.5.3 The Multi-channel mixed cross-section right-angle nozzle

Figure 3.31 shows a double-channel mixed cross-section right-angle cold spray nozzle. Block A at the throat of the nozzle divides the nozzle throat into channel A and channel B; combined with the design experience of a single-channel mixed cross-section right-angle cold spray nozzle , locating the spray particle inlet of the double-channel mixed cross-section right-angle cold spray nozzle inside the connection between the throat and the contraction section can increase the heating time of the nitrogen gas to the particles; expand the multi-channel mixed cross-section right-angle cold spray nozzle the expansion length is set to 25 mm to ensure that the particles have sufficient deposition speed before depositing on the substrate.
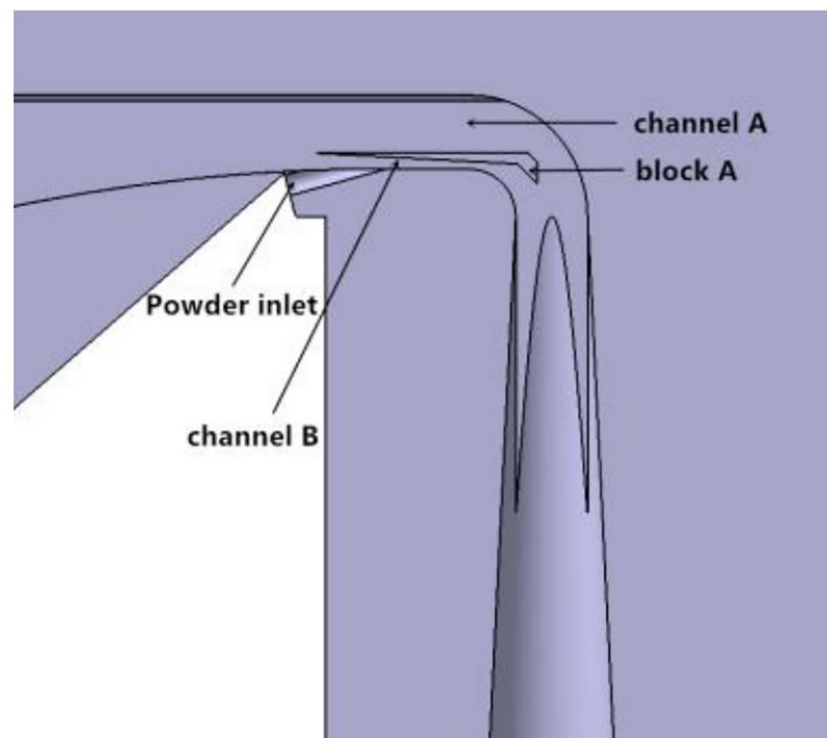

Fig. 3.31. The double-channel mixed cross-section right-angle cold spray nozzle.

As shown in Figure 3.32, the inlet pressure is 5 MPa, the initial temperature is 600 K, and the flow conditions of Al_2O_3, Al and Cu particles of different particle

sizes inside the double-channel mixed cross-section right-angle cold spray nozzle.
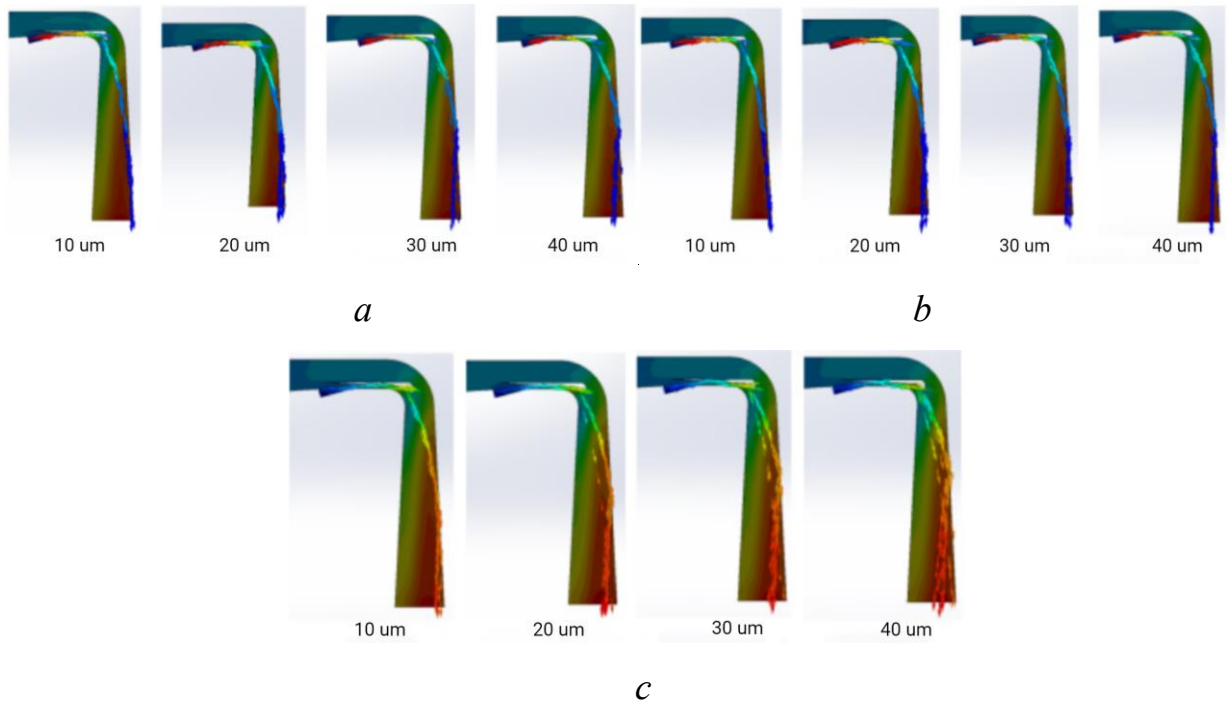
a − The Al_2O_3 particles flow trajectory; b –The Al particles flow trajectory; c –
The Cu particles flow trajectory

Fig. 3.32. The flow trajectory of Al_2O_3, Al, and Cu particles of different sizes (10-30 um) in the double-channel nozzle.

It can be seen from Figure 3.32 that all three types of particles collide with the inner wall of the expansion section of the nozzle. The particles will decelerate during the deposition, which is detrimental to spraying. When the particles enter channel B from the injection port, the particles collide with the inner wall of channel B of the nozzle. deposition occurs because the direction of particle injection is at an angle to the direction of gas flow; deposition of spray particles in channel B is unavoidable, but particle depositions on the inner wall of the expansion section of the nozzle should be minimized. The main acceleration stage of particles is in the expansion section of the nozzle, otherwise it will affect particle acceleration.

It can be seen from Figure 3.32 that under the same working conditions, as the particle size increases, the earlier the particle hits the inner wall of the nozzle

expansion section; because the larger the particle size, the larger the particle surface area, the greater the resistance encountered during the particle acceleration process. Large, indicating that particle size is also an important factor affecting particle acceleration. In the expansion section of the nozzle, the high-velocity gas area is biased to the right side of the expansion section, showing an asymmetric distribution along the axial direction of the expansion section.

Figure 3.33 shows the velocity analysis of particles just entering the expansion section of the double-channel nozzle. The nitrogen velocity is V_2, and the initial particles velocity entering the expansion section is V_1. Therefore, the actual velocity of particles in the nozzle is V_3, but the velocity direction of V_3 it is not along the axial direction of the nozzle expansion section, so the particles will hit the inner wall of the expansion section during acceleration. From a theoretical analysis, the target velocity of particles in the expansion section of the nozzle is V_3^*, so it is necessary to ensure that the carrier gas velocity is V_2^*, so that the particles will not collide with the inside of the nozzle during the acceleration process in the expansion section.
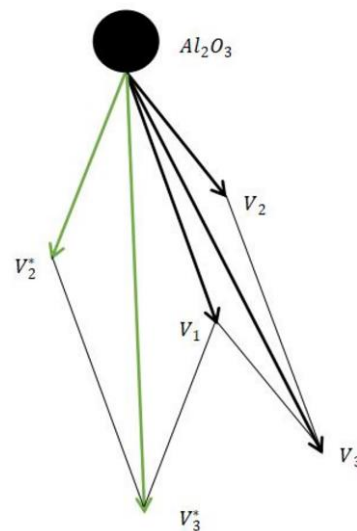

Fig. 3.33. Velocity analysis of particles just entering the expansion section

In order to ensure that the particles will not collide with the inner wall of the nozzle expansion section during acceleration, block B is added on the basis of the

166

double-channel mixed type cross-section right-angle cold spray nozzle. The block B at the nozzle throat divides the nozzle throat into channel B and channel C, as shown in Figure 3.34, are the specific parameters of the optimized three-channel mixed cross-section right-angle cold spray nozzle and throat channel. After the particles are accelerated in channel A, they merge with the nitrogen coming in from channel B, thereby changing the velocity direction of the particles, ensuring that the particles will not collide with the inner wall of the nozzle expansion section, and completing the acceleration of the particles in the nozzle.
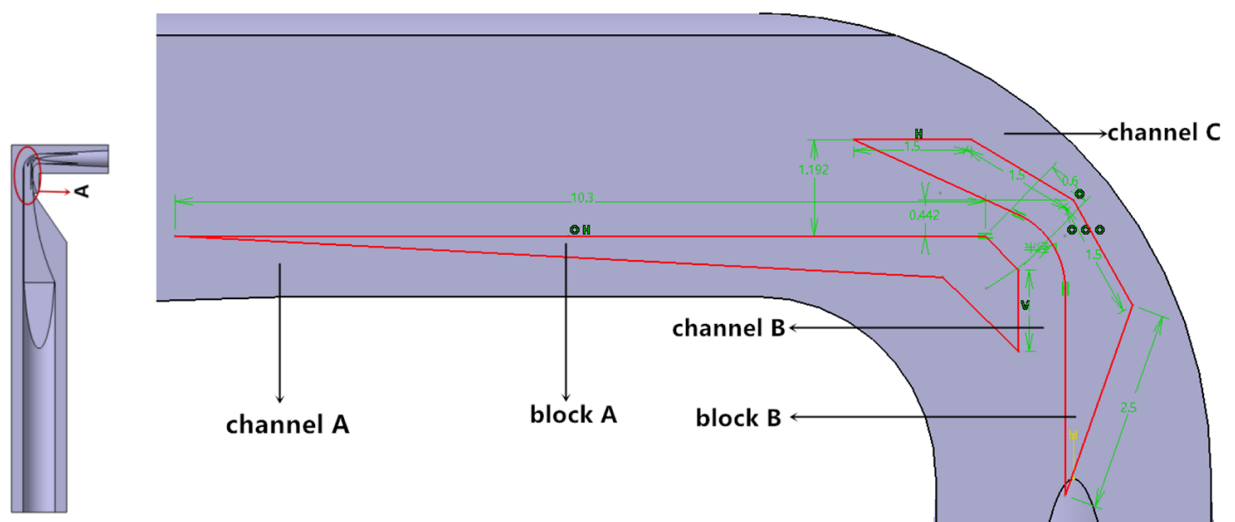

Fig. 3.34. The specific parameters of the three-channel mixed cross-section right-angle cold spray nozzle and throat channel

The Al_2O_3 particles with particle sizes of 10um, 20um, and 30um were simulated and analyzed in a three-channel mixed cross-section right-angle cold spray nozzle. The temperature range is 800 K - 1000 K, the gas pressure range is 3-5 MPa, and the spraying distance is 20 mm. It is obtained that the velocity of Al_2O_3 particles before reaching the substrate/coating, as shown in Table 3.21.

Table. 3.21 − The velocity before the Al_2O_3 particles reach the substrate under different working conditions

N_2 Pressure / MPa	N_2 Temperature/ K	Powder size /um	Velocity/ m/s
3	800	10	551.691
		20	454.704
		30	402.650
	900	10	584.719
		20	477.986
		30	420.891
	1000	10	607.147
		20	493.696
		30	433.343
4	800	10	576.308
		20	479.043
		30	430.683
	900	10	603.584
		20	498.367
		30	446.833
	1000	10	624.004
		20	507.352
		30	455.895
5	800	10	597.075
		20	502.665
		30	450.424
	900	10	625.237
		20	522.341
		30	466.143
	1000	10	652.233
		20	590.753
		30	483.301

It can be seen from Table 3.21 that nitrogen pressure, temperature, and particle size of Al_2O_3 particles will all affect the particle velocity Al_2O_3 in the nozzle; Alhulaifi [174] scholars also reached the same conclusion. The contribution rate of influencing factors to the objective function can be studied using RSM, and the contribution rate of each influencing factor can be obtained. From Table 3.21, it can be seen that the impact of Al_2O_3 particle size on velocity is greater than the pressure and temperature of nitrogen, so it is recommended to choose particle size. Al_2O_3

particles with diameters of 10 um and 20 um.

Figure 3.35 shows the flow trajectory conditions of 10 um and 20 um Al_2O_3 particles inside the expansion section of the nozzle under different working conditions.
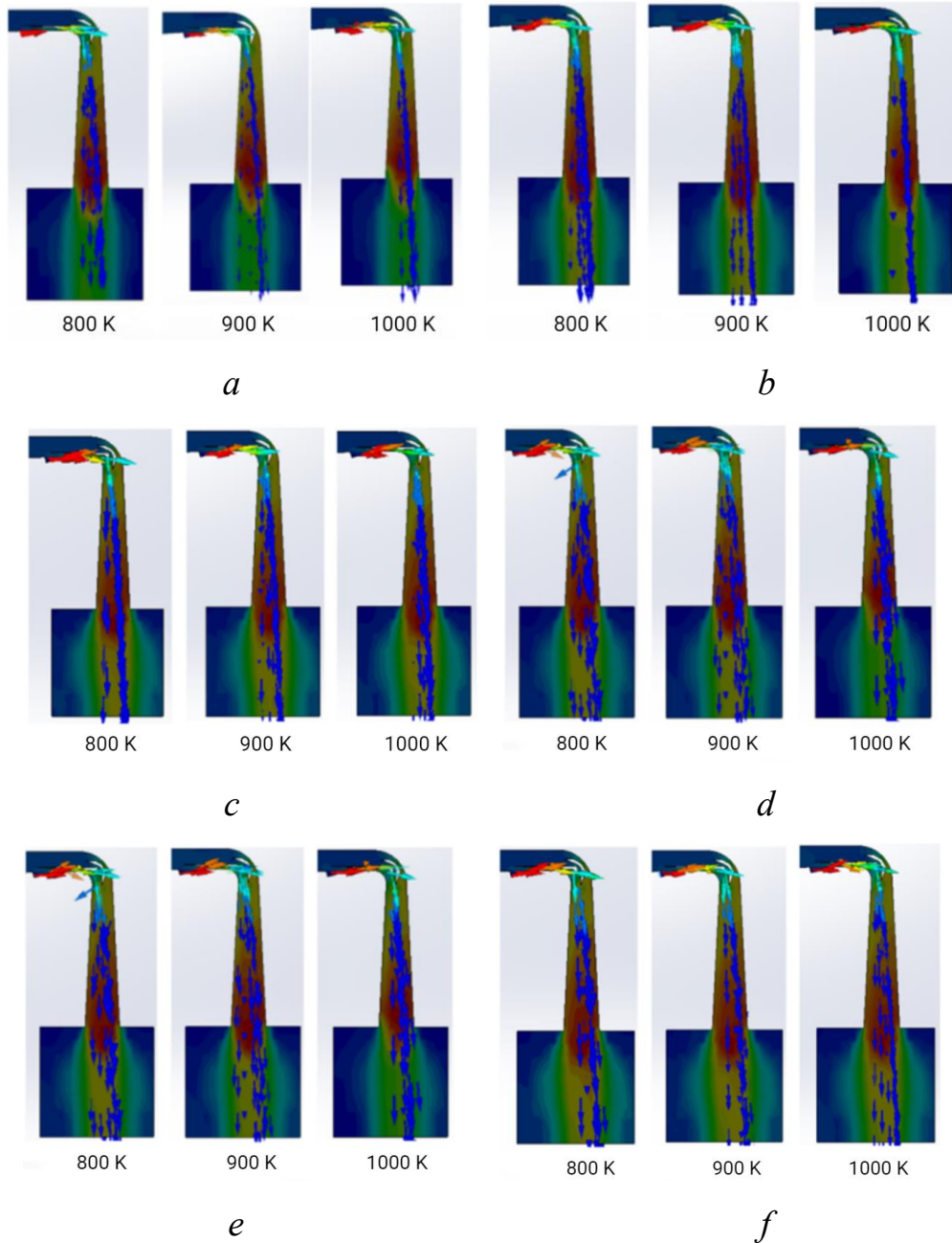
a – 10 um, 3 MPa; b –10 um, 4 MPa; c – 10 um, 5 MPa; d – 20 um, 3 MPa; e – 20um, 4 MPa; f – 20 um, 5 MPa

Fig. 3.35. Al_2O_3 particles flow trajectory in the nozzle throat and expansion section under different working conditions.

It can be seen from Figure 3.35 that the three-channel mixed cross-section right-angle cold spray nozzle can ensure that all Al_2O_3 particles can be smoothly ejected from the exit of the nozzle, the Al_2O_3 particles will not collide during the acceleration process inside the expansion section of the nozzle; the vast majority of Al_2O_3 particles flow out from the velocity center area at the exit of the expansion section, ensuring that the Al_2O_3 particles are in the best acceleration state; the velocity flow field in the expansion section of the three-channel mixed cross-section right-angle cold spray nozzle is symmetrically distributed along the axial direction; adding channel B can improve the recovery coefficient (H) of Al_2O_3 particles in the three-channel mixed cross-section right-angle cold spray nozzle, the nitrogen flow of channel B can slightly adjust the outflow direction of the particles coming from channel A, thereby improving the utilization rate of Al_2O_3 particles in the spraying process and better economy.

3.5.4 The velocity and temperature analysis of particles in the three-channel nozzle

The critical velocity of particles is the main indicator that determines whether the particles can be deposited on the substrate; the critical velocity is related to the material properties and temperature; the critical velocity calculation equations 3.13 and 3.14 can be used to calculate the particle velocity. The critical velocity of materials Al, Al6061, Cu, Ni, Zn, and Mg at different temperatures; the critical velocity of some materials are referred to [173, 175] as shown in Table 3.22.

$$V_{Critical} = \sqrt{C_p(0.7 \cdot T_m - T_i)}; \tag{3.13}$$

$$V_{Critical} = \sqrt{\frac{F_1 \cdot 4 \cdot \sigma_{TS} \cdot \left(1 - \frac{T_i - T_r}{T_m - T_r}\right)}{\rho} + F_2 \cdot C_p(T_m - T_i)}, \tag{3.14}$$

where C_p – the specific heat;

   T_m – the melting point;

   T_i – impact temperature;

   $F_1 = 3.8$，$F_2 = 0.3$;

   ρ – the particle density;

   σ_{TS} – the tensile strength;

   T_r – the reference temperature (293 K).

Table. 3.22 – The velocity and temperature parameters of different particles before they deposit on the substrate after being accelerated by three-channel nozzle.

Particles	Temperature / K	400	500	600	700	800	900	1000	1100	1200
Al_2O_3	V_{max} /m/s	437	489	532	566	597	625	652	677	701
	T_{impact} / K	366	437	507	579	651	724	797	873	944
Ni	V_{max} /m/s	-	-	-	-	-	-	546	569	582
	$V_{critical}$ /m/s	-	-	-	-	-	-	574	564	552
	T_{impact} / K		-	-	-	-	-	796	874	950
Cu	V_{max} /m/s	-	-	456	481	504	-	-	-	-
	$V_{critical}$ /m/s	-	-	480	467	452	-	-	-	-
	T_{impact} / K	-	-	510	582	655	-	-	-	-
Mg	V_{max} /m/s	487	547	602	644	-	-	-	-	-
	$V_{critical}$ /m/s	630	600	570	540	-	-	-	-	-
	T_{impact} / K	368	441	513	586	-	-	-	-	-
Al	V_{max} /m/s	462	518	568	-	-	-	-	-	-
	$V_{critical}$ /m/s	570	544	517	-	-	-	-	-	-
	T_{impact} / K	367	439	510	-	-	-	-	-	-
Al6061	V_{max} /m/s	-	585	625	647	671	-	-	-	-
	$V_{critical}$ /m/s	-	573	557	541	532	-	-	-	-
	T_{impact} / K	-	410	526	639	756	-	-	-	-
Zn	V_{max} /m/s	398	443	-	-	-	-	-	-	-
	$V_{critical}$ /m/s	299	274	-	-	-	-	-	-	-
	T_{impact} / K	368	441	-	-	-	-	-	-	-

where V_{max} – Maximum velocity before the particle deposited on the substrate;

   $V_{critical}$ – Critical velocity of powder deposition;

   T_{impact} – Maximum temperature before the particle deposited on the

substrate.

The critical velocity of Zn particles is very low. When the temperature is 400 K, the critical velocity is 299 m/s; when the temperature is 500K, the critical velocity is 274 m/s; therefore, the deposition of Zn particles on the substrate is easy to achieve, which is caused by the Zn particles. The physical properties of Zn determine that when the temperature is greater than 500 K, Zn particles will become soft, which is beneficial to deposition.

Al particles are easy to obtain, low density, high ductility, and good corrosion resistance, making them the most common raw material in cold spraying; Al particle is a very easy material to deposit when the temperature is 400 K-600 K , the deposition velocity of Al particles ranges from 517-570 m/s, and the melting point of Al particle is 900 K, so the temperature of nitrogen does not need to be too high to achieve deposition on the substrate; research shows that some relatively minor problems appear on the surface of pure Al coatings. Shallow craters with smooth edges indicate that the surface roughness of the pure Al coating is large [176], the porosity is high, the hardness is low, and the wear resistance is poor, which seriously restricts the application of cold spray Al coatings [177].

The critical velocity of Mg particles is higher than that of Zn particles and Al particles when the temperature is 400 -600 K, the critical velocity of Mg particles is 629 - 573 m/s.

The deposition of Ni particles is more difficult. When the temperature is 1100 K, the critical velocity is 564 m/s; when the temperature is 1200 K, the critical velocity is 552 m/s; Ni is a high-temperature resistant material and has high hardness, so the deposition of Ni particles is relatively difficult; Ni particles require higher carrier gas (nitrogen, helium) temperature.

The influence of ceramic Al_2O_3 on the relative coating performance [178, 179], Analyzed the acceleration characteristics of Al_2O_3 in the three-channel nozzle has important guidance and reference significance; Through calculation and

analysis, it can be known that the melting point of Al_2O_3 is very high, so the critical velocity of Al_2O_3 is very large, so it is difficult to deposit Al_2O_3 particles; Continue to spray Al_2O_3 particles on the pure Al coating with higher roughness and higher porosity, so as to reduce the porosity and roughness of the pure Al coating surface [176]; Therefore, Al_2O_3 particles can be used as a spray material for tamped and strengthened coating, and the velocity before the deposition with the coating is guaranteed to be greater than 590 m/s.

As shown in Table 3.22, the nitrogen pressure is 5 MPa, the particle size is 10um, and the spraying distance is 20 um. The velocity and temperature parameters of the particles before they deposited on the substrate after being accelerated through the three-channel mixed cross-section right-angle cold spray nozzle. It can be seen from the parameters in Table 3.22 that the critical velocity is related to the physical properties of the particles, and is also related to the temperature of the nitrogen. The higher the temperature, the smaller the critical velocity; the criterion for determining whether the particles can be deposited is the velocity when the particles reach the substrate greater than the critical velocity of the particles; increasing the temperature of nitrogen can increase the velocity of the particles before they reach the substrate, indicating that increasing the temperature is beneficial to the deposition of particles on the substrate.

It can be seen from Table 3.22 that the five types of particles are accelerated and heated in the three-channel mixed cross-section right-angle cold spray nozzle; nitrogen at the same temperature, the heating effect of the particle is similar; comparing the temperature of the particles before they reach the substrate/coating, it shows the particles have been heated during the acceleration process in the nozzle, which will be beneficial to the deposition process of the particles.

Combining the physical properties of Al_2O_3 particles, it can be seen that Al_2O_3 particles are a very good material for consolidating coatings; through numerical simulation, the nitrogen temperature is 400 - 1200 K, and the speed of Al_2O_3 particles before reaching the substrate/coating is 437 - 701 m/s, which can

suitable for the compaction of Cu, Mg, Al, Al6061, and Zn coatings. The simulation results show that the three-channel mixed cross-section right-angle cold spray nozzle can deposit a variety of materials on the substrate.

3.5.5 Results and discussion

This section discusses analyzes and demonstrates the structures of single-channel and multi-channel mixed cross-section right-angle cold spray nozzles. The research results show that the three-channel mixed cross-section right-angle cold spray nozzle is feasible; the influence of spray parameters (nitrogen pressure, temperature, and particle size) on the acceleration and heating characteristics after particle injection is analyzed.

The three-channel nozzle has better heating characteristics than the single-channel nozzle; it has better acceleration characteristics and particle utilization efficiency than the double-channel nozzle, and the velocity flow field in the expansion section is more uniformly distributed along the axial direction.

Particle size has the greatest contribution to particle velocity; The position where particles collide with the inner wall of the expansion section is related to the particle size. The larger the particle size, the earlier the particle will hit the inner wall of the nozzle expansion section. The particle size is proportional to the resistance it receives.

The three-channel nozzle can correct the velocity direction of the particles that are partially resisted by flowing inside the nozzle, thereby ensuring that the particles will not collide with the inner wall of the expansion section during the acceleration process of the expansion section, and the particles that are subject to resistance will all exit from the exit of the expansion section. The velocity center area flows out, thereby improving the utilization of the resistance received during the spraying process.

The three-channel mixed cross-section right-angle cold spray nozzle can realize

the deposition of a variety of granular materials (Al, Al6061, Cu, Mg, and Zn) on the substrate; it can also achieve the velocity conditions required for the compaction of the coating by the particles Al_2O_3. At the same time, the three-channel mixed cross-section right-angle cold spray nozzle is suitable for spraying in tight spaces. It has the characteristics of small expansion section length and simple operation.

This section focuses on the acceleration and heating characteristics of commonly used particles in a three-channel mixed cross-section right-angle cold spray nozzle; later analysis of the velocity characteristics of particles turning in the throat and the impact of the chamfering of the edges of block A and B on the throat on the nitrogen flow field and the influence of the acceleration characteristics of sprayed powder, a multi-factor coupling effect was established to improve the three-channel mixed cross-section right-angle cold spray nozzle.

3.6 Conclusion for the Chapter 3

This chapter mainly analyzes traditional nozzles, single-channel and multi-channel right-angle nozzles. The existing nozzle is analyzed and studied by introducing single factor optimization method and multi-factor coupling optimization method.

1) From the single factor analysis, it is concluded that the length of the expansion section of the Dymet Laval nozzle is one of the key factors affecting the exit velocity of Al particles; by increasing the length of the expansion section of the nozzle, a better acceleration effect of Al particles can be ensured, thereby to achieve the requirements of deposition on the substrate; the joints of the nozzle expansion sections are rounded to make the gas in the nozzle more uniform in the acceleration process.

2) In multi-factor analysis, spraying parameters are optimized by introducing the RSM and the BPNN optimization based on GA.

The RSM was used to analyze and study the influence of spraying parameters

on the optimal velocity of Al and Cu particles at the exit of the nozzle and the velocity before reaching the substrate. And obtain the optimal spraying parameters of Al and Cu particles; by studying the gas temperature, gas pressure, and particle size on the acceleration weight ratio of Al and Cu particles in the nozzle. The velocity of Al particles at the exit of the nozzle and the velocity when they reach the surface of the substrate have the greatest influence on the particle size. The biggest influence on the velocity of Cu particles at the nozzle outlet is the particle size, and the biggest influence on the velocity of Cu particles when they reach the substrate surface is the gas pressure.

The spraying parameters of Al6061 and Cu particles were optimized based on GA optimization BPNN. By establishing a multi-technical parameter network 3-8-1 structural model, the velocity of particles at the outlet of the right-angle nozzle can be accurately predicted. It is concluded that the combination parameters of Cu and Al6061 particles and the optimal velocity of the right-angle nozzle outlet are 520.71 m/s and 571.23 m/s respectively.

3) In the study of right-angle nozzles, the circular nozzle at the nozzle outlet has better effect than the rectangular nozzle; the outlet center velocity of the circular nozzle with the same throat section is greater than that of the rectangular nozzle; and the viscous boundary layer effect is better, the effective circulation area is larger. The maximum velocity of the airflow near the exit of the right-angle nozzle at particle inlet A is 663.4 m/s, and has the best acceleration effect on particles. It can effectively avoid particle depositions inside the right-angle nozzle, thereby reducing the acceleration process of particles in the right-angle nozzle loss of medium kinetic energy.

4) In the study of multi-channel right-angle nozzles, the three-channel nozzle has better heating characteristics than the single-channel nozzle, better acceleration characteristics and particle utilization efficiency than the two-channel nozzle, and the expansion section of the three-channel nozzle The velocity flow field is more uniformly distributed along the axial direction; during the acceleration of particles

in the three-channel nozzle, the particle size has the greatest contribution to particle acceleration. The three-channel right-angle nozzle can deposit a variety of particulate materials (Al, Al6061, Cu, Mg, and Zn) on the substrate; It can also achieve the velocity conditions required for particle compaction coating.

CHAPTER 4

CALCULATION METHOD AND RESEARCH ON THE HIGH-VELOCITY DEPOSITION PROCESS BETWEEN PARTICLES AND SUBSTRATE

4.1 Analysis of single particle deposition model method

This section uses the ALE, the SPH, and CEL methods to simulate the deposition of Al6061 particles on the Al6061 substrate. By studying the effects of particle temperature and substrate temperature on deformation during deposition. And compare the above three methods. The CEL method was then used to simulate the impact of the temperature of the particles and the substrate on the deposition process of Al6061 particles of different particle sizes.

4.1.1 Simulate the influence of particle temperature on deposition based on the ALE, the SPH, and CEL methods

4.1.1.1 Simulation of single particle deposition based on the ALE method

The ALE method is used to simulate the single particle deposition process for solution, in which the deposition model between the particles and the substrate is a two-dimensional model. In order to reduce calculation time and ensure calculation accuracy, some scholars choose a planar axisymmetric model. To uses a full-scale deposition model in order to better characterize the impact of particle temperature on the deposition process. To uses spherical particles with a particle size of 20 um. Both the particles and the matrix adopt uniform and fine quadrilateral meshes, and the bottom of the matrix adopts fixed constraints; the initial temperature of the substrate is 400 K; the initial velocity of the particles is 585 m/s; the particle

temperature 400 - 700 K.

As shown in Figure 4.1 shows a single particle deposition model using the two-dimensional ALE method; the grid size of the deposition area of the substrate and the grid size of the particles are 1um; the grid size of the non-deposition area on the substrate can be 2 um. During the numerical simulation process, when the grid is refined to a certain extent, the Lagrangian grid will be excessively distorted during the deposition between the particles and the substrate, causing the calculation program to terminate, resulting in the inability to continue the simulation process. This is consistent with the results described in Chapter 1.6 and Chapter 3.2. Although mesh refinement can improve the accuracy of simulation, mesh distortion will cause the calculation results to terminate or reduce the calculation accuracy.
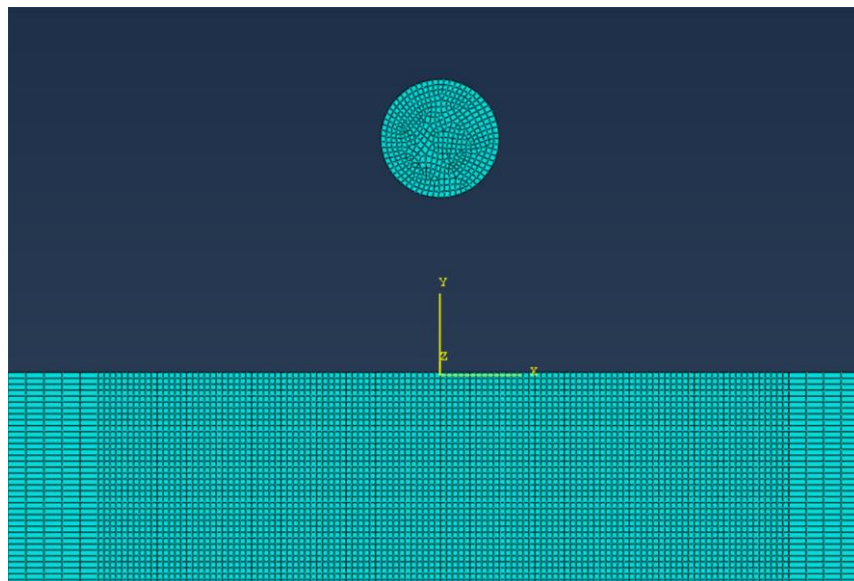

Fig. 4.1. The single particle deposition model using the two-dimensional the ALE method

Figure 4.2 shows the deformation diagram of a single particle simulated by the ALE method after hitting the Al6061 substrate at a temperature of 400 -700 K; the initial temperature of the substrate is 400 K; the initial velocity of the particle is 585 m/s; and the particle temperature range is 400-700 K.
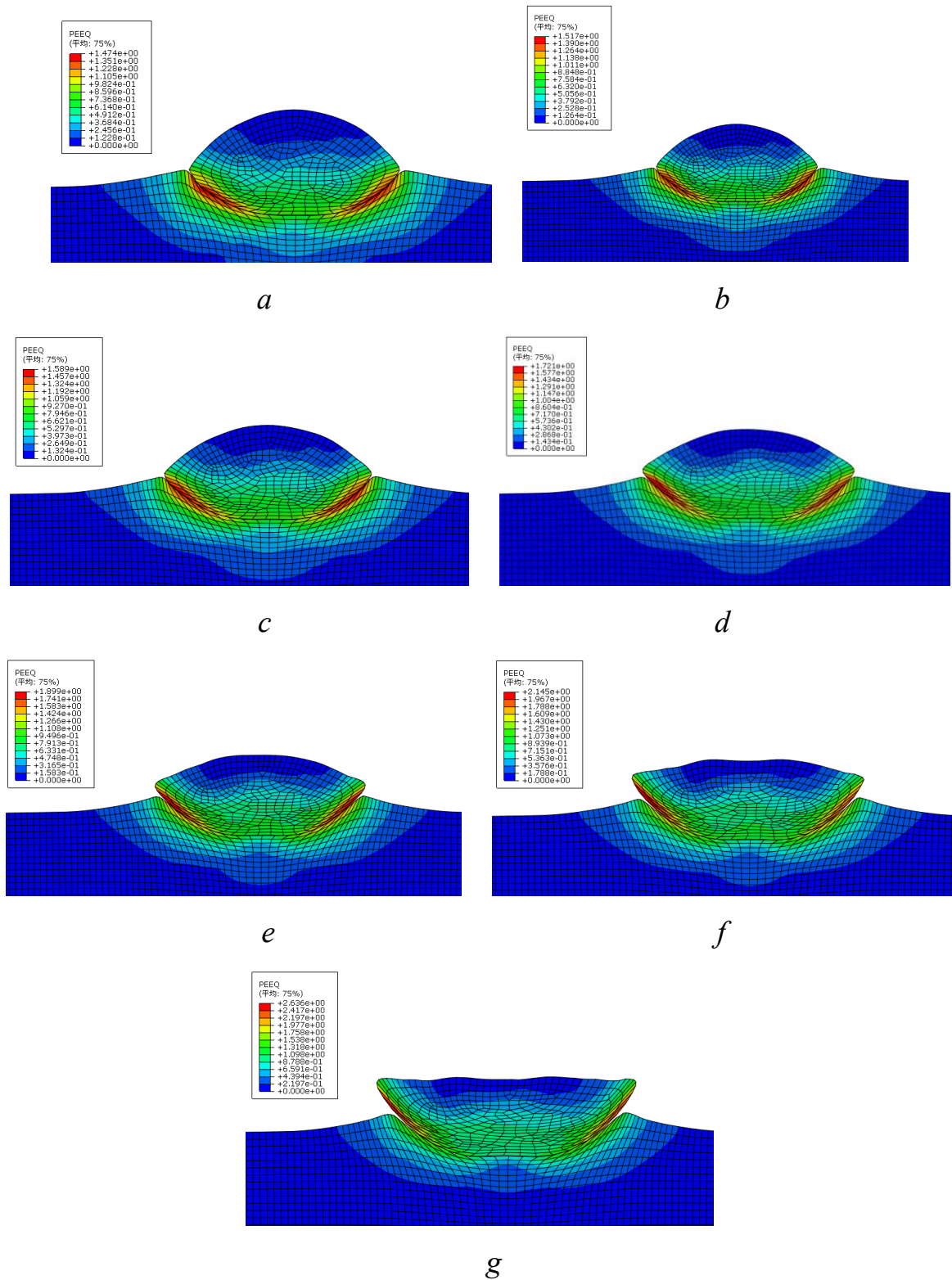
a – particle temperature 400 K; *b* – particle temperature 450 K; *c* – particle

temperature 500 K; *d* – particle temperature 550 K; *e* – particle temperature 600 K;

f – particle temperature 650 K; *g* –particle temperature 700 K

Fig. 4.2. The ALE method simulates the deformation diagram of a single particle

after deposited on the Al6061 substrate at a temperature of 400 - 700 K

It can be seen from Figure 4.2 that during the single particle deposition process, increasing the particle temperature can accelerate the softening of the particles and is conducive to deposition; especially when the particle temperature reaches above 600 K; and when the particle temperature reaches 700 K, the particles will splash during the impact process shooting trend. Hu and Tan [97] proposed the coefficient Y; Y is used to characterize the degree of particle deformation during the deposition process. The larger the Y value, the smaller the height of the particles after deformation, and the deeper the depth of the foundation pit. Increasing the temperature of the particles can increase the value of Y; it can be clearly seen in Figure 4.2 that the deformation degree of the particles is significantly greater than the deformation degree of the substrate, because the initial temperature of the substrate is 400 K; if the temperature of the substrate is increased, the impact of the particles on the impact will increase the depth of the foundation pit behind the base material. Table 4.1 shows the deformation coefficient (K) after the impact of particles at different temperatures. It shows that particle temperature is an important factor affecting the deformation coefficient (K). At the same time, the mesh size has a greater impact on the deformation coefficient (K).

Table. 4.1 − The deformation coefficient (K) after a single particle hits the Al6061 substrate at a temperature of 400-700 K.

Particle Temperature	400 K	450 K	500 K	550 K	600 K	650 K	700 K
K	0.56	0.5	0.47	0.436	0.397	0.334	0.283

The formation process of cold spray coating is a process in which particles continuously impact the matrix and the formed coating. Numerical analysis of the deposition process between single particles and the substrate can help to better understand the bonding mechanism between the particles and the matrix. In Figure 4.3, the same point is taken to observe the change of PEEQ with time during the

deposition. Figure 4.3 shows the changes in PEEQ during the entire process for particles at different temperatures. PEEQ is the cumulative result of plastic strain during the entire deposition deformation process of particles; combined with the analysis of the Figure 4.2, it can be seen that when the particles are completely deposited and in contact with the substrate surface, the plastic strain distribution after particle deformation is not uniform and is mainly concentrated in the foundation pit. both sides. As the temperature of the particles increases, the plastic deformation of the selected reference point increases significantly. Because the increase in particle temperature further accelerates the deformation of particles during deposition.
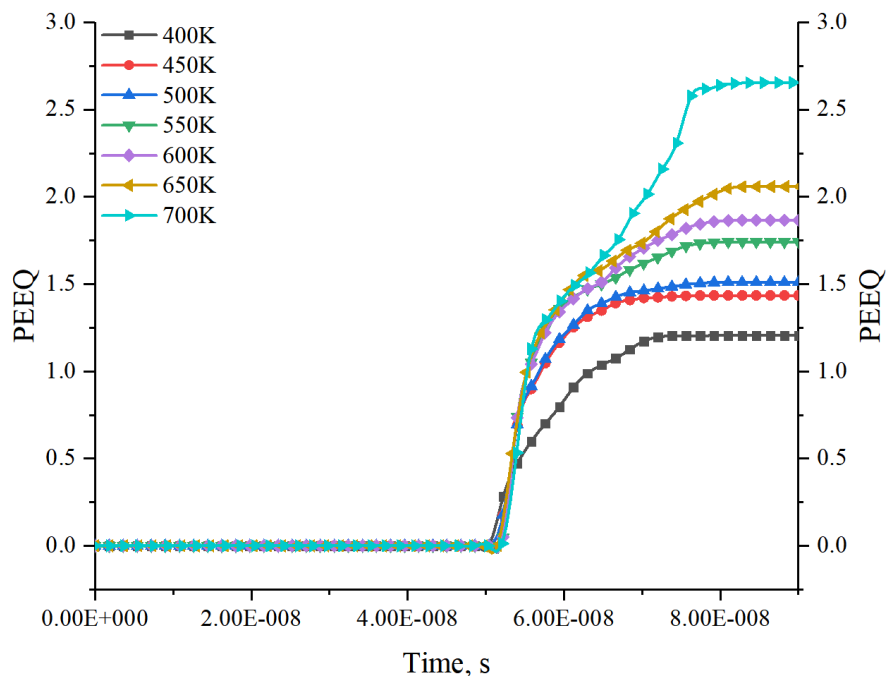

Fig. 4.3. PEEQ the entire process for particles at different temperatures.

4.1.1.2 Simulation of single particle deposition based on the SPH method

The SPH method is used to simulate the single particle deposition process for solution. The deposition model between the particle and the substrate is a three-dimensional model; the purpose is to better characterize the impact of particle temperature on the deposition process. Figure 4.4 shows the SPH method to simulate the single particle deposition solution model. Both the particles and the matrix adopt

uniform and fine regular hexahedral grids; the grid size of the deposition area of the substrate and the grid size of the particles is 0.1 um; the grid size of the non-deposition area of the substrate is 0.3 um, saving calculation time; the matrix Fixed constraints are used at the bottom; unlike the ALE method, the SPH method can effectively simulate complex problems such as large material deformation, moving material interfaces, and phase changes, so the grid size can be of the first order of magnitude. The particle size is 20 um spherical particles. The initial temperature of the substrate is 400 K; the initial velocity of the particles is 585 m/s; the particle temperature: 400-700 K.
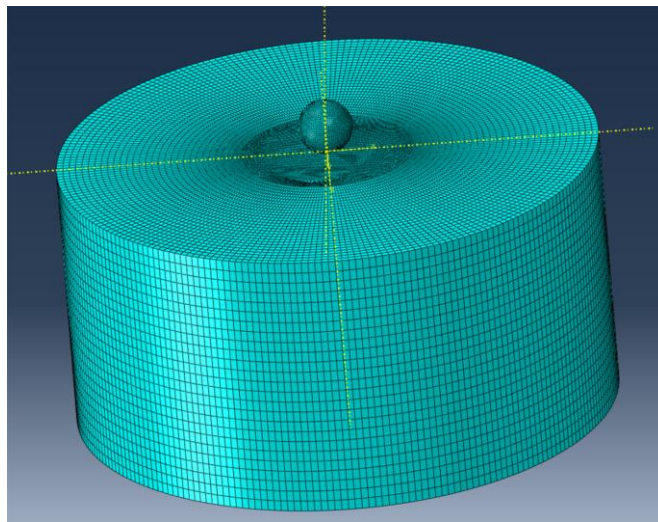

Fig. 4.4. The SPH method simulates single particle deposition solution model.

Figure 4.5 shows the deformation diagram of a single particle simulated by the SPH method after deposited on the Al6061 substrate at a temperature of 400-700 K. It can be seen from the Figure 4.5 that the deposition of Al6061 particles simulated by the SPH method is roughly the same as the particle deformation morphology obtained by the ALE method.
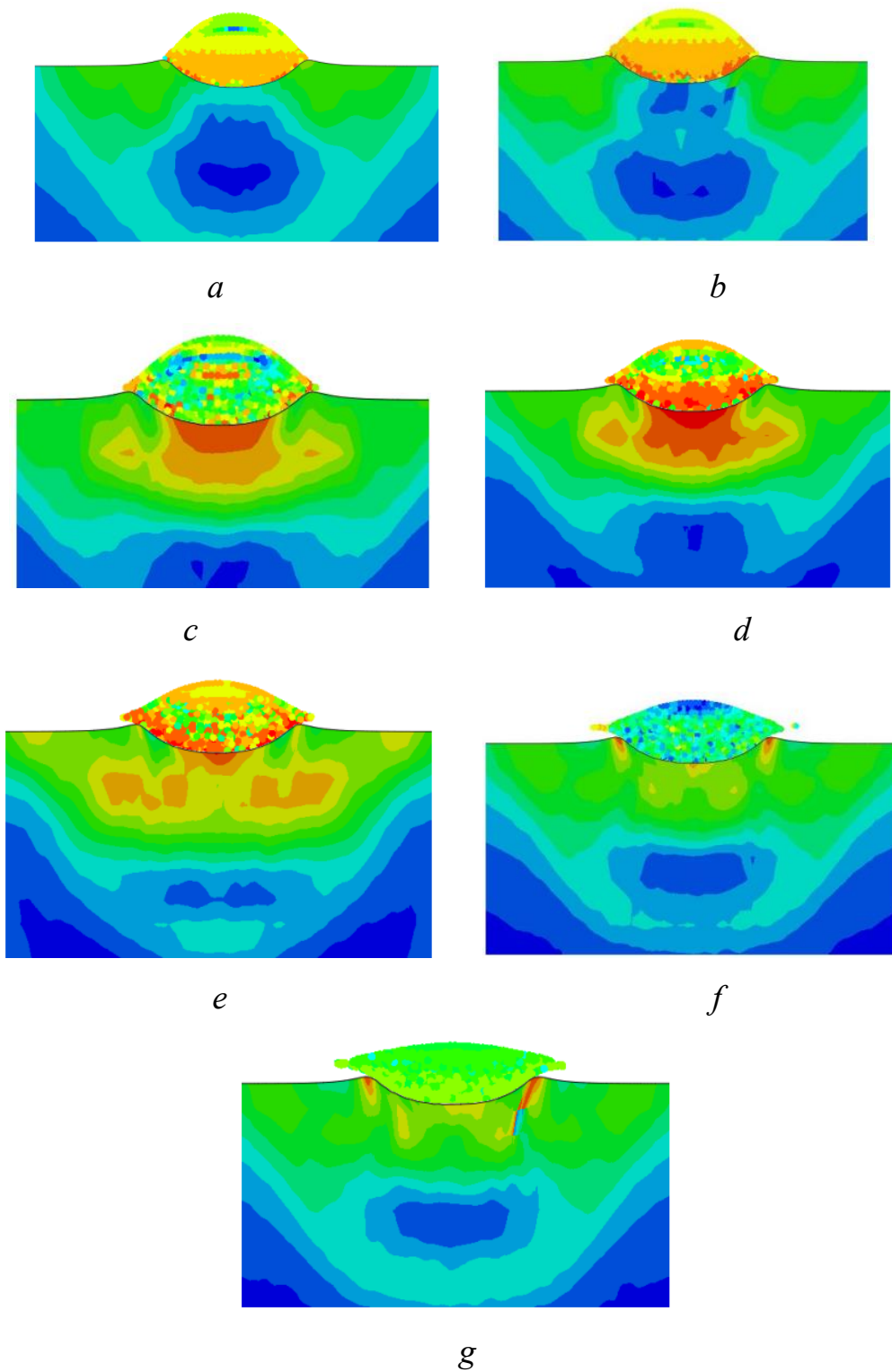
a – particle temperature 400 K; *b* – particle temperature 450 K; *c* – particle temperature 500 K; *d* – particle temperature 550 K; *e* –particle temperature 600 K; *f* – particle temperature 650 K; *g* – particle temperature 700 K

Fig. 4.5. The SPH method simulates the deformation diagram of a single particle after deposited on the Al6061 substrate at a temperature of 400-700 K

The SPH method shows that during the single particle deposition process, increasing the particle temperature has a more obvious softening effect on the particles. Especially when the temperature of the particles is greater than 600 K, the particle softening effect is most significant, Sputtering occurs when the particles deposit with the substrate. The particles experience strong plastic deformation when they contact the surface of the substrate; when the particle temperature reaches 700 K, the particles after depositing on the substrate are basically flat on the surface of the substrate, and serious sputtering occurs at the particle boundaries. This shows that if want to obtain good deposition results, excessively increasing the particle temperature is not the best solution. It is recommended to increase the temperature of the substrate appropriately.

Design a set of single-particle deposition model simulation experiments with a particle temperature of 600 K, a substrate temperature of 500 K, and a particle velocity of 585 m/s. As shown in Figure 4.6, the deformation diagram of single particle Al6061 at various moments during impact on the substrate. It can be seen from the Figure 4.6 that increasing the temperature of the substrate can effectively improve the deposition effect of particles on the substrate. As the particles continue to impact the surface of the substrate to form a foundation pit, the depth of the foundation pit gradually increases. When the deposition time reaches 40.5 ns, the increase in the depth of the foundation pit is no longer obvious. The particles continue to undergo plastic deformation when they impact the substrate at high velocity, and a small degree of sputtering occurs at the edges. When the particles deposited for 49 ns, the particles did not rebound, indicating that the particles and the substrate did not separate. Although the SPH method has shown many advantages over other methods in simulating cold spray particle impact, the application of the SPH method in the field of cold spray deposition is still in its initial stage. It is recommended to conduct in-depth research on the particle deposition mechanism and coating property analysis in the future.
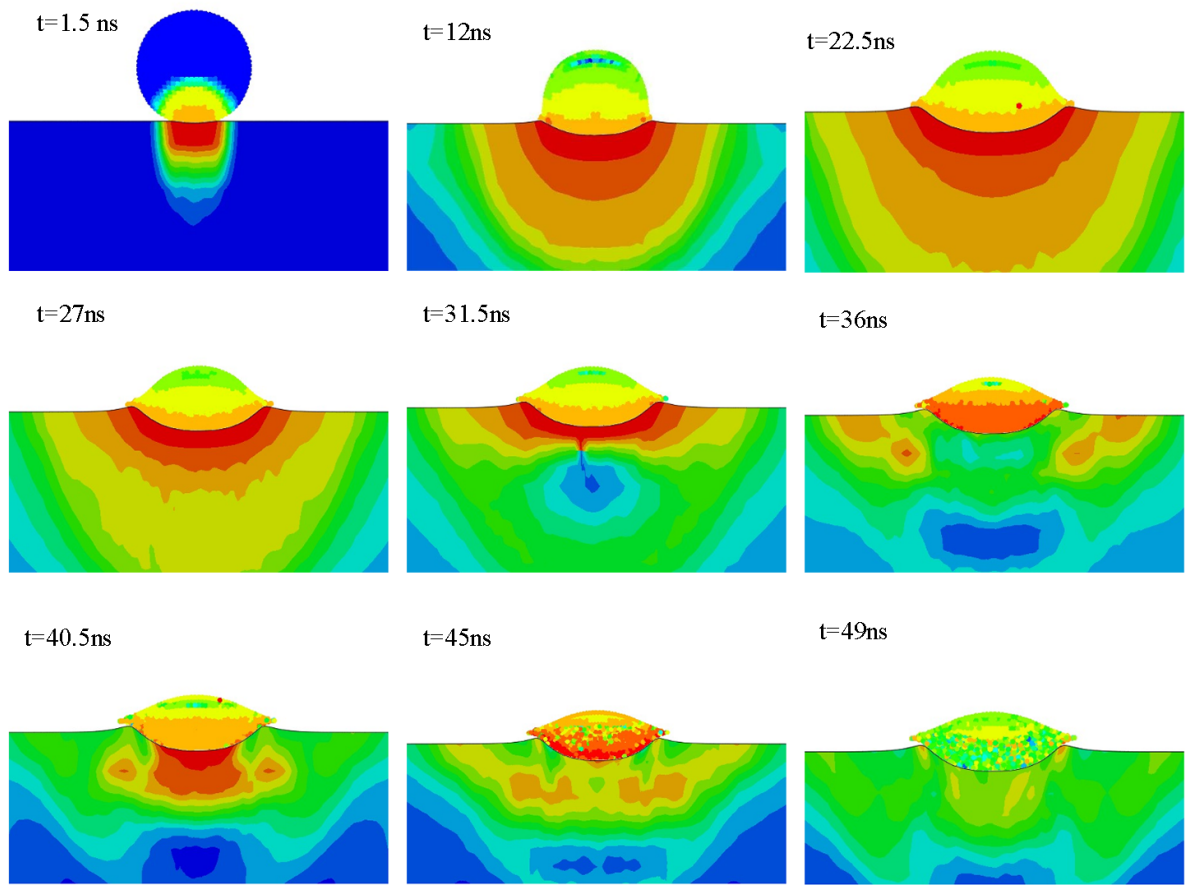
Fig. 4.6. Deformation diagram of Al6061 at various times

Hu and Tan [98] used the SPH method to simulate the deposition of various particles of Al, Ti, Cu, Ti6Al4V, Tungsten, and Ni; by studying the deformation results of particles impacting the substrate at different speeds. As shown in Figure 4.7, the SPH method simulates the deposition of various metal single particles; the ratio Y of particle deformation and foundation pit depth after impacting the substrate at different speeds is calculated. As shown in Table 4.2 [98]. Combining Table 4.2 and Figure 4.6, it can be seen that the particles velocity is related to the value of K, and the particle size is related to the depth of the foundation pit formed after the particles impact the substrate. Particle size is also an important factor affecting cold spray deposition.

V=600 m/s   V=650 m/s   V=700 m/s   V=800 m/s   V=820 m/s

a

V=600 m/s   V=700 m/s   V=800 m/s   V=900 m/s   V=1000 m/s

b

V=350 m/s   V=400 m/s   V=500 m/s

c

V=650 m/s   V=750 m/s   V=800 m/s

d

V=400 m/s   V=450 m/s   V=500 m/s

e

V=400 m/s   V=500 m/s   V=600 m/s
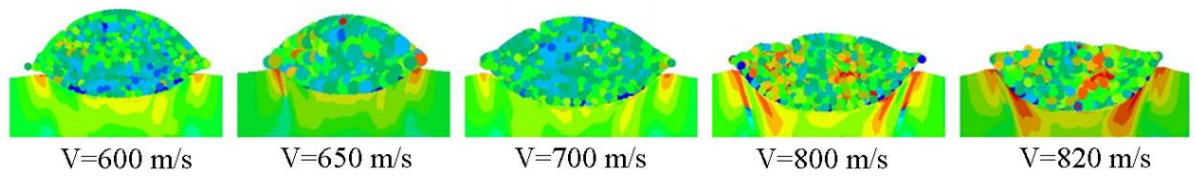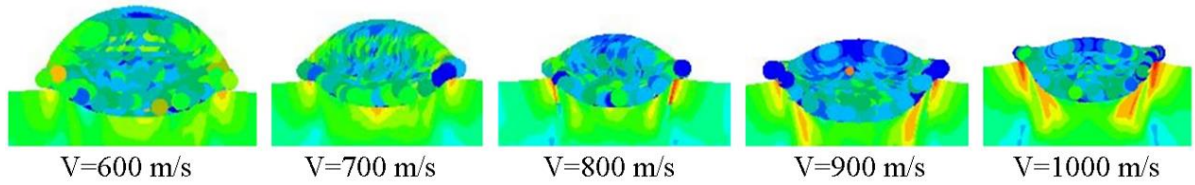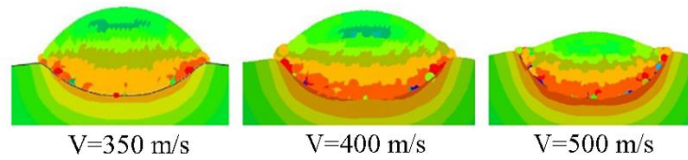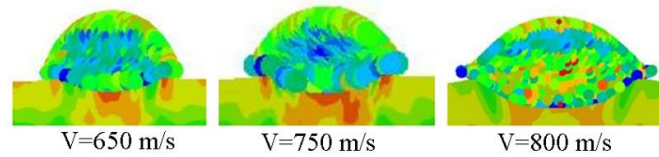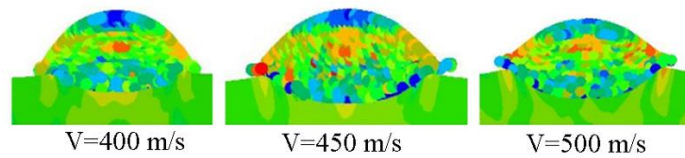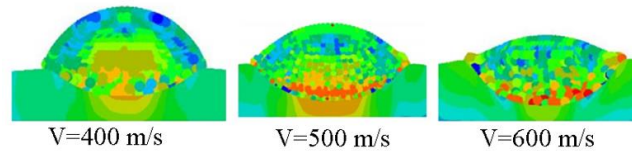
f

a – Al/Al; *b* – Ti/Ti; *c* – Cu/Cu; *d* – Ti6Al4V/Ti6Al4V; *e* –Tungsten/Tungsten; *f* – Ni/Ni

Fig. 4.7. The SPH method simulates the deposition of multiple metal single particles [98]

Table 4.2 – The deformation coefficient (K) after single particle deposited on the Al6061 substrate at a temperature of 400-700 K

Parameters	Al	Ti	Cu	Ti6Al4V	Tungsten	Ni
K / V (m/s)	0.55/600	0.54/600	0.51/350	0.46/650	0.47/400	0.57/400
	0.51/650	0.52/700	0.47/400	0.5/750	0.45/450	0.48/500
	0.55/700	0.58/800	0.54/500	0.46/850	0.44/500	0.43/600
	0.4/800	0.44/900	-	-	-	-
	0.49/870	0.42/1000	-	-	-	-

4.1.1.3 Simulation of single particle deposition based on the CEL method

The CEL method is also a commonly used calculation method for simulating high-velocity deposition processes, which is different from the ALE method and the SPH method. Both the base material and the particles of the ALE method and the SPH method are Lagrangian entities; the CEL method nests the particles in the Eulerian domain to form a particle model, and then partially nests the particle model in a base composed of Lagrangian entities. Within the material, Figure 4.8 shows the single particle deposition model simulated by the CEL method. The grid of the Euler domain in the CEL model is fixed in space, and particles can flow within the grid, which allows several different substances to coexist in the same unit. Therefore, a series of problems caused by excessive mesh distortion can be effectively avoided.
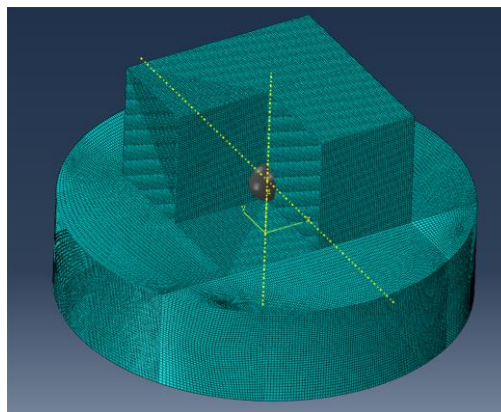

Fig. 4.8. The CEL method simulates single particle deposition model

The CEL method is used to simulate the single particle deposition process for solution, in which the deposition model between the particles and the substrate is a three-dimensional model. Both the Euler domain and the substrate adopt uniform and fine regular hexahedral meshes. The part of the Euler domain that intersects with the substrate is divided into a deposition area. The grid size of the deposition area is 1 um, and the grid size of the non-deposition area is 1-2 um. The grid model size of the Euler domain is 1. The size is kept consistent just to ensure that the combination of particles and substrate after deposition can be accurately observed. The Al6061 particles in this section are spherical particles with a particle size of 20 um. The initial temperature of the substrate is 400 K; the initial velocity of the particles is 585 m/s; the particle temperature 400 - 700 K.

Figure 4.9 shows the deformation diagram of a single particle simulated by the CEL method after deposit on the Al6061 substrate at a temperature of 400 - 700 K. It can be observed from the Figure 4.9 that the effects of simulating particle depositions with the substrate at different temperatures through the CEL method are very similar to the results of the ALE and the SPH methods.

When the particle temperature is 400 - 550 K, the deformation of the upper part of the particle is not very obvious. The plastic deformation area is mainly concentrated in the contact area between the particle and the substrate. The overall deformation results are similar to those obtained by the ALE method and the SPH method.

However, in the settlement results of the CEL method model, there is un-fallen metal sputtering at the contact edge between the particles and the substrate; It can be seen from the result diagram after the deposition that the plastic deformation in the contact area is greater than the ALE method simulation calculation result. When the particle temperature reaches 600 - 700K, the overall plastic deformation of the particle is significantly enhanced, and the overall particle shows a flat shape.
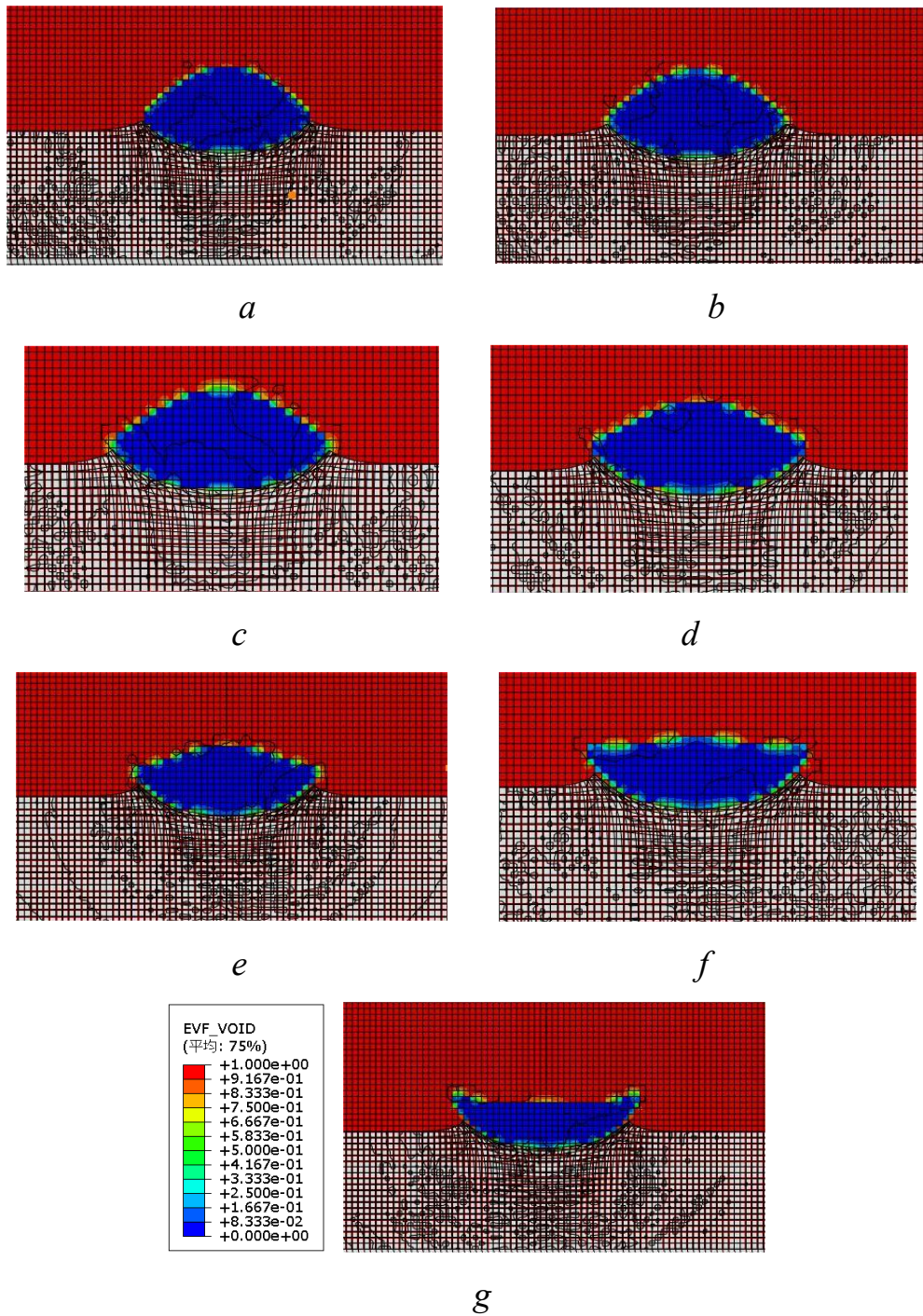
a – particle temperature 400 K; *b* – particle temperature 450 K; *c* – particle temperature 500 K; *d* – particle temperature 550 K; *e* – particle temperature 600 K; *f* – particle temperature 650 K; *g* – particle temperature 700 K

Fig. 4.9. The cross-sectional view of the EVF voids simulated by the CEL method after a single particle deposit on the Al6061 substrate at a temperature of 400-700 K

By comparing the deformation, the final deformation coefficient K, the K value simulated by the CEL method is smaller than the K value obtained by the ALE method. When the particle temperature reaches 700 K, the degree of deformation further increases, especially at the edge of the contact area between the particles and the substrate. The range of metal sputtering is obviously stronger than the results obtained by the ALE method and the SPH method. In the single particle deposition model established by the CEL method, the particles essentially flow in the Euler domain. Therefore, since the grid nodes are fixed in space, the particles can flow in the grid, so there is no grid distortion. Therefore, during the simulation particles can run normally during the deposition process until the deposition is completely completed; Therefore, based on this advantage, the CEL method can refine the grid. Therefore, it shows that the deposition model established by the CEL method can obtain more accurate calculation results.

In the numerical simulation of particle depositions simulated by the ALE method, increasing the temperature of the base material can effectively increase the depth of the foundation pit. Therefore, based on the CEL method, three sets of single particle deposition model simulation experiments were established with particle temperatures of 600K, 650 K, and 700 K, substrate temperature of 500 K, and particle speed of 585 m/s.

Figure 4.10 shows the deformation of Al6061 particles in the Euler domain at each moment of the deposition model with a particle temperature of 600 - 700 K and a substrate temperature of 500 K. It can be seen from the Figure 4.10 that the temperature of the substrate will affect the depth of the foundation pit. As the temperature of the substrate increases, the ratio K of particle deformation to the pit will increase. This also proves that the temperature of the substrate is also an important factor affecting particle deposition.
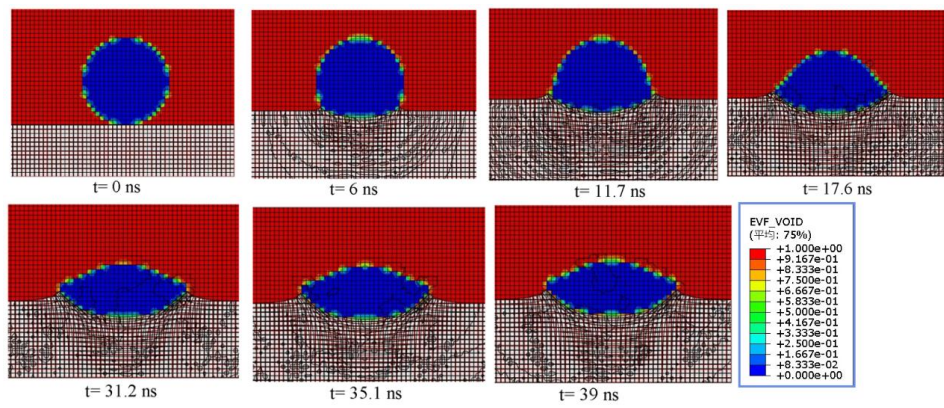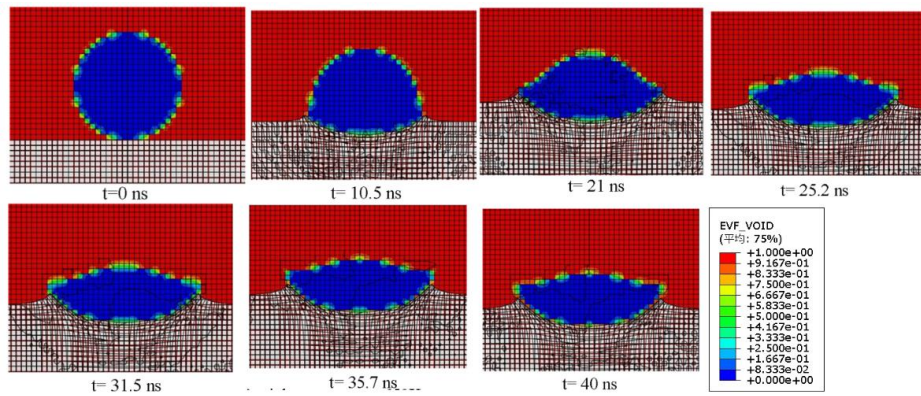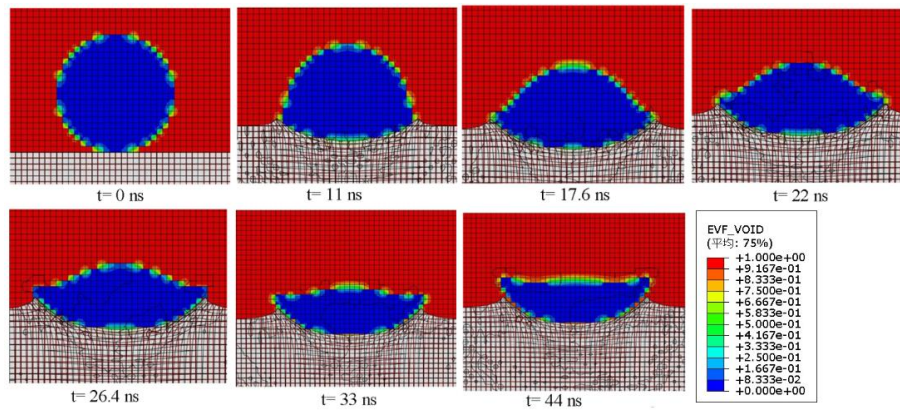
a − particle temperature 600 K, substrate temperature 500 K; *b* − particle temperature 650 K, substrate material temperature is 500 K; *c* − particle temperature is 700 K, base material temperature is 500 K

Fig. 4.10. The cross-sectional view of EVF voids after Al6061 particles impact on the substrate at various times in the deposition model with particle temperature 600-700 K and substrate temperature 500 K

By analyzing the Figure 4.10, when the particle temperature reaches 650 K, the plastic deformation of the contact area of the particles increases significantly after deposition with the substrate, indicating that the contact area is most susceptible to adiabatic shearing and the particles and the substrate can be combined. When the temperature of the particles reaches 700 K, the phenomenon of thermal softening due to excessive temperature during the deposition between the particles and the substrate is significantly greater, and the jets at the edges of the particles are more obvious. At the same time, the substrate also has a tendency to have jets. And when the particles complete the impact, they do not appear to be separated from the substrate, but are closely combined, which indicates that the particles have completed the deposition process. The deposition model established by the CEL method. The CEL method allows the materials of the particles and the substrate to coexist in the same grid unit. When the particles and the substrate are in the same unit, the interface cannot be clearly distinguished, so the particles do not rebound. Therefore, the deposition model established by the CEL method is a good method for simulating particle deposition.

4.1.2 Simulating the influence of particle size on single particle deposition process based on the CEL method

The particle size simulation is based on the CEL method to solve the single particle deposition process; this section simulates spherical particles with a particle size of 20 - 60 um, the initial temperature of the substrate is 500 K; the initial velocity of the particles is 585 m/s; the substrate temperature: 500 K; the particles are studied the effect of diameter on the deposition of Al6061 particles on the Al6061 substrate. Observe the bonding of the particles to the substrate after impact. Figure 4.11 is the cross-sectional view of the EVF voids after particles of different sizes impact on the substrate at different temperatures.
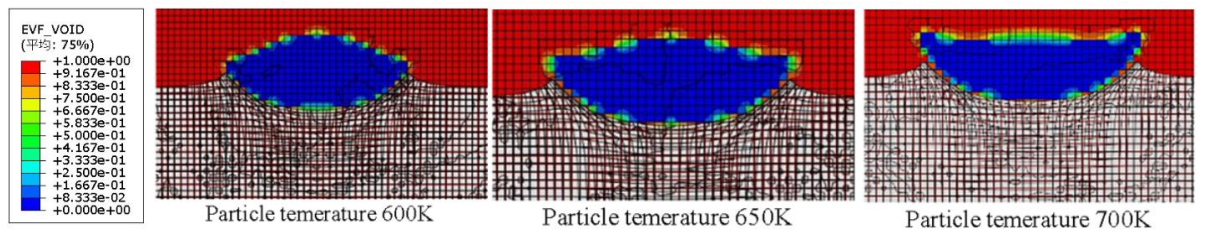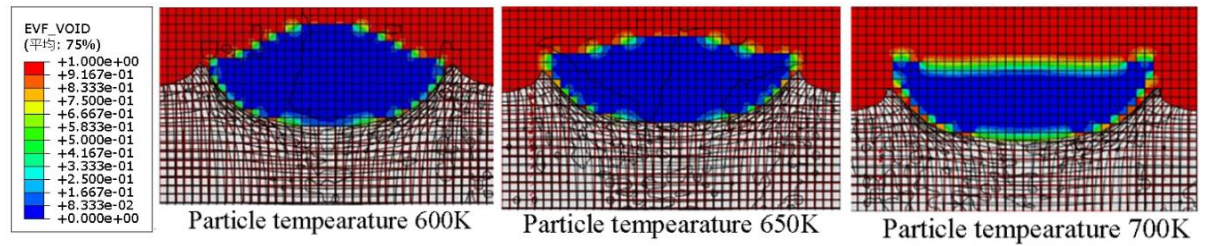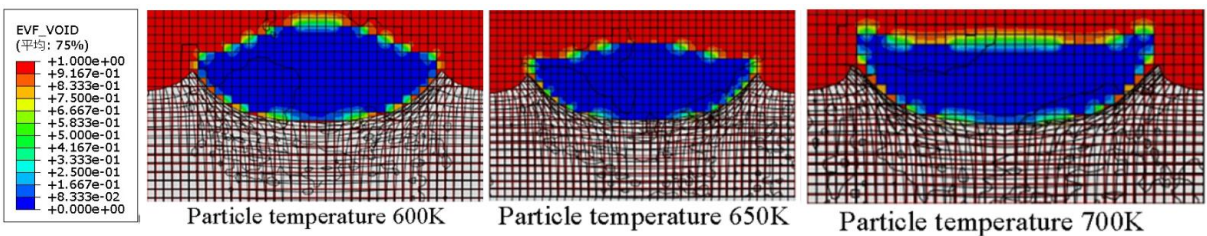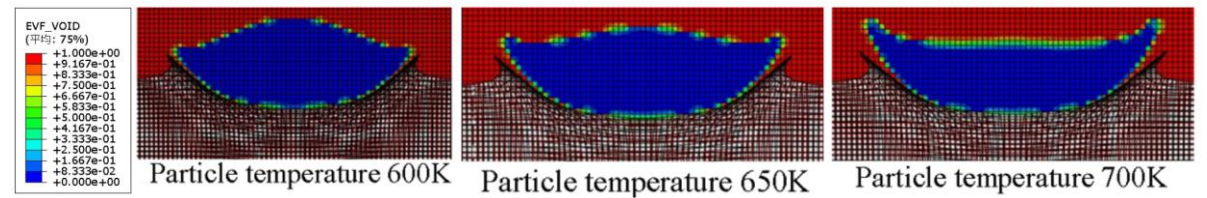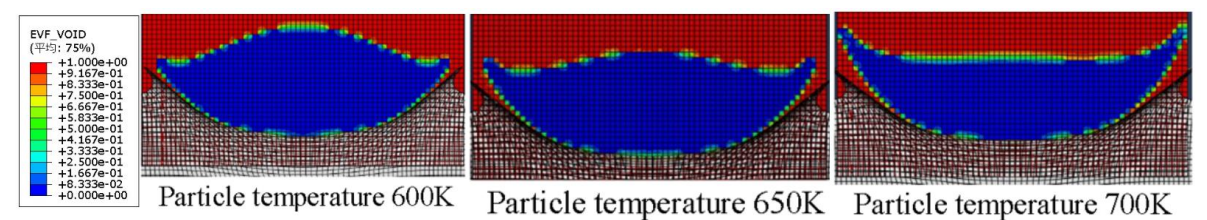
a – particle size 20 um; *b* − particle size 30 um; *c* − particle size 40 um; *d* − particle size 50 um; *e* − particle size 60 um

Fig. 4.11. Cross-sectional view of EVF voids after particles of different sizes deposit on the substrate at a particle temperature of 600 K, 650 K, and 700 K

It can be seen from the Figure 4.11 that the particles temperature and size will affect the results of the particles depositing on the substrate. Increasing the particles temperature can effectively improve the deposition effect of the particles on the substrate. When the particle temperature reaches 700 K, the thermal softening effect of the particles is very obvious. As the particle size increases, the depth of the pit formed after the particles impact the substrate becomes larger. This is because for particles with the same velocity, the larger the particle size, the greater the kinetic energy of the particles. When the particles impact the substrate at high velocity, the kinetic energy it is converted into internal energy, and at the same time, the particles undergo severe plastic deformation, and finally are deposited on the substrate. When the particle size is greater than 40 um, the particle temperature is 650 K, and metal sputtering occurs after the particles hit the substrate. When the particle size is 60 um and the particle temperature is 650 K and 700 K, the sputtering range at the edge of the particle is the most significant. The edges of the particles after impact are separated from the substrate.

Observing Figure 4.11(e), the contact part after the particles deposit on the substrate are located in the bottom. The color of the bottom is blue, indicating that the particles after impact have not contacted the substrate. Detachment occurs indicating that the deposition of particles is effective. The CEL method can accurately simulate large deformation of particles because the particles flow in the grid in the Euler domain, so there is no grid distortion, thus ensuring that the single-particle deposition model runs until the deposition is completely completed.

By simulating the single particle deposition process based on the CEL method, it can be seen that the shapes of the impact particles after impacting the substrate are diverse and complex. Therefore, it is necessary to use the CEL method to simulate the multi-particle impact model to simulate the formation of the coating in the actual cold spray process. Based on the advantages of the CEL method, particles flow in the grid in the Euler domain, thereby ensuring that the grid will not be distorted. A

multi-particle deposition model can be established to study the porosity of cold spray coatings.

4.2 The Multi-particle particle model and deposition model analysis

The CEL is currently a method that can better simulate the deposition process of cold spray multi-particles with different particle sizes, especially when the particles large deformation occurred during the deposition process. This method is better than other limited methods in the range of large deformation, large displacement and large strain. Meta-techniques offer greater accuracy and robustness, with the advantage of wrapping particles in Eulerian domains, which avoids the need for remeshing and highly distorted elements [180]; The CEL cannot numerically study the deformation of particles. Instead, it tracks the material as it flows through the grid by calculating the Eulerian volume fraction in each cell. If the material completely fills the cell, its EVF is 1, which is not present in the element. This material, then its EVF is 0, and the sum of the volume fractions of all materials in the unit is less than 1, then the rest of the unit will automatically fill the void material, and the void material has no mass and strength [181].

4.2.1 The Multi-particle model with different particle sizes

4.2.1.1 Establish multi-particle model based on Solidworks / Catia

The multi-particle model for cold spray multi-particle deposition can be completed through Solidworks or Catia. The spray material is selected to be Al6061 particles; the particle size range is 20 - 70 um; the number of particles is 100. Through the three-dimensional modeling software, the particle sizes of 20 um, 30 um, 40 um, 50 um, 60 um, and 70 um are separately modeled. Obtain the number of each particle size according to the cumulative probability distribution of typical

particle size distribution particle sizes. Select a suitable cuboid area, and then place each particle in the assembly in a fixed position within the cuboid area. Here the cuboid region can be regarded as the Euler domain in Abaqus-Explicit. It should be noted that the Euler domain must wrap all particles; the particles in this area must be distributed individually, and there must be no contact between each particle. Figure 4.12 shows a particle model of multi-particles with different particle sizes.
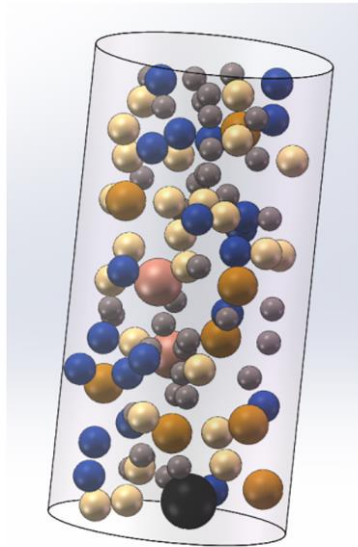
Fig. 4.12. The multi-particle model of different particle sizes completed through SolidWorks modeling

4.2.1.2 Establishing multi-particle model based on Python script

Multi-particle modeling of cold spray multi-particle deposition can be accomplished via Python scripts, as refer to appendix A. Select particles of Al6061 as the spraying material; the particle size range is 30-50 um. Select the particle size range of 30-50 um to ensure the influence of large particle size particles on small particle size during the later deposition process. The numerical difference between the largest particle and the smallest particle should not be too large. In the actual cold spray process, particle size is also an important factor affecting the deposition results; the number of particles is 200. The choice to increase the number of particles

197

here is to ensure that when calculating the average porosity of the coating, there will be no duplication of sampling groups, thereby ensuring the accuracy of the calculation results. The cumulative probability distribution of particle size is described by the log-normal function. Build multi-particle models through custom algorithms. By inputting the number and volume percentage of particles, multiple particles are randomly distributed within the Euler domain, avoiding overlap between particles in this process. The principle is to determine whether the distance between particles in space coordinates is greater than the sum of the radii between particles to avoid overlapping of particles.

$$\sqrt{(x_i - x_j)^2 + (y_i - y_j)^2 + (z_i - z_j)^2} > R_1 + R_2, \qquad (4.1)$$

where $(x_{i/j},\ y_{i/j},\ z_{i/j})$ – the spatial coordinate of the particle in the Euler domain;

R_1 and R_2 – the radius of the particles.

4.2.2 The Multi-particle deposition model

4.2.2.1 The material model

The cold spray process involves high strain rates, plastic deformation and temperature changes. In order to simulate the deposition effect of Al6061 particles on the same substrate, it is assumed that the material is isotropic. The J-C model is added to characterize the high dependence of rate and temperature; equations (4.2) and (4.3) are the definitions of the J-C model. At the same time, the erosion and cracking phenomena that occur under high-velocity impact must also be taken into account, and the failure initiation model must be added. All model parameters are shown in Table 4.3 [182, 183]. The ratio of plastic energy converted into heat is 0.9 [184].

$$\sigma = \left(A + B\varepsilon_p^n\right)\left[1 + C\, ln\left(\frac{\dot{\varepsilon}_p}{\dot{\varepsilon}_0}\right)\right]\left[1 - \left(\frac{T-T_r}{T_m-T_r}\right)^m\right]; \qquad (4.2)$$

$$C = \begin{cases} C_1 \ \ and \ \ \dot{\varepsilon}_0 = 1 \ if \ \ \dot{\varepsilon}_p \leq \dot{\varepsilon}_c \\ C_2 \ \ and \ \ \dot{\varepsilon}_0 = \dot{\varepsilon}_c \ if \ \ \dot{\varepsilon}_p > \dot{\varepsilon}_c \end{cases}, \qquad (4.3)$$

where σ – the flow stress;

$\dot{\varepsilon}_p$ – the strain rate;

$\dot{\varepsilon}_0$ – the reference strain rate;

T_r – a reference temperature;

T_m – the melting temperature of the material;

A, B, n, and m – the model parameters;

C_1 and C_2 – coefficients.

The additional increase in flow stress when the applied $\dot{\varepsilon}_p$ greater than the critical plastic strain rate [185].

Table. 4.3 – Material properties for Al6061.

Properties	Parameters	Value
General	Density ρ, kg/m3	2700
	Specific heat Cp , J/(kg·K)	1009
	Thermal conductivity coefficient λ, W/(m·K)	155
	Melting temperature Tm, K	925
	Inelastic heat fraction	0.9
	Elastic modulus, GPa	69.11
	Poisson's ratio, v	0.331
	Shear modulus, GPa	25.9
Johnson-Cook plasticity parameters	A(MPa)、 B(MPa)、 n、 m、	270,154.3,0.239,1.42
	Reference strain rate	1
	Reference temperature $Tref$, K	298
	C_1 C_2, $\dot{\varepsilon}_c$	0.002, 0.0029, 597.2
Failure initiation	d_1, d_2, d_3, d_4, d_5	-0.56, 1.45,0.47,0.011,1.6

4.2.2.2 The particle velocity, temperature, and predefined fields

The work in this dissertation is to study the effect of the temperature of the particles and substrate on the coating after deposition. All Al6061 particles need to be given a certain speed value to ensure that all Al6061 particles can be uniform and orderly particles/substrates, and particles/particles deposit. As stated above, all particles are included in the Euler domain, so the essence is that all particles flow in the Euler domain, and the deposition process after deposition will be completed in the Euler domain.

Control the temperature range of Al6061 particles and substrate, and study the effects of different temperature conditions on the post-deposition coating. A coupled temperature-displacement dynamic step with an appropriate time period is assigned to track the entire multi-particle impact process from the start of the simulation to the complete stop of all particles. The contact model uses dynamic, temperature-displacement and display models; the tangential behavior, normal behavior, and friction coefficient are defined. Material assignment to all particles in a predefined field. Use the discrete field volume fraction tool to set parameters for all particles in the Euler domain, and calculate the volume fraction of all particles in the Euler domain through field data to ensure smooth progress in later calculations.

4.2.2.3 Relevant parameter settings and assembly of the base material

In the work of this dissertation, the materials of the substrate and particles are the same, but the material property settings in the modeling are different. The substrate should be set to a square Lagrangian domain. The advantage is that the deposition can be observed accurately and clearly. The contact surface between the final particles and the substrate. The grid of the substrate is divided from the inside to the outside, and the grid density decreases in sequence; the central area of the substrate is the main site for multi-particle deposition, so the grid in the central area

should be controlled as small as possible, and the grid size in the particle impact area should be close to the Euler domain the grid size of the pulling domain is mainly to ensure better resolution in the subsequent analysis process. The grid model selects the Lagrangian C3D8RT element type, where T represents temperature; C3D8RT: eight-node thermally coupled hexahedral element, three-way linear displacement, three-way linear temperature, reduced integration, hourglass control; in order to ensure that the analysis process will not affect the calculation due to grid distortion, the particle grid settings are enhanced with hourglass control at the same time, set the unit distortion control. The analysis step time of the entire analysis process is roughly estimated based on the time it takes for the particles furthest from the matrix to reach the substrate. The substrate needs to be assigned a temperature field by defining a fixed initial temperature field for all nodes of the substrate model 400 K.

During the assembly process, the multi-particle model is wrapped in the Euler domain, and its essence is that the particles flow at high velocity in the Euler domain. The bottom part of the Euler domain overlaps the top part of the substrate in the Lagrangian domain. This step is to ensure that the particles after the deposition can still be completely included in the Euler domain, so that the coating formed after the deposition is still in the Euler domain. within the range to ensure the integrity of the calculation results. The contact algorithm automatically calculates and tracks the interface between the two domains, ignoring the heat exchange between the particles and the substrate, considering the process to be adiabatic [37].

4.3 Numerical study on simulating multi-particle deposition process based on the CEL method

This section proposes to use the CEL method to simulate the deposition process of cold spray multi-particles on the Al6061 substrate. A multi-particle wrapped model is embedded in the deposition model created by the CEL to simulate the deposition process of multi-particle Al6061 particles on the Al6061 substrate. By

studying the particle/substrate and particle/particle depositions, the shape of the coating is observed. and the temperature distribution on the surface of Al6061 substrate after deposition.

4.3.1 The simulation model

This simulation model was jointly completed by SolidWorks/ Pyhon language and Abaqus-Explicit. Solidworks/ Pyhon language completed the modeling of 100 particle models with particle sizes of 20-70 um. A multi-particle wrapped model is embedded in a deposition model created by the CEL to simulate the deposition process of cold sprayed multi-particle Al6061 particles on the Al6061 substrate.

Figure 4.13 shows the appearance of 100 particle models with particle sizes of 20-70 um before deposition. Typical particle size distribution measured using a microvolume laser particle analyzer. The cumulative probability distribution of particle size is estimated by a lognormal function, as shown in Figure 4.14 for the distribution of Al6061 particle size and number. This work adopts the assumption of uniform distribution to confine the affected particles to the central region of the dense grid of the substrate.
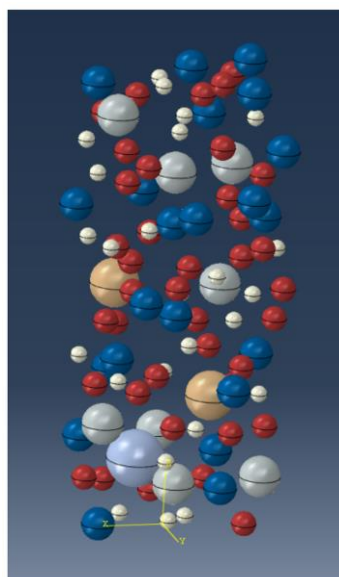

Fig. 4.13. 100 particles model with particle size of 20-70 um
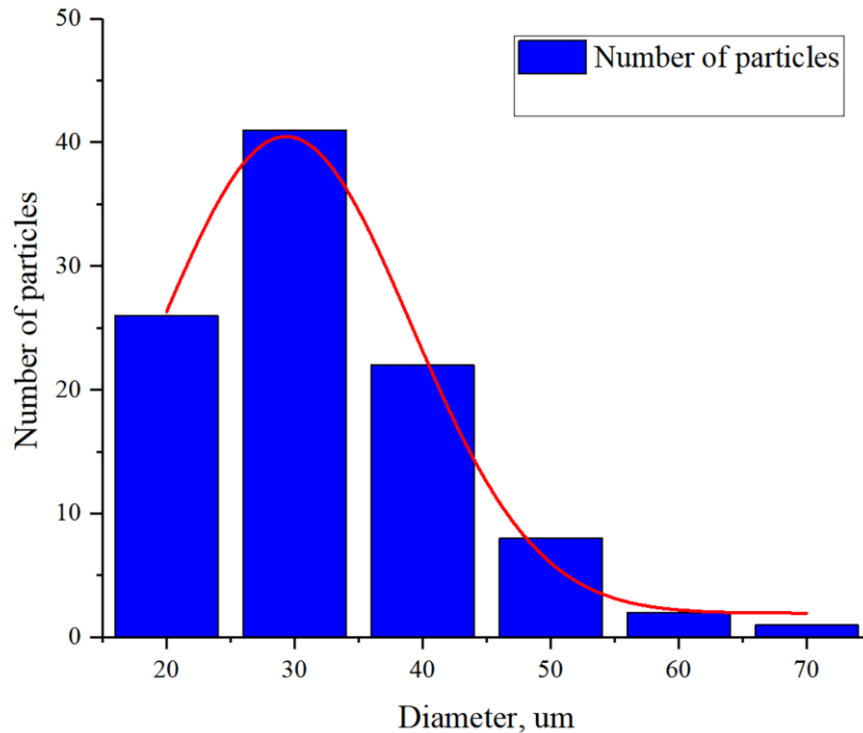
Fig. 4.14. Distribution of particle size and number of Al6061

It should be noted that all particles must be wrapped in the Euler domain, as shown in Figure 4.15. It should be noted that the Euler domain must wrap all particles and the deposition area, as shown in Figure 4.15. The blue area is the Euler domain. It should be noted that the Euler domain is set to a cuboid. The advantage is that it can generate a uniform hexahedral structure grid [186], reduce the time required for analysis, and ensure that the mass loss is reduced in the Euler domain grid, while at the same time it is convenient for the convergence of the results during the calculation process; some scholars set the Euler domain as a cylinder [187]. The disadvantage is that the grid generated by the cylinder is mainly a tetrahedral grid, which is not easy to converge during the calculation process. Thermal coupling is added to the Euler domain grid, EC3D8RT: the node thermal coupling is purely Euler hexahedral element, reduced integration, hourglass control (using distortion and enhancement control), and at the same time, the nonlinear and large deformation effects of the material are considered during the simulation process.
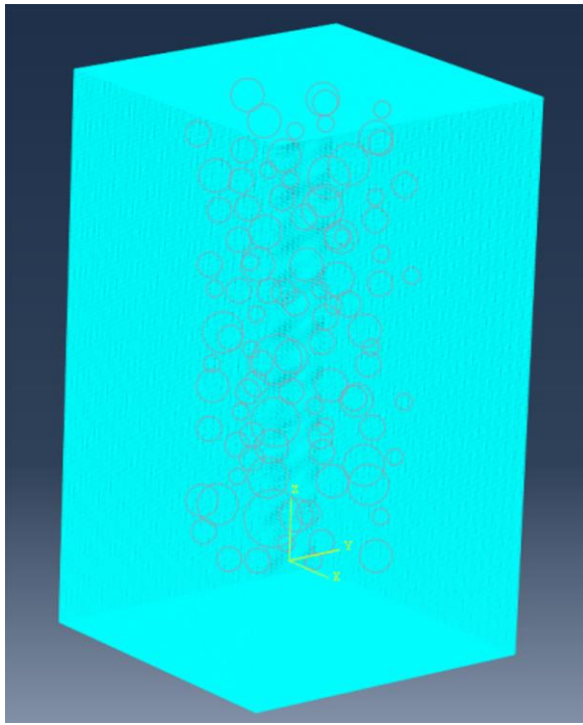
Fig. 4.15. The multi-particles contained in Eulerian domain

4.3.2 The material and deposition models

The CEL framework can simulate the deposition process of cold sprayed Al6061 multi-particles on the Al6061 substrate. Assuming that the material is isotropic, an inelastic heat share parameter needs to be set, and its properties are shown in Table 4.3. Plastic hardening uses the J-C model to describe the dependence of material behavior on rate and temperature [187], and adds a hardening J-C model representation that depends on the change rate.

The parameters of the J-C model are obtained by least squares curve fitting of the deformed particle shapes measured in the Advanced Laser Induced Projectile Impact (ALIPIT) test [184]. The ratio of plastic energy converted into heat is 0.9 [185]. The corresponding thermal response of a material is defined by its temperature-dependent thermal properties, such as specific heat, thermal conductivity and thermal expansion [186].

In the load predefined field, set the corresponding temperature field (K) and velocity field (m/s) for 100 particle models with sizes of 20-70 um. The velocity of

all Al6061 particles is set to 585 m/s and the temperature is 400 K [167]. Ensure that all Al6061 particles can produce particle/substrate particles and particle/particle depositions evenly and orderly. As mentioned above, all Al6061 particles are wrapped in the Euler domain, so the essence is that all Al6061 particles flow in the Euler domain, and the deposition process including post-deposition will be completed in the Euler domain. For some steps, please refer to Chapter 4.2.2.2. Figure 4.16 shows a 1/2 section view of the multi-particle deposition model.
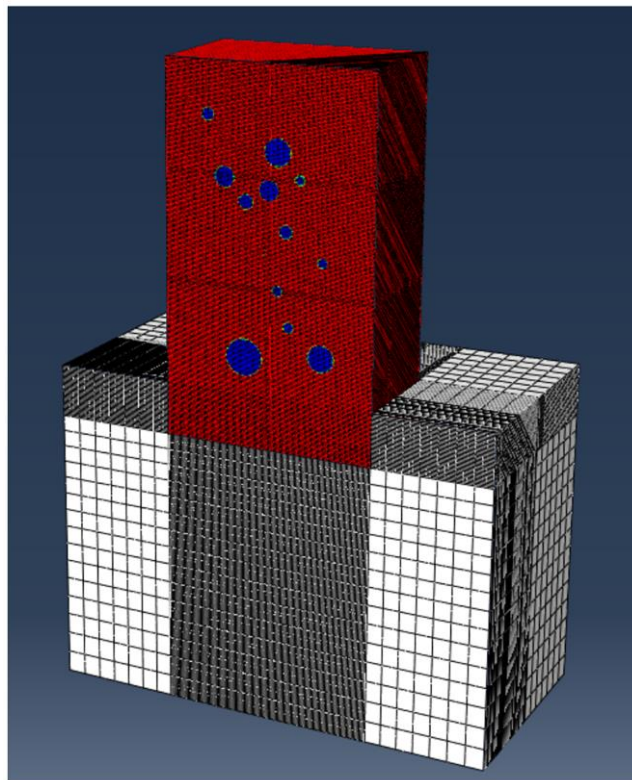
Fig. 4.16. The 1/2 section view of the multi-particle deposition model

4.3.3 Results and discussion

Figure 4.17 shows a cross-sectional view of the EVF voids after multi-particles are deposited on the substrate. The EVF void value of the red area is 1, indicating a gap area, and the EVF void value of the blue area is 0, indicating that the element is filled with material. It can be clearly observed from Figure 4.17 that there are still red areas in the coating after the deposition, and there are gaps in the model after the

deposition. It shows that there are gaps in the model after the deposition. It can be seen from the Figure 4.17 that there is no gap in the contact between the model coating and the substrate after the deposition. It is said that the simulated deposition is successful.

EVF_VOID
(平均: 75%)
+1.000e+00
+9.167e-01
+8.333e-01
+7.500e-01
+6.667e-01
+5.833e-01
+5.000e-01
+4.167e-01
+3.333e-01
+2.500e-01
+1.667e-01
+8.333e-02
+0.000e+00
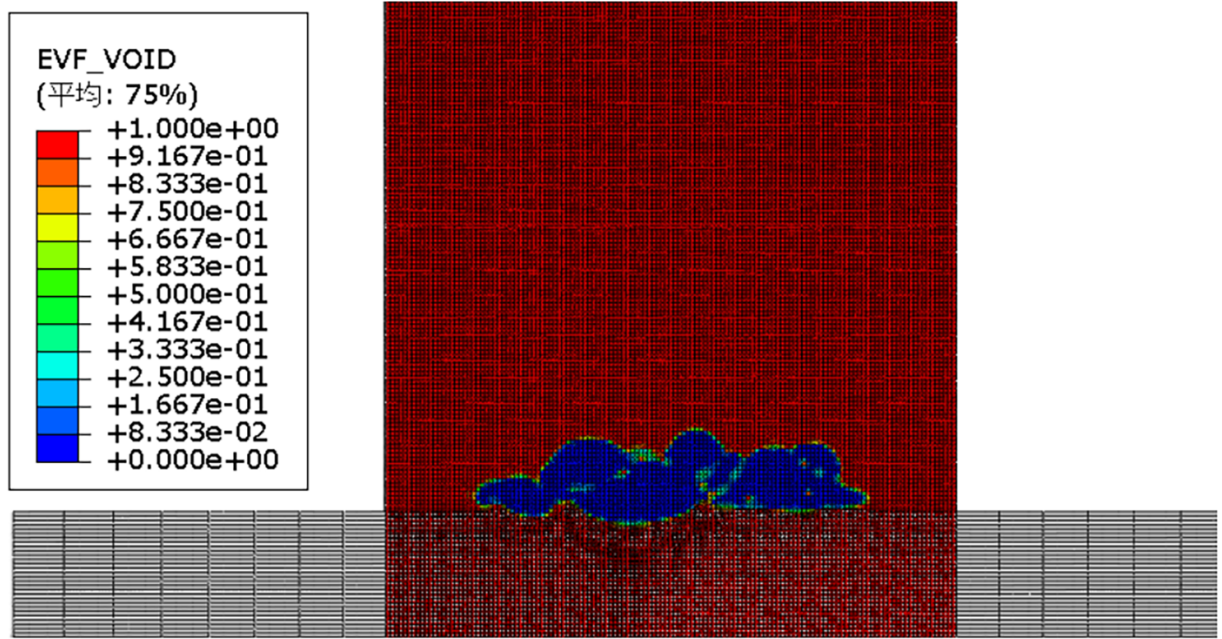
Fig. 4.17. The cross-sectional view of EVF voids after multi-particle deposition on the substrate

As mentioned above, the grid in the Euler domain will not deform with the particles. The essence is that the particles flow in the Euler domain. This shows that the multi-particle deposition model established by the CEL method to simulate the actual cold spray process can be used to monitor and calculate the coating porosity, which cannot be achieved by the ALE method and the SPH method. Regarding the calculation of coating porosity from the multi-particle deposition model, a sample model can be collected in the coating and the average EVF pore percentage calculated as a numerical value for the porosity of the coating. In the actual cold spraying process, porosity always exists in the coating; eliminating porosity has always been an area of focus.

Figure 4.18 shows the temperature cross-section of the Al6061 substrate after

being deposited with Al6061 particles; the initial substrate temperature is 600 K; it can be seen from Figure 4.18 that the maximum temperature on the surface of the substrate after deposition is 528.2 K, and the maximum temperature is located after the deposition of particles and particles. Because the particles deposited and squeezed during the deposition process, thus generating a large amount of heat; select 5 points from Figure 4.18 and observe the temperature changes of these nodes before and after deposition.
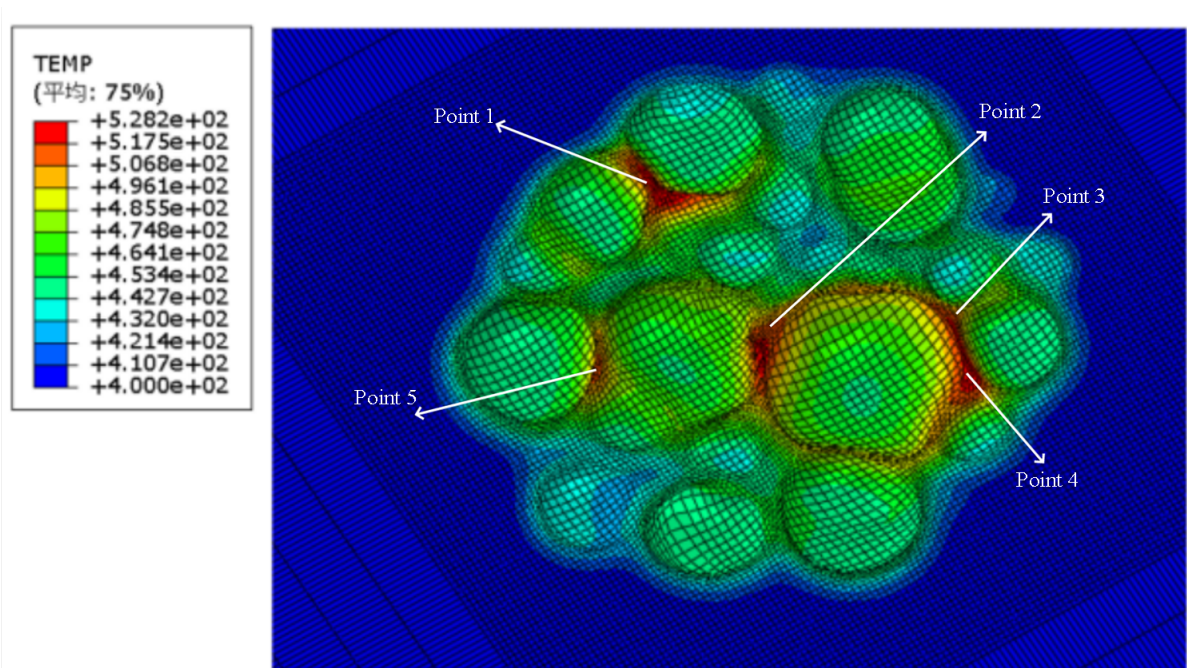
Fig. 4.18. The temperature of Al6061 substrate after particle deposition

As shown in Figure 4.19, the substrate temperature points 1-5 temperature changes over time during the deposition process. From Figure 4.19 it can be seen that the temperature curve of substrate points 1-4 temperature appears multiple inflection points. Each inflection point represents an occurrence at that location. Each impact causes an increase in the temperature of the substrate surface. The temperature curve of substrate point 5 temperature shows only one sharp increase in temperature, followed by a rapid decrease in temperature, which indicates that only one deposition occurred at substrate points 5. The multi-particles generate a large amount of heat during the deposition with the substrate/Al6061 particles, and the

temperature drops sharply after the deposition ends. Through the analysis of the simulation results of the multi-particle deposition model, it was found that during the multi-particle impact process, the matrix was squeezed into the gaps between the coating particles due to thermal softening, excessive plastic deformation and thermal expansion. After spraying, as the interface temperature dropped, the modulus of the substrate extruded into the coating gap due to plastic deformation returns to normal temperature, thereby bonding with the substrate.
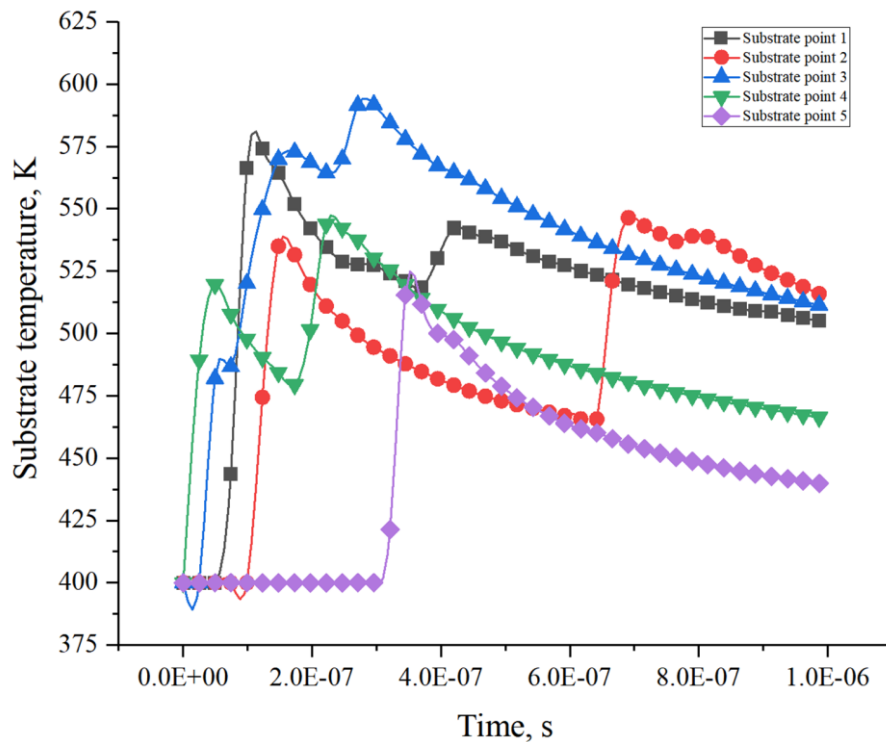
Fig. 4.19. Substrate point 1-5 temperature changes over time during the deposition process

As shown in Figure 4.20, the mutual conversion between kinetic energy and internal energy of multi-particles in the entire deposition model, almost all kinetic energy is converted into internal energy, and the process is stable, indicating that the entire deposition model has good stability. As can be seen from Figure 4.20, the kinetic energy and internal energy curves of the model are symmetrical about $y=0.529$. The loss of kinetic energy and thermal energy is not considered in the model, so all kinetic energy is converted into internal energy. It can also be seen

from the Figure 4.20 that in the multi-particle model, when the time step reaches 980ns during the deposition process, the whole deposition process ends, which is completely consistent with the total range stated above of 900-1000 ns.
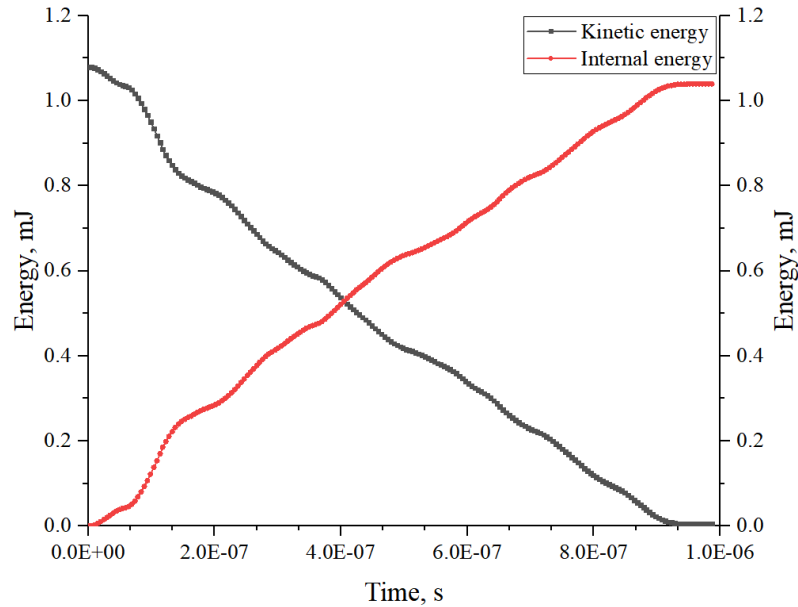
Fig. 4.20. The ALLKE and ALLIE variation for the whole model during the entire simulation

4.3.4 Summary of results

This section proposes to use the CEL method to simulate the deposition process of cold spray multi-particles on the Al6061 substrate. A multi-particle wrapped model is embedded in the deposition model created by CEL to simulate the deposition process of multi-particle Al6061 particles on the Al6061 substrate.

Using the CEL method to establish a multi-particle deposition model to simulate the actual cold spray process can be used to monitor and calculate coating porosity, which cannot be achieved by the ALE method and the SPH method. By calculating the value of EVF Void of the coating after simulated deposition, the calculated void ratio is used as the value to characterize the porosity of the coating.

The temperature change and distribution of the surface of the substrate after deposition of the multi-particle deposition model; the maximum temperature on the

surface of the substrate after deposition is 528.2 K, and the maximum temperature is located at the interface between particles after deposition. Observing the temperature change curves of five points on the substrate with time steps, the temperature curve of substrate point 1-4 temperature has multiple inflection points, indicating that multiple impacts caused the temperature to rise, and then the temperature dropped rapidly.

During the multi-particle deposition process, the matrix is squeezed into the gaps between the coating particles due to thermal softening, excessive plastic deformation and thermal expansion. After the spraying is completed, as the interface temperature decreases, the matrix is squeezed into the gaps in the coating due to plastic deformation. The modulus of the base material returns to room temperature, thereby bonding with the base material.

4.4 Simulating multi-particle deposition based on the CEL method: studying the influence of particle and substrate temperature on deposition

This section proposes a method using the CEL method to build a multi-particle model in the Euler domain to simulate the deposition process of multi-particle Al6061 particles on the Al6061 substrate. By studying the effects of particles and substrates at different temperatures on the deposition process, it is observed that the shape of the coating and the temperature distribution on the surface of the substrate after deposition and the effect of temperature on porosity.

4.4.1 The particles model and Eulerian domain

A typical particle size distribution measured using a microvolume laser powder analyzer is shown in Figure 4.21. The cumulative probability distribution of the particle sizes shown is estimated by a lognormal function.
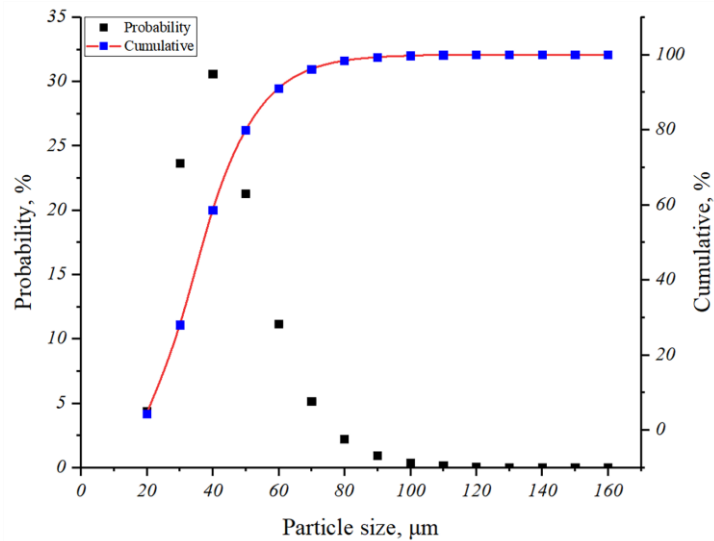
Fig. 4.21. Particle size distribution and cumulative distributions

In order to accurately represent the actual cold spray process, this section generates particles by uniformly sampling mass fraction parameters. The position coordinates of each particle are randomly assigned within the Euler domain. As shown in Figure 4.22, 200 Al6061 particles with a diameter of 20-70 um are modeled through a Python script (as see Appendix A).

a   *b*
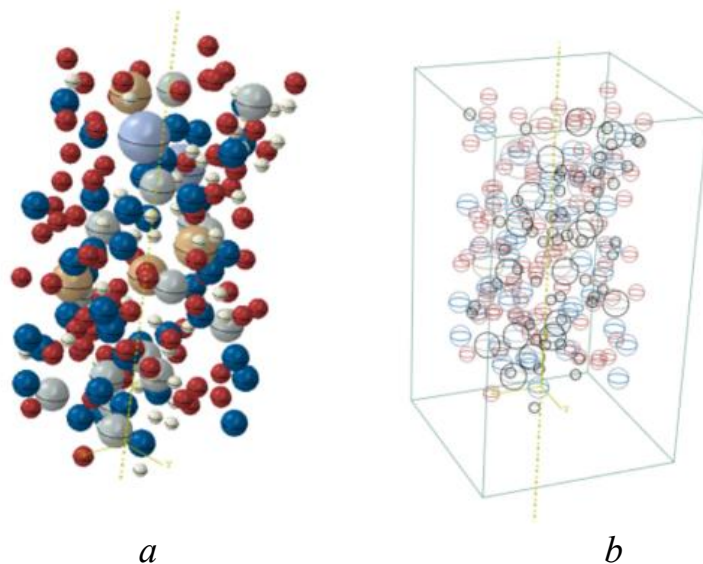
a – multi-particle model established by Python script; *b* – Al6061 particles in the Eulerian domain

Fig. 4.22. The Al6061 Multi-particle model

It is necessary to ensure that each particle is distributed independently and there is no contact between particles to meet the conditions for simulated spraying. The Euler domain must wrap all particles. The Euler domain is set to the long method. The advantage is that it can generate a uniform hexahedral structure mesh. Some scholars set the Euler domain as a cylinder. The mesh generated by the cylinder is mainly a tetrahedral mesh, it is difficult to converge during the calculation process.

4.4.2 Material model, velocity, temperature, and predefined fields

Simulate the multi-particle deposition process through the CEL method. Assuming that the material is isotropic, an inelastic heat share parameter needs to be set, and its properties are shown in Table 4.3. Plastic hardening adopts the J-C model to describe the dependence of material behavior on rate and temperature, and adds a hardening J-C model representation that depends on the change rate equations (4.2) and (4.3). For the settings of some material models, please refer to Chapter 4.2.2.1.

The work of this section investigates the effect of particle and substrate temperature on post-deposition coatings. Reference [167] gives all Al6061 particles velocity value of 585 m/s in this work to ensure that all Al6061 particles can be uniformly ordered particles/substrates, and particle/particles deposit. As stated above, all particles are included in the Euler domain, so the essence is that all particles flow in the Euler domain, and the deposition process will be completed in the Euler domain.

This section controls the temperature range of Al6061 particles and Al6061 substrate to 400-700 K, and increases the temperature by 50 K for each working condition, and studies the effects of different temperature working conditions on the post-deposition coating. A coupled temperature-displacement dynamic step with an appropriate time period is assigned to track the entire multi-particle impact process from the start of the simulation to the complete stop of all particles, with a total range

of 970 to 100 ns; where the contact model adopts dynamic, temperature-displacement, Explicit model; define tangential and normal behavior as well as friction coefficient. Assign materials to all particles in the predefined field; use the discrete field volume fraction tool to set parameters for all particles in the Euler domain, and calculate the volume fraction of all particles in the Euler domain through field data to ensure that later the calculation proceeds smoothly.

The model of the substrate is Lagrangian, which ensures that the contact surface between the deposited particles and the substrate can be accurately observed. When meshing the substrate, the mesh density decreases from the inside to the outside; the central area of the substrate is the main deposition site, so the mesh size in this area is smaller.

All the particles mentioned above are wrapped in the Euler domain, as shown in the red area in figure 4.23.
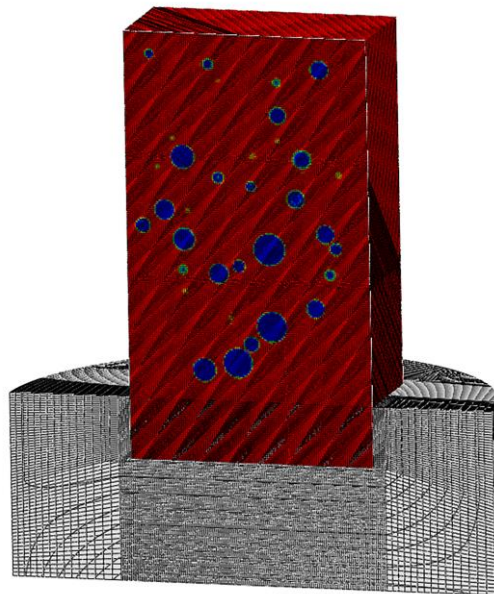

Fig. 4.23. The half-section view of model assembly and meshing

The essence is that the particles flow at high speed in the Euler domain, so the bottom of the Euler domain and the top of the substrate in the Lagrangian domain perform partial overlap to ensure that the Al6061 particles after deposition can still

213

be completely included in the Euler domain, so that the coating formed after the deposition is still within the Euler domain, ensuring the integrity of the calculation results; From the Figure 4.23, Half-section view of model assembly and meshing. The contact algorithm automatically calculates and tracks the interface between the two domains, ignoring the heat exchange between the particles and the substrate, considering the process to be adiabatic [15].

4.4.3 Results and discussion

Single factor influence was used to study the influence of the temperature of Al6061 particles and substrate on the deposited coating. Figure 4.24 shows a cross-sectional view of the EVF of the coating after deposition of particles in the temperature range of 400-700 K, substrate temperature is constant 400 K. Figure 4.25 shows a cross-sectional view of the EVF of the coating after deposition of substrate in the temperature range of 400-700 K, particles temperature is constant 400 K. The EVF void value, the red EVF void has a value of 1, indicating the void area. The value of blue EVF void is 0, which means that the element is filled with material; observing the value of EVF void can characterize the porosity of the coating.

Observing the thickness of the coating, it can be seen that changing the particle temperature has a more obvious control effect on the porosity of the coating. Increasing the temperature of the particles is beneficial to the deposition process. The substrate temperature is constant, and increasing the temperature of the particles can reduce the porosity of the coating increases the density of the deposited coating. By simulating the deposition of multiple particles on a substrate using the CEL method, the porosity of the coating after deposition can be monitored.
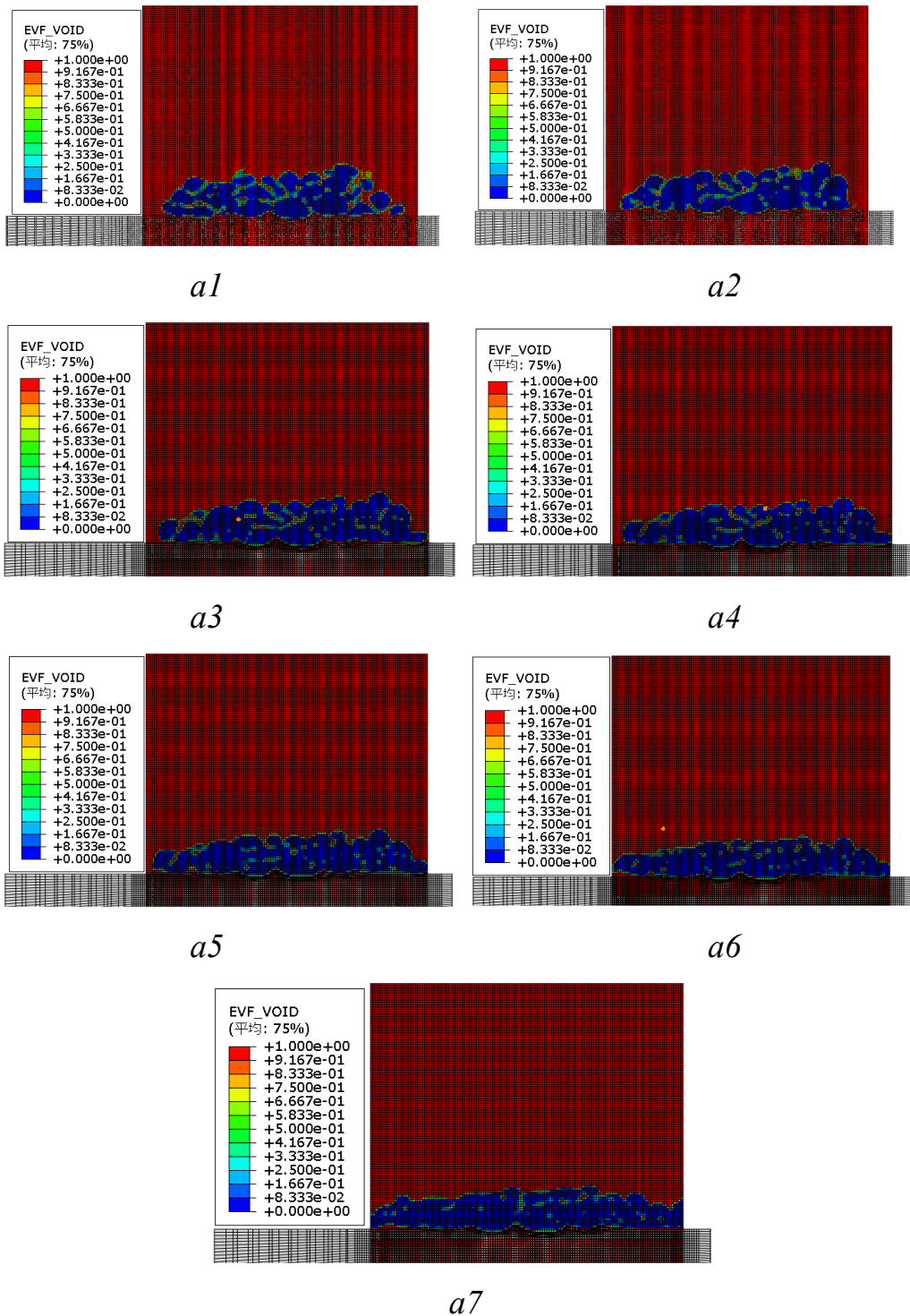
a1 – Particle temperature 400 K; *a2* – Particle temperature 450 K; *a3* – Particle temperature 500 K; *a4* – Particle temperature 550 K; *a5* – Particle temperature 600 K; *a6* – Particle temperature 650 K; *a7* – Particle temperature 700 K

Fig. 4.24. The cross-sectional view of the EVF of the coating after deposition of particles in the temperature range of 400-700 K, substrate temperature is constant 400 K.
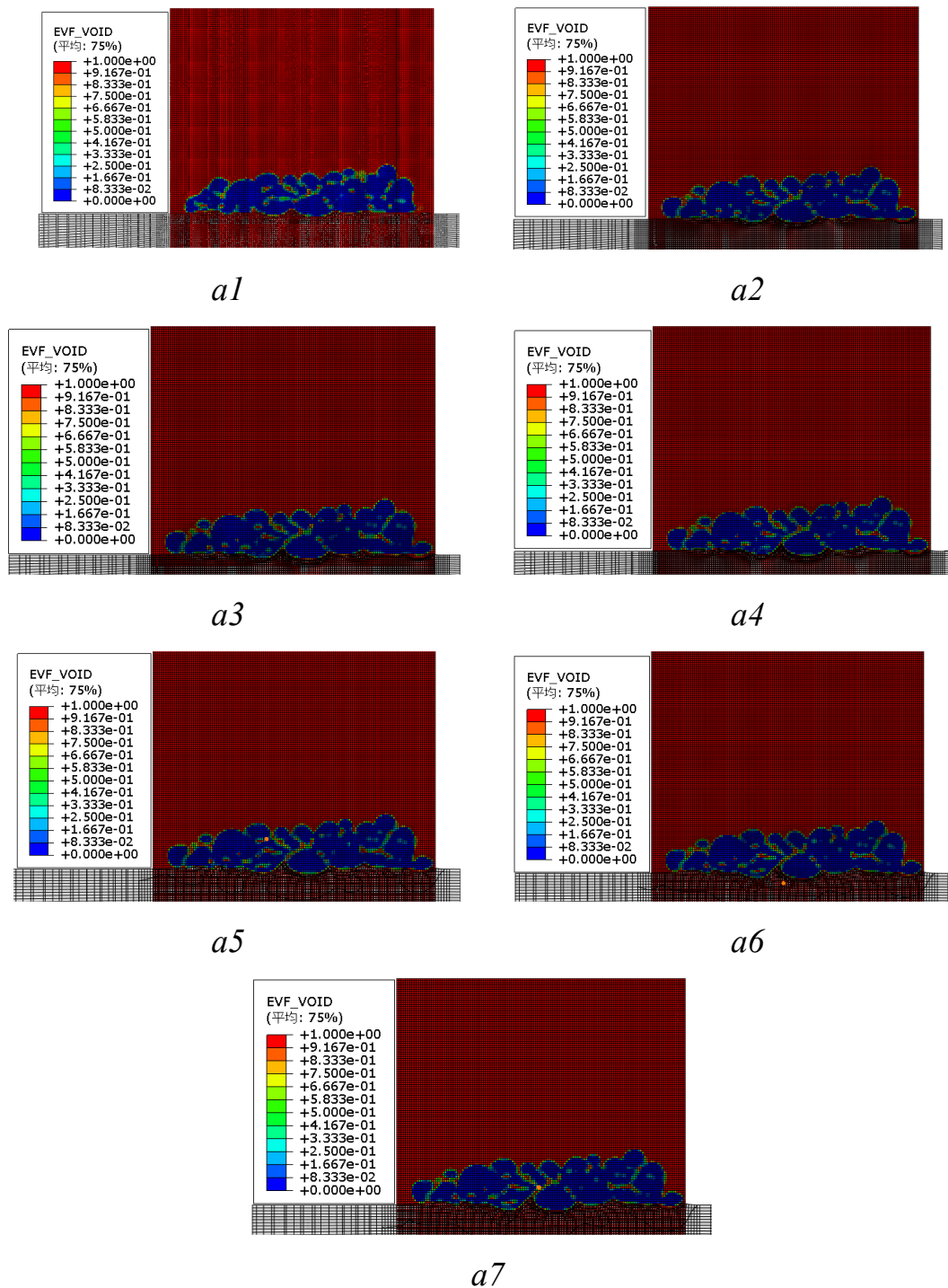
a1 – substrate temperature 400 K; *a2* – substrate temperature 450 K; *a3* – substrate temperature 500 K; *a4* – substrate temperature 550 K; *a5* – substrate temperature 600 K; *a6* – substrate temperature 650 K; *a7* – substrate temperature 700 K

Fig. 4.25. The cross-sectional view of the EVF of the coating after deposition of substrate in the temperature range of 400-700 K, particle temperature is constant 400 K.

216

Figure 4.26 shows the temperature distribution on the surface of the substrate after particles of different temperatures impact the constant-temperature substrate. Figure 4.26 shows that there are many pits on the surface of the substrate. The high-temperature areas of the substrate after the deposition are mainly distributed in pits and pits. The junction can also be explained as: the high temperature zone is mainly located at the extrusion part between particles. During the deposition process, the particles impact the surface of the substrate to form pits, and the junction of the pits generates a large amount of heat due to the high-speed extrusion of the particles, causing the substrate to heat up rapidly, and the temperature is higher than the initial temperature of the substrate, which is conducive to the mechanical interlocking between the particles and the substrate.
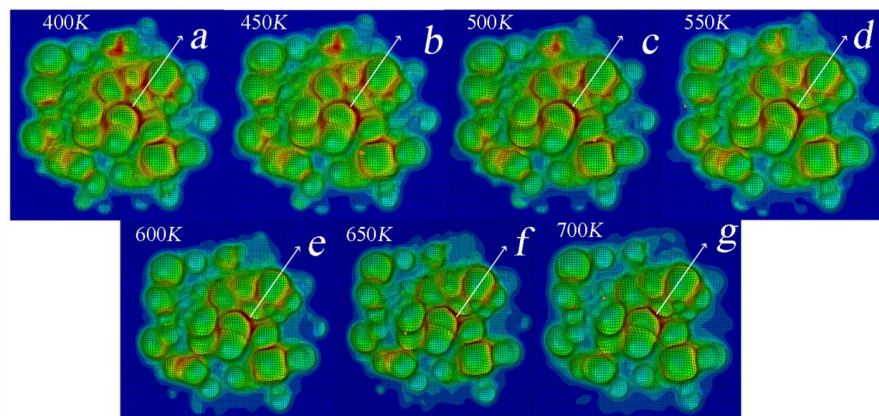
Fig. 4.26. Temperature distribution on the surface of the substrate after Al6061 particles of different temperatures impact the constant-temperature substrate

In Figure 4.26, select seven points a, b, c, d, e, f, and g on the same part of the substrate surface, and observe the temperature changes of these five points during the deposition process under different temperature conditions are shown in Figure 4.27. From the temperature curve of the substrate surface, it can be seen that the temperature of the substrate surface dropped briefly, then rose sharply and then dropped again. Due to a large number of particles continuously hit the surface of the substrate, causing the surface of the substrate to heat up rapidly. This process is a

deposition between the particles and the substrate, and the temperature of the substrate reaches a peak during this process. When some particles complete the deposition on the substrate, the subsequent particles continue to hit the particles that have completed the deposition. This process is a deposition between particles. This process transfers less heat to the substrate, so the temperature of the substrate decreases. During the temperature drop of the substrate, the temperature of the substrate decreases. An oscillation curve appears, because the subsequently deposited particles continue to deposit with the previous coating. And a small part of the heat generated during the deposition is transferred to the substrate, causing the temperature drop rate of the substrate to change. When the thickness of the coating reaches a certain value, the particles very little temperature is transferred to the substrate, so the surface temperature of the substrate decreases steadily.
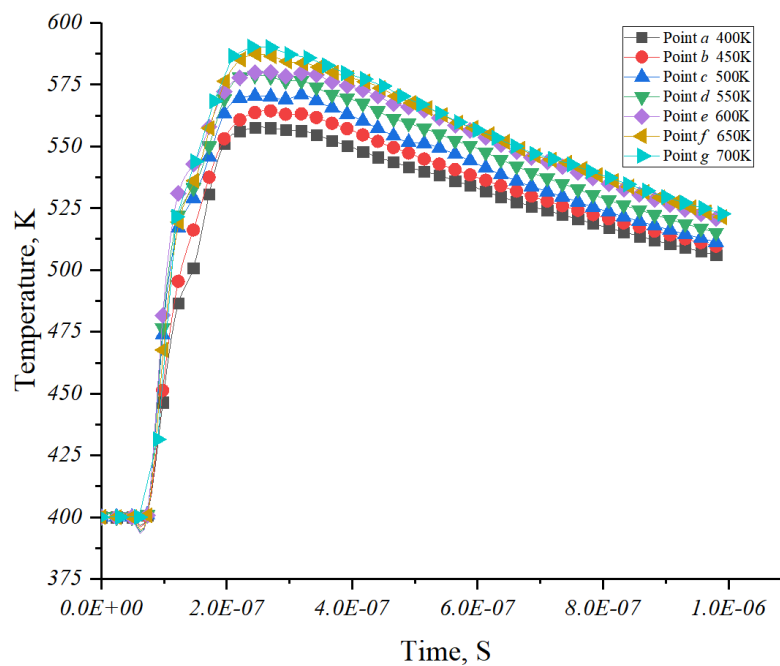
Fig. 4.27. Temperature changes over time at selected points on the substrate surface

Figure 4.28 shows cross-sectional view of coating temperature after deposition of particles and substrate in the temperature range of 400-700 K.
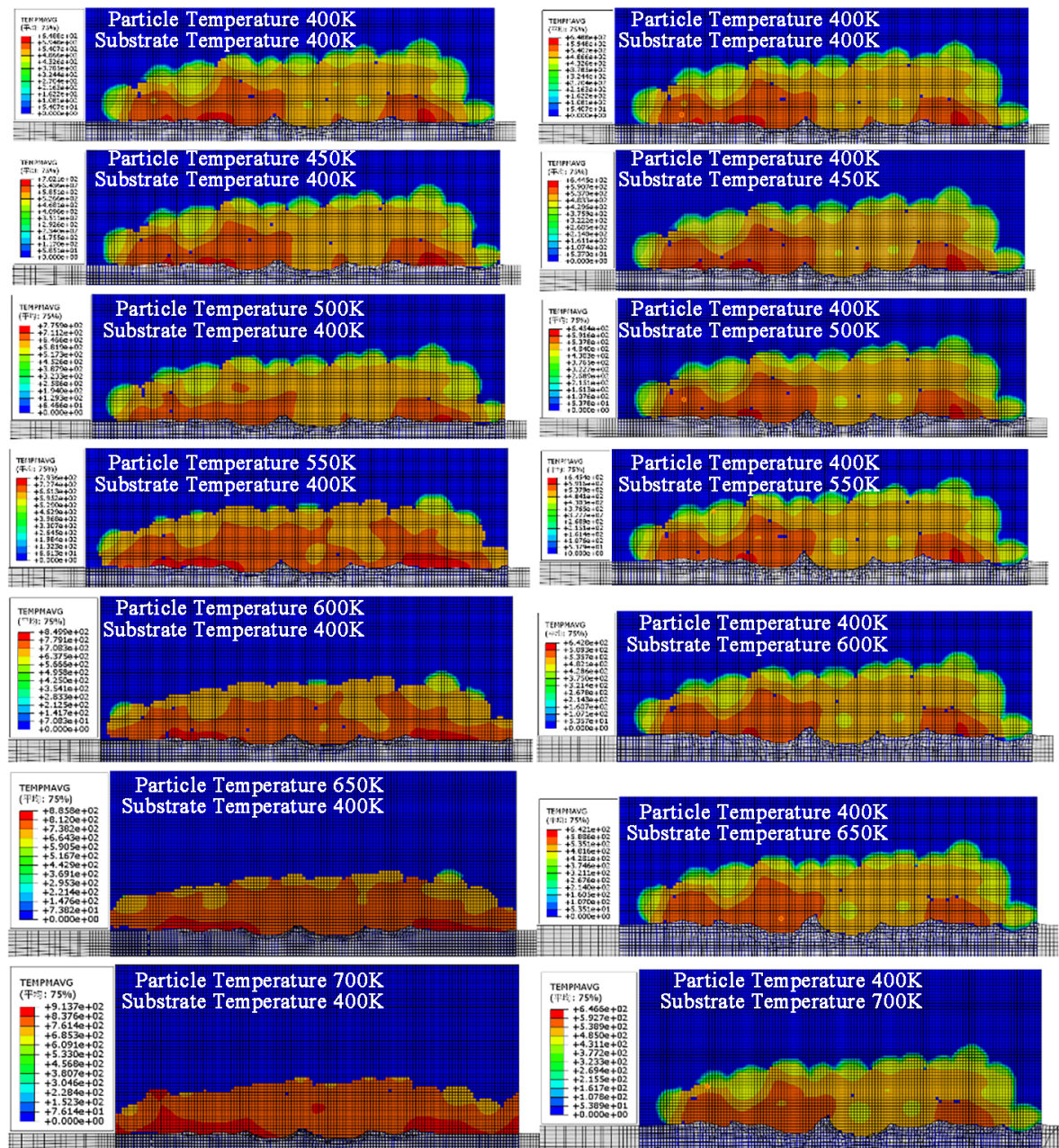
Fig. 4.28. Temperature cross-section of the coating surface after deposition of particles and substrate in the temperature range of 400-700 K

It can be seen from Figure 4.28 that the high-temperature area of the coating after the deposition of the particles is mainly located at the contact area between the particles and the substrate. As the temperature of the particles increases, the high-temperature area also increases; by observing the thickness of the coating after deposition, it is better to change the temperature of the particles than to change the temperature of the substrate. When the substrate temperature is constant, after the

particle temperature reaches 650 K, the coating changes after deposition are no longer significant, which shows that there is an optimal temperature range for Al6061 particle deposition. Observing the temperature cross section of the substrate, it can be seen that the particles temperature does not have a significant impact on the surface of the substrate after deposition; during the deposition process, it shows that the temperature generated by the deposition between particles mainly acts between particles. As can be seen from Figure 4.28, the substrate temperature has no obvious effect on the coating. Because during the deposition process, most of the mechanical bite between particles occurs. The changes that affect the temperature of the substrate are mainly particles that deposit with the substrate.

Figure 4.29 shows temperature cross-section of the substrate after deposition of particles and substrate in the temperature range of 400-700 K. It can be seen from Figure 4.29 that the substrate temperature is constant. Increasing the particles temperature does not have a significant effect on the substrate temperature after deposition. Based on the analysis of Figure 4.26, the rapid heating stage of the substrate is caused by the direct impact of particles on the substrate. When the subsequent particles deposit with the particles, the heating of the substrate is not significant. The results are the same as shown in Figure 4.28. The particles temperature is constant. Increasing the substrate temperature can increase the deposition depth of the particles on the substrate, which is beneficial to the combination of the substrate and the coating after deposition. when the substrate temperature exceeds 650 K, sputtering occurs on the surface of the substrate. Excessive substrate temperature causes the material to soften, and the high temperature zone is mainly located at the connection of the pits, which is the same as the result in Figure 4.26.
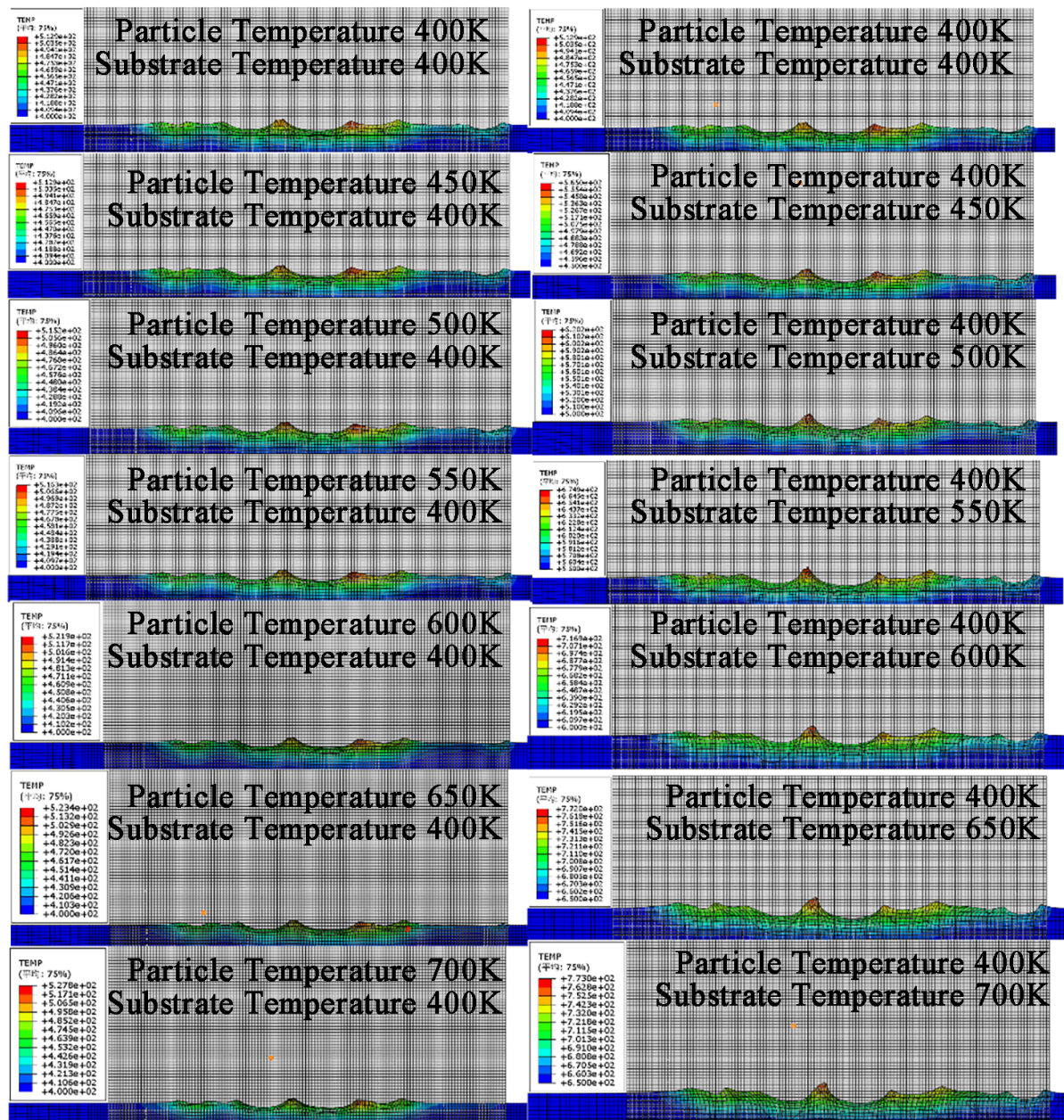
Fig. 4.29. Temperature cross-section of the substrate after deposition of particles and substrate in the temperature range of 400-700 K

4.4.4 Summary of results

Study the effects of Al6061 particles and substrates at different temperatures on the deposition results, the shapes of the coating and substrate after deposition are observed, as well as the coating and the temperature distribution of the substrate cross section; Currently the CEL method can accurately simulate the multi-particle

deposition method of cold spray deposition. Changing the particle temperature has a more obvious control effect on the porosity of the deposited coating, thereby improving the density of the deposited coating; preheating the particles can effectively reduce the porosity; simulate multi-particles on the base through the CEL method the deposition on the material allows monitoring of the porosity of the coating after deposition, which is not possible with the ALE and the SPH methods. After particles of different temperatures impact the constant-temperature substrate, the high-temperature area on the surface of the substrate is mainly located at the junction of pits; this is the result of high-speed extrusion between particle depositions. The latter particles have little effect on the temperature change of the substrate. When the particle temperature reaches 650 K, the coating changes after deposition are no longer significant, indicating that there is an optimal temperature range for Al6061 particle deposition; therefore, excessively increasing the temperature of the particles is not the best solution. Increasing the temperature of the substrate can increase the depth of particle deposition on the substrate, which is beneficial to the combination of the substrate and the coating after deposition.

4.5 Simulation of the effect of multi-particle temperature on coating porosity based on the CEL method

There are currently two methods for checking the porosity of coatings. One is to obtain experimentally and characterize the coating through cross-sectional SEM image analysis or XMT. The other is to use numerical simulation methods to predict the porosity of the coating. The single-particle deposition model simulated by the CEL method cannot represent the interaction between coating accumulation, particle size, velocity, and temperature. Therefore, it is necessary to simulate the process of multi-particle formation of coatings. The multi-particle deposition model is between the microscopic method of single particle simulation and the macroscopic method of homogeneous material deposition. Multi-particle deposition models can be used

to simulate complex interactions between multiple particles, which cannot be achieved by single-particle deposition models.

This section simulates the deposition of Al6061 particles/substrate by establishing a multi-particle deposition model and changes the particle temperature to study the porosity of the coating. The CEL method has the characteristics of high accuracy and robustness and was selected as the simulation method for the multi-particle deposition model. Multiple groups of sampling methods are used in the coating to calculate the porosity of the sampling groups to further characterize the entire porosity. Take several groups of cuboid samples from the coating, and calculate the value of the void area of each group of samples. Finally, find the average value as the value of the void area of the coating under a certain working condition, and identify this value as the porosity of the coating.

4.5.1 The multi-particle deposition model

The CS process can be viewed as a process in which multiple particles continuously impact the substrate. Several different finite element techniques described in the introduction are used to model the spatial discretization of CS processes. The CEL method is considered to be the most robust and accurate solution for simulating the CS process at present. Its characteristic is that the CEL deposition model contains both the Eulerian domain and the Lagrangian domain. In the Eulerian domain, granular materials are not constrained by predefined elemental discretization. Particles flow freely within a discrete domain of fixed elements, and the volume fraction value characterizes the specific number of particles that each element can contain at any given time and is compatible with large deformations of particles in depositions.

4.5.1.1 The Multi-particle model and material model

The particle size distribution of multi-particles is shown in Figure 4.21. The cumulative probability distribution of particle size is described by the log-normal function. Choose a multi-particle particle size of 30-50 um and particles number of 200. The establishment of the multi-particle model is implemented using Python scripts, as see appendix A. The multi-particle model is established through a custom algorithm. By inputting the number and volume percentage of particles, multiple particles are randomly distributed in the Euler domain. In this process, overlap between particles is avoided. Its principle whether the distance between particles in spatial coordinates is greater than the sum of the radii between particles, a mathematical expression to avoid particle overlap (as see equation (4.1)).

4.5.1.2 The deposition model

The work of this dissertation is to study the effect of particles at different temperatures on the porosity of the coating. All Al6061 particles are given a velocity value of 585 m/s, so that all particles can deposit. The temperature of the particles is 600-700 K, increasing by 50 K for each working condition; the substrate temperature is 400 K. Assign a coupled temperature-displacement dynamic step with an appropriate time period to track the entire multi-particle impact process from the start of the simulation to the complete stop of all particles, with a total range of 970 to 1000 ns. As mentioned above, all particles are included in the Euler domain, so the entire process of simulating multi-particle deposition by the deposition model will be completed in the Euler domain. The model of the base material is Lagrangian, so part of the Euler domain in the entire deposition model should be nested in the base material to ensure that the coating formed after the deposition is still in the Euler domain, ensuring the integrity of the calculation results. It should be noted that the partial mesh size of the Euler domain and the deposition substrate should be kept

consistent as much as possible. Figure 4.30 shows 1/4 section view of multi-particle deposition model. The contact algorithm automatically calculates and tracks the interface between the two domains, ignoring the heat exchange between the particles and the substrate, considering the process to be adiabatic. For other parameter settings, refer to Chapters 4.2.2.2 and 4.2.2.3.
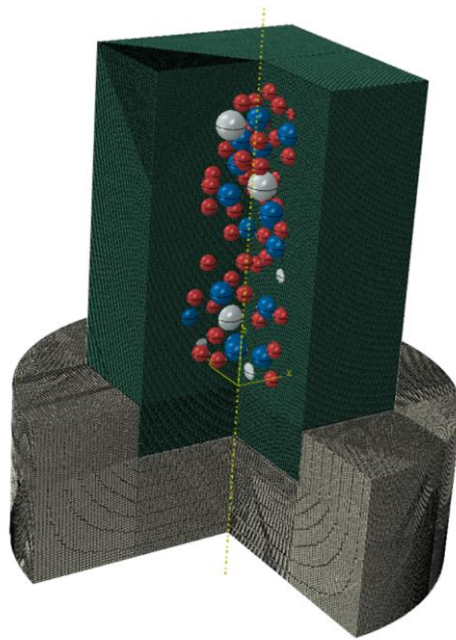
Fig. 4.30. The 1/4 section view of multi-particle deposition model

4.5.2 Results and discussion

Figure 4.31 shows a cross-sectional view of the EVF of voids in the coating formed after multi-particle depositions at different temperatures. The red EVF void value is 1, indicating the gap area, the blue EVF void value is 0, indicating that the element is filled with material. Observing the value of EVF void can characterize the porosity of the coating. It can be found from the Figure 4.30 that there are void areas inside the coating; the thickness of the coating decreases significantly when the temperature of the particles is increased, indicating that increasing the temperature of the particles is beneficial to the CS process. Observing the cross-section, the void value inside the coating decreases. Therefore, the porosity of the

coating can be characterized by calculating the value of the void area of the coating after simulated spraying, which is what the ALE and the SPH methods cannot achieve; this is due to the fact that the grid in the Eulerian domain in the CEL method does not follow the particles change due to deformation. In order to better and more accurately express the porosity of the coating, we take several groups of cuboid samples in the coating, calculate the value of the void area of each group of samples, and finally obtain the average value as the coating's porosity under certain working conditions. The value of the void area is considered to be the porosity of the coating.
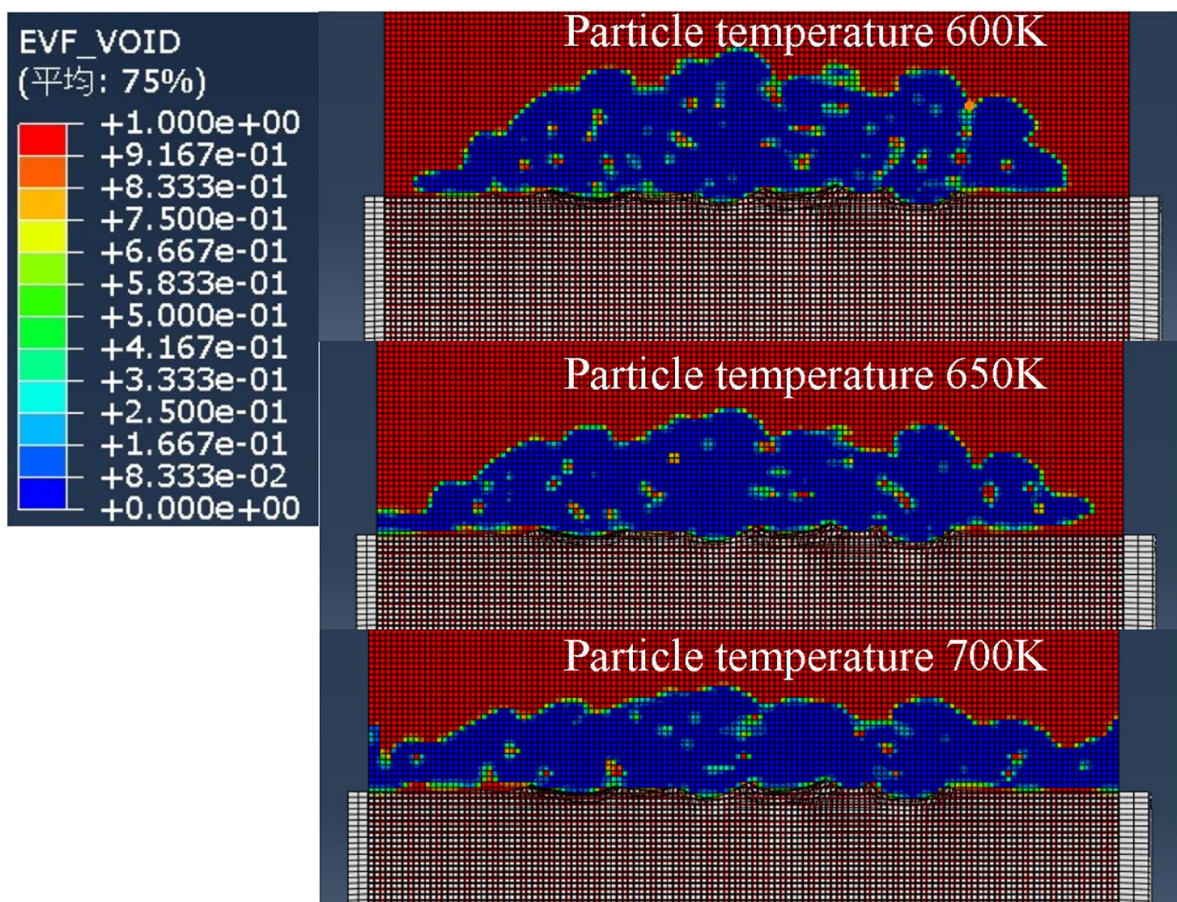
Fig. 4.31. The cross-sectional view of EVF voids of a multi-particle coating

Figure 4.32 shows the mutual conversion between kinetic energy and internal energy of particles in the entire deposition model. The time to complete the deposition was within the estimated time frame. Almost all kinetic energy is converted into internal energy, and the process is stable, indicating that the entire

deposition model has good stability.
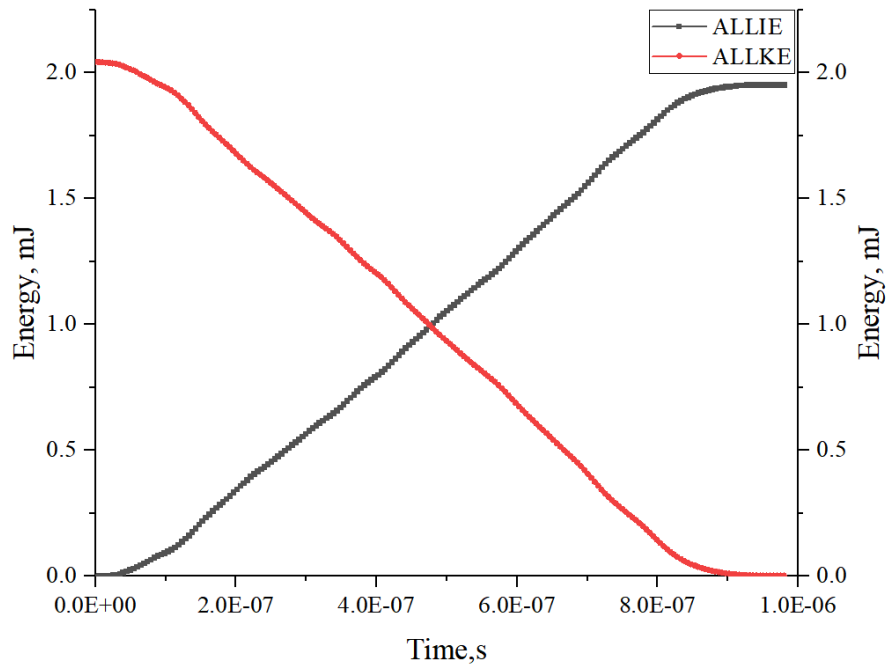
Fig. 4.32. The ALLKE and ALLIE variation for the whole model during the entire simulation

Four groups of EVF cuboids with dimensions of 900 um×900 um×30 um was selected from the coating for each working condition, and the cuboid samples were distributed as far as possible inside the center of the coating, as shown in the sampling area map in Figure 4.33. In the Python script, most of the multi-particle arrangements tend to be in the central area; the coating at the same height is selected for sampling under all working conditions, and then 4 groups of samples are selected from this layer, which allows the final calculation results to characterize the coating the porosity is more representative. It can be seen from observation that when the coating height is 90 um. increasing the temperature of the particles will reduce the void value of the coating with the same height, which is the same as the result expressed in Figure 4.31. Increasing the particles temperature can reduce the porosity, which is consistent with our conjecture.
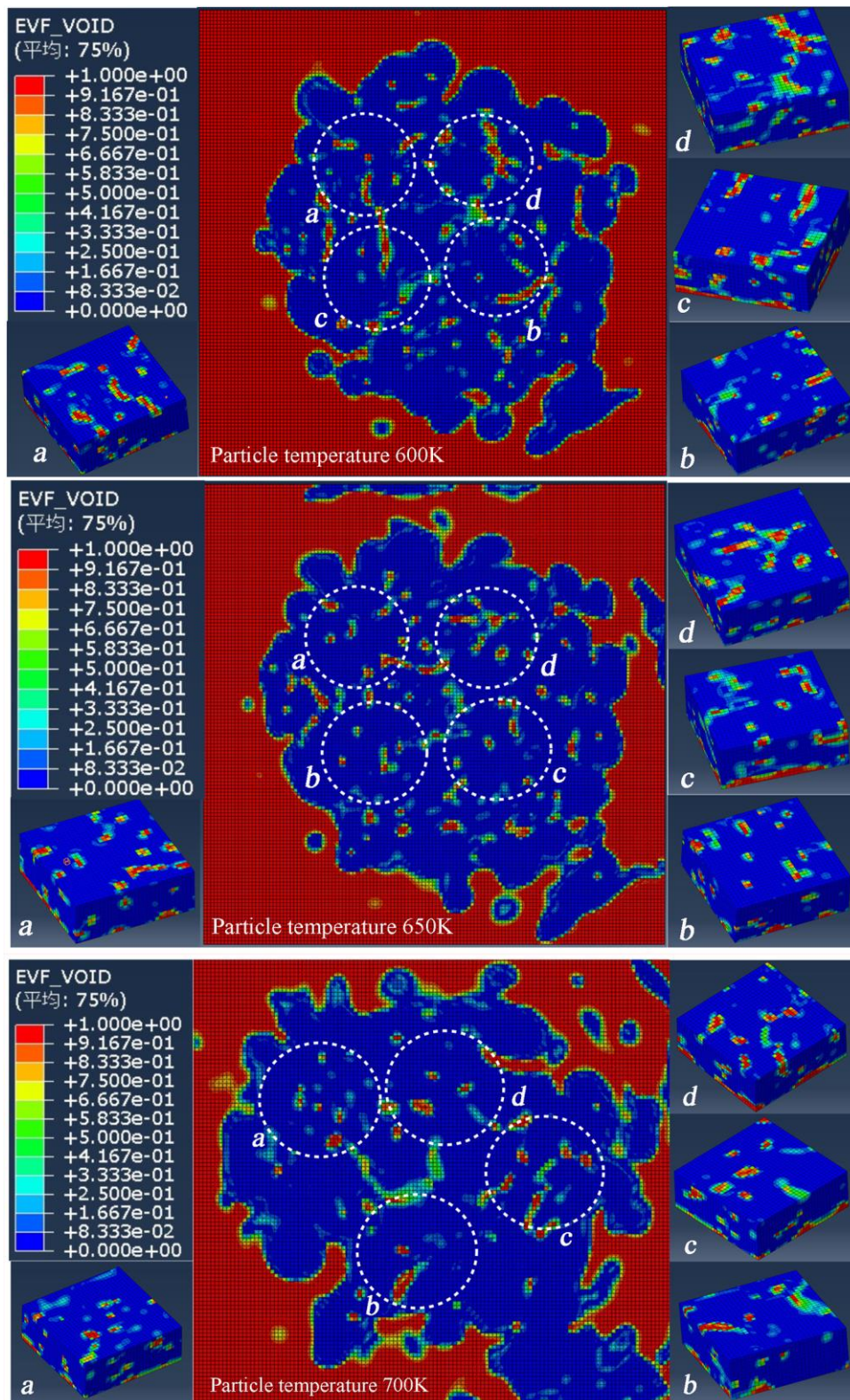
Fig. 4.33. Sampling area map

It is obvious from Figure 4.34 that increasing the temperature of the particles can reduce the porosity. When the particle temperature goes from 600 K to 650 K, the porosity of the coating decreases faster than when the particle temperature

changes from 650 K to 700 K. This shows that continuously increasing the particle temperature is not the best way to reduce porosity. To ensure the lowest porosity, there is an optimal particle temperature range. The particle temperature is 600 K, the average porosity of the coating is 5.08%; The particle temperature is 650 K, the average porosity of the coating is 4.02%; The particle temperature is 700 K, the average porosity of the coating is 3.58%. This is the result obtained using single factor research method.
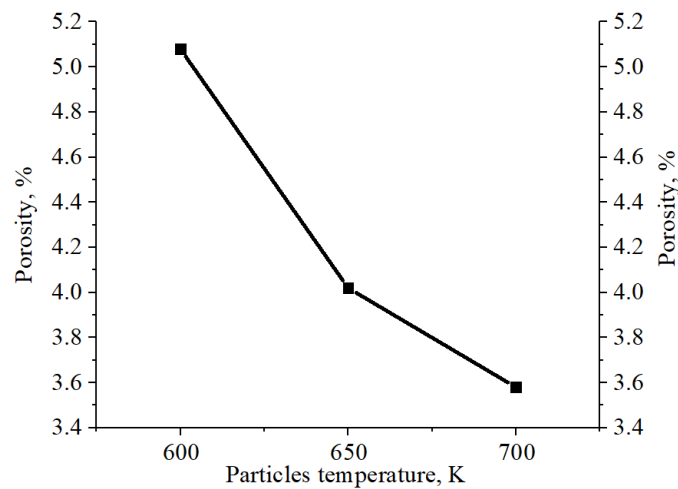
Fig. 4.34. The average porosity of the coating obtained at different temperatures

In order to understand the process of porosity reduction in more detail, the void area percentages of 12 groups of EVF cuboids under temperatures conditions were compared individually, and then each group of EVF cuboids was divided into 10 layers and calculated separately. Their value for the void area of the coating. As shown in Figure 4.35 porosity of each layer in the sampling group are shown. The first set of data corresponds to the top of the coating, and the 10th set of data corresponds to the bottom of the coating. Combined with Figure 4.34, it can be seen that the porosity curve decreases as the particle temperature increases, and the porosity of each layer corresponding to the same position of the coating also decreases. The porosity of the coating at the bottom layer is the highest, and the porosity of the coatings on layers 6-9 is lower. This happens to indicate that the inside of the deposited coating is compacted, which is consistent with the CS process.

The reason for the greater porosity between the particles and the substrate is that the temperature difference between the two is large. Compared with the interfacial bonding between the particles, the temperature of the substrate has little effect on the porosity [125]. Increasing the substrate temperature will facilitate the connection between the particles and the substrate [126]. It is suggested here that appropriately raising the substrate temperature will benefit the CS process and achieve the requirement that the temperature difference between the particles and the substrate should not be too large.
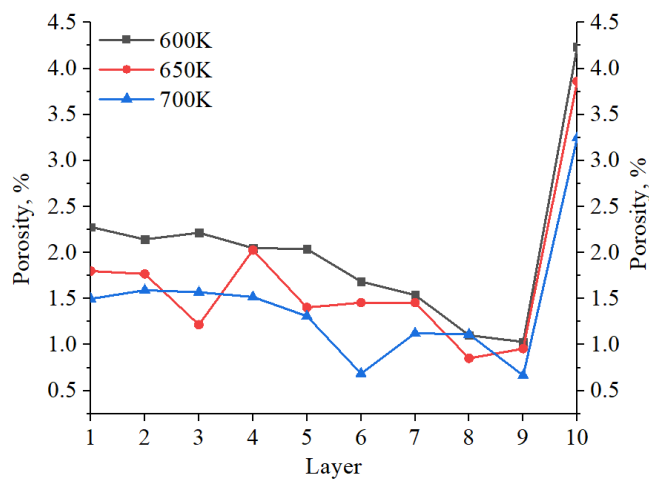
Fig. 4.35. The average porosity of each layer coating obtained at different temperatures

4.5.3 Summary of results

This section uses the CEL method to establish a multi-particle Al6061 deposition model by studying the relationship between the particle temperature and the porosity of the coating. Four groups of samples were taken from the coating surface under different temperature conditions, the porosity of the four groups of samples was calculated, and finally, their average value was taken as the porosity of the coating. The results show that the average porosity of the coating under the three temperature conditions is 600 K – 5.08%; 650 K – 4.02%; 700 K – 3.58%. Increasing the temperature of the particles can effectively reduce the porosity of the coating.

During the deposition process of multiple particles, the inside of the deposited coating will be compacted. In the CEL method, the grid in the Euler domain will not deform with the particles, and the value of the EVF void area can accurately express the porosity of the coating. The substrate temperature will affect the combination of coating and particles with the substrate, it is recommended that the temperature difference between the particles and the substrate should not be too large. Finally, it is recommended to study the coupling of multi-factors affecting the porosity of the coating.

4.6 Optimizing the porosity of Al6061 coating based on the RSM

In this section, particle temperature, substrate temperature, and particle velocity are used as independent variables. The three variables interact with each other in pairs. A linear regression equation model of Al6061 coating porosity is established through Design-Expert, and the RSM is used to predict the Al6061 coating. Optimum spray parameters for porosity. In Chapter 3, the RSM and GA optimize the BPNN are used to optimize spraying parameters; Both methods are multi-factor coupling impact analysis methods. Optimization of spraying parameters by neural network using the algorithm is highly probabilistic and highly dependent on programming algorithms [188, 189]. Therefore, it is more reliable to use the RSM to optimize the spraying parameters of Al6061 coating porosity.

4.6.1 The experimental design

The three-factor and three-level BBD experimental design method was adopted, the particle temperature, substrate temperature, and particle velocity were selected as key test factors. The porosity of the Al6061 coating was used as the target, and – 1, 0, and +1 respectively represented the numerical simulation factor levels, as shown in Table 4.4 for the design parameters.

Table. 4.4 − Design parameters of Al6061

Level	Factors		
	T_p / K	T_s / K	V_p / m/s
	Particle temperature	Substrate temperature	Particle velocity
-1	600	500	585
0	650	550	635
+1	700	600	685

4.6.2 Experimental results and analysis

Design-Expert DX10 data analysis software is used to process and analyze the numerical simulation results. The experimental arrangement and results are shown in Table 4.5.

Table. 4.5 − Simulation arrangement and results.

Run	High and low level code			Actual value			Impact V (m/s)
	Particle temperature	Substrate temperature	Particle velocity	Particle temperature (K)	Substrate temperature (K)	Particle velocity (m/s)	
1	0	0	0	650	550	635	2.65
2	+1	-1	0	700	500	635	2.49
3	0	-1	-1	650	500	585	3.91
4	0	-1	+1	650	500	685	1.89
5	0	0	0	650	550	635	2.65
6	+1	0	+1	700	550	685	1.71
7	0	0	0	650	550	635	2.65
8	-1	-1	0	600	500	635	2.73
9	0	+1	-1	650	600	585	3.89
10	-1	0	+1	600	550	685	2.01
11	-1	0	-1	600	550	585	4.25
12	0	0	0	650	550	635	2.65
13	0	+1	+1	650	600	685	1.83
14	+1	+1	0	700	600	635	2.42
15	+1	0	-1	700	550	585	3.61
16	-1	+1	0	600	600	635	2.73
17	0	0	0	650	550	635	2.65

4.6.2.1 Establishment of the linear regression equation for the porosity of Al6061 coating

The porosity regression equation of Al6061 coating

$$Y = 63.43 - 0.0104X_1 + 0.0227X_2 - 0.1757X_3 - 6.9999X_1X_2 + 3.4X_1X_3 - 4X_2X_3 - 8.5X_1^2 - 1.45X_2^2 + 1.065X_3^2, \qquad (4.4)$$

Table 4.6 shows the variance analysis of the porosity of Al6061 coating; It can be seen from the Table 4.6 that the model P < 0.0001, and the model regression equation is extremely significant. The correlation between the three factors and the experimental indicators is significant, the fitting degree is very good, and the error is small, indicating that the model is suitable for predicting the porosity of Al6061 coating.

Table. 4.6 − variance analysis of the porosity of Al6061 coating

Source	Sum of Squares	df	Mean Square	F Value	P-Value Prob>F
model	9.06	9	1.01	361.74	< 0.0001
X_1	0.27	1	0.27	98.82	< 0.0001
X_2	2.842E-003	1	2.842E-003	1.02	0.3458
X_3	8.35	1	8.35	3002.81	< 0.0001
X_1X_2	1.225E-003	1	1.225E-003	0.44	0.5282
X_1X_3	0.029	1	0.029	10.39	0.0146
X_2X_3	4.000E-004	1	4.000E-004	0.14	0.7158
X_1^2	1.901E-003	1	1.901E-003	0.68	0.4357
X_2^2	5.533E-003	1	5.533E-003	1.99	0.2013
X_3^2	0.30	1	0.30	107.28	< 0.0001
Residual	0.019	7	2.782E-003	-	-
Lack of Fit	0.019	3	6.492E-003	2.37	-
Pure Error	0.000	4	0.000	-	-

4.6.2.2 The degree of influence of each test factor on the test indicators

The contribution rate of experimental factors to experimental indicators is shown in Table 4.7. According to the F Value, the contribution rate of the three influencing factors of particle temperature, substrate temperature, and particle velocity to the porosity of the Al6061 coating can be judged. It shows that the particle velocity has the greatest impact, followed by particle temperature, and the substrate temperature has the least impact.

Table. 4.7 – The contribution rate of experimental factors to experimental indicators

Test index	Contribution rate of experimental factors			Contribution ranking
	X_1	X_2	X_3	
Y	98.82	1.02	3002.81	$X_3 > X_1 > X_2$

4.6.3 The impact and analysis summary of the interaction of various influencing factors on indicators

As shown in Figure 4.36, the interaction of three factors on the porosity of Al6061 coating is shown. From Figure 4.36 and combined with the analysis of the contribution rate of experimental factors to experimental indicators in Table 4.5, it can be seen that the contribution rate of particle velocity is more significant. Taking the Al6061 coating porosity as the target, the optimal Al6061 coating porosity is predicted to be 1.969%, as shown in Figure 4.37.
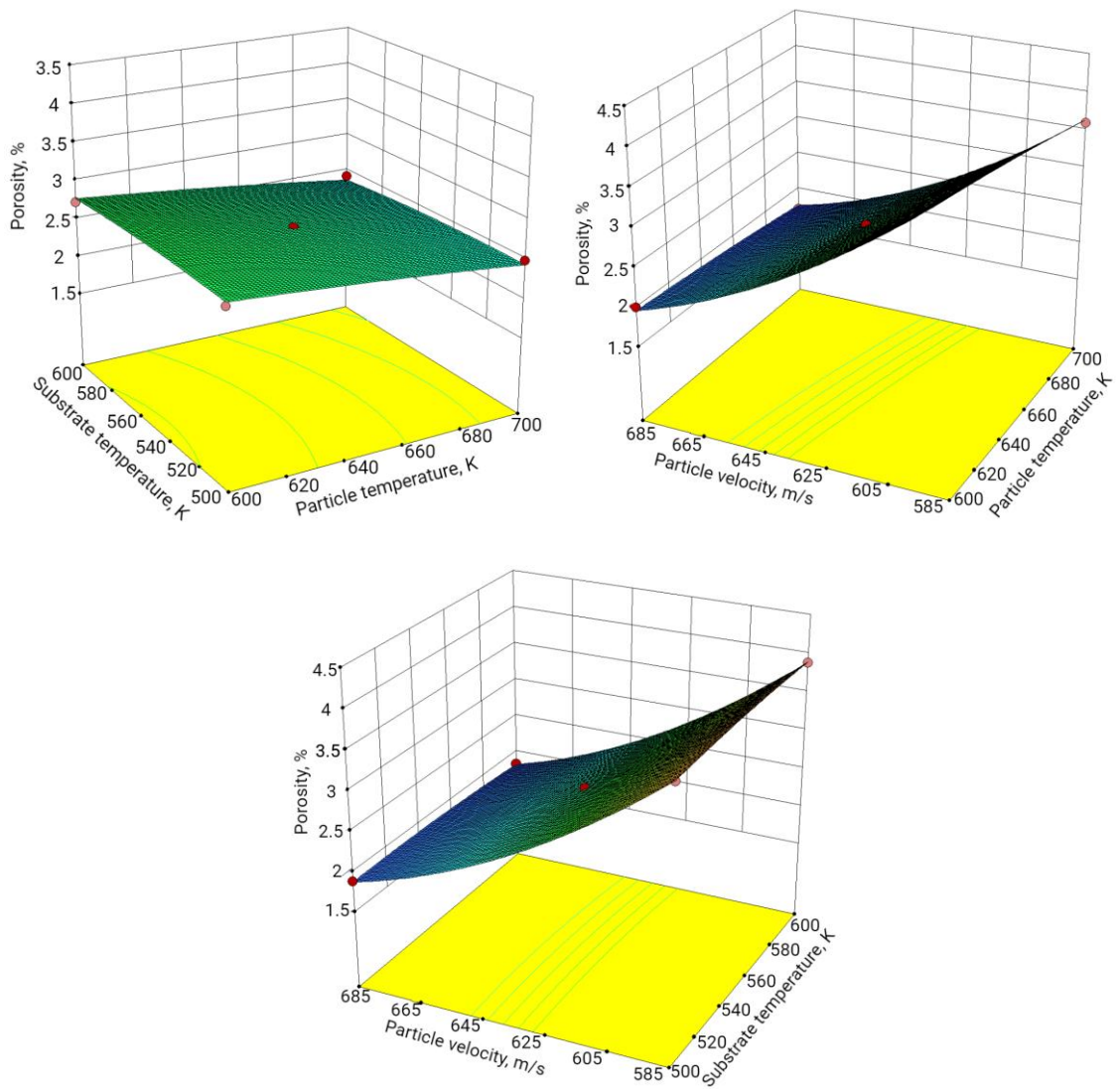
Fig. 4.36. The interaction of three factors on the porosity of Al6061 coating
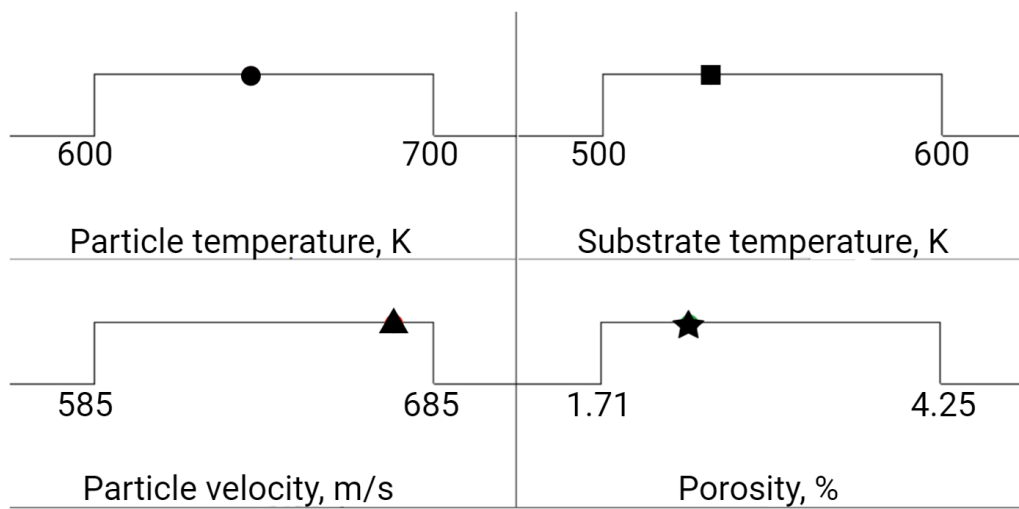
Fig. 4.37. Numerical simulation Al6061 coating porosity under optimal parameter

conditions

Figure 4.38 shows a cross-sectional view of the EVF voids of the Al6061 coating obtained with optimal spraying parameters.
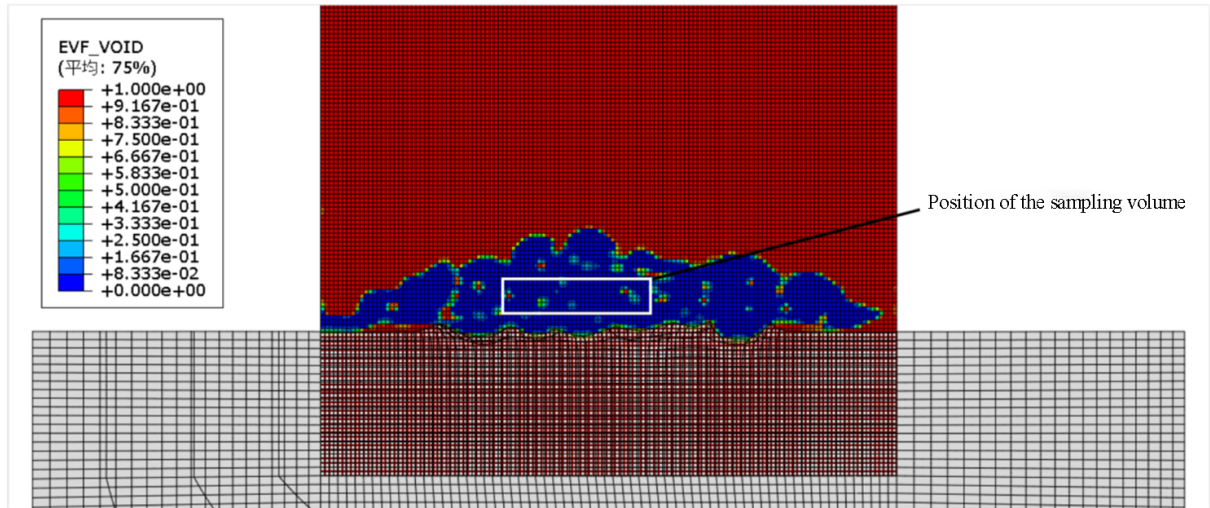
Fig. 4.38. The cross-sectional view of the EVF voids of the Al6061 coating obtained with optimal spraying parameters

Select the sample at the same height in the middle area of the layer. As shown in Figure 4.39, there are 4 sets of porosity sampling cuboids sliced from the central area of the coating. The size of each group of sampling cuboids is 20*20*10 um. In order to characterize the porosity level more accurately, multiple sets of sampling were used to calculate the average value of multiple sets of samples as the coating porosity. Figure 4.40 shows the cross-sectional view of the EVF voids after slicing each layer 1-5 of the four groups of sampling cuboids; Figure 4.41 shows the cross-sectional view of the EVF voids after slicing each layer 6-10 of the four groups of sampling cuboids. Through calculation, the porosity value of each layer in the sample is shown in Figure 4.42, the average porosity of the four groups of sampling cuboids is 1.91875%.
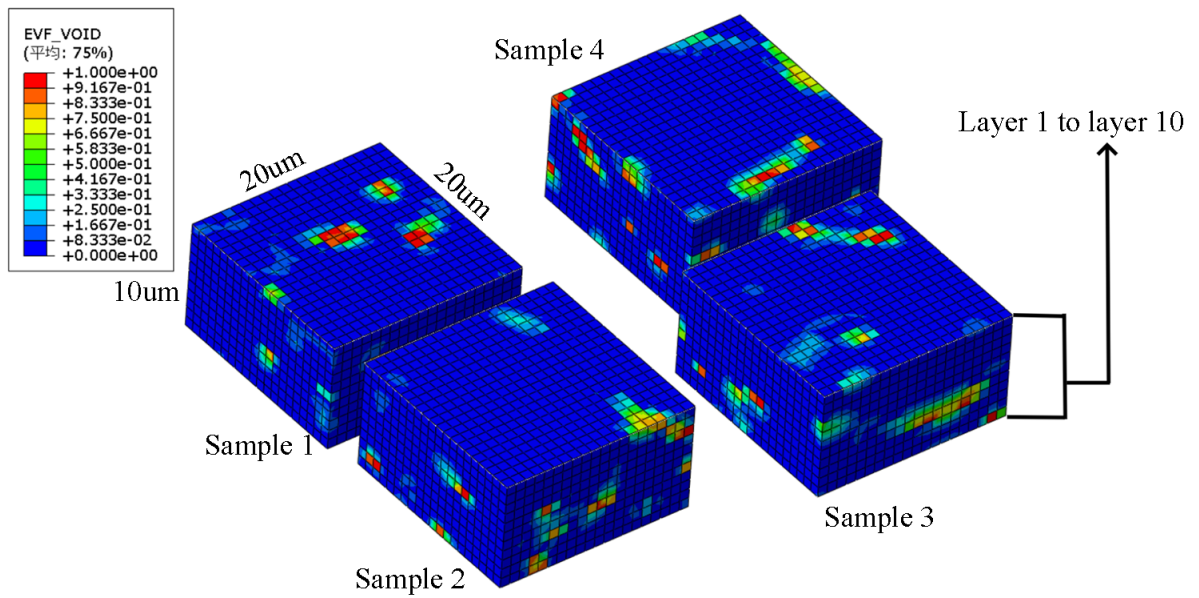
Fig. 4.39. Porosity sampling cuboid sliced from the middle area of the coating
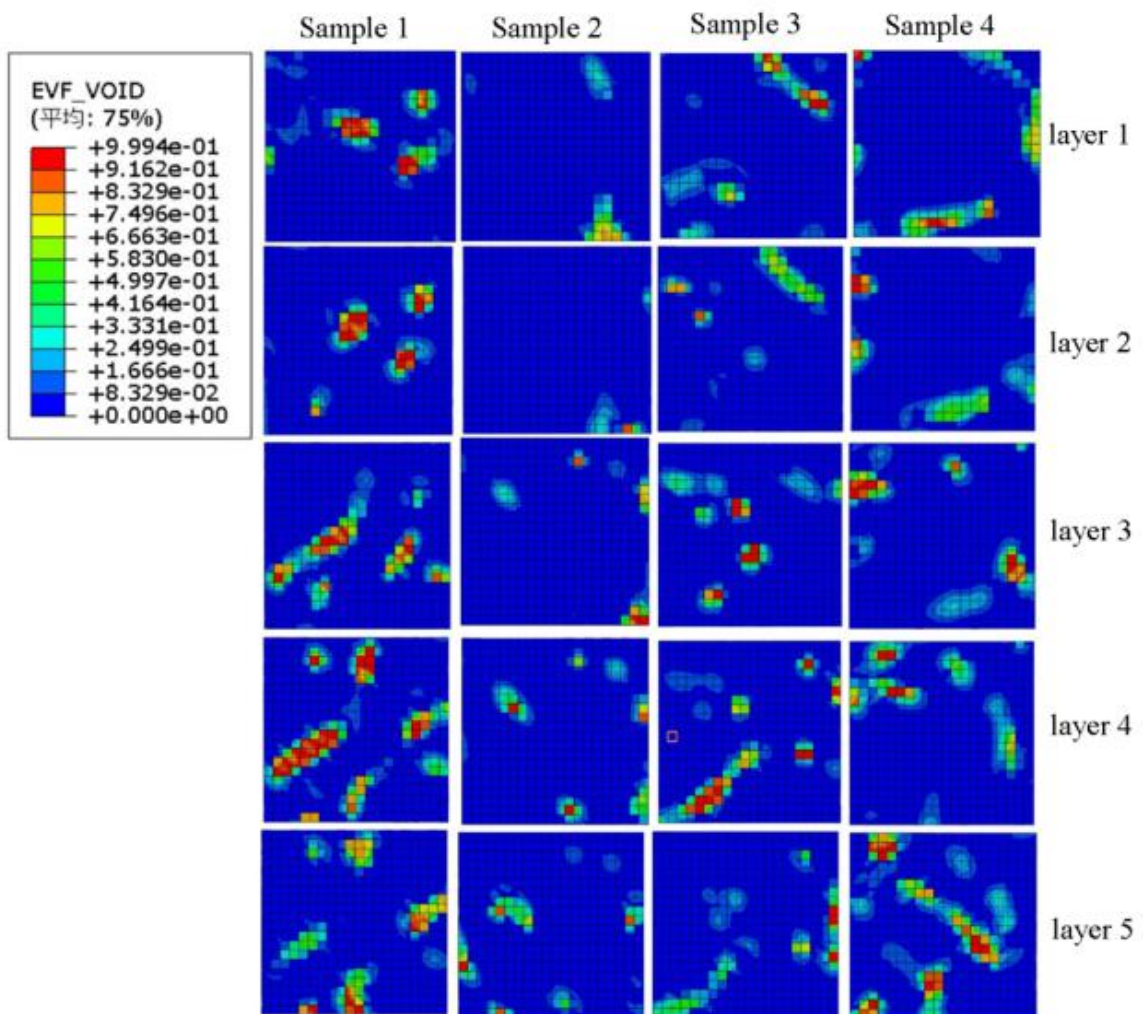
Fig. 4.40. The cross-sectional view of the EVF voids after slicing each layer 1-5 of

the four groups of sampling cuboids.

237
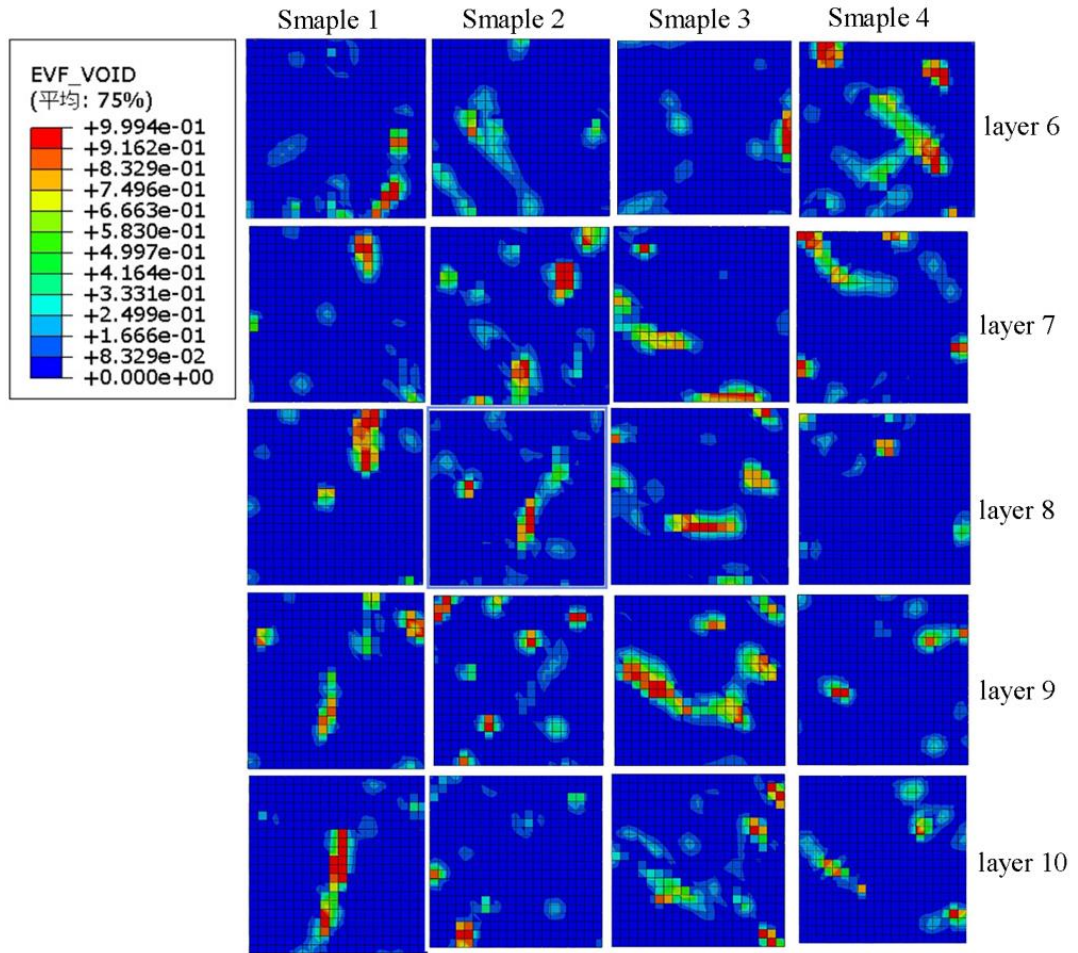
Fig. 4.41. The cross-sectional view of the EVF voids after slicing each layer 6-10 of the four groups of sampling cuboids.
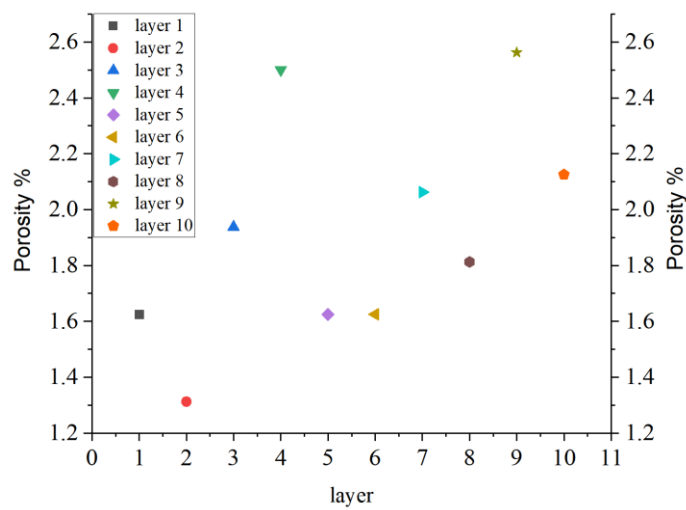
Fig. 4.42. The porosity value of each layer in the sample

The optimal Al6061 coating porosity was obtained through the RSM. Compare the predicted values with the simulation values. Table 4.8 shows the optimized parameter Al6061 coating porosity predicted value and simulation value and error. It can be seen from the results that the error between the predicted value and the simulation value of Al6061 coating porosity is only 2.55%; It shows that the regression equation about the porosity of Al6061 coating established through the RSM is reliable, and the simulation results can be effectively predicted through the regression equation.

Table. 4.8 − Optimized parameter Al6061 coating porosity predicted value and simulation value, and error.

Parameters	Factor			Predicted value	Simulation value	Error
	Particle temperature K	Substrate temperature K	Particle velocity m/s	P_e / %	P_r/ %	δ/%
Value	649.692	536.437	672.385	1.969	1.91875	2.55%

4.6.4 Summary of results

This section uses the CEL method to establish a multi-particle Al6061 deposition model, and optimize the particle temperature, substrate temperature, and particle velocity through the RSM. The regression equation for the void ratio of the Al6061 coating was established by pairwise interaction between the three variables, and the predicted value for the void ratio of the Al6061 coating was 1.969%. From the multi-factor coupling figures, it can be seen that the particle velocity has the greatest influence on the void ratio of the Al6061 coating, followed by the particle temperature, and the smallest influence is the substrate temperature. Optimum spraying parameters particle temperature 649.692 K, substrate temperature 536.437 K, particle velocity 672.385 m/s. In the calculation process of the void ratio of the Al6061 coating, multiple groups of samples were used to take the average, and the

void ratio value of the Al6061 coating under the optimal spraying parameters was obtained as 1.91875%. The error between the predicted value and the simulation value obtained through numerical simulation is only 2.55%.

4.7 Conclusion for the Chapter 4

1) Particle temperature and substrate temperature are both important factors affecting the deposition process. Particle temperature has the most significant impact on the deformation of particles after impact. In the process of simulating single particle depositions using the ALE, the SPH and, the CEL methods, increasing the particle's temperature will accelerate the thermal softening of the particles. The ALE method will cause the simulation calculation process to terminate early when simulating large particle deformations. Because of its robustness, the CEL method can well simulate the particle deposition process of actual cold spraying.

2) The CEL method establishes a multi-particle deposition model to simulate the actual cold spray process, which can be used to monitor and calculate coating porosity, which cannot be achieved by the ALE and the SPH methods. After multiple particles impact the surface of the substrate, the highest temperature is located at the interface between particles after deposition.

3) The impact of particle temperature on the coating is more obvious than the temperature of the substrate. Changing the particle temperature has a more obvious control effect on the porosity of the deposited coating, thereby increasing the density of the deposited coating. Preheating the particles can effectively reduce porosity. When the particle temperature reaches 650 K, the coating changes after deposition are no longer significant, indicating that there is an optimal temperature range for Al6061 particle deposition.

4) A multi-particle Al6061 deposition model was established using the CEL method. The average porosity of the coating under the three temperature conditions is 600 K – 5.08%; 650 K – 4.02%; 700 K – 3.58%. Increasing the particle

temperature can effectively reduce the porosity of the coating; during the deposition process of multiple particles, the inside of the deposited coating will be compacted. The temperature of the substrate will affect the combination of the coating and the substrate. It is recommended that the temperature difference between the particles and the substrate should not be too large.

5) The RSM studied the influence of multiple factors on the porosity of Al6061 coating. It was found that the velocity of particles has the greatest influence on the porosity of Al6061 coating, followed by particle temperature, and the smallest influence is the substrate temperature. The optimal spraying parameters were obtained through optimization particle temperature 649.692 K, substrate temperature 536.385 K, particle velocity 672.385 m/s, and Al6061 coating porosity 1.969%. The porosity of the Al6061 coating obtained during the simulation process was 1.91875%, and the error between the predicted value and the simulation value was only 2.55%.

CONCLUSIONS AND SUGGESTIONS FOR FUTURE WORK

This dissertation studies the supersonic flow field characteristics inside and outside the nozzle during the cold spraying process, the acceleration behavior of powder particles, the entrance position of particles, the multi-channel mixed cross-section right-angle cold spray nozzle, the multi-factor coupling optimization of the spray parameters of particles in the nozzle, and the particle deposition behavior with the substrate, the influence of technical parameters on the coating during particle deposition and the optimization of coating porosity were analyzed in detail. The effects of factors such as the length of the nozzle expansion section, the cross-sectional shape of the nozzle outlet, and the location of the particle inlet on the supersonic flow field and particle acceleration behavior inside and outside the cold spray nozzle were studied; the acceleration characteristics of various spray powder particles in a multi-channel mixed cross-section right-angle cold spray nozzle. Research on optimization of cold spray nozzle spraying parameters based on response surface analysis method and GA optimization BPNN. The effects of particle temperature and velocity as well as substrate temperature on the spray deposition process of Al6061 particles were studied. Python programming language is used to build multi-particle models, embedding the multi-particle model into the CEL deposition model. The CEL method was used to study the effect of spraying parameters on the porosity of Al6061 coating. Optimize the spraying process through response surface analysis to obtain the best Al6061 coating porosity under the ideal spraying parameters. Aiming at different research points, numerical calculation methods were used for analysis, and the following main conclusions were obtained:

1) The influence of the length of the Dymet nozzle expansion section and the inlet pressure on the acceleration characteristics of the particle was studied by a single factor method. The results showed that when the inlet pressure was 1.0 MPa and the nozzle expansion section length was 210mm, the optimal particle velocity

could be obtained, and it was recommended to round the joints in the Dymet nozzle expansion section.

2) Based on the critical velocity standard when the powder particles contacted the substrate surface, the influence of the acceleration characteristics of Al and Cu particles in the designed linear nozzle was optimized by the RSM. The results showed that the speeds of Al and Cu particles at the nozzle outlet were 502.54 m/s and 478.41 m/s; the speeds of Al and Cu particles before impacting the substrate were 494.5 m/s and 478.83 m/s, by comparing the predicted values of particle velocity with the simulation values obtained from numerical simulations. The error between the predicted value and the actual value of the Al particle velocity at the Laval nozzle outlet is 1.6 %. The error between the predicted value and the simulation value of the velocity before deposition on the substrate is 0.2 %. The error between the predicted value and the simulation value of the Cu particle velocity at the Laval nozzle outlet is only 0.1 %. The error between the predicted value and the simulation value of the Al particle velocity before deposition on the substrate is only 0.2 %. Overall, the regression equation for the outlet velocity V_e at the Laval nozzle outlet and particle velocity V_p before deposition on the substrate are reliable. Therefore, the results can be effectively used by the regression prediction approach. Achieving the basic requirements for the deposition of the two particles under the optimal spraying parameters.

3) Based on the critical velocity standard when the particles contact the substrate surface, the acceleration characteristics of Al6061 and Cu particles in the designed right-angle nozzle are optimized by the GA+BPNN. This method is implemented by programming, which reflects the research trend of cross-disciplinary integration of materials science + mathematical model + computer. The results show that by establishing a BPNN structure of 3-8-1, the optimal speeds of Al6061 and Cu particles at the right-angle nozzle outlet can be obtained: 571.23m/s and 520.71m/s.

4) The effect of the particle inlet of the right-angle nozzle on the acceleration

characteristics of various particles is studied. The results show that the outlet center velocity of the circular cross section nozzle is better than the rectangular cross section nozzle, and the viscous boundary layer effect is better, thereby ensuring a larger effective flow area. The particle inlet A scheme can achieve the acceleration of various particles, and the maximum gas flow velocity is 663.4m/s. This scheme can effectively avoid the hit and even accumulation of particles on the inner wall of the right-angle nozzle, thereby reducing the kinetic energy loss of particles during acceleration in the right-angle nozzle.

5) Based on the research of single-channel right-angle nozzle, a multi-channel mixed cross-section right-angle nozzle is further proposed. This type of nozzle can be used for surface spraying of special outer surface parts and inner surface parts. The nozzle can be operated as a handheld or robotic arm. The results show that the three-channel right-angle nozzle has better particle acceleration characteristics and particle utilization efficiency. The particle size has the most significant effect on the particle acceleration characteristics. The three-channel right-angle nozzle achieves the critical velocity of various particle materials (Al, Al6061, Cu, Mg, Zn) when deposited on the substrate.

6) The ALE, SPH and CEL methods are used to simulate the deposition of Al6061 single particles. The results show that the particle velocity and temperature have the most significant effects on the deformation of particles after deposition. The increase of particles can effectively accelerate the thermal softening of particles during the collision process. A new method for evaluating the influence of powder particle temperature-velocity parameters on substrate deposition using the particle deformation coefficient K is proposed.

7) In the study of multi-particle models, two schemes for creating multi-particle models are proposed: Solidworks assembly method and Python programming method. Among them, the establishment of the multi-particle model was completed through Python programming. The characteristic of this method is that the multi-particle model method can more accurately simulate the disordered arrangement of

particles in space during the real cold spraying process. This method provides a new idea for establishing a model for simulating cold spraying particle deposition.

8) Based on the single-factor analysis method, the CEL method is used to simulate the deposition of multi-particles. The results show that changing the particle temperature has a more obvious control effect on the porosity of the deposited coating, thereby improving the density of the deposited coating. Particle preheating can effectively improve the density of the Al6061 coating. When the particle temperature reaches 650K, the coating thickness no longer changes significantly, indicating that there is an optimal temperature range for the preparation of the Al6061 coating. In the study of the effect of particle temperature on the porosity of the coating, the average porosity of the coating under the three particle temperature conditions is 600 K – 5.08%; 650 K – 4.02%; 700 K – 3.58%. It further shows that increasing the temperature of the particles can effectively reduce the porosity of the coating, and the inside of the Al6061 coating will be compacted.

9) In order to be closer to the real cold spray process, the coating porosity is analyzed and optimized by introducing multi-factor coupling effects. Through the RSM, it was concluded that particle velocity has the greatest impact on the porosity of Al6061 coating. The goal spraying parameters were obtained through optimization particle temperature 649.692 K, substrate temperature 536.385 K, particle speed 672.385 m/s, and predicted coating porosity of 1.969%. The porosity of the coating obtained by the optimal spraying parameters is 1.91875%, and the error between the predicted value and the simulation value is only 3.3%.

Suggestions for future work.

1) The research results show that the proposed optimization method has proven to be an effective tool for optimizing the spray parameters of cold spray nozzles and Al6061 coatings. However, due to academic level and time constraints, there are inevitable flaws in the research process. In the three-channel mixed cross-section right-angle cold spray nozzle, the channel size of the throat part of the nozzle is less than 1 mm. Therefore, the requirements for processing accuracy are very high, and

I hope to conduct research, analysis, and demonstration through experiments in the future. All the work in the dissertation is based on the results obtained by numerical simulation. It will be more meaningful to compare the conclusions in the article with experiments in the future.

2) In the research field of simulating the deposition mechanism of cold spray particles, the commonly used spray materials are metal materials and have been widely studied. However, few scholars have used ceramic materials in simulating the cold spray deposition process. Ceramic materials are inherently brittle, which is particularly meaningful in cold spray deposition simulations. For example Al_2O_3; at the same time, Al_2O_3 is also a good particle for compacting the coating. Therefore, it is necessary to add more spray materials in future research, and accurately grasp the deformation behavior of more particles and substrates through a combination of numerical calculations and experiments, just to explore the mechanism of the cold spray deposition process.

3) At the same time, in the study of simulating cold spray deposition, it is recommended to try to develop a multi-particle model suitable for two or more materials and simulate the preparation of composite coatings through the CEL method in the future. This will enrich the methods and approaches for numerical simulation of cold spray particle deposition.

REFERENCES

1. Stoltenhoff, T., Kreye, H. & Richter, H.J. An analysis of the cold spray process and its coatings. Therm Spray Tech. 2002;211:542-50.

2. Tan, K., Markovych, S., Shorinov, O., & Hu, W. Deposition of protective and restorative coatings onto aircraft and engines parts printed with 3D technologies. Відкрита науково-практична студентська конференція факультету авіаційних двигунів (ФАД) «Сучасні проблеми двигунобудування, енергетики та інтелектуальної механіки»: Збірник тез доповідей конференції. – Харків: Національний аерокосмічний університет ім. М.Є. Жуковського «Харківський авіаційний інститут». 2020; С. 41.

3. He Jianbin, Xu Yan, Zhou Jianping. Research Progress of Additive Manufacturing Technology for Metal. Machine Tool & Hydraulics. 2020;48(1):171-75.

4. Wang Shijie, Wang Haidong, Luo Feng. Current research status of arc-based metal additive manufacturing technology. High-end Equipment Manufacturing. 2018;1:19-22.

5. Frazier, W. E.. Metal Additive Manufacturing: A Review. Journal of Materials Engineering and performance. 2014;23(6):14001.

6. Huang, Y., Leu, M. C., Mazumder, J., & Donmez, A. Additive Manufacturing: Current State, Future Potential, Gaps and Needs, and Recommendations. Journal of Manufacturing Science and Engineering. 2015;137(1):337-50.

7. Hu, W., Markovych, S., Shorinov, O., & Tan, K. Deposition of protective and restorative cold spraying coating on aircraft parts made of titanium alloys. Відкрита науково-практична студентська конференція факультету авіаційних двигунів (ФАД) «Сучасні проблеми двигунобудування, енергетики та інтелектуальної механіки»: Збірник тез доповідей конференції. – Харків: Національний аерокосмічний університет ім. М.Є. Жуковського «Харківський авіаційний інститут». 2020; С. 40.

8. Tan, K., Markovych, S., Hu, W., Shorinov, O., & Wang, Y. Review of manufacturing and repair of aircraft and engine parts based on cold spraying technology and additive manufacturing technology. Aerospace Technic and Technology. 2020;(3):53-70.

9. Yang Qiang, Lu Zhongliang, Huang Fuxu. Research status and development trends of titanium alloy laser additive manufacturing technology. Aviation Manufacturing Technology. 2016;12:1-6.

10. M. A., Popescu, A. C., & Mihailescu, I. N. Metal matrix composites synthesized by laser-melting deposition: a review. Materials. 2020;13(11):2593.

11. Fu Chengxue, Lei Xiaowei, Jia Xiaofei. Research and application progress of titanium alloy laser additive manufacturing technology. Welded Pipe. . 2023;46(8):11-18+24.

12. Kruth, J. P., Froyen, L., Van Vaerenbergh, J., Mercelis, P., Rombouts, M., & Lauwers, B. Selective Laser Melting of Iron-based Powder. Journal of materials processing technology. 2004;149(1-3):616-22.

13. Du, Baorui., Yao, Jun., Zheng, Huilong., Yu, Hao., Lin, Hongjie., & Ding, Ruochen. Optimization Design and Manufacturing Technology for Aero-Engine Nozzle Based on Selective Laser Melting Fabrication. Aeronautical Manufacturing Technology. 2019;62(11):14-18.

14. Liu, Yi., So, Xinkun., Huang, Jing., Xinjia, Guangxiong., Li, Hua. Applications and Perspectives of Cold Spray Technique. Surface Technology. 2016;45(9):25-31.

15. Wang, Zemin., Huang, Wenpu., Zeng, Xiaoyan. Status and Prospect of Selective Laser Melting Machines. Journal of Netshape Forming Engineering. 2019;11(4):21-28.

16. Chen, Shuai., Tao, Fenghe., Jia, Changzhi., Yang, Jianchun. Status and Progress of Selective Laser Melting Forming Technology. Proceedings of the 2015 3rd International Conference on Machinery, Materials and Information Technology Applications. 2015;11.

17. Zou, Tianchun., Ou, Yao. Effect of heat treatment on microhardness of laser selective melting of AlSi7Mg alloy. Hot Working Technology. 2019;48(24):123-26.

18. Herzog, D., Seyda, V., Wycisk, E., & Emmelmann, C. Additive Manufacturing of Metals. Acta Materialia. 2016;117:371-92.

19. Huang Chunping, Huang Shuowen, Liu Fincheng. Metal material additive manufacturing technology. Metal processing (thermal processing). 2016;2:34-38.

20. Sacco, E., & Moon, S. K. Additive manufacturing for space: status and promises. The International Journal of Advanced Manufacturing Technology. 2019;105:4123-46.

21. Chen G Q, Shu X, Zhang B G. State-of-arts of Electron Beam Freeform Fabrication Technology. Transactions of the China Welding Institution 2018;39(8):123-28.

22. Yadroitsev, I., Shishkovsky, I., Bertrand, P., & Smurov, I. Manufacturing of Fine-structured 3D Porous Filter Elements by Selective Laser Melting. Applied Surface Science. 2009;255(10):5523-27.

23. Zhang Y, Wu L, Guo X. Additive Manufacturing of Metallic Materials: A Review. Journal of Materials Engineering and Performance. 2018;27(1):1-13.

24. Palčič, I., Balažic, M., Milfelner, M., & Buchmeister, B. Potential of laser engineered net shaping (LENS) technology. Materials and Manufacturing Processes. 2009;24(7/8):750-53.

25. Song Wenqing, Li Xiaoguang, & Qu Shen. rospects for the application of metal additive manufacturing technology in aero-engines. Metal processing (thermal processing). 2016;2:44-46.

26. B. Vamsi Krishna, Susmita Bose, & Amit Bandyopadhyay. Low stiffness porous Ti structures for load-bearing implants. Acta Biomaterialia. 2007;3(6):997-06.

27. Mughal, M. P., Fawad, H., & Mufti, R. A. Three-dimensional Finite-element Modelling of Deformation in Weld－Based Rapid Prototyping. Proceedings

of the Institution of Mechanical Engineers: Part C: Journal of Mechanical Engineering Science. 2006;220(6):875-85.

28. Chen, C., Wang, Y., Ao, T., & Hui, G. Theoretical Study on Horizontal-Type SAW Device with Dual Function of Sensing and Removal of Non-specific Binding. Acta Physica Polonica A ISSN 1898-794X. 2024;145(5):281-81.

29. Su Xianyong, Zhou Xianglin, Cui Hua. Research progress of cold spray technology. Surface Technology. 2007;36(5):71-74.

30. Malachowska A. Analysis of the cold gas spraying process and determination of selected properties of metallic coatings on polymers. Limoges; 2016.

31. Xiong Jun. Multi-layer single-pass GMA additive manufacturing forming characteristics and deposition size control. Harbin: Harbin Institute of Technology. 2014.

32. H. Assadi, F. Gärtner, T. Stoltenhoff, H. Kreye. Bonding Mechanism in Cold Gas Spraying. Acta Materialia. 2003;51. Iss. 15:4379-94.

33. S. Grigoriev, A. Okunkova, A. Sova, P. Bertrand, I. Smurov. Cold Spraying: From Process Fundamentals Towards Advanced Applications. Surface & Coatings Technology. 2015;268:77-84.

34. Hu, W., Tan, K., Markovych, S., Cao, T. Research on structure and technological parameters of multi-channel cold spraying nozzle. Eastern-European Journal of Enterprise Technologies. 2021; 5(1):6-14.

35. Tan Kun. Analysis of Particle Parameters of Multi-Channel Mixed Cross-Section Right-Angle Cold Spray Nozzle Structure. Integrated Computer Technologies in Mechanical Engineering 2023. 2023;1008:52-56.

36. Shorinov, O. Finite element analysis of thermal stress in Cu2O coating synthesized on Cu substrate. Archives of Materials Science and Engineering. 2022. 2022;367(6):565-74.

37. Grujicic, M., Zhao, C. ., Tong, C., DeRosset, W. ., & Helfrich, D. Analysis of the impact velocity of powder particles in the cold-gas dynamic-spray process.

Materials Science and Engineering: A. 2004;368(1-2):222-30.

38. Hu, W., Markovych, S., Tan, K., Shorinov, O., & Cao, T. A Research on wear resistance coating of aircraft titanium alloy parts by cold spraying technology. Aerospace Technic and Technolog. 2020;(3):61-71.

39. Kulmala, M., & Vuoristo, P. Influence of process conditions in laser-assisted low-pressure cold spraying. Surface and Coatings Technology. 2008;202(18):4503-08.

40. Yin, S., Wang, X., Li, W., & Xu, B. Numerical Investigation on Effects of Interactions Between Particles on Coating Formation in Cold Spraying. Journal of Thermal Spray Technology. 2009;18(4):686-93.

41. Zhao Guofeng, Wang Yingying, Zhang Hailong. Research progress on cold spray equipment and cold spray technology application. Surface Technology. 2017;46(11):198-05.

42. Moridi, A., Hassani-Gangaraj, S. M., Guagliano, M., & Dao, M. Cold Spray Coating: Review of Material Systems and Future Perspectives. Surface Engineering. 2014;30(6):369-95.

43. Hussain, T., McCartney, D. G., Shipway, P. H., & Zhang, D. Bonding Mechanisms in Cold Spraying: The Contributions of Metallurgical and Mechanical Components. Journal of Thermal Spray Technology. 2009;18(3):364-79.

44. M. Grujicic., J.R. Saylor., D.E. Beasley., W.S. DeRosset., & D. Helfritch. Computational Analysis of the Interfacial Bonding between Feed-Powder Particles and the Substrate in the Cold-gas Dynamic-spray Process. Applied Surface Science. 2003;219(3/4):211-27.

45. Choi, W. B., Li, L., Luzin, V., Neiser, R., Gnäupel-Herold, T., Prask, H. J., & Gouldstone, A. Integrated Characterization of Cold Sprayed Aluminum Coatings. Acta Materialia. 2007;55(3):857-66.

46. Bae, G., Kumar, S., Yoon, S., Kang, K., Na, H., Kim, H. J., & Lee, C. Bonding Features and Associated Mechanisms in Kinetic Sprayed Titanium Coatings. Acta Materialia. 2009;57(19):5654-66.

47. Wang, Y. Y., Liu, Y., Li, C. J., Yang, G. J., & Kusumoto, K. Electrical and Mechanical Properties of Nano-structured TiN Coatings Deposited by Vacuum Cold Spray. Vacuum. 2012;86(7):953-59.

48. Fan S Q., Li C J., & Yang G J. Influence of TiCl4 Treatment on Performance of Dye-sensitized Solar Cell Assembled with Nano-TiO2 Coating Deposited by Vacuum Cold Spraying. Rare Metals. 2006;25(s1):163-68.

49. Christoulis, D. K., Guetta, S., Irissou, E., Guipont, V., Berger, M. H., Jeandin, M., & Ogawa, K. Cold-spraying Coupled to Nano-pulsed Nd-YaG Laser Surface Pre-treatment. Journal of Thermal Spray Technology. 2010;19(5):1062-73.

50. Ghiasi H, Pasini D, Lessard L. The Laserassisted Cold Spray Process and Deposit Characterisation. Surface & Coatings Technology. 2009;203(19):2851-57.

51. Takana, H., Ogawa, K., Shoji, T., & Nishiyama, H. Computational Simulation of Cold Spray Process Assisted by Electrostatic Force. Powder Technology. 2008;185(2):116-23.

52. Shorinov, O., Dolmatov, A., & Polyvian, S. The effect of process temperature and powder composition on microstructure and mechanical characteristics of low-pressure cold spraying aluminum-based coatings. Materials Research Express. 2023;10(2):026401.

53. Jodoin, B., Richer, P., Bérubé, G., Ajdelsztajn, L., Yandouzi, M., & Erdi, A. Pulsed-Cold Gas Dynamic Spraying Process: Development and Capabilities. Journal of Thermal Spray Technology. 2007;13:236-42.

54. Luo X., & Olivier H. Gas Dynamic Principles and Experimental Investigations of Shock Tunnel Produced Coatings. Journal of Thermal Spray Technology. 2009;4:546-54.

55. Beese, A. M., Carroll, B. E. Review of Mechanical Properties of Ti-6Al-4V Made by Laser-Based Additive Manufacturing Using Powder Feedstock. JOM. 2015;68(3):724-34.

56. Grigorievb. S, Okunkovab. A. Cold Spraying: From Process Fundamentals Towards Advanced Applications. Surface & Coatings Technology. 2015;268(5):77-

84.

57. Hu, W., Markovych, S., Tan, K., Shorinov, O., & Cao, T. SURFACE REPAIR OF AIRCRAFT TITANIUM ALLOY PARTS BY COLD SPRAYING TECHNOLOGY. Aerospace technic and technology. 2020;(3):30-42.

58. Zhang, Z., Meng, T. L., Lee, C. J. J., Wei, F., Ba, T., Zhang, Z. Q., & Pan, J. Experimental and Numerical Study of Al2219 Powders Deposition on Al2219-T6 Substrate by Cold Spray: Effects of Spray Angle, Traverse Speed, and Standoff Distance. Materials. 2023;16(15):5240.

59. Zhao M. Numerical study of the influence of particle and substrate parameters on the deposition characteristics of sprayed particles in cold spraying. Chongqing University. 2015.

60. Fukanuma H, Ohno N. In-flight particle velocity measurements with DPV-2000 in cold spray. Surface and Coatings Technology. 2016;5(201):1935-41.

61. Jodoin B, Ajdelsztajn L. Effect of particle size, morphology, and hardness on cold gas dynamic sprayed aluminum alloy coatings. Surface and Coatings Technology. 2006;201(6):3422-29.

62. Langseth M. Perforation of 12mm thick steel plates by 20mm diameter projectiles with flat, hemispherical and conical noses: part II: numerical simulations. International Journal of Impact Engineering. 2002;27(1):37-64.

63. Alkhimov, A. P, Kosarev, V. F. Gas-dynamic spraying. An experimental study of the spraying process. Journal of Applied Mechanics and Technical Physics. 1998;39(2):318-23.

64. Alkhimov, A. P, Kosarev, V. F. A method of cold gas-dynamic deposition. Doklady Akademii Nauk SSSR. 1990;315(5):1062-65.

65. Wang, X. F., LI. G., Yin, S., & Li, W. Y. Effect of non-vertical incidence angles of particles on bonding performance in cold spraying. Materials Science and Technolog. 2008;16(2):149-52.

66. Hu, W. J., Tan, K., Markovych, S., & Liu, X. L. Study of a cold spray nozzle throat on acceleration characteristics via CFD. Journal of Engineering Sciences.

2021;8(1):19-24.

67. Yin S. A systematic investigation on the acceleration behavior and deposition mechanism of cold sprayed particles. Dalian University of Technology. 2012.

68. Li, Jia., Yun, Cui., Guang, Liu., & Ziyun, Zheng. Research on cold spraying aluminum coating and its wear resistance. Ordnance Material Science and Engineering. 2017;40(3):70-80.

69. Xuefei, Li., Jinglong, Li., Wenya, Li. Application and prospect of cold spraying in welding engineering. Welding & Joining. 2008;9:13-16.

70. Lijing, Yang., Pingxiang, Zhang., Shaopeng, Wang., Zhengxian, Li. Research Progress of Oxidizing Sensitive Non-ferrous Metals Produced by Cold Spray. Thermal Spray Technology. 2018;10(4):23-32.

71. Tan, K., Markovych, S., Hu, W., Shorinov, O., & Wang, Y. Review of application and research based on cold spray coating materials. Aerospace Technic and Technology. 2021;1:47-59.

72. Zhou Xianglin, Zhang Jishan, Wu Xiangkun. Advanced cold spraying technology and application. Mechanical Industry Press. 2011.

73. Wang Hangong, Cha Bolin. Supersonic spraying technology. 2005.

74. Dolmatov A. I. Polyviany S. A. Interaction of Solid Particles from a Gas Stream with the Surface of a Flat Nozzle. Metallophysics and Advanced Technologies. 2021;43(3):319-28.

75. Li Wenya, Chang-Jiu Li. Optimal design of a novel cold spray gun nozzle at a limited space. Journal of thermal spray technology. 2005;14(3):391-96.

76. Li Wenya, Hanlin Liao, Hong-Tao Wang, Chang-Jiu Li, Ga Zhang, C. Coddet. Optimal design of a convergent-barrel cold spray nozzle by numerical method. Applied Surface Science. 2006;253(2):708-13.

77. Zhou Xianglin, Su Xianyong, Cui Hua. Simulation study on the influence of particle material properties on cold spray impact behavior. Acta Metallurgica Sinica. 2008;44(11):1286-91.

78 Ding Li, Wang Xiaofang, Sun Tao. Research on the bonding process of particles and substrates in cold spray material modification technology. Mechanical Engineering Materials. 2004;10:26-28+47.

79 Li Wenya, Li Jiujiu, Wang Yuyue, et al. Effects of parameters of cold sprayed Cu particles on their collision deformation behavior. Acta Metallurgica Sinica. 2005;03:282-86.

80 Su Xianyong. Numerical simulation analysis of cold spray particle collision process. Master's thesis. University of Science and Technology Beijing. 2007.

81. Wang Xiaofang, Li Gang, Yin Shuo. Analysis of the influence of non-vertical incidence of particles on the formation of cold spray coatings. Materials Science and Technology, 2008;02:149-52.

82. Huang Guosheng, Wang Hongren, Chen Guangzhang. Numerical simulation research on cold spray zinc coating. Proceedings of the Yuxiang Cup 10th National Youth Corrosion and Protection Technology Paper Review Conference and the 8th China Youth Corrosion and Protection Symposium. 2007.

83. Dykhuizen R C, Smith M F, Gilmore D L. Impact of high velocity cold spray particles. Journal of Thermal Spray Technology. 1999;8(4):559-64.

84. B. Pauwels, G. Van Tendeloo, W. Bouwen, L. Theil Kuhn, P. Lievens, H. Lei, M. Hou. low-energy-deposited Au clusters investigated by high-resolution electron microscopy and molecular dynamics simulations. Physical review B. 2000;62:10383-93.

85. Gao Hong. Research on shock wave and particle deposition process in cold spray. Chongqing University, PhD dissertation.2010.

86. Kari-Heinz Muller. Cluster-beam deposition of thin films: a molecular dynamics simulation. Journal of applied physics. 1986;61(7):2516-21

87. Horngming Hsieh, R. S. Averback. Molecular-dynamics simulations of collisions between energetic clusters of atoms and metal substrates. Physical review B. 1992;45:4417-30.

88. Hellmut Haberland. Molecular-dynamics simulation of thin-film growth by

energetic cluster impact. Physical review B. 1995; 51:11061-67.

89. Li Rongwu, Pan Zhengying, Huo Yukun. Molecular dynamics simulation of thin films deposited with low energy Cu clusters. Acta Physica Sinica. 1996; 45(7): 1113-21.

90. Xie Jun, Pan Zhengying, Man Zhenyong. Computer simulation study of C60 deposition on the surface of reconstructed diamond. Journal of Fudan University. 1998,;37(1): 37-42.

91. Zhang Qingyu. Study on the microscopic mechanism of film growth by depositing energy-carrying particles. Journal of Dalian University of Technology; 1999; 39(6): 730-35.

92. Zhang Qingyu, Ma Tengcai, Pan Zhengying, Tang Jiayong. Computer simulation of growth of Au/Au(100) epitaxial thin films deposited by energy-carrying atoms. Acta Physica Sinica. 2000;49(6): 1124-31

93. Zhang Chao, Lu Haifeng, Zhang Qingyu. Molecular dynamics simulation of the interaction between low-energy Pt atoms and Pt(111) surface. Acta Physica Sinica; 2002; 51(10): 2329-34

94. Kazumasa Yorizane, Yasunori Yamamura. Molecular dynamics studies of thin film growth by ionized cluster beam deposition. Computational materials science; 1999;14: 241-47.

95. Ralf Aderjan, Herbert M. Urbassek. Molecular-dynamics study of craters formed by energetic Cu cluster impact on Cu. Nuclear instruments and methods in physics research B. 2000;164: 697-04.

96. S.C. Lee, Nong M. Hwang, B. D. Yu, D.-Y. Kim. Molecular dynamics simulation on the deposition behavior of nanometer-sized Au clusters on a Au(001) surface. Journal of crystal growth. 2001; 223: 311-20.

97. Hu, W., Tan, K., Markovych, S., Cao, T. A simple method for determining the critical velocity value of cold spraying via SPH. nternational Conference on Artificial Intelligence and Advanced Manufacturing(AIAM 2021), Manchester, United Kingdom, 2021: 215-21.

98. Hu W. J. Effects of metal particles on cold spray deposition onto Ti-6Al-4V alloy via Abaqus/Explicit. Journal of Engineering Sciences.20207(2):19-25.

99. Malachowska A. Analysis of the cold gas spraying process and determination of selected properties of metallic coatings on polymers. Limoges. 2016.

100. Fernandez, R., Jodoin, B. Cold Spray Aluminum–Alumina Cermet Coatings: Effect of Alumina Content.Therm Spray Tech. 2018;27:603–23.

101. A. Manap, O. Nooririnah, H. Misran, T. Okabe & K. Ogawa. Experimental and SPH study of cold spray impact between similar and dissimilar metals. Surface Engineering. 2014;30(5):33541.

102. Abreeza MANAP, Kazuhiro OGAWA, Tomonaga OKABE, Numerical Analysis of Interfacial Bonding of Al-Si Particle and Mild Steel Substrate by Cold Spray Technique Using the SPH Method. Journal of Solid Mechanics and Materials Engineering. 2016;6(3):24150.

103. Xie J, Nélias D, Walter-Le Berre H. Simulation of the cold spray particle deposition process. Journal of Tribology. 2015;137(4):041101.

104. Profizi, P., Combescure, A., & Ogawa, K. SPH modeling of adhesion in fast dynamics: Application to the Cold Spray process. Comptes Rendus Mécanique. 2016344(4-5):211-24.

105. Zhang Xiong, Lu Mingwan, Wang Jianjun. Research progress on arbitrary Lagrangian-Eulerian description method. Journal of Computational Mechanics. 1997;1:93-04.

106]. Wang Hequan, Zhang Bo, Yuan Fuhe. Residual stress detection and simulation research on plasma sprayed NiCrAl coating on titanium alloy surface. Thermal Processing Technology. 2018; 47(22):147-51.

107. Wen-Ya Li; Shuo Yin; Xiao-Fang Wang. Numerical investigations of the effect of oblique impact on particle deformation in cold spraying by the SPH method. 2010;256(12):3725-34.

108. Yin, S., Wang, X., Xu, B., & Li, W. Examination on the Calculation

Method for Modeling the Multi-Particle Impact Process in Cold Spraying. Journal of Thermal Spray Technology. 2010;19(5):1032-41.

109. Fardan, A., Berndt, C. C., & Ahmed, R. Numerical modelling of particle impact and residual stresses in cold sprayed coatings: A review. Surface and Coatings Technology. 2021;409:126835.

110. Wang Feng, Zhao Ming. Numerical analysis of the deposition process of cold spray particles on the surface of cast iron and Q235 steel. Materials Herald, 2016; 30(10):135-38.

111. Wang Hequan, Zhang Bo, Yuan Fuhe, etc. Research on residual stress detection and simulation of plasma sprayed NiCrAl coating on titanium alloy surface. Thermal Processing Technology. 2018;47(22):147-51.

112. Tan, K. Numerical Study on Simulating the Deposition Process of Cold Spray Multi-Particle Al-6061 based on CEL Method. Mechanics and Advanced Technologies. 2024;8(1(100)):23-9.

113. Tan, K., Hu, W., Shorinov, O., & Wang, YR. Simulating multi-particle deposition based on CEL method: studying the effects of particle and substrate temperature on deposition. Aerospace Technic and Technology. 2024;1(193):64-75.

114. Manafi Farid H, McDonald A, Hogan JD. Impact Deposition Behavior of Al/B4C Cold-Sprayed Composite Coatings: Understanding the Role of Porosity on Particle Retention. Materials. 2023; 16(6):2525.

115. Weiller, Sebastien, and Francesco Delloro. A numerical study of pore formation mechanisms in aluminium cold spray coatings. Additive Manufacturing. 2022; 60:103193.

116. J. Xie, D. Nelias, H. W. Berre, K. Ogawa, Y. Ichikawa. Simulation of the Cold Spray Particle Deposition Process. Tribol. 2015;137.

117. Li, W., Gao, W. Some Aspects on 3D Numerical Modeling of High Velocity Impact of Particles in Cold Spraying by Explicit Finite Element Analysis. Appl. Surf. Sci. 2009;255(18):7878-92.

118. S. Bagherifard, S. Monti, M.V. Zuccoli, M. Riccio, J. Kondas and M.

Guagliano. Cold Spray Deposition for Additive Manufacturing of Freeform Structural Components Compared to Selective Laser Melting. Mater. Sci. Eng. A. 2018;721:339-50.

119. M. Hassani-Gangaraj, D. Veysset, V.K. Champagne, K.A. Nelson and C.A. Schuh, Adiabatic Shear Instability is not Necessary for Adhesion in Cold Spray. Acta Mater. 2018;158:430-39.

120. B. Yildirim, S. Muftu and A. Gouldstone, Modeling of High Velocity Impact of Spherical Particles. Wear. 2011;270:703-13.

121. MacDonald, D.; Fernández, R.; Delloro, F.; Jodoin, B. Cold spraying of armstrong process titanium powder for additive manufacturing. Therm. Spray Technol. 2017;26:598-09.

122. S.H. Zahiri, D. Fraser, S. Gulizia, and M. Jahedi. Effect of Processing Conditions on Porosity Formation in Cold Gas Dynamic Spraying of Copper. Therm. Spray Technol. 2005;15:422-30.

123. M. Terrone, A. A. Lordejani, J. Kondas, S. Bagherifard. A numerical Approach to design and develop freestanding porous structures through cold spray multi-material deposition. Surface and Coatings Technology. 2021; 421:127423.

124. Weiller, Sebastien, and Francesco Delloro. A numerical study of pore formation mechanisms in aluminium cold spray coatings. Additive Manufacturing. 2022;60:103193.

125. Song, X., Ng, K. L., Chea, J. M.-K., Sun, W., Tan, A. W.-Y., Zhai, W., Liu, E. Coupled Eulerian-Lagrangian (CEL) simulation of multiple particle impact during Metal Cold Spray process for coating porosity prediction. Surface and Coatings Technology. 2020;385:125433.

126. Tan, K., Markovych, S., Hu, W., Wang, Y., Shorinov, O., & Wang, Y. On the characteristics of cold spray technology and its application in aerospace industries.International Conference on Mechanical Engineering and Materials (ICMEM2020). Ser: Earth and Environmental Science. 2021;719(3):032023.

127. Yang Shiming, Tao Wenquan. Heat Transfer. Beijing: Higher Education

Press. 2007.

128. Wu Zhonglei. Internal flow field simulation and structural optimization design of cold spray gun nozzle. Henan University of Science and Technology. 2011.

129. Yin Shuo. Research on acceleration behavior and deposition mechanism of cold spray powder particles. Dalian University of Technology. 2012.

130. Wu Jianghang, Han Qingshu. Theory Methods and Applications of Computational Fluid Dynamics. Beijing Science Press. 1988.

131. Zhou Yulin. One-dimensional unsteady fluid mechanics. Beijing: Science Press. 1990.

132. Cheng Jiangwei. Numerical simulation study of gas-solid two-phase jet in cold spray process. Henan University of Science and Technology. 2011.

133. Kun, T., Jie, H. W., Markovych, S., & Wang, Y. Optimization of cold spray nozzles based on the response surface methodology. Journal of Engineering Sciences. 2024;11(1):1-11.

134. Wang Xinyue, Yang Qingzhen. Fundamentals of Thermodynamics and Gas Dynamics. Xi'an: Northwestern Polytechnical University Press. 2005.

135. Van Steenkiste, T. H. Kinetic spray coatings. Surface and Coatings Technology. 1999;111(1):62-71.

136. Papyrin A, Kosarev V, Klinkov S. Cold spray technology. Elsevier. 2006.

137. Shorinov, O., Dolmatov, A., Polyvian, S., & Balushok, K. Optimization of cold spray process parameters to maximize adhesion and deposition efficiency of Ni+Al2O3 coatings. Materials Research Express. 2023;10(12):126401

138. Dai, Z., Xu, F., Wang, J., & Wang, L. Investigation of dynamic contact between cold spray particles and substrate based on 2D SPH method. 2020;284:112520.

139. Liu Jingsong. Simulation of collision characteristics of supersonic laser deposition Stellite 6 particles based on Abaqus. Hangzhou: Zhejiang University of Technology. 2016.

140. Bai Yang. Controllable preparation and performance regulation of low-

pressure cold spray aluminum-based composite coatings. China University of Petroleum (East China). 2017.

141. Zhao Ming. Numerical study on the influence of particle and substrate parameters on the deposition characteristics of spray particles in cold spraying. Chongqing: Chongqing University. 2015.

142. Yin, S., Wang, X. F., Xu, B. P., & Li, W. Y. Examination on the calculation method for modeling the multi-particle impact process in cold spraying. Journal of Thermal Spray Technology. 2010;19:1032-41.

143. Zhang Z L, Long T, Chang J Z. A smoothed particle element method (SPEM) for modeling fluid-structure interaction problems with large fluid deformations. Comput Method Appl Mech Eng. 2019;356:261-93.

144. Liu M B, Liu G R. Smoothed particle hydrodynamics (SPH): An overview and recent developments. Arch Comput Method Eng. 2010;17:25-76.

145. Sun P N, Le Touzé D, Oger G. An accurate FSI-SPH modeling of challenging fluid-structure interaction problems in two and three dimensions. Ocean Eng. 2021;221:108552.

146. Wang P, Zhang A M, Ming F. A novel non-reflecting boundary condition for fluid dynamics solved by smoothed particle hydrodynamics. Fluid Mech. 2019;860:81-14.

147. Yang X, Kong S C. Smoothed particle hydrodynamics modeling of fuel drop impact on a heated surface at atmospheric and elevated pressures. Phys Rev E. 2020;102:033313.

148. Zhang C, Rezavand M, Zhu Y. SPHinXsys: An open-source meshless, multi-resolution and multi-physics library. Softw Impact. 2020;6:100033.

149. Xu F, Zhao Y, Yan R. Multidimensional discontinuous SPH method and its application to metal penetration analysis. Int J Numer Meth Eng. 2013;93:1125-46.

150. Li Yuchun, Shi Dangyong. Basic theory and engineering practice of ANSYS 11.0/LS-DYNA. Beijing: China Water Conservancy and Hydropower Press.

2008.

151. Bui, H. H., Sako, K., & Fukagawa, R. Numerical simulation of soil–water interaction using smoothed particle hydrodynamics (SPH) method. Journal of Terramechanics. 2007;44(5):339-46.

152. Colin, F., Egli, R., & Lin, F. Y. Computing a null divergence velocity field using smoothed particle hydrodynamics. Journal of Computational Physics. 2006;217(2):680-92.

153. Hallquist J O . LS-DYNA Theoretical manual. CA:Livermore Software Technology Corporation. 1998.

154. Johnson, G. R., & Cook, W. H. Fracture characteristics of three metals subjected to various strains, strain rates, temperatures and pressures. Engineering Fracture Mechanics. 1985;21(1):31-48.

155. Li W Y, Liao H, Wang H T, et al. Optimal design of a convergent-barrel cold spray nozzle by numerical method[J]. Applied Surface Science, 2006, 253(2): 708-13.

156. King, P. C., Bae, G., Zahiri, S. H., Jahedi, M., & Lee, C. An Experimental and Finite Element Study of Cold Spray Copper Impact onto Two Aluminum Substrates. Journal of Thermal Spray Technology. 2010;19(3):620-34.

157. Xie, Jing; Nélias, Daniel; Walter-Le Berre, Hélène; Ogawa, Kazuhiro; Ichikawa, Yuji. Simulation of the Cold Spray Particle Deposition Process. Journal of Tribology. 2015;137(4):041101.

158. I. Smojver; D. Ivančević. Bird strike damage analysis in aircraft structures using Abaqus/Explicit and coupled Eulerian Lagrangian approach. 2011;71(4):489-98.

159. Gang Qiu; Sascha Henke; Jürgen Grabe. Application of a Coupled Eulerian–Lagrangian approach on geomechanical problems involving large deformations. 2011;38(1):30-39.

160. M. Terrone, A. A. Lordejani, J. Kondas., & S. Bagherifard. A numerical Approach to design and develop freestanding porous structures through cold spray

multi-material deposition. Surface and Coatings Technology. 2021;421:127423.

161. A.I. Dolmatov and O. V. Bilchuk, Simulation of Process of Solid Particles Sputtering with Dimet Nozzle, Metallofiz. Noveishie Tekhnol. 2019;41(7):927-40.

162. Hu, W., Tan, K., Markovych, S., Cao, T. Structural Optimization of the Special Cold Spraying Nozzle via Response Surface Method. In: Nechyporuk, M., Pavlikov, V., Kritskiy, D. (eds) Integrated Computer Technologies in Mechanical Engineering - 2021. ICTM 2021. Lecture Notes in Networks and Systems. 2021;367. Springer, Cham.

163. Feng Wang, Ming Zhao. Simulation of particles deposition behavior in cold sprayed Mganti-corrosion coating. Materials and Manufacturing Processes. 2015.

164. H. Canales, A. Dolmatov, S. Markovich. Thermal Spray 2011: Proceedings of the International Thermal Spray Conference (DVS-ASM). 2011;01:835.

165. WANG Xiaofang, Li Gang. Effect of non-vertical incidence angles of particles on bonding performance in cold spraying. MATER IALS SCIENCE & TECHNOLOGY. 2008;(02):149-52.

166. Liu. Y, Xiao. Z, Yang. Q, Wang. L, Chen. H. Transactions of the Chinese Society for Agricultural Machinery. 2013;44:171.

167. Tan, K. Analysis of spray particles entrance of Right-angle cold spray nozzle based on CFD. Mechanics and Advanced Technologies. 2023;7(3):325-29.

168. Wang Hangong, Cha Bolin. Supersonic spraying technology. Science Press. 2005.

169. Zhou Xianglin, Zhang Jishan, Wu Xiangkun. Advanced cold spraying technology and application. Mechanical Industry Press. 2011.

170. Li, Q. Structure Design and Optimization of Cold Spray Gun. The Shenyang University of Technology. 2008.

171. Wenya, L., Changjiu, L. Optimal design of a novel cold spray gun nozzle at a limited space. Journal of Thermal Spray Technology. 2005;14:391-96.

172. Kun, T., Jie, H. W., Markovych, S., & Wang, Y. Dimet Laval nozzle

expansion section analysis and optimization. Journal of Engineering Sciences. 2021;8(2):6-10.

173. Zhu J-H., Zhang W-H., &Xia L. Topology optimization in aircraft and aerospace structures design. Archives of Computational Methods in Engineering. 2016;23:595-622.

174. Alhulaifi., A. S., Buck., & G. A. A Simplified Approach for the Determination of Critical Velocity for Cold Spray Processes. Journal of Thermal Spray Technology 2014;23(8):1259-69.

175. H. Canales., A. Litvinov, S., Markovych., & A. Dolmatov. Calculation of the critical velocity of low pressure cold sprayed materials. Issues of design and production of aircraft structures. 2014;3:86-91.

176. Li Linbo., Luo Hongjie., Du Hao., Ren Yupeng., Qiu Xiang., & Xiong Tianying. Influence of alumina content on apparent morphology and microstructure of cold sprayed Al-Al2O3 composite coatings. Surface Technology. 2021;5:1-11.

177. Chen Jin-xiong., Wang Qun., & Luo Si-si. Microstructure and properties of cold sprayed Al-Al2O3 coating on AZ31 magnesium alloy. The chinese journal of nonferrous metals. 2018;28(9):1720-29.

178. Gong Jian-guo., Jia Zheng-mei., & Gao Li. Performance study of cold spraying Al/SiO2 coating on AZ31 magnesium alloy. Light metals. 2018;5:43-47.

179. Wang Hong-tao., Yao Hai-long., & Yi Zhi-hai. Microstructure and properties of cold-sprayed SiC/Al nanocomposite coatings[J]. China surface engineering. 2018;31(6):98-08.

180. J. Xie, D. Nelias, H. W. Berre, K. Ogawa, Y. Ichikawa. Simulation of the Cold Spray Particle Deposition Process. Tribol. 2015:137.

181. Dassault Systemes. ABAQUS Analysis User's Manue, 6.11 ed. Simulia, Providence. 2011. Chap. 24.

182. Xie, W., Alizadeh-Dehkharghani, A., Chen, Q., Champagne, V. K., Wang, X., Nardi, A. T., Lee, J.-H. Dynamics and Extreme Plasticity of Metallic Microparticles in Supersonic Collisions. Scientific Reports. 2017;7:1.

183. Berthelot J-M, Sefrani Y. Damping analysis of unidirectional glass and Kevlar fibre composites. Composites Science and Technology. 2004;64:1261-78.

184. M.A. Meyers. Plastic Deformation at High Strain Rates. Dynamic Behavior of Materials. 2007:323-81.

185. Lin, E., Chen, Q., Ozdemir, O. C., Champagne, V. K., & Müftü, S. Effects of interface bonding on the residual stresses in cold-sprayed Al-6061: a numerical investigation. Journal of Thermal Spray Technology. 2019;28:472-83.

186. Fardan, A., Berndt, C. C., & Ahmed, R. Numerical modelling of particle impact and residual stresses in cold sprayed coatings: A review. Surface and Coatings Technology. 2021;409:126835.

187. Hassani-Gangaraj, M., Veysset, D., Champagne, V. K., Nelson, K. A., & Schuh, C. A. Adiabatic shear instability is not necessary for adhesion in cold spray. Acta Materialia. 2018;158:430-39.

188. W. J. Hu, K. Tan, S. Markovych, T. T. Cao, and X. L. Liu. Research on the Adhesive Mechanism of Al + Ti Mixed Powders Deposited on Ti6Al4V Substrate by CS Using Abaqus/Explicit. Metallofiz. Noveishie Tekhnol. 2022;44(5):613-21.

189. Hu, W., Tan, K., Oleksandr, S., & Cao, T. Study on multi-parameter of cold spraying technology via RSM and BP+ GA methods. 5th International Conference on Artificial Intelligence and Advanced Manufacturing (AIAM 2023). 2023:282-78.

190. Tan, K., Hu, W., Shorinov, O., & Wang, YR. Multi-parameter coupled optimization of Al6061 coating porosity based on the response surface method. Aerospace Technic and Technology. 2024;3(195):59-67.

APPENDIX A

List of the applicant's publications on the topic of the dissertation

Articles in scientific periodical publications included in category «A» of the List of scientific specialized publications of Ukraine, or in foreign publications indexed in the Web of Science Core Collection and/or Scopus databases:

1. Kun, T., Jie, H. W., Markovych, S., & Wang, Y. Dimet Laval nozzle expansion section analysis and optimization. Journal of Engineering Sciences, 2021, 8(2): F6-F10. DOI: https://doi.org/10.21272/jes.2021.8(2).f2. (Scopus)

2. Kun, T., Jie, H. W., Markovych, S., & Wang, Y. Optimization of cold spray nozzles based on the response surface methodology. Journal of Engineering Sciences, 2024, 11(1): F1-F11. DOI: https://doi.org/10.21272/jes.2024.11(1).f1. (Scopus)

3. Hu, W. J., Tan, K., Markovych, S., & Liu, X. L. Study of a cold spray nozzle throat on acceleration characteristics via CFD. Journal of Engineering Sciences, 2021, 8: 19-24. DOI: https://doi.org/10.21272/jes.2021.8(1).f3. (Scopus)

4. Hu, W., Tan, K., Markovych, S., & Cao, T. Research on structure and technological parameters of multi-channel cold spraying nozzle. Eastern-European Journal of Enterprise Technologies, 2021, 5(1(113)):6-14. DOI: https://doi.org/10.15587/1729-4061.2021.242707. (Scopus, SJR=0.402, Q3)

5. W. J. Hu, K. Tan, S. Markovych, T. T. Cao, and X. L. Liu. Research on the Adhesive Mechanism of Al + Ti Mixed Powders Deposited on Ti6Al4V Substrate by CS Using Abaqus/Explicit. Metallofiz. Noveishie Tekhnol, 2022, 44(5):613-621. DOI: https://doi.org/10.15407/mfint.44.05.0613. (Scopus, SJR=0.402, Q3)

Articles in scientific periodical publications included in the List of scientific specialized publications of Ukraine (category «Б»):

6. Tan, K., Markovych, S., Hu, W., Shorinov, O., & Wang, YR. Review of manufacturing and repair of aircraft and engine parts based on cold spraying technology and additive manufacturing technology. Aerospace Technic and Technology, 2020 (3): 53-70. DOI: https://doi.org/10.32620/aktt.2020.3.06.

7. Tan, K., Markovych, S., Hu, W., Shorinov, O., & Wang, YR. Review of

application and research based on cold spray coating materials. Aerospace Technic and Technology, 2021 (1): 47-59. DOI: https://doi.org/10.32620/aktt.2021.1.05.

8. Tan, K., Hu, W., Shorinov, O., & Wang, YR. Simulating multi-particle deposition based on CEL method: studying the effects of particle and substrate temperature on deposition. Aerospace Technic and Technology, 2024, 1(193): 64-75. DOI: https://doi.org/10.32620/aktt.2024.1.06.

9. Tan, K. Analysis of spray particles entrance of Right-angle cold spray nozzle based on CFD. Mechanics and Advanced Technologies, 2023, 7(3(99)): F1-F11. DOI: https://doi.org/10.20535/2521-1943.2023.7.3.292244.

10. Tan, K. Numerical Study on Simulating the Deposition Process of Cold Spray Multi-Particle Al-6061 based on CEL Method. Mechanics and Advanced Technologies, 2024, 8(1(100)). DOI: https://doi.org/10.20535/2521-1943.2024.8.1(100).295144.

11. Tan, K., Hu, W., Shorinov, O., & Wang, YR. Multi-parameter coupled optimization of Al6061 coating porosity based on the response surface method. Aerospace Technic and Technology, 2024, 3(195): 59-67. DOI: https://doi.org/10.32620/aktt.2024.3.05.

12. Hu, W., Markovych, S., Tan, K., Shorinov, O., & Cao, T. RESEARCH ON WEAR RESISTANCE COATING OF AIRCRAFT TITANIUM ALLOY PARTS BY COLD SPRAYING TECHNOLOGY. Aerospace Technic and Technology, 2020, (6): 61-71. DOI: https://doi.org/10.32620/aktt.2020.6.07.

13. Hu, W., Markovych, S., Tan, K., Shorinov, O., & Cao, T. SURFACE REPAIR OF AIRCRAFT TITANIUM ALLOY PARTS BY COLD SPRAYING TECHNOLOGY. Aerospace Technic and Technology, 2020, (3): 30-42. DOI: https://doi.org/10.32620/aktt.2020.3.04.

14. Tan Kun. Analysis of Particle Parameters of Multi-Channel Mixed Cross-Section Right-Angle Cold Spray Nozzle Structure. Integrated Computer Technologies in Mechanical Engineering (ICTM). ICTM 2023. Lecture Notes in Networks and Systems, LNNS. 1008, pp. 52 – 65, 2024, Kharkiv, Ukraine. DOI:

https://doi.org/10.1007/978-3-031-61415-6_5. (Scopus)

15. Tan, K., Markovych, S., Hu, W., Wang, Y., Shorinov, O., & Wang, Y. On the characteristics of cold spray technology and its application in aerospace industries. International Conference on Mechanical Engineering and Materials (ICMEM2020). Ser: Earth and Environmental Science. 2021. vol. 719(3), p.032023. DOI: https://doi.org/10.1088/1755-1315/719/3/032023. (Scopus)

16. Hu, W., Tan, K., Markovych, S., Cao, T. Structural Optimization of the Special Cold Spraying Nozzle via Response Surface Method. Integrated Computer Technologies in Mechanical Engineering (ICTM). ICTM 2021. Lecture Notes in Networks and Systems, vol. 367, pp. 110 – 122, 2022, Kharkiv, Ukraine. DOI: https://doi.org/10.1007/978-3-030-94259-5_11. (Scopus)

17. Hu, W., Tan, K., Markovych, S., Cao, T. A simple method for determining the critical velocity value of cold spraying via SPH. International Conference on Artificial Intelligence and Advanced Manufacturing (AIAM 2021). Manchester, England. pp. 215-221. 2021. DOI: https://doi.org/10.1109/AIAM54119.2021.00052. (Scopus)

18. Hu, W., Tan, K., Oleksandr, S., & Cao, T. Study on multi-parameter of cold spraying technology via RSM and BP+ GA methods. 5th International Conference on Artificial Intelligence and Advanced Manufacturing (AIAM 2023). pp. 272-278. 2021. DOI: https://doi.org/10.1049/icp.2023.2950. (Scopus).

19. Hu, W., Markovych, S., Shorinov, O., Tan, K. Deposition of protective and restorative cold spraying coating on aircraft parts made of titanium alloys. Відкрита науково-практична студентська конференція факультету авіаційних двигунів (ФАД) «Сучасні проблеми двигунобудування, енергетики та інтелектуальної механіки»: Збірник тез доповідей конференції. – Харків: Національний аерокосмічний університет ім. М.Є. Жуковського «Харківський авіаційний інститут», 2020. – С. 40. https://drive.google.com/file/d/1trS11rljWf1ylXnAkefWSohV8rkH5p28/view

20. Tan, K., Markovych, S., Shorinov, O., Hu, W. Deposition of protective and

restorative coatings onto aircraft and engines parts printed with 3D technologies. Відкрита науково-практична студентська конференція факультету авіаційних двигунів (ФАД) «Сучасні проблеми двигунобудування, енергетики та інтелектуальної механіки»: Збірник тез доповідей конференції. – Харків: Національний аерокосмічний університет ім. М.Є. Жуковського «Харківський авіаційний інститут», 2020. – С. 41. https://drive.google.com/file/d/1trS11rljWf1ylXnAkefWSohV8rkH5p28/view

APPENDIX B

Multi-particle model Python script

#This Python script takes 4 particles of different diameters as examples, which can be further added according to the needs of the deposition model.

```
regionR                #Cylinder area radius
regionH                #Cylindrical area height
R1                     #Radius of particle 1
countR1                #Number of particles 1
R2                     #Radius of particle 2
countR2                #Number of particles 2
R3                     #Radius of particle 3
countR3                #Number of particles 3
R4                     #Radius of particle 4
countR4                #Number of particles 4
iteration1 = 100000    #Particle 1 Iterations
iteration2 = 100000    #Particle 2 Iterations
iteration3 = 100000    #Particle 3 Iterations
iteration4 = 100000    #Particle 4 Iterations

from abaqus import *
from abaqusConstants import *
import random

myModel = mdb.models["Model-1"]
mysketch_1 = myModel.ConstrainedSketch(name='mysketch_1', sheetSize=200.0)

#create ball
R=["R1", "R2", "R3", "R4"]
i = 0
for Radius in [R1, R2, R3, R4]:
    partName = "Particle-{}".format(R[i])
    i += 1
    mysketch_2 = myModel.ConstrainedSketch(name='mysketch_2', sheetSize=200.0)
    mysketch_2.ConstructionLine(point1=(0.0, -100.0), point2=(0.0, 100.0))
    curve = mysketch_2.CircleByCenterPerimeter(center=(0.0, 0.0), point1=(Radius, 0.0))
    mysketch_2.autoTrimCurve(curve1=curve, point1=(-Radius, 0.0))
    mysketch_2.Line(point1=(0.0, Radius), point2=(0.0, -Radius))
    myPart2    =    myModel.Part(name=partName,    dimensionality=THREE_D,
type=DEFORMABLE_BODY)
    myPart2.BaseSolidRevolve(sketch=mysketch_2,                    angle=360.0,
flipRevolveDirection=OFF)
    del mysketch_2
```

```python
    #Assembly
    myAssembly = myModel.rootAssembly

    def interCheck(point,center,radius1,radius2):
        sign = True
        for p in center:
            if      sqrt((point[0]-p[0])**2+(point[1]-p[1])**2+(point[2]-p[2])**2)      <=
(radius1+radius2):
                sign = False
                break
        return sign


    # caculate Radius of particle 1
    count = 0
    count1 = 0
    centerR1 = []
    while True:
        while True:
            disX = random.uniform(-regionR+R1, regionR-R1)
            disY = random.uniform(-regionR+R1, regionR-R1)
            if disX**2+disY**2<=(regionR-R1)**2:
                break
        disZ = random.uniform(R1, regionH-R1)
        if len(centerR1)==0:
            centerR1.append([disX,disY,disZ])
        else:
            if interCheck([disX,disY,disZ],centerR1,R1,R1):
                centerR1.append([disX,disY,disZ])
                count += 1

        if count >= countR1:
            break
        count1 +=1
        if count1 >= iteration1:
            break

    # caculate Radius of particle 2
    count = 0
    count1 = 0
    centerR2 = []
    while True:
        while True:
            disX = random.uniform(-regionR+R2, regionR-R2)
            disY = random.uniform(-regionR+R2, regionR-R2)
```

```python
            if disX**2+disY**2<=(regionR-R2)**2:
                break
        disZ = random.uniform(R2, regionH-R2)
        if len(centerR2) == 0:
            centerR2.append([disX,disY,disZ])
        else:
            if interCheck([disX,disY,disZ],centerR2, R2, R2):
                if interCheck([disX,disY,disZ],centerR1,R2,R1):
                    centerR2.append([disX,disY,disZ])
                    count += 1
        if count >= countR2:
            break
        count1 +=1
        if count1 >= iteration2:
            break


# caculate Radius of particle 3
count = 0
count1 = 0
centerR3 = []
while True:
    while True:
        disX = random.uniform(-regionR+R3, regionR-R3)
        disY = random.uniform(-regionR+R3, regionR-R3)
        if disX**2+disY**2<=(regionR-R3)**2:
            break
    disZ = random.uniform(R3, regionH-R3)
    if len(centerR3) == 0:
        centerR3.append([disX,disY,disZ])
    else:
        if interCheck([disX,disY,disZ],centerR3,R3,R3):
            if interCheck([disX,disY,disZ],centerR2, R3, R2):
                if interCheck([disX,disY,disZ],centerR1,R3,R1):
                    centerR3.append([disX,disY,disZ])
                    count += 1
    if count >= countR3:
        break
    count1 +=1
    if count1 >= iteration3:
        break

# caculate Radius of particle 4
count = 0
count1 = 0
centerR4 = []
```

```python
    while True:
        while True:
            disX = random.uniform(-regionR+R4, regionR-R4)
            disY = random.uniform(-regionR+R4, regionR-R4)
            if disX**2+disY**2<=(regionR-R4)**2:
                break
        disZ = random.uniform(R4, regionH-R4)
        if len(centerR4) == 0:
            centerR4.append([disX,disY,disZ])
        else:
            if interCheck([disX,disY,disZ],centerR4,R4,R4):
                if interCheck([disX,disY,disZ],centerR3, R4, R3):
                    if interCheck([disX,disY,disZ],centerR2, R4, R2):
                        if interCheck([disX,disY,disZ],centerR1,R4,R1):
                            centerR4.append([disX,disY,disZ])
                            count += 1
        if count >= countR4:
            break
        count1 +=1
        if count1 >= iteration4:
            break


    for index in range(1,len(centerR1)):
        myAssembly.Instance(name='Particle-R1-{}'.format(index),
part=myModel.parts["Particle-R1"], dependent=ON)
        myAssembly.translate(instanceList=('Particle-R1-{}'.format(index),),
vector=tuple(centerR1[index]))
    for index in range(1,len(centerR2)):
        myAssembly.Instance(name='Particle-R2-{}'.format(index),
part=myModel.parts["Particle-R2"], dependent=ON)
        myAssembly.translate(instanceList=('Particle-R2-{}'.format(index),),
vector=tuple(centerR2[index]))
    for index in range(1,len(centerR3)):
        myAssembly.Instance(name='Particle-R3-{}'.format(index),
part=myModel.parts["Particle-R3"], dependent=ON)
        myAssembly.translate(instanceList=('Particle-R3-{}'.format(index),),
vector=tuple(centerR3[index]))
    for index in range(1,len(centerR4)):
        myAssembly.Instance(name='Particle-R4-{}'.format(index),
part=myModel.parts["Particle-R4"], dependent=ON)
        myAssembly.translate(instanceList=('Particle-R4-{}'.format(index),),
vector=tuple(centerR4[index]))
```